ELASTOHYDRODYNAMIC LUBRICATION OF BIG END BEARINGS UNDER STEADY AND CYCLIC LOADS

A thesis submitted for the Degree of
Doctor of Philosophy
in Mechanical Engineering at the
University of Canterbury,
Christchurch, New Zealand

M. B. Aitken

1989

To

D.J.A

ABSTRACT

Lubrication of the big-end bearing is re-examined under elastohydrodynamic assumptions. All current models were found to be in someway deficient, motivating the development of a new consistent schema.

Uniform axial film-thickness assumptions and parabolic axial pressure profiles are combined with curved-beam and planar Finite Element housings to produce a single dimensional EHL model. Body-forces due to con-rod motion were found to be a necessary part of the elasticity implementation.

The role of discretisation and surface displacement interpolation errors are investigated under steady load conditions. Under dynamic load, ring, housing and previous experimental works are compared.

Increased dynamic journal action from housing distorsion was found to lead to film collapses not present in equivalent rigid bearing analyses; these collapses are likened to vapour cavitation. Correlation of dynamic film-thickness measurements with the elastic solutions are generally improved over rigid predictions.

With regard to minimum film thickness, inertial 'ring' solutions gave similar values to housing solutions with and without gas loading; this facilitates non-dimensionalisation. Two separate minimum-film régime were subsequently identified : one in the con-rod neck and a second, at higher load, in the cap. The first condition sees thicker minimum films than the rigid bearing; the second, thinner films with an increased sensitivity to load.

Non-dimensionalisation of this transition along with bearing flexibility and load enabled new tribological measures to be developed; the influence of elastic geometry on minimum film thickness is sufficiently well portrayed to make these useful design tools.

ACKNOWLEDGEMENTS

The author would like to thank :

Professor H. McCallion for bringing a most valuable resource to this work : his experience, patience and thoughts.

My 'family' : Ella and Norma for their sacrifices, Ruth, Noel and Neil (!); all have been ever supportive during a difficult period.

Fellow postgrads, past and present, for the realisation that we are not in this alone.

Roger and Kevin for doubling the readership and finally Beverley, for the typing of this thesis.

The financial support of a Todd Motors Research Scholarship is gratefully acknowledged.

CONTENTS

APPENDIX A1 Spatial Film Derivative

APPENDIX A2 Friction Tractions

APPENDIX A3 Volume Flux

APPENDIX A4 Connecting-Rod Dynamics

- (a) Kinematics
- (b) Rod Dynamics
- (c) Piston Dynamics
- (d) Rod-Piston Equilibrium
- (e) System Solution
- (f) Structural-Dynamic Consistency
- (g) Non-Dimensional Load

APPENDIX A5 Curved Beam Constants and Matrices

APPENDIX A6 Elastic Displacement Trial Functions

APPENDIX A7 Ruston-Hornsby : 200, 400, 700 rpm results

APPENDIX A8 Bearing Parameters

- (a) Ruston and Hornsby Bearing
- (b) Fantino's Bearing

CHAPTER ONE

INTRODUCTION

One of the principle tenets of solid mechanics was enunciated by Hooke[1] as the Latin anagram

'*ceiiinosssttuu*'

This was later revealed to be 'as the extension so the force' or, in a more modern idiom, structures resist external forces through deflection.

In many engineering situations dimensional considerations allow such deformations to be ignored. Unfortunately lubricating oil-films are not one of them: the development over the last 30 years of elastohydrodynamic lubrication (EHL) theory is witness to this. Although much of this body of work pertains to the counterformal contact problem[2,3], the particular case of the big-end bearing is in essence no different. Here the characteristic dimension is that of bearing clearance, typically three orders of magnitude less than the basic geometry: oil-film forces and con-rod body-forces then exact an influence on dynamic film geometry; con-rod bolt forces, bearing shell crushing forces, machining and fixturing forces on static film geometry.

Consequently, the success (or otherwise) of a big-end bearing rests with the designer having an appreciation of these diverse interactions; this is demonstrably the case for the various static effects. Dynamic interactions and their cyclic ramifications are, in comparison, poorly understood if not misunderstood: this thesis attempts in some small way to redress this situation.

1.1 Literature

Many of the earlier journal bearing researchers recognised deformation as being important: Reynolds[4] discussed the influence of elasticity on bearing clearance; Carl[5] attributed reduced experimental peak pressures and positional shifts in minimum film thickness to distorsion. However, by 1966, the review paper of Campbell[6] on the state of reciprocating bearing research revealed not a single elastic analysis. This situation was however about to change, two separate approaches having been initiated :

- the flexible liner problem
- the big-end housing problem

The liner problem began in the work of Higginson[7] and O'Donoghue[8]; Higginson used a thin liner or 'Winkler' foundation†, O'Donoghue, thick liner geometry; both used long bearing oil-film assumptions. The latter group subsequently investigated a variety of effects : validity of thin liner assumptions[9]; finite as opposed to long bearing theory[10]; approximate finite length solutions[11]. Conway later tackled the isoviscous assumptions[12] along with a short bearing analysis of thin liners in [13]. Benjamin[14] further extended these solutions to a liner of finite length, in the process addressing numerical convergence problems. The liner problem still attracts interest today[15], however it bears little resemblance to the con-rod problem: liners are circumferentially symmetric whilst the con-rod has at most, a single circumferential symmetry; strong coupling between elasticity and oil-film consequently develop for non-symmetric con-rod loadings.

The second approach, that of elastic housings, was sign-posted by the work of Ibrahim[16] : elastic distorsion of static con-rod housings under various load configurations were presented and seen to be important. Lubrication analysis of

---

† deflection is proportional to pressure

the problem followed in the thesis of Allen[17]: despite an invalid dynamic formulation, sound planar ring solutions were developed on the steady-state equation subset[22]. Oh[18] later presented a comprehensive Finite Element analysis incorporating the distorsion of a three-dimensional housing on a finite length bearing. Fantino[19] presented a similar analysis using planar elastic relationships, additionally incorporating a piezoviscous lubricant; the development of oscillatory pressure distributions in this work generated considerable discussion. Stafford[20] building on Allen's steady-state approach, presented further planar Finite Element solutions.

Experimental works accompanied these theoretical solutions: Frene[21] investigated the distorted forms of an araldite rod using speckle interferometry; Bozaci[22] determined pressure distributions and distorted forms on a geometry mimicking that of Allen. This latter work verified the multiple pressure peaks first observed by Allen.

With hindsight, it is probably fair to say that research during this period lost sight of the fact that the steady state con-rod problem is by-and-large pathological; Martin's[23] 1983 review paper on 'Developments in Engine Bearing Design' reflects this, eagerly looking towards the then forthcoming con-rod work of Fantino[24].

This work was the first major attempt at extending the steady-state model to the time domain: a short bearing Reynolds equation approximation was coupled to planar (two-dimensional) elastic geometry, deformations being determined on the basis of mean oil-film pressure. Unfortunately, two major errors mar this implementation: Reynolds' equation was applied to a frame of reference in which it was not invoked; elasticity loadings were misrepresented by the exclusion of body-force displacements. These errors have unfortunately propagated not only into their later works[25,26], but also into the wider literature.

Smith[27] incorporates both of Fantino's errors in a plane strain, short bearing model. However, he did manage to dispose of one of the offending terms in Fantino's equations. LaBouff[28] published finite bearing solutions using a correct form of Reynolds' equation, their planar elasticity description only including the effects of pressure deflections.

In an adventurous departure from Fantino's model, Oh[29] incorporates in a finite length bearing model, the additional effects of axial deformation. A correct form of Reynolds' equation is used however deformations are again determined solely on the basis of pressure. This error carries over into their subsequent works: in [30], *a priori* axial pressure distributions are introduced into the calculation to reduce computation; [31] uses this improved method to investigate 'optimal' con-rod geometries.

The first work to incorporate body-force deflections was that of van der Tempel[32,33]. This work was based on a plane strain elastic model and a short bearing approximation; a correct form of Reynolds' equation was invoked unfortunately in conjunction with an inconsistent model of body-forces. These forces are simulated by attaching point masses to surface nodes, nodes which only displace radially: exclusion of the tangential displacements results in only half the strain energy of these actions appearing in the structure.

To date, none of these dynamic solutions have been verified experimentally; in fact, one has to go back to the work of Butcher[34], Hiruma[35] and Goodwin[36] to find relevant experimental measurements. This is something of a misdemeanour considering the complexity of the problem.

Of all the accompanying EHL developments, probably the most telling have been in solution techniques. The earlier steady-state works mainly used direct iteration[17,18]: these solutions required the use of damping to stabilise the iterations which, in turn, slowed convergence. Benjamin[14] indicated the direction of future work; he found Newton-Raphson techniques particularly useful

under conditions of heavy load.

Newton-Raphson has since been expanded by Rohde[37] into a 'unified treatment' for EHL problems. Its robustness and rapid convergence are however countered by increased computational cost and complexity: many analysts seem reluctant to submit to this, damped iterative schemes still being present[24]. Oh[38] and Kostreva[39] have since refined Rhode's treatment into a complementarity problem.

More recently, multi-grid techniques have been introduced to the EHL problem[40,41]. These techniques promise fast convergent solutions, although to be fair, very little effort has gone into optimising the Newton-Raphson schemes: Kostreva's use of non-linear optimisation solvers is a first step in this direction.

All-in-all, the transient EHL con-rod problem is both challenging and attractive: challenging experimentally in that the processes are dynamic and the films thin; challenging theoretically in that sophisticated numerical procedures are necessary to generate any solution at all; attractive in that it quite likely holds the key to understanding plain bearing failure phenomena.

1.2 Scope of the Present Work

This thesis investigates the elastic con-rod problem on two fronts :

Firstly, conspicuous discrepancies have arisen in the various forms of Reynolds' equation used in the literature. Furthermore, serious misconceptions have proliferated regarding con-rod loadings; neither of these issues have been addressed by the current literature. Thus, we firstly investigate the question of theory: Chapter Two develops a consistent schema for the dynamic con-rod problem; Chapters Three through to Six look at the solution and, in particular, the verification of this model against existing theoretical and experimental works.

The second issue to be addressed is that of mechanisms: Despite a mounting body of work on the elastic con-rod, very little information has

percolated into the literature regarding elastic oil-film behaviour. Moreover, few, if any guidelines have emerged for the designer: Chapter Six provides detailed information on film mechanisms as affected by elasticity; Chapter Seven presents a dimensionless characterisation of elastic bearing 'performance'.

We begin this investigation by looking at the governing equations.

CHAPTER TWO

GOVERNING EQUATIONS

Analysis of an elastohydrodynamic lubrication problem requires the simultaneous solution of fluid-film and elasticity equations. This Chapter develops the relevant expressions for this work.

The equations governing lubricating film behaviour are firstly re-examined in light of small surface displacements, coordinate systems and film geometry specific to connecting rods being introduced.

Cavitation boundary conditions incorporating traditional gas cavitation procedures and a tentative vapour cavitation mechanism are constructed completing the fluid-film description.

Planar elastic relationships, developed in integral form, are then used to clarify rod loadings. Simplified consistent loading régimes are presented. The particular elastic descriptions used in this work; thick curved beams and isotropic plane-stress relationships, are briefly introduced.

Finally, the two sets of relationships are coupled to complete the EHL description.

Discretisation and solution of these equations are dealt with in Chapters Three and Four respectively.

2.1 Fluid Film Equations

To outline the inherent assumptions of Reynolds' equation, a schematic derivation adopting an isoviscous[19] incompressible approach is firstly presented. Detailed treatments have been given elsewhere.[42,43]

2.1.1 *Generalised Reynolds Equation*

In an inertial reference frame, the equations governing the motion of an isoviscous incompressible Newtonian fluid may be written as follows :[44]

- Conservation of mass

$$\text{div } \underset{\sim}{v} = 0$$

- Conservation of momentum

$$\rho \frac{D\underset{\sim}{v}}{Dt} = \rho \underset{\sim}{b} - \text{grad } p - \mu \text{ curl curl } \underset{\sim}{v}$$

where $\underset{\sim}{v}$, ρ, p and μ represent fluid velocity, density, pressure and dynamic viscosity respectively.

We assume that inertial forces $\rho \frac{D\underset{\sim}{v}}{Dt}$ and body force $\rho \underset{\sim}{b}$ are small compared to forces resulting from pressure and viscosity. This simplifies the governing equations to :

$$\text{div } \underset{\sim}{v} = 0 \; ; \; \text{grad } p = - \mu \text{ curl curl } \underset{\sim}{v} \qquad (2.1)$$

Reducing the flow geometry to that of a thin film, one can assume : (F2.1)

$$v_\theta \; ; \; v_z >> v_r$$

Writing

$$\underset{\sim}{\nabla} \times (\underset{\sim}{\nabla} \times \underset{\sim}{v}) = - \nabla^2 \underset{\sim}{v}$$

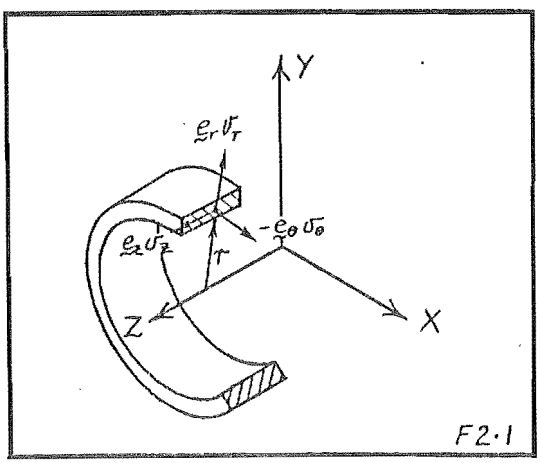

and neglecting the curvature of the fluid-film to obtain :

$$\nabla^2 \underset{\sim}{v} \simeq (0, \nabla^2 v_\theta, \nabla^2 v_z) ; \qquad \nabla^2 v_i \simeq \left[\frac{\partial^2 v_i}{\partial r^2} + \frac{1}{r^2}\frac{\partial^2 v_i}{\partial \theta^2} + \frac{\partial^2 v_i}{\partial z^2}\right] ,$$

one then assumes that viscous shear effects dominate ,

$$\frac{\partial^2 v_i}{\partial r^2} >> \frac{\partial^2 v_i}{\partial \theta^2}; \frac{\partial^2 v_i}{\partial z^2} \qquad \text{giving}$$

$$\text{curl curl } \underset{\sim}{v} \simeq - \left[\frac{\partial^2 v_\theta}{\partial r^2}\, \underset{\sim}{e}_\theta + \frac{\partial^2 v_z}{\partial r^2}\, \underset{\sim}{e}_z\right] .$$

The statement of conservation of momentum then becomes :

$$\underset{\sim}{\nabla} p = \mu \frac{\partial^2 \underset{\sim}{v}}{\partial r^2}$$

where $p = p(\theta,z,t)$; $\underset{\sim}{\nabla} = (\frac{1}{r}\frac{\partial}{\partial \theta}\underset{\sim}{e}_\theta + \frac{\partial}{\partial z}\underset{\sim}{e}_z)$; $\underset{\sim}{v} = (v_\theta \underset{\sim}{e}_\theta + v_z \underset{\sim}{e}_z)$.

Integrating twice and applying the boundary conditions (F2.2) :

$$\underset{\sim}{v}|_{r=h_i} = \underset{\sim}{V}_i + \dot{\underset{\sim}{g}}$$

where $\underset{\sim}{V}_i$ = surface velocity with respect to frame x-y

$\dot{\underset{\sim}{g}}$ = velocity of frame x-y relative to frame X-Y

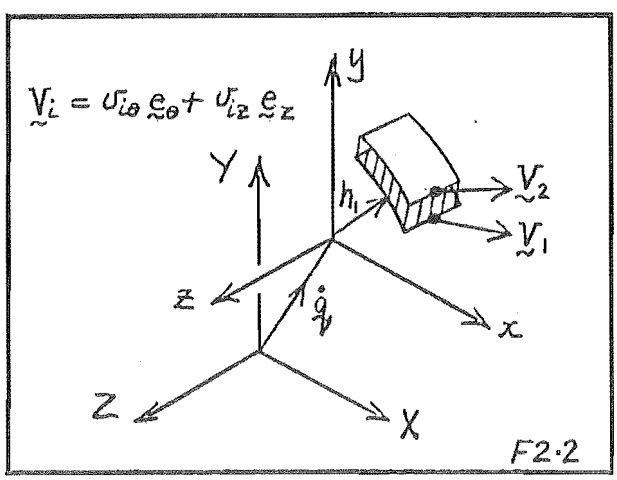

gives

$$\underset{\sim}{v} = \frac{1}{2\mu}\underset{\sim}{\nabla} p (r-h_1)(r-h_2) + \underset{\sim}{V}_1\left[\frac{r - h_2}{h_1 - h_2}\right] - \underset{\sim}{V}_2\left[\frac{r - h_1}{h_1 - h_2}\right] + \dot{\underset{\sim}{g}} \qquad (2.2)$$

Substituting into (2.1) and integrating through the film :

$$\int_r \text{div } \underset{\sim}{v}\, dr = (v_{r_2} - v_{r_1}) + \int_r \underset{\sim}{\nabla} . \underset{\sim}{v}\, dr \quad \text{provided}$$

$$\text{div } \dot{\underset{\sim}{q}} = 0 \; ; \frac{\partial^2 \dot{\underset{\sim}{q}}}{\partial r^2} = 0 \tag{2.3}$$

Applying Leibniz's formula[45], Reynolds' equation is obtained in the following form :[42]

$$\underset{\sim}{\nabla}.(h_2-h_1)^3\underset{\sim}{\nabla}p = 6\mu[2(v_{r_2}-v_{r_1})-\underset{\sim}{\nabla}(h_2+h_1).(\underset{\sim}{V}_2-\underset{\sim}{V}_1)+(h_2-h_1)\underset{\sim}{\nabla}.(\underset{\sim}{V}_2+\underset{\sim}{V}_1)] \tag{2.4}$$

Auxiliary conditions (2.3) define families of reference frames in which (2.4) holds : rigid body motions satisfy such conditions.

Expressions contained within (2.4) all reference fixed spatial points of the film-plane, the fundamental equations being Eulerian. Consequently, terms v_{ri} represent material surface velocities at fixed points in space. To emphasise the material nature of these velocities we write $\frac{Dh_i}{Dt} = v_{ri}$. Rearranging (2.4), Reynolds' equation becomes : ($h = h_2 - h_1$)

$$\underset{\sim}{\nabla} \cdot h^3 \underset{\sim}{\nabla} p = 6\mu[2(\frac{Dh_2}{Dt} - \underset{\sim}{\nabla}h_2 \cdot \underset{\sim}{V}_2) - 2(\frac{Dh_1}{Dt} - \underset{\sim}{\nabla}h_1 \cdot \underset{\sim}{V}_1) + \underset{\sim}{\nabla} \cdot h(\underset{\sim}{V}_2 + \underset{\sim}{V}_1)] \tag{2.5}$$

All dynamic terms are now contained in the first two expressions of the right hand side, these constituting the spatial derivative denoted $\frac{\partial}{\partial t}$: equation (2.5) can then be written :

$$\underset{\sim}{\nabla} \cdot h^3 \underset{\sim}{\nabla} p = 6\mu[2\frac{\partial h}{\partial t} + \underset{\sim}{\nabla} \cdot h(\underset{\sim}{V}_2 + \underset{\sim}{V}_1)] \tag{2.6}$$

where $$\frac{\partial h_i}{\partial t} = \frac{Dh_i}{Dt} - \underset{\sim}{\nabla} h_i . \underset{\sim}{V}_i \qquad (2.7)$$

This is the generalised form of Reynolds' equation to be used in this work. Interpretation of spatial film derivative (2.7) can create confusion, Appendix A1 takes a closer look at its components.

In the following sections, specific coordinate systems and film-geometry assumptions appropriate to connecting-rods are introduced. For further information on friction traction and volume flux expressions see Appendices A2 and A3.

2.1.2 *Film Geometry and Kinematics*

One of the predominant geometric features of big-end bearings is that they are of necessity short; length-diameter ratios are typically much less than unity. Thus, for the purposes of this analysis, it may be reasonably assumed that the journal bearing is perfectly aligned.

Furthermore, experimental evidence[21,22] suggests that, as a first approximation, an analysis based on mean axial surface displacements would suffice. Considerable simplification results, displacements being determined using mean axial pressures in conjunction with plane-stress relationships.

Thus, in the following section, film geometry and kinematics are presented on the premise that the film thickness is axially constant, varying only as a function of the circumferential coordinate. Geometry then becomes planar and can be conveniently analysed using phasor notation.

(a) Coordinate Systems :

Two coordinate systems are defined as follows :

Inertial system X-Y centred on the crankshaft main bearings and aligned with the centre of the small-end; *translating* coordinate system x-y, attached to the centre of the undeformed bearing housing (F2.3).

Translation of the x-y origin can be described by

$$\mathfrak{g} = Re^{i\omega_1 t}$$

where

R = crank-throw radius

ω_1 = crank angular velocity

$(e^{i\omega_1 t} = \cos\omega_1 t + i \sin\omega_1 t)$.

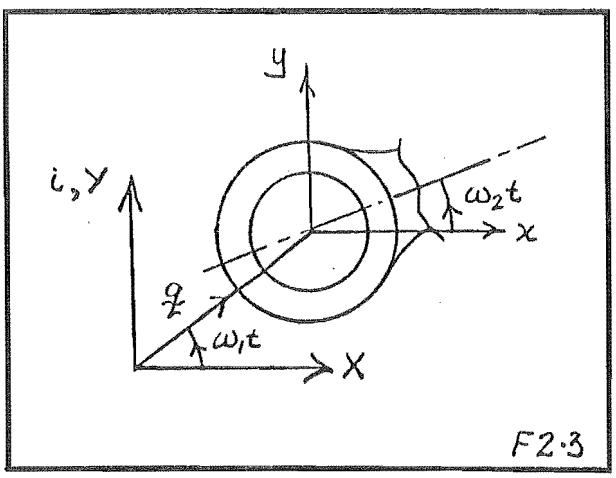

F2·3

This satisfies auxiliary criteria (2.3) on $\dot{\mathfrak{g}}$ vindicating the use of Reynolds' form (2.6) in reference frame x-y.

(b) Journal Kinematics :

Using the coordinate systems defined previously, the location of a material point on the journal (F2.4) with respect to reference frame x-y, is given by

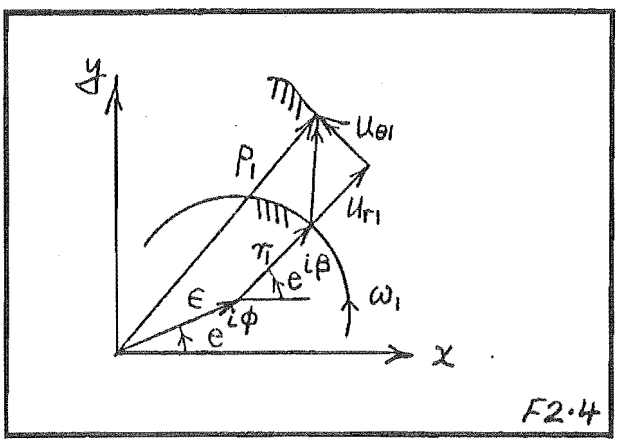

F2·4

$$p_1 = \epsilon e^{i\phi} + e^{i\beta}(r_1 + u_{r_1} + iu_{\theta_1}) \; ; \; \beta = \omega_1 t + \psi \qquad (2.8)$$

where

ϵ = journal centre eccentricity

ϕ = journal centre attitude

r_1 = journal radius

ω_1 = journal angular velocity

u_{r_1} = radial elastic journal displacement

u_{θ_1} = tangential elastic journal displacement

β = journal angular position (x-y frame) .

Differentiating (2.8) with respect to time, one obtains an expression for the velocity of the material point :

$$\dot{p}_1 = (\dot{\epsilon}+i\epsilon\dot{\phi})e^{i\phi} + (\dot{u}_{r_1}-\omega_1 u_{\theta_1}+i(\dot{u}_{\theta_1}+(r_1+u_{r_1})\omega_1))e^{i\beta} \qquad (2.9)$$

(c) Bearing Housing Kinematics :

The location of a material point on the bearing housing (F2.5) with respect to the x-y frame is given by

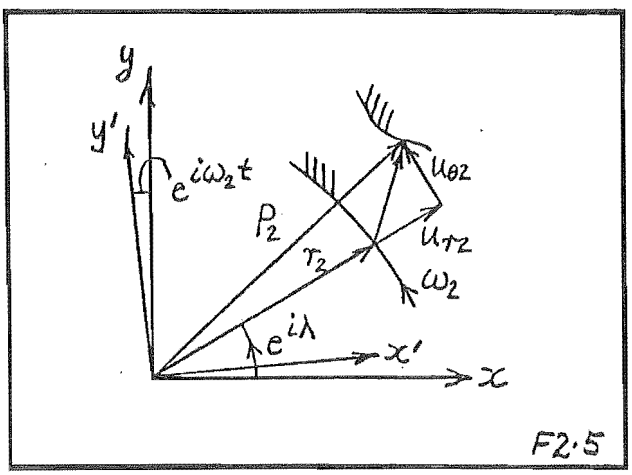

F2·5

$$p_2 = e^{i\lambda}(r_2 + u_{r_2} + iu_{\theta_2}) \; ; \; \lambda = \omega_2 t + \theta' \qquad (2.10)$$

where

r_2 = bearing radius

ω_2 = bearing angular velocity

u_{r_2} = radial elastic bearing deformation

u_{θ_2} = tangential elastic bearing deformation

λ = bearing angular position (x-y frame) .

Surface velocity of the material point is then :

$$\dot{p}_2 = (\dot{u}_{r_2} - \omega_2 u_{\theta_2} + i(\dot{u}_{\theta_2} + (r_2 + u_{r_2})\omega_2))e^{i\lambda} \qquad (2.11)$$

(d) **Film Kinematics :**

The kinematic expressions presented thus far all reference actual material points. Reynolds' equation (2.6) is however spatially referenced; kinematic expressions at fixed points in space are required. This discrepancy is corrected through Taylor series expansion of the material expressions back to the undeformed spatial reference frame. This procedure is aided considerably by elastic displacements being geometrically small :

$$0(u_{i_1}) = 0(u_{i_2}) = 0(\epsilon) = 0(r_2 - r_1) << 0(r)^{\dagger}$$

Taking equation (2.8) and perturbing by $\Delta\beta$:

$$\hat{p}_1 = \hat{p}_1(\beta + \Delta\beta) = p_1(\beta) + \Delta\beta \frac{\partial p_1}{\partial \beta} + 0(\Delta\beta^2)$$

$$= \epsilon e^{i\phi} + (r_1 + u_{r_1})e^{i\beta}\left[1 + \Delta\beta\left[\frac{1}{r_1 + u_{r_1}}\frac{\partial u_{r_1}}{\partial \beta} - \frac{u_{\theta_1}}{r_1 + u_{r_1}}\right]\right.$$

$$\left. + i\left[\frac{u_{\theta_1}}{r_1 + u_{r_1}} + \Delta\beta\left[1 + \frac{1}{r_1 + u_{r_1}}\frac{\partial u_{\theta_1}}{\partial \beta}\right]\right]\right] + 0(\Delta\beta^2)$$

$\hat{p}_1$ is determined at the initially undeformed position by setting :

$$\Delta\beta = \frac{-u_{\theta_1}}{r_1 + u_{r_1}}$$

Assuming $0(\Delta\beta) = 0\left[\frac{1}{r_1 + u_{r_1}}\frac{\partial u_{i_1}}{\partial \beta}\right]$, then

$$\hat{p}_1 = \epsilon e^{i\phi} + (r_1 + u_{r_1})e^{i\beta} + 0(\Delta\beta^2) \qquad (2.12)$$

similarly, for the bearing housing

$$\hat{p}_2 = (r_2 + u_{r_2})e^{i\lambda} + 0(\Delta\beta^2) \qquad (2.13)$$

---

† $0(\cdot) \equiv$ the order of $(\cdot)$

Just as position vectors are corrected from material to spatial reference frames, so too must velocities (2.9)(2.11) : taking equation (2.9) and perturbing by $\Delta\beta$

$$\hat{\dot{p}}_1 = \hat{\dot{p}}_1(\beta+\Delta\beta) = \dot{p}_1(\beta) + \Delta\beta \frac{\partial \dot{p}_1}{\partial \beta} + 0(\Delta\beta^2)$$

$$= (\dot{\epsilon} + i\epsilon\dot{\phi})e^{i\phi}$$

$$+ e^{i\beta}\left[\dot{u}_{r_1} - \omega_1 u_{\theta_1} - \Delta\beta\left[\dot{u}_{\theta_1} + (r_1 + u_{r_1})\omega_1 - \frac{\partial \dot{u}_{r_1}}{\partial\beta} + \omega_1 \frac{\partial u_{\theta_1}}{\partial\beta}\right]\right.$$

$$\left. + i(\dot{u}_{\theta_1} + (r_1 + u_{r_1})\omega_1 + \Delta\beta\left[\dot{u}_{r_1} - \omega_1 u_{\theta_1} + \frac{\partial \dot{u}_{\theta_1}}{\partial\beta} + \omega_1 \frac{\partial u_{r_1}}{\partial\beta}\right]\right)\right]$$

At the initially undeformed position $\left[\Delta\beta = -\frac{u_{\theta_1}}{r_1 + u_{r_1}}\right]$

$$\hat{\dot{p}}_1 = (\dot{\epsilon}+i\epsilon\dot{\phi})e^{i\phi} + [\dot{u}_{r_1} + i(\dot{u}_{\theta_1} + (r_1+u_{r_1})\omega_1)]e^{i\beta} + 0(\Delta\beta^2) \qquad (2.14)$$

Extension to the bearing housing yields :

$$\hat{\dot{p}}_2 = [\dot{u}_{r_2} + i(\dot{u}_{\theta_2} + (r_2 + u_{r_2})\omega_2)]e^{i\lambda} + 0(\Delta\beta^2) \qquad (2.15)$$

At this stage housing and journal equations are completely disconnected; film-thickness provides the unifying factor: define film-thickness h in relation to reference frame x-y at spatial angular coordinate θ ($\theta' = \theta - \omega_2 t$), then

$$H = he^{i\theta} = e^{i\theta}\left[(r_2 + u_{r_2}) - \epsilon e^{i(\phi-\theta)} - (r_1 + u_{r_1})e^{i(\beta-\theta)}\right]$$

The imaginary component leads to the identity :

$$e^{i(\beta-\theta)} = \left[1 - i\frac{\epsilon}{r_1 + u_{r_1}}\sin(\phi - \theta)\right] + 0(\Delta\beta^2) \tag{2.16}$$

which gives on back substitution :

$$he^{i\theta} = e^{i\theta}[(r_2 + u_{r_2}) - (r_1 + u_{r_1}) - \epsilon\cos(\phi - \theta)] + 0(\Delta\beta^2) \tag{2.17}$$

Substituting (2.17) into (2.12) and (2.14), the kinematic description of the journal to $0(\Delta\beta)$ becomes :

$$\hat{p}_1 = e^{i\theta}\left[\epsilon\cos(\phi-\theta) + r_1 + u_{r_1}\right] \tag{2.18}$$

$$\dot{\hat{p}}_1 = e^{i\theta}\Big[(\dot{\epsilon} + i\epsilon\dot{\phi})e^{i(\phi-\theta)} +$$

$$\dot{u}_{r_1} + \epsilon\omega_1\sin(\phi-\theta) + i(\dot{u}_{\theta_1} + (r_1 + u_{r_1})\omega_1)\Big] \tag{2.19}$$

bearing housing relationships become :

$$\hat{p}_2 = e^{i\theta}[r_2 + u_{r_2}] \tag{2.20}$$

$$\dot{\hat{p}}_2 = e^{i\theta}[\dot{u}_{r_2} + i(\dot{u}_{\theta_2} + (r_2 + u_{r_2})\omega_2)] \tag{2.21}$$

Component–wise Representation : Rewriting the above equations in the vector notation of Section 2.1.1, displacement and velocity terms with respect to reference frame x-y (F2.6) become :

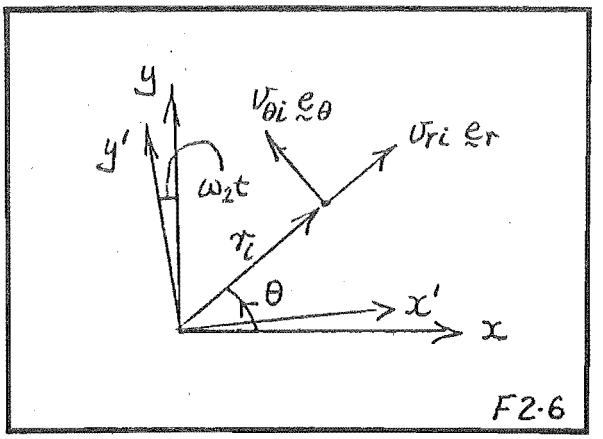

F2·6

$$
\begin{aligned}
h_2 &= r_2 + u_{r_2} \\
\frac{Dh_2}{Dt} &= \dot{u}_{r_2} \\
v_{\theta_2} &= \dot{u}_{\theta_2} + (r_2 + u_{r_2})\omega_2 \\
h_1 &= r_1 + u_{r_1} + \epsilon\cos(\phi-\theta) \\
\frac{Dh_1}{Dt} &= \dot{\epsilon}\cos(\phi-\theta) - \epsilon(\dot{\phi}-\omega_1)\sin(\phi-\theta) + \dot{u}_{r_1} \\
v_{\theta_1} &= \dot{\epsilon}\sin(\phi-\theta) + \epsilon\dot{\phi}\cos(\phi-\theta) + (r_1 + u_{r_1})\omega_1 + \dot{u}_{\theta_1} \\
(v_{z_1} &= v_{z_2} = 0) \text{ which are collectively labelled}
\end{aligned}
\tag{2.22}
$$

2.1.3 *Reynolds' Equation : x–y frame*

Taking expressions (2.22), Reynolds' spatial expression (2.7) to terms $0(\omega r\Delta\beta)$ becomes :

$$\frac{Dh_1}{Dt} - \underset{\sim}{\nabla}h_1 \cdot \underset{\sim}{V}_1 = \dot{u}_{r_1} - \omega_1 \frac{\partial u_{r_1}}{\partial\theta} + \dot{\epsilon}\cos(\phi-\theta) - \epsilon\dot{\phi}\sin(\phi-\theta)$$

$$\frac{Dh_2}{Dt} - \underset{\sim}{\nabla}h_2 . \underset{\sim}{V}_2 = \dot{u}_{r_2} - \omega_2 \frac{\partial u_{r_2}}{\partial\theta}$$

whilst the steady-state term to similar order is :

$$\underset{\sim}{\nabla}.h(\underset{\sim}{V}_1 + \underset{\sim}{V}_2) = (\omega_1 + \omega_2)\left[\frac{\partial u_{r_2}}{\partial\theta} - \frac{\partial u_{r_1}}{\partial\theta} - \epsilon\sin(\phi-\theta)\right]$$

Reynolds' equation to terms $0(\omega r\Delta\beta)$ becomes :

$$\underset{\sim}{\nabla}.h^3 \underset{\sim}{\nabla}p - q = 0 \tag{2.23}$$

where

$$h = c - \epsilon\cos(\phi-\theta) + u_{r_2} - u_{r_1}$$

$$q = 6\mu\left[2\left[\left[\dot{u}_{r_2} - \omega_2\frac{\partial u_{r_2}}{\partial\theta}\right] - \left[\dot{u}_{r_1} - \omega_1\frac{\partial u_{r_1}}{\partial\theta}\right] - \dot{\epsilon}\cos(\phi-\theta) + \epsilon\dot{\phi}\sin(\phi-\theta)\right)\right.$$

$$\left. + (\omega_1 + \omega_2)\left[\frac{\partial u_{r_2}}{\partial\theta} - \frac{\partial u_{r_1}}{\partial\theta} - \epsilon\sin(\phi-\theta)\right]\right]$$

$h = h(\theta,t)$ = film thickness

$c = r_2 - r_1$ = radial bearing clearance

μ = dynamic viscosity

$$\underset{\sim}{\nabla} = \left[\frac{1}{r}\frac{\partial}{\partial\theta}\underset{\sim}{e}_\theta + \frac{\partial}{\partial z}\underset{\sim}{e}_z\right] ; (\dot{}) = \frac{D(\ )}{Dt}$$

This equation is in essence the one developed by Fantino[46]. He however, erroneously interprets elastic velocities as :

$$\dot{u}_{ri} \equiv \dot{u}_{ri} - \omega_i u_{\theta i}$$

an assumption which sets the spatial angular coordinate moving with the material point during deformation. Such terms only appear if velocity expressions are not corrected to a spatial reference frame as per Section 2.1.2d.

To alleviate the complications of interpolating material displacements and velocities from the rotating con-rod frame to the fixed x-y frame, equations (2.23) are now transformed to the x′-y′ con-rod frame.

2.1.4 *Reynolds' Equation : $x' - y'$ frame*

To shift equations (2.23) into the x′-y′ frame (F2.6) we move to an observation frame rotating at ω_2 : there

$$\phi' = \phi - \omega_2 t \; ; \; \theta' = \theta - \omega_2 t \; ; \; \dot{\phi}' = \dot{\phi} - \omega_2$$

substituting into h and q one obtains :

$$h' = c - \epsilon\cos(\phi' - \theta') + u_{r_2} - u_{r_1}$$

$$q' = 6\mu\left[2(\dot{u}_{r_2} - \left[\dot{u}_{r_1} - (\omega_1 - \omega_2)\frac{\partial u_{r_1}}{\partial \theta}\right] - \dot{\epsilon}\cos(\phi' - \theta') + \epsilon\dot{\phi}'\sin(\phi' - \theta')\right]$$

$$+(\omega_1 - \omega_2)\left[\frac{\partial u_{r_2}}{\partial \theta} - \frac{\partial u_{r_1}}{\partial \theta} - \epsilon\sin(\phi' - \theta')\right]\Bigg]$$

One can alternatively view this as setting ω_2 to zero and letting ω_1 be $\omega_1 - \omega_2$, ϕ be ϕ', θ be θ' in the x-y frame (equation (2.23)). This symmetry does not exist in Fantino's interpretation; his additional terms $\omega_i u_{i\theta}$ are not frame invariant.

One final assumption remains to be introduced, journal rigidity : we assume the journal to be rigid in comparison to the housing. This assumption, discussed further in Section 4.2.3, leads to the final specific form of Reynolds' equation used in this work :

$$\underset{\sim}{\nabla} \cdot h^3 \underset{\sim}{\nabla} p - q = 0 \qquad (2.24)$$

where $h = c - \epsilon\cos(\phi' - \theta') + u_{r_2}$

$$q = 6\mu\left[2(\dot{u}_{r_2} - \dot{\epsilon}\cos(\phi' - \theta') + \epsilon\dot{\phi}'\sin(\phi' - \theta')) + \omega_1 s\left[\frac{\partial u_{r_2}}{\partial\theta} - \epsilon\sin(\phi' - \theta')\right]\right]$$

$h = h(\theta', t)$ = film thickness

$c = r_2 - r_1$ = radial bearing clearance

$s = 1 - \frac{\omega_2}{\omega_1}$ = speed modifying factor [47]

μ = dynamic viscosity

$\underset{\sim}{\nabla} = \left[\frac{1}{r}\frac{\partial}{\partial\theta}\underset{\sim}{e}_\theta + \frac{\partial}{\partial z}\underset{\sim}{e}_z\right]$; $(\dot{}) = \frac{D(\ )}{Dt}$

Derivation of this form of Reynolds' equation was first attempted by Allen[17]. He unfortunately failed to include elastic squeeze terms $\dot{u}_{r_2}$.

In the sections that follow, boundary conditions reflecting a cavitating oil-film are introduced, completing the boundary value formulation. Important *a priori* pressure assumptions are introduced in Chapter Three.

2.1.5 *Cavitation Boundary Conditions*

Two forms of cavitation, distinguished by their time scale t, are recognised in the literature :

- Gas cavitation[48] : $t \simeq 0(\frac{1}{\omega_1})$
- Vapour cavitation[49] : $t << 0(\frac{1}{\omega_1})$

Traditionally these phenomena have been treated collectively using gas cavitation theory. However, such implementations proved unsuitable under adverse film conditions, necessitating a different approach.

(a) Gas Cavitation :

Transient gas cavitation is treated using a Stieber-Swift boundary condition. Whilst agreement with more exhaustive models[50,51] is conditional[48], its redeeming feature is that of automatic implementation[52], a consequence of the weak formulation of Reynolds' equation presented in Section 3.1.1.

(b) Vapour Cavitation :

Transient vapour cavitation has largely been ignored in the literature, yet its presence in heavily loaded bearings has been both observed[49] and implicated in bearing failures[53,54]. Treatment of this phenomena has recently been attempted by Brewe[55] using gas cavitation algorithms[51]. Implementation in this study is in the form of Sommerfeld type conditions : negative pressures model cavity flow without contributing to the film's deformation or load carrying capacity. Brewe discusses similar treatments.

(c) Mathematical Representation :

To formally define the above conditions, assume initially that the oil film cannot sustain sub-atmospheric pressures, that is $p > 0$. Two regions Ω_1 and Ω_2 can then be defined with the following boundaries (F2.7) :

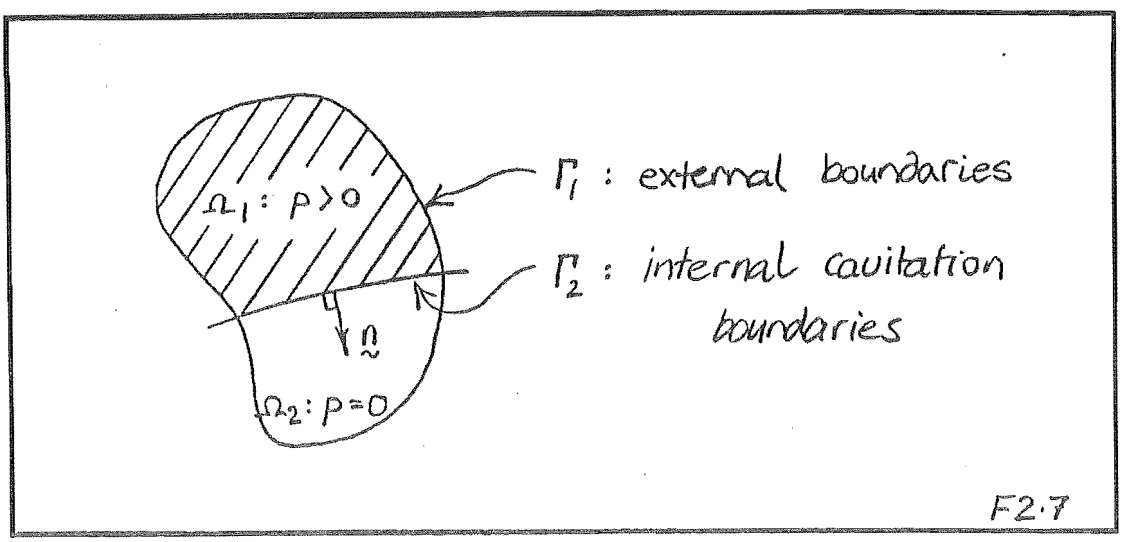

F2.7

The associated boundary conditions are given by :

$$\Gamma_1 : p = 0 \qquad \Gamma_2 : \frac{\partial p}{\partial \underset{\sim}{n}} = p = 0 \text{ (Stieber-Swift)} \tag{2.25}$$

where $\underset{\sim}{n}$ is the unit boundary normal.

Relaxing our initial assumption ($p > 0$), we define sub-atmospheric regions Ω_3 within Ω_1 as (F2.8) :

$$\Omega_3 = \{\underset{\sim}{a} : p < 0 , \| \underset{\sim}{s} \| \leq s_{crit}\} \tag{2.26}$$

where $\| \underset{\sim}{s} \|$ is some measure of the size of Ω_3. The associated boundary condition is given by (F2.8) :

$$\Gamma_1 : p = 0 \tag{2.27}$$

Once Ω_3 reaches critical size s_{crit}, degeneration occurs :

$$\| \underset{\sim}{s} \| > s_{crit} \; ; \; \Omega_3 \equiv \Omega_2$$

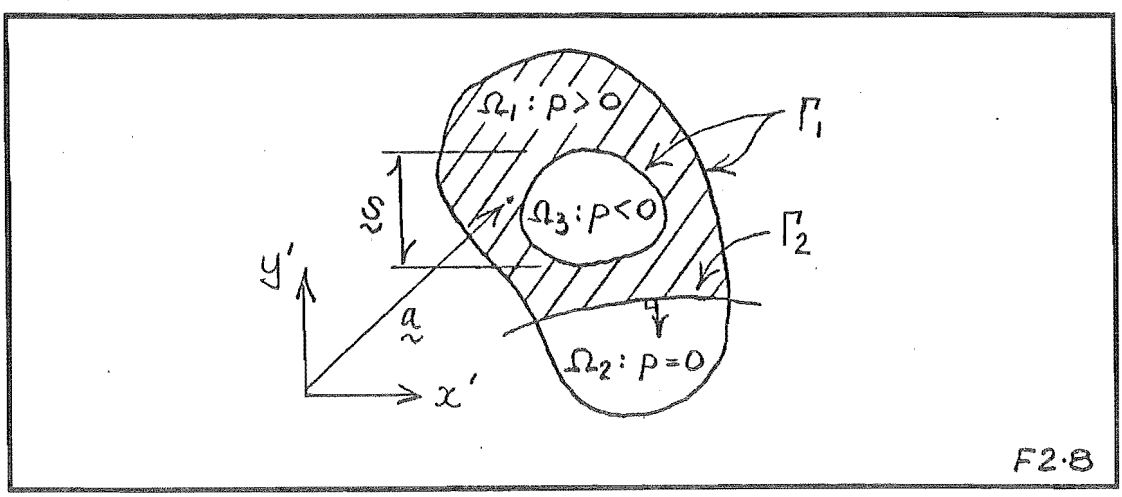

F2·8

Discussion of the implementation and choice of parameters for these procedures can be found in Section 4.1.2.

2.2 Elasticity Equations

Developments in Finite Element Methods have enabled sophisticated techniques to be brought to bear upon the 'art' of con-rod design[56,57,58]. These studies mainly address the question of adequate strength, concentrating on stress analysis. However, in terms of bearing performance, strain distribution is equally important[59], yet frequently ignored. Importantly, dynamic loading is also often mis-represented, however useful work remains.

Spikes[59], by introducing the concept of 'relative stiffness', presents a useful overview of distortion in relation to bearing performance. The detailed effects of some static loadings have been parameterised[16,58], however distortion under dynamic loading and out-of-plane distortion remain largely unexplored for con-rod type geometries.

In the following sections, elasticity models incorporating consistent dynamic loading régime are presented using planar geometry.

2.2.1 *Dynamic Loading*

The con-rod is a rather interesting machine element; body forces and tribological tractions perform the dual function of transmitting load whilst simultaneously defining its motion (F2.9). To clarify these interactions, the following relationships are developed :

(a) **Field Equations :**

Assuming small elastic displacements, the field equations for a plane isotropic body can be written as[60] : (Navier's Equation)

$$[(\lambda + \mu)\,\underset{\sim}{\nabla}\,(\underset{\sim}{\nabla}.\underset{\sim}{u}) + \mu\underset{\sim}{\nabla}^2\underset{\sim}{u}] + \rho\underset{\sim}{b} = \rho(\ddot{\underset{\sim}{u}} + \ddot{\underset{\sim}{r}}) \qquad (2.28)$$

where

$\underset{\sim}{u}$ - elastic displacements

$\underset{\sim}{r}$ - rigid-body displacements

$\rho\underset{\sim}{b}$ - body forces

ρ - material density

λ,μ - Lamé constants.

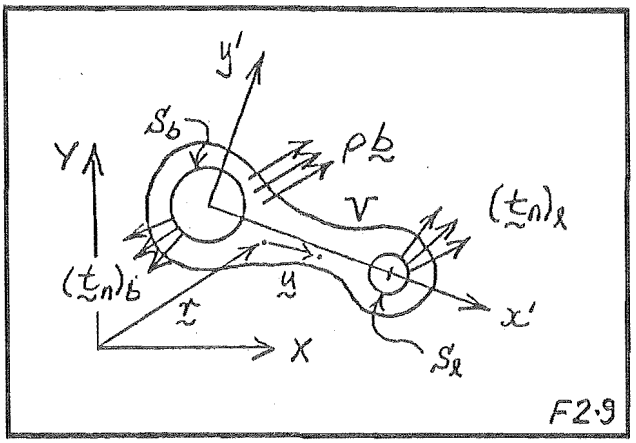

F2.9

Integrating over the body V, one obtains the Principle of Linear Momentum :[60]

$$\int_V \rho\underset{\sim}{b}dV + \int_S \underset{\sim}{t}_n dS = \int_V \rho(\ddot{\underset{\sim}{u}} + \ddot{\underset{\sim}{r}})\, dV \qquad (2.29)$$

where $\underset{\sim}{t}_n$ is a traction vector on surface S. The separate terms can be quantified as follows :

(b) **Traction Forces** : $\int_S \underset{\sim}{t}_n\, dS$

Tractions $(\underset{\sim}{t}_n)_b$ and $(\underset{\sim}{t}_n)_\ell$ at the big and little ends can be distinguished by evaluating surface integral S (F2.9) :

$$\int_S \underset{\sim}{t}_n dS = \int_{S_b} (\underset{\sim}{t}_n)_b dS_b + \int_{S_\ell} (\underset{\sim}{t}_n)_\ell dS_\ell .$$

Each traction vector can be determined as follows (F2.10) :

$$\int_S \underset{\sim}{t}_n dS = \int_S \begin{bmatrix} \sigma & -\tau \\ \tau & \sigma \end{bmatrix} \begin{Bmatrix} \cos\theta \\ \sin\theta \end{Bmatrix} dS$$

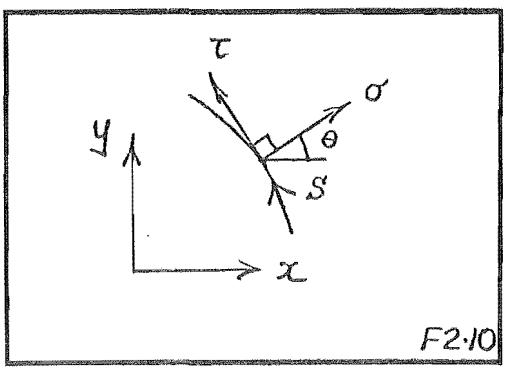

F2.10

For analysis purposes it is usual to ignore the τ contribution since $\tau << \sigma$ (Appendix A2). Rewriting in terms of pressure and with respect to the x′-y′ frame :

$$\int_S \underset{\sim}{t}_n dS = \int_S p \begin{Bmatrix} \cos\theta' \\ \sin\theta' \end{Bmatrix} dS = \underset{\sim}{t}' \qquad (2.30)$$

where $dS = r\, d\theta' dz$, θ' measured anti-clockwise from x′.

(c) **Inertia Forces :** $\int_V \rho(\ddot{\underset{\sim}{u}} + \ddot{\underset{\sim}{r}})\, dV$

Two types of rigid-body motions $\underset{\sim}{r}$ contribute to inertia forces : crank throw motions and bearing clearance motions. The former are known and incorporated as body forces $\rho\underset{\sim}{b}$ within con-rod reference frame x′-y′. The latter are normally neglected as they are small in comparison with crank-throw motions, this being vindicated by several studies.[61]

Elasticity displacement inertias, $\ddot{\underset{\sim}{u}}$, are similarly neglected by assuming (i) that the rods operational frequency is much lower than its associated eigen-spectrum, and (ii) noting that $\underset{\sim}{u} << \underset{\sim}{r}$.

Inertia forces are thus transformed into a body force representation in reference frame x′-y′ :

$$\int_V \rho\underset{\sim}{b} dV = -\int_V \rho\ddot{\underset{\sim}{r}} dV \qquad (2.31)$$

(d) **Equilibrium Statement :**

Grouping known forces together as $\underset{\sim}{f}$ and incorporating the above assumptions, then in reference frame x′-y′ equations (2.29) become :

$$\int_{S_b} p \begin{Bmatrix} \cos\theta' \\ \sin\theta' \end{Bmatrix} dS_b + \underset{\sim}{f} = 0 \qquad (2.32)$$

where

$$\underset{\sim}{f} = \int_{S_\ell} (\underset{\sim}{t}_n)_\ell dS_\ell + \int_V \rho \underset{\sim}{b} dV$$

This expression is a statement of linear equilibrium of the con-rod. Resultant force $\underset{\sim}{f}$ at the big-end can be determined in any convenient manner, provided it satisfies angular equilibrium. Linear and angular equilibrium of the rod are this way guaranteed. Appendix A4 presents a lumped mass approach.

The assumptions outlined in this section result in a considerably simplified elastic analysis : plane quasi-static procedures in con-rod reference frame x′-y′ replace a full dynamic analysis.

2.2.2 *Elasticity Models*

To facilitate structural analysis, it is convenient to invoke St Venant's principle and only model the region of interest to the study, V^* (F2.11). Body forces $\rho\underset{\sim}{b}$ are then split into two : $\underset{\sim}{b}^*$ on V^* and $(\underset{\sim}{b}-\underset{\sim}{b}^*)$ on $(V-V^*)$. Reactions $\underset{\sim}{r}_i^*$ appear at 'suitably remote' constraints c_i^* introduced along A-B.

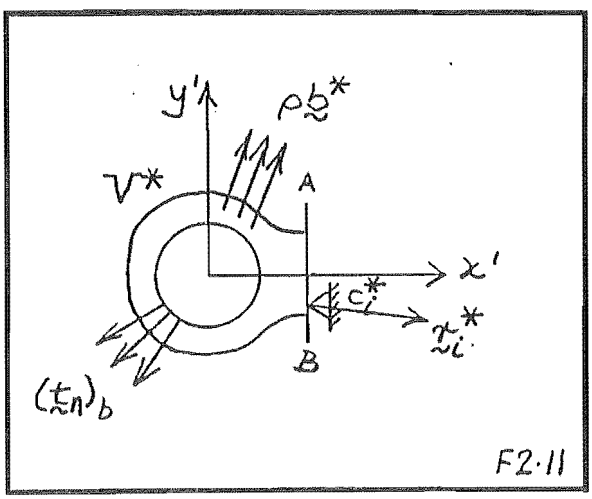

A consistent treatment of loading is achieved by simultaneously applying $(\underset{\sim}{t}_n)_b$, satisfying equilibrium relationships (2.32), and $\underset{\sim}{b}^*$, determined by geometry V^* (Appendix A4). Reactions $\underset{\sim}{r}_i^*$ will then represent tractions $(\underset{\sim}{t}_n)_\ell$ and remaining body forces $(\underset{\sim}{b}-\underset{\sim}{b}^*)$.

If the application of $\underset{\sim}{b}^*$ on V^* is neglected[24] or misrepresented[32,33], a fictitious reaction to the $\underset{\sim}{b}^*$ component of $(\underset{\sim}{t}_n)_b$ will instead appear in $\underset{\sim}{r}_i^*$. Erroneous displacement fields will result.

In the course of this study, two elasticity implementations were pursued. Continuity with the earlier work of Allen[17] and Stafford[20] was achieved through rigid-elastic curved beam models (F2.12). These progressed to full elastic descriptions using plane-stress theory.

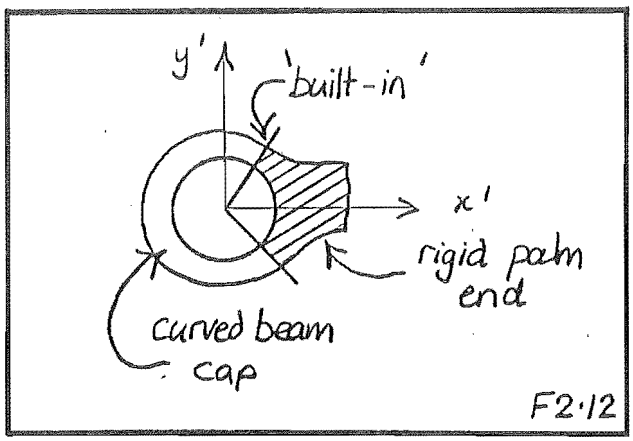

The equations governing these theories are now briefly outlined.

(a) **Curved Beam Equations :**

The equations governing technical bending theory of thick curved beams[62] can be summarised as follows :

Field Equations : (Sign convention F2.13) (2.33)

$$a\left[u_r^{iii} - u_\theta^{ii}\right] - b\left[1 + c\right]\left[u_\theta^{ii} + u_r^{i}\right] = 0$$

$$a\left[u_r^{iv} - u_\theta^{iii}\right] + b\left[1 + c\right]\left[u_\theta^{i} + u_r\right] = 0$$

where

$$a = \frac{EiI}{r_c^3} \; ; \; b = \frac{EA}{r_c}; \; c = \frac{E}{GK} \cdot \frac{a}{b}$$ and

E - Young's modulus

G - Modulus of Rigidity

K - Shear coefficient

A - Section area

I - 2nd Moment area

r_c - Centroid radius

r_o - Neutral axis radius

r_i - Intrados radius

r_e - Extrados radius

$$(\,)' = \frac{d(\,)}{d\theta}$$

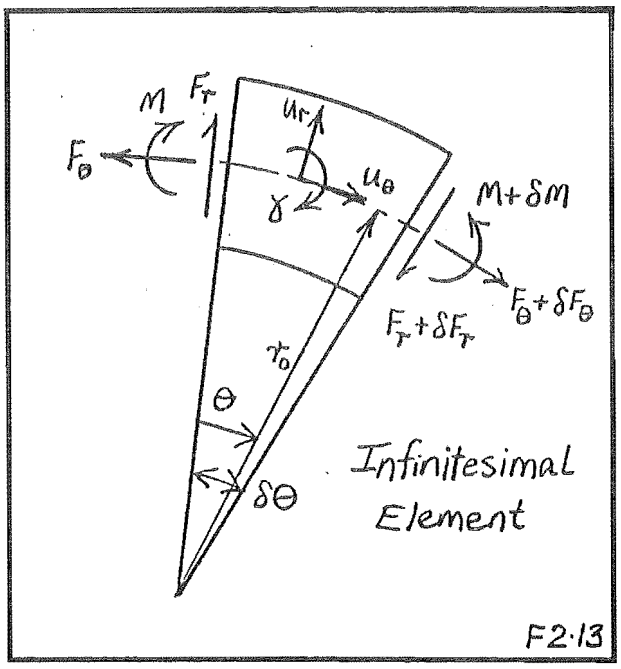

i is a section dependent constant given in Appendix A5.

Boundary Conditions : (2.34)

$$F_r = \frac{r_c}{r_0} a\left[\left[u_r^{iii} - u_\theta^{ii}\right] - \frac{bc}{a}\left[u_\theta^{ii} + u_r^{i}\right]\right]$$

$$F_\theta = \frac{r_c}{r_0} b\left[u_\theta^{i} + u_r\right]$$

$$\frac{M}{r_c} = a\left[\left[u_r^{ii} - u_\theta^{i}\right] - \frac{bc}{a}\left[u_\theta^{i} + u_r\right]\right]$$

$$r_c\gamma = -\left[\frac{r_c}{r_0}\left[u_r^{i} - u_\theta\right] + \frac{c}{a}F_r\right].$$

These equations incorporate deformation due to bending, shear and tension effects : Thin Beam Theory[63,64] can be obtained by excluding the effects of shear deformation ($c = 0$, $r_0 = r_c$, $i = 1$) ; Inextensional Thin Beam Theory[17] by further excluding tension effects ($a = 0$).

Surface tractions and body forces are incorporated using equivalent work concepts (see Section 3.2.1).

(b) **Plane Elasticity Equations :**

Under the assumptions of Section 2.2.1, field equations for a plane isotropic body (2.28), become :

$$[(\lambda + \mu) \underset{\sim}{\nabla} (\underset{\sim}{\nabla} \cdot \underset{\sim}{u}) + \mu \underset{\sim}{\nabla}^2 \underset{\sim}{u}] + \rho \underset{\sim}{b} = 0 \qquad (2.35)$$

where $\underset{\sim}{b} = - \ddot{\underset{\sim}{r}}$

For plane-stress conditions, the Lamé constants are :

$\lambda = \nu E/(1 - \nu^2)$; $\mu = E/2(1 + \nu)$; ν = Poisson's Ratio

Surface traction boundary conditions are introduced in Section 3.2.2 using Weighted Residual procedures.

2.3 System Equations

Previous sections have introduced equations governing separate system components. The outcome when coupled, is an unconventional fluid-structure interaction problem : fluid cavitation features at the structural interface.

This fluid 'inhomogeneity' directly influences coupling procedures, the equations being constructed in terms of surface pressures so as to accommodate cavitation boundary conditions. Solution procedures are consequently restricted, although developments in cavitation modelling[38,51] are easing such restrictions.

Before proceeding with the coupling of these sub-systems, some rationalisation of notation is in order.

2.3.1 *Nomenclature*

The remaining work in this study focuses solely on connecting-rod big-end bearings in rotating reference frame x′-y′. For clarity, it is convenient to drop the primed notation associated with this frame giving $\phi \equiv \phi'$.

Similarly, subscripts of Section 2.2.1 and regions Ω of Section 2.1.5 can be reconciled to give :

$$\Omega \equiv S_b \quad \text{hence} \quad d\Omega \equiv dS_b \quad .$$

Whilst defining

$$r \equiv r_2 \; ; \; \omega \equiv \omega_1 \; ; \; u_r = u_{r_2}$$

allows subscripts distinguishing surface type to be dropped.

2.3.2 *Sub–System Coupling*

Reynolds' equation as it stands is under-prescribed : two additional constraints are required for a full system prescription. These are traditionally provided by rod equilibrium statements (2.32), frequently in reworked forms[24,47,65,66,67] compatible with the system solution techniques employed.

In this work they are used directly[68], the resulting system equations become :

System Equations :

$$\left\| \begin{array}{l} \underset{\sim}{\nabla} \cdot h^3 \underset{\sim}{\nabla} p \quad - \quad q \quad = \quad 0 \\ \int_{\Omega} p \begin{Bmatrix} \cos\theta \\ \sin\theta \end{Bmatrix} d\Omega + \underset{\sim}{f} \quad = \quad 0 \end{array} \right\| \tag{2.36}$$

where $h = c - \epsilon\cos(\phi - \theta) + u_r$

$$q = 6\mu\left[2(\dot{u}_r - \dot{\epsilon}\cos(\phi - \theta) + \epsilon\dot{\phi}\sin(\phi - \theta)) + \omega s\left[\frac{\partial u_r}{\partial\theta} - \epsilon\sin(\phi - \theta)\right]\right]$$

and

$\epsilon = \epsilon(t)$	=	journal eccentricity
$\phi = \phi(t)$	=	journal attitude
$p = p(\theta,z,t)$	=	film pressure
$h = h(\theta,z)$	=	film thickness
$\underset{\sim}{f} = \underset{\sim}{f}(t)$	=	external bearing load

$$\underset{\sim}{\nabla} = \left[\frac{1}{r}\frac{\partial}{\partial\theta}\underset{\sim}{e}_\theta + \frac{\partial}{\partial z}\underset{\sim}{e}_z\right] \; ; \; d\Omega = r d\theta dz \; ; \; (\dot{}) = \frac{D(\;)}{Dt}$$

Spatial Boundary Conditions : (2.37)

Ω_1 boundaries : $\Gamma_1 : p = 0 \; ; \; \Gamma_2 : p = \frac{\partial p}{\partial \underset{\sim}{n}} = 0$

Ω_2 boundaries : $\Gamma_1 : p = 0$

Temporal Boundary Conditions : (2.38)

Since $\underset{\sim}{f}(t) = \underset{\sim}{f}(t + T)$ (periodicity T)

then $\epsilon(t) = \epsilon(t + T)$

$\phi(t) = \phi(t + T)$

$p(t) = p(t + T)$

To the author's knowledge, no closed form solution incorporating elastic deformation exists even for a steadily loaded bearing. Simple steady truncated flow constructions such as Conway's[13] 'Winkler' foundation and the solutions of Higginson[7] and O'Donoghue[8] all require some numerical computation. Less restrictive steady-state models[17,18,19,20] have to-date come about through increased computational complexity.

Extension of steady-state procedures to the time domain exacerbates computational problems. The simplist and most popular approach[24,27,32] is the short bearing approximation $\frac{\partial p}{\partial \theta} \equiv 0$ used in conjunction with a circumferentially varying displacement field. This is somewhat presumptuous, as it precludes coupling between circumferential pressure flows and displacements which only vary in the circumferential direction. The alternative finite length solutions[28,29] represent a comprehensive but computationally expensive approach.

This work takes a route occupying the middle ground : fluid-film discretisation incorporates a full, although approximate complement of flows; planar circumferential displacements replace those of a full elastic housing. Details of these discretisations form the subject of the following Chapter.

CHAPTER THREE

NUMERICAL DISCRETISATION

In this Chapter, Finite Element Methods[69] are used to develop algebraic analogues of the differential equations presented previously. Versatile treatments of space-time domains are this way fashioned.

Spatial discretisation of the fluid-film equations via the Method of Weighted Residuals[70] is firstly used to incorporate *a priori* axial pressure dependencies. The resulting approximate expressions, retaining a full complement of flows, are one-dimensional facilitating economic solutions. Temporal discretisation is developed using a Time Recurrence Scheme[69], the fluid-film description being completed by non-dimensionalisation.

Curved beam elements are next constructed using exact solutions of technical beam theory[62], distributed loadings being developed through equivalent work relationships. A brief development of plane elasticity is included. The resulting expressions are non-dimensionalised and partitioned in accordance with the fluid-film equations.

Finally, discretised matrix expressions of the system equations of Section 2.3 are presented.

Solution and validation of these equations is dealt with in Chapters Four and Five respectively.

3.1 Fluid Film Discretisation

In the following sections, a discretisation of the governing equations over spatial domain Ω, consisting of circumferential and axial coordinates, and temporal domain T, the time coordinate, is presented.

3.1.1 *Spatial Discretisation*

Spatial domain Ω is firstly divided circumferentially into sub-domains Ω^e, each containing the entire axial coordinate z. Ω thus becomes a piecewise union of sub-domains :

$$\Omega = \bigcup_e \Omega^e \; ; \; \bigcap_e \Omega^e = \phi$$

If the dependent variables are similarly constructed piecewise,

$$p = \bigcup_e p^e$$

then the governing equations can be developed in local sub-domains Ω^e and conveniently assembled into global form Ω for solution[69].

(a) Method of Weighted Residuals : (MWR)

Within each subdomain it is usual to approximate the exact solution :

$$p^e \simeq \tilde{p}^e,$$

$\tilde{p}^e$ satisfying the essential boundary conditions. Substituting into system equations (2.36) produces residual or error functions R_i :

$$R_1 = \underset{\sim}{\nabla}.h^3\underset{\sim}{\nabla}\tilde{p}^e \quad - \quad q^e \tag{3.1}$$

$$R_2 = \int_{\Omega^e} \cos\theta \; \tilde{p}^e d\Omega^e \quad + \quad f_x^{\,e} \tag{3.2}$$

$$R_3 = \int_{\Omega^e} \sin\theta \; \tilde{p}^e d\Omega^e \quad + \quad f_y^{\,e} \tag{3.3}$$

Error R_1 is then distributed over Ω^e according to weighting function w^e (also satisfying the essential boundary conditions) and set to zero in the following integrated sense :

$$\int_{\Omega^e} R_1 w^e d\Omega^e = \int_{\Omega^e} (\underset{\sim}{\nabla}.h^3 \underset{\sim}{\nabla}\tilde{p}^e - q^e) w^e d\Omega^e = 0 \ .$$

Scalar residuals R_2 and R_3 are set identically to zero.

Continuity requirements on $\tilde{p}^e$ can be relaxed by integrating by parts and applying the divergence theorem :

$$\int_{\Omega^e} (\underset{\sim}{\nabla}.h^3 \underset{\sim}{\nabla}\tilde{p}^e) w^e d\Omega^e = - \int_{\Omega^e} h^3 (\underset{\sim}{\nabla}\tilde{p}^e . \underset{\sim}{\nabla} w^e) d\Omega^e + \int_{\Gamma^e} h^3 (\underset{\sim}{\nabla}\tilde{p}^e . \underset{\sim}{n}) w^e d\Gamma^e \ .$$

Setting $\int_{\Gamma^e} h^3 (\underset{\sim}{\nabla}\tilde{p}^e . \underset{\sim}{n}) w^e d\Gamma^e = 0$ everywhere, the residual expression for R_1 becomes :

$$\int_{\Omega^e} R_1 w^e d\Omega^e = - \int_{\Omega^e} (h^3 \underset{\sim}{\nabla}\tilde{p}^e . \underset{\sim}{\nabla} w^e + q^e w^e) d\Omega^e = 0. \qquad (3.4)$$

The solution of this expression satisfies the essential boundary conditions identically. Natural boundary conditions will be satisfied on all remaining boundaries in accordance with the residual expression :

$$\int_{\Gamma^e} (\underset{\sim}{\nabla}\tilde{p}^e . \underset{\sim}{n}) w^e d\Gamma^e = 0 \ . \qquad (3.5)$$

The above procedure is the Method of Weighted Residuals[70].

(b) **Approximation Functions :**

To maintain a subdomain setting, the dependent variables are constructed locally as follows :

$$\tilde{p}^e = \begin{cases} \phi_i^e(\theta,z)\tilde{p}^e{}_i : (\theta,z) \in \Omega^e \\ 0 \qquad\quad : (\theta,z) \notin \Omega^e \end{cases} .$$

Trial functions ϕ_i^e, thus describe the functional variation of $\tilde{p}$ over Ω^e.

Weights w^e are similarly defined as :

$$w^e = \psi_i^e(\theta,z) \ .$$

Axial Pressure Dependence : Short journal bearings ($\frac{L}{D} < \frac{1}{2}$) are known to have strong parabolic pressure behaviour in the z coordinate. This dependence is incorporated into the trial functions using the 'simplest Ritz approximation' : a single trial function g(z) spanning the z domain (F3.1) :

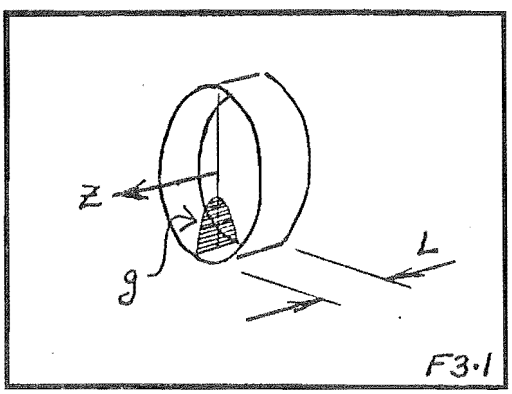

F3.1

$$\phi_i^e(\theta,z) = g(z)N_i^e(\theta)$$

where

$$g(z) = [1-(\frac{2z}{L})^2]$$

Weighting functions are defined according to Galerkin's method :

$$\psi_i^e = \phi_i^e \ .$$

One consequence of this Ritz approximation is the constraint in the z dependence of the pressure induced flows : From Appendix A3, volume flux $\underset{\sim}{Q}$ can be written as :

$$\underset{\sim}{Q} = -\frac{h^3}{12\mu}\left[\frac{g}{r}\frac{\partial N_i^e}{\partial\theta}\underset{\sim}{e}_\theta + \frac{\partial g}{\partial z}N_i^e\underset{\sim}{e}_z\right]\tilde{p}_i^e + \frac{h}{2}(\omega rs)\underset{\sim}{e}_\theta \ .$$

Pressure induced circumferential flows thus behave parabolically in the z coordinate; pressure induced axial flows behave linearly. Circumferential carried flows are constant with respect to coordinate z (F3.2).

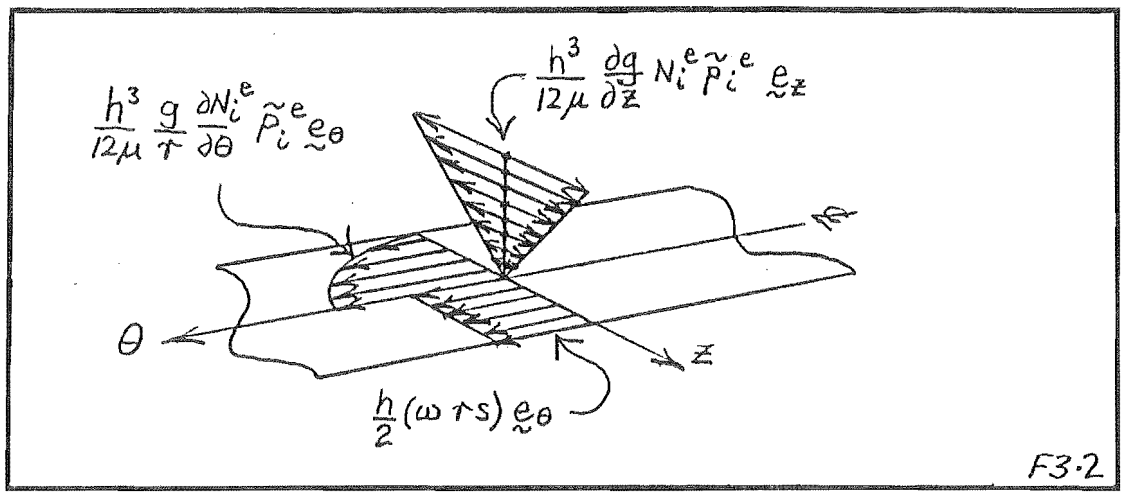

F3.2

These can be compared to the traditional 'short' bearing model in which the circumferential pressure flows are excluded, or the 'long' bearing model in which the axial pressure flows are ignored.

(c) Spatial Algebraic Form :

The z dependence in the residual expressions can be eliminated by integrating the z terms to yield :

$$-\int_{\theta^e}\left[h^3\left[\frac{\alpha}{r^2}\frac{\partial N_i^e}{\partial\theta}\frac{\partial N_j^e}{\partial\theta}+\beta N_i^e N_j^e\right]\tilde{p}_j^e+\gamma q^e N_i^e\right]rd\theta^e = 0 \qquad (3.6)$$

$$\int_{\theta^e}\left[\gamma\cos\theta N_i^e\tilde{p}_i^e\right]rd\theta^e + f_x^e = 0 \qquad (3.7)$$

$$\int_{\theta^e}\left[\gamma\sin\theta N_i^e\tilde{p}_i^e\right]rd\theta^e + f_y^e = 0 \qquad (3.8)$$

where $\alpha = \int g^2 dz$; $\beta = \int\left[\frac{dg}{dz}\right]^2 dz$; $\gamma = \int g dz$.

Ritz approximation g, a device first presented in variational form by Rohde[71], effectively reduces the dimensionality of the equations from θ-z to θ only. Such procedures, apparently commonplace in finite-difference work since 1942[11], offer the economy of a one-dimensional solution without the flow truncation associated with 'short' and 'long' bearing models.

Related information on variational approaches to lubrication problems is available in the literature[18,72,73,74,75,76,77,78]. Mathematical aspects of such approaches are dealt with in references [52,79,80,81,82].

3.1.2 *Temporal Discretisation*

As with the spatial domain, the time domain T is split into a piecewise union of subdomains, T^e. The governing equations are then constructed locally but unlike the spatial domain, solved locally using a Time Recurrence Scheme[69]. The complete solution over T is then made up of successive solutions over subdomains T^e.

(a) Time Recurrence Scheme : (TRS)

MWR can be used to construct a recurrence scheme by choosing a subset of the temporal trial functions as weighting functions : Incorporate into the trial functions a linear temporal form $\overline{N}$:

$$(\phi_i^e)^j = g(z)N_i^e(\theta)\overline{N}^j(t) \quad (j=1,2)$$

where $\overline{N}^1(t) = (1 - \frac{t}{\Delta t})$

$\overline{N}^2(t) = \frac{t}{\Delta t}$

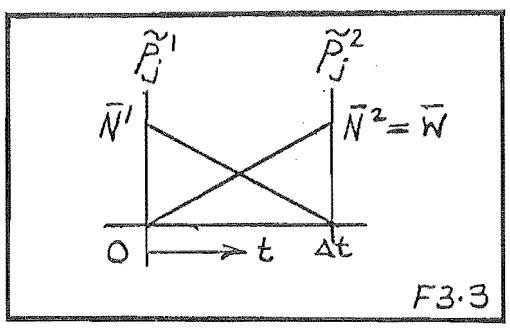

F3.3

superscript j denoting time level (F3.3).

Dependent variable $\tilde{p}^e$ can then be written as :

$$\tilde{p}^e = gN_j^e\left[\overline{N}^1\tilde{p}_j^1 + \overline{N}^2\tilde{p}_j^2\right] \tag{3.9}$$

Assuming $\tilde{p}_j^1$ is known, $\tilde{p}_j^2$ can be determined by the previous residual statements using the j weighting constraints :

$$\psi_j^e(\theta,z,t) = g(z)N_j^e(\theta)\overline{W}(t)\,. \tag{3.10}$$

This gives a Two-point Recurrence Scheme[69].

Clearly, function $\overline{W}$ can take a variety of forms. However, given that the system is reputedly 'stiff'[83], a prudent choice would preclude schemes which are not unconditionally stable (A-stable)[84]. The Galerkin form $\overline{W} = \overline{N}^2$, shown to be A-stable on linear equations, is the one chosen for this work. It offers good accuracy and a damped oscillatory behaviour[69,85].

Further discussion on stiffness and its implications can be found in references [84], [86].

(b) **Temporal Algebraic Form :**

Adjusting residual statements (3.6-3.8) to include temporal error residuals gives :

$$-\int_{\overline{\Omega}^e}\left[h^3\left[\frac{\alpha}{r^2}\frac{\partial N_i^e}{\partial\theta}\frac{\partial N_j^e}{\partial\theta}+\beta N_i^e N_j^e\right]\overline{N}^k\tilde{p}_j^k+\gamma q^e N_i^e\right]\overline{W}\,d\overline{\Omega}^e = 0 \tag{3.11}$$

$$\int_{\overline{\Omega}^e}\left[\cos\theta\gamma N_j^e\overline{N}^k\tilde{p}_j^k\right]\overline{W}\,d\overline{\Omega}^e + \int_{T^e}\left[\overline{N}^k f_x^k\right]\overline{W}\,dT^e = 0 \tag{3.12}$$

$$\int_{\overline{\Omega}^e}\left[\sin\theta\gamma N_j^e\overline{N}^k\tilde{p}_j^k\right]\overline{W}\,d\overline{\Omega}^e + \int_{T^e}\left[\overline{N}^k f_y^k\right]\overline{W}\,dT^e = 0 \tag{3.13}$$

where $dT^e = dt^e$, $d\overline{\Omega}^e = rd\theta^e dt^e$. Forcing term q^e, given by :

$$q^e = 6\mu\left[2(\dot{u}_r - \dot{\epsilon}\cos(\phi-\theta) + \epsilon\dot{\phi}\sin(\phi-\theta)) + \omega s\left[\frac{\partial u_r}{\partial\theta} - \epsilon\sin(\phi-\theta)\right]\right]$$

contains several time dependent terms. These are discretised as follows :

$$\epsilon = \overline{N}^k\epsilon^k \;;\; \phi = \overline{N}^k\phi^k \;;\; s = \overline{N}^k s^k$$

$$u_r = \overline{N}^k u_r^k \;;\; \frac{\partial u_r}{\partial\theta} = \overline{N}^k\left[\frac{\partial u_r}{\partial\theta}\right]^k$$

and

$$\dot{u}_r = \dot{\overline{N}}^k u_r^k \;;\; \dot{\epsilon} = \dot{\overline{N}}^k\epsilon^k \;;\; \dot{\phi} = \dot{\overline{N}}^k\phi^k \;.$$

3.1.3 *Non–Dimensionalisation*

As a first step towards a dimensionless analysis, peak axial pressure $\tilde{p}$ is rewritten in terms of the mean axial pressure $\bar{p}$:

$$\bar{p} = \frac{1}{L}\int_z g dz\, \tilde{p} = \frac{\gamma}{L}\tilde{p} \ .$$

Constants α, β, γ can be evaluated to obtain :

$$\alpha = \frac{8}{15}L\ ;\ \beta = \frac{16}{3}\cdot\frac{1}{L}\ ;\ \gamma = \frac{2}{3}L \ .$$

Introducing the dimensionless parameters :

$$\hat{h} = \frac{h}{c}\ ;\ \hat{\epsilon} = \frac{\epsilon}{c}\ ;\ \hat{u}_r = \frac{u_r}{c}\ ;\ \hat{t} = \omega t\ ;\ \hat{\theta} = \theta$$

c and ω defined previously, forcing term q^e becomes :

$$q^e = 6\mu\omega c\left[2\left[\dot{\hat{u}}_r - \dot{\hat{\epsilon}}\cos(\phi-\theta) + \hat{\epsilon}\dot{\phi}\sin(\phi-\theta)\right] + s\left[\frac{\partial \hat{u}_r}{\partial\theta} - \hat{\epsilon}\sin(\phi-\theta)\right]\right]$$

where $(\dot{\hat{\cdot}}) \equiv \frac{d}{d\hat{t}}(\hat{\ })$. Rewriting Reynolds' equation (3.11) in terms of $\bar{p}$, one obtains :

$$-\int_{\Omega^e}\left[\hat{h}^3\left[\hat{\alpha}\frac{\partial N_i^e}{\partial\theta}\frac{\partial N_j^e}{\partial\theta} + \beta N_i^e N_j^e\right]\overline{N}^k\hat{p}_j^k + \hat{q}^e N_i^e\right]\overline{W}\, d\hat{\Omega}^e = 0 \qquad (3.14)$$

where $\hat{h} = 1 - \hat{\epsilon}\cos(\phi-\theta) + \hat{u}_r\ ;\ d\hat{T}^e = d\hat{t}^e\ ;\ d\hat{\Omega}^e = d\hat{\theta}^e\, d\hat{t}^e$

$$\hat{p} = \frac{1}{6\mu\omega}\left[\frac{c}{L}\right]^2\bar{p}\ ;\ \hat{q} = \frac{q}{6\mu\omega c}\ ;\ \hat{\alpha} = \frac{24}{5}\left[\frac{L}{D}\right]^2\ ;\ \beta = 12\ ;\ D = 2r \ .$$

The force balance equations can be treated similarly :

$$\int_{\hat{\Omega}^e} \left[\cos\theta N_j^e \overline{N}^k \hat{p}_j^k\right] \overline{W}\, d\hat{\Omega}^e + \int_{\hat{\Gamma}^e} \left[\overline{N}^k \hat{f}_x^k\right] \overline{W}\, d\hat{\Gamma}^e = 0 \qquad (3.15)$$

$$\int_{\hat{\Omega}^e} \left[\sin\theta N_j^e \overline{N}^k \hat{p}_j^k\right] \overline{W}\, d\hat{\Omega}^e + \int_{\hat{\Gamma}^e} \left[\overline{N}^k \hat{f}_y^k\right] \overline{W}\, d\hat{\Gamma}^e = 0 \qquad (3.16)$$

where

$$\hat{f}_i^k = \frac{1}{6\mu\omega n r L}\left[\frac{c}{L}\right]^2 f_i^k \text{ , n the number of journal lands.}$$

This form of the discretised fluid-film equations is the final one used in this work. Traditional 'short-bearing' equations are obtained by setting $\hat{\alpha} = 0$.

Matrix representation of these equations is given in Section 3.3. Derivation of discretised friction traction and volume flux expressions is performed in Appendices A2 and A3 respectively.

3.2 Elasticity Discretisation

This section briefly develops discretised versions of the two elasticity models presented in Section 2.2.2. Comprehensive treatments are presented elsewhere[62,63,64,69,87].

Non-dimensionalisation of the resulting expressions, in particular that of the curved beam, introduces useful new dimensionless parameters incorporating beam thickness. These are the subject of further investigation in proceeding Chapters.

3.2.1 *Curved Beam Discretisation*

A finite element discretisation of the curved beam equations is developed through the exact solution of the technical beam theory presented earlier. This solution is given by the following complementary function in angular coordinate θ :

$$\begin{Bmatrix} u_r \\ u_\theta \\ r_c\gamma \end{Bmatrix} = \begin{bmatrix} -\sin\theta & -\cos\theta & -\theta\sin\theta & -\theta\cos\theta & -1 & 0 \\ -\cos\theta & \sin\theta & (c_3\sin\theta-\theta\cos\theta) & (c_3\cos\theta+\theta\sin\theta) & \theta & 1 \\ 0 & 0 & c_1c_4\sin\theta & c_1c_4\cos\theta & c_1\theta & c_1 \end{bmatrix} \begin{Bmatrix} \alpha_1 \\ \vdots \\ \alpha_6 \end{Bmatrix} \tag{3.17}$$

Constants c_i are given in Appendix A5. An expression for the internal forces can be similarly determined :

$$\begin{Bmatrix} F_r \\ F_\theta \\ \frac{M}{r_c} \end{Bmatrix} = \frac{EI}{r_c^3} \begin{bmatrix} 0 & 0 & c_6\sin\theta & c_6\cos\theta & 0 & 0 \\ 0 & 0 & -c_6\cos\theta & c_6\sin\theta & 0 & 0 \\ 0 & 0 & -c_5\cos\theta & c_5\sin\theta & -c_2 & 0 \end{bmatrix} \underset{\sim}{\alpha} \tag{3.18}$$

This general solution is used to construct solutions over element domains θ^e as follows.

(a) **Element Stiffness :**

Using equation (3.17), the six components of $\underset{\sim}{\alpha}$ are determined in terms of the six displacements of the finite element of F3.4. Writing :

$$\underset{\sim}{u} = \begin{Bmatrix} u_{r_1} \\ u_{\theta_1} \\ r_c\gamma_1 \\ u_{r_2} \\ u_{\theta_2} \\ r_c\gamma_2 \end{Bmatrix} = [X]\,\underset{\sim}{\alpha}$$

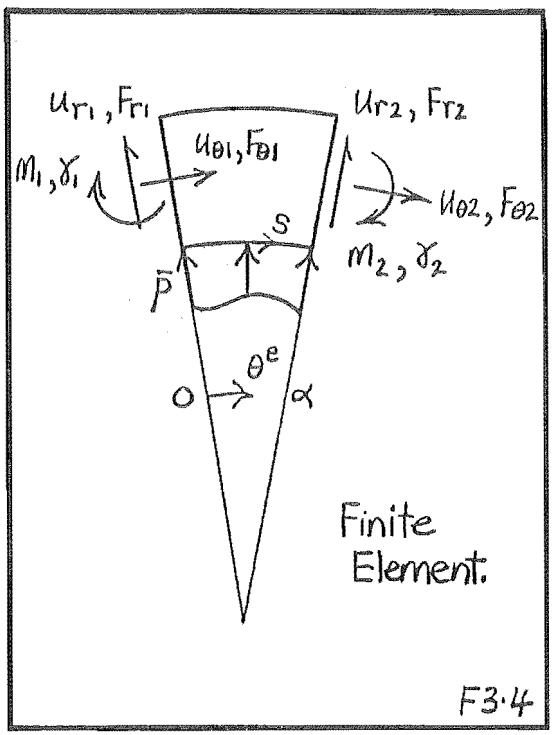

then $\underset{\sim}{\alpha} = X^{-1}\underset{\sim}{u}$.

Nodal forces are defined similarily :

$$\underset{\sim}{f} = \begin{Bmatrix} F_{r_1} \\ F_{\theta_1} \\ M_1/r_c \\ F_{r_2} \\ F_{\theta_2} \\ M_2/r_c \end{Bmatrix} = \frac{EI}{r_c^3}[Y]\underset{\sim}{\alpha}$$

Element stiffness matrix K^e is then given by :

$$\frac{EI}{r_c^3}K^e\underset{\sim}{u} = \underset{\sim}{f} \quad \text{where} \quad K^e = YX^{-1} \tag{3.19}$$

Matrices X and Y are given in Appendix A5.

(b) Distributed Loadings :

Equations (3.19) only accept loadings in terms of nodal forces. Equivalent work expressions are used to convert distributed loadings to nodal forces.

Pressure Tractions : Work performed by pressure acting at the surface is given by :

$$\phi_W = - \int_S p u_r dS = - nrL \int_{\theta^e} \bar{p} u_r d\theta^e \quad .$$

Assuming :

$$\bar{p} = <N>^e \underset{\sim}{\bar{p}} \qquad \text{(see F3.4)}$$

and

$$u_r = <x_1> X^{-1} \underset{\sim}{u}$$

where $<N>^e$ are the pressure shape functions of Section 3.1.1.b and $<x_1>$ the first row of equation (3.17), then †:

$$\phi_W = - \underset{\sim}{u}^T (X^{-1})^T nrL \int_0^{\alpha} <x_1>^T <N>^e d\theta^e \underset{\sim}{\bar{p}} \quad .$$

Writing $W = \int_0^{\alpha} <x_1>^T <N>^e d\theta^e$, then forces $\underset{\sim}{f}_p$ producing equivalent work ϕ_W are given by :

$$\underset{\sim}{f}_p = nrLA^e \underset{\sim}{\bar{p}} \quad \text{where} \quad A^e = (X^{-1})^T W \quad . \qquad (3.20)$$

W is given in Appendix A5 where <N> are assumed to be quadratic Lagrangian shape functions.

---

† superscript T denotes matrix transposition.

Body Forces : Work performed by body force $\rho \underset{\sim}{b} = \rho(b_r, b_\theta)$ across housing width W is given by :

$$\phi_W = -\int_{r,\theta} \underset{\sim}{\delta}.\underset{\sim}{b}\, \rho W r\, dr^e d\theta^e \; ; \; \underset{\sim}{\delta} = \langle u_r, u_\theta \rangle^T$$

writing

$$\underset{\sim}{\delta} = \begin{Bmatrix} u_r \\ u_\theta \end{Bmatrix} = \begin{bmatrix} \langle x_1 \rangle \\ \langle x_2 \rangle \end{bmatrix} X^{-1}\, \underset{\sim}{u}$$

$\langle x_2 \rangle$ being the second row of equation (3.17), ϕ_W becomes :

$$\phi_W = -\underset{\sim}{u}^T (X^{-1})^T W \rho \int_\theta \begin{bmatrix} \langle x_1 \rangle \\ \langle x_2 \rangle \end{bmatrix}^T \left[\int_r \underset{\sim}{b} r dr^e \right] d\theta^e \; .$$

Assuming $\underset{\sim}{b} = \underset{\sim}{b}_1 + r\underset{\sim}{b}_2$, $b_i = b_i(\theta,t)$, then :

$$\int_r \underset{\sim}{b} r dr^e \simeq r_c t\, \underset{\sim}{b}_c \qquad \text{(assuming } \frac{t}{2r_c} \text{ small)}$$

Interpolating $\underset{\sim}{b}_c$ using the pressure shape functions $\langle N \rangle^e$

$$\underset{\sim}{b}_c = \begin{bmatrix} \langle N \rangle & \langle 0 \rangle \\ \langle 0 \rangle & \langle N \rangle \end{bmatrix}^e \begin{Bmatrix} \underset{\sim}{b}_r \\ \underset{\sim}{b}_\theta \end{Bmatrix}_c \; .$$

the equivalent work expression becomes :

$$\phi_W = -\underset{\sim}{u}^T (X^{-1})^T \rho W r_c t \int_\theta \begin{bmatrix} \langle x_1 \rangle \\ \langle x_2 \rangle \end{bmatrix}^T \begin{bmatrix} \langle N \rangle & \langle 0 \rangle \\ \langle 0 \rangle & \langle N \rangle \end{bmatrix}^e d\theta^e \begin{Bmatrix} \underset{\sim}{b}_r \\ \underset{\sim}{b}_\theta \end{Bmatrix}_c$$

Writing $M = \int_0^{\alpha} \left[\langle x_1 \rangle^T \langle N \rangle, \langle x_2 \rangle^T \langle N \rangle \right]^e d\theta^e$, then equivalent forces $\underset{\sim}{f}_b$ producing work ϕ_w are given by :

$$\underset{\sim}{f}_b = \rho r_c W \; t \; V^e \underset{\sim}{b} \tag{3.21}$$

where $V^e = (X^{-1})^T M$ and $\underset{\sim}{b} = \langle \underset{\sim}{b}_r, \underset{\sim}{b}_\theta \rangle^T_c$.

M can be constructed from W given in Appendix A5.

3.2.2 *Plane Elasticity Discretisation*

The plane elasticity equations presented earlier are discretised using the Finite Element Method[69,87]; the following cartesian form is obtained from a Galerkin treatment[88] :

$$\int_V \begin{bmatrix} (2\mu+\lambda)\frac{\partial N_i}{\partial x}\frac{\partial N_j}{\partial x} + \mu\frac{\partial N_i}{\partial y}\frac{\partial N_j}{\partial y}, & \lambda\frac{\partial N_i}{\partial x}\frac{\partial N_j}{\partial y} + \mu\frac{\partial N_i}{\partial y}\frac{\partial N_j}{\partial x} \\ \lambda\frac{\partial N_i}{\partial y}\frac{\partial N_j}{\partial x} + \mu\frac{\partial N_i}{\partial x}\frac{\partial N_j}{\partial y}, & (2\mu+\lambda)\frac{\partial N_i}{\partial y}\frac{\partial N_j}{\partial y} + \mu\frac{\partial N_i}{\partial x}\frac{\partial N_j}{\partial x} \end{bmatrix} W dV \begin{Bmatrix} (u_x)_j \\ (u_y)_j \end{Bmatrix}$$

$$= \int_V \rho \begin{Bmatrix} N_i \underset{\sim}{b} \\ N_i \end{Bmatrix} nL dV + \int_S \begin{Bmatrix} N_i \underset{\sim}{t}_n \\ N_i \end{Bmatrix} W dS \quad . \tag{3.22}$$

Body forces and surface tractions are discretised as follows :

$$\underset{\sim}{b} = \begin{Bmatrix} b_x \\ b_y \end{Bmatrix} = \begin{bmatrix} \overline{M}_j & 0 \\ 0 & \overline{M}_j \end{bmatrix} \begin{Bmatrix} (b_x)_j \\ (b_y)_j \end{Bmatrix} \tag{3.23}$$

$$\underset{\sim}{t}_n \, dS = \begin{Bmatrix} -\bar{p}dy \\ \bar{p}dx \end{Bmatrix} = \begin{bmatrix} 0 & -M_j \\ M_j & 0 \end{bmatrix} \begin{Bmatrix} dx \\ dy \end{Bmatrix} \begin{Bmatrix} \bar{p}_j \end{Bmatrix} \tag{3.24}$$

Volume and area matrices can then be determined as :

$$V = \rho W \int_V \begin{bmatrix} N_i \overline{M}_j & 0 \\ 0 & N_i \overline{M}_j \end{bmatrix} dV \tag{3.25}$$

$$A = nL \int_S \begin{bmatrix} 0 & -N_i M_j \\ N_i M_j & 0 \end{bmatrix} \begin{Bmatrix} dx \\ dy \end{Bmatrix} \tag{3.26}$$

Shape functions N_i, M_i, $\overline{M}_i$ are discussed in Section 4.2.2.

The complete elastic description then becomes :

$$K\underset{\sim}{u} = A\underset{\sim}{\bar{p}} + V\underset{\sim}{b} \tag{3.27}$$

where $\underset{\sim}{u} = \langle \underset{\sim}{u}_x, \underset{\sim}{u}_y \rangle^T$ and K, the stiffness matrix of equation (3.22).

3.2.3 *Non–Dimensionalisation*

Planar Finite Element analyses are notoriously dimensional in nature, however a dimensionless approach can be achieved by introducing the following parameters :

$$\hat{x} = \frac{x}{r}; \hat{y} = \frac{y}{r}; \hat{\mu} = \frac{\mu}{E}; \hat{\lambda} = \frac{\lambda}{E} \quad .$$

The global mesh is thus determined in terms of bearing radius r.

Substituting into equation (3.27) one obtains :

$$E\,\overline{\underline{K}}\,\underset{\sim}{u} = r\,\frac{nL}{W}\,\overline{\underline{A}}\,\underset{\sim}{\bar{p}} + \rho r^2\,\overline{\underline{V}}\,\underset{\sim}{b} \quad . \tag{3.28}$$

where $\overline{\underline{K}}$, $\overline{\underline{A}}$ and $\overline{\underline{V}}$ are the dimensionless global stiffness, area and volume matrices respectively. Assuming :

$$\underset{\sim}{\hat{u}} = \frac{\underset{\sim}{u}}{c}; \underset{\sim}{\hat{p}} = \frac{1}{6\mu\omega}\left[\frac{c}{L}\right]^2 \underset{\sim}{\bar{p}}; \underset{\sim}{\hat{b}} = \frac{1}{\omega^2 R}\underset{\sim}{b}$$

then $$\underset{\sim}{\hat{u}} = \Lambda(\overline{\underline{K}}^{-1}\overline{\underline{A}})\,\underset{\sim}{\hat{p}} + \Xi(\overline{\underline{K}}^{-1}\overline{\underline{V}})\,\underset{\sim}{\hat{b}} \tag{3.29}$$

where $$\Lambda = \frac{24\mu\omega}{E}\left[\frac{L}{D}\right]^2\left[\frac{r}{c}\right]^3\frac{nL}{W}\;;\; \Xi = \frac{\rho}{E}(\omega r)^2\left[\frac{r}{c}\right]\left[\frac{R}{r}\right] \quad .$$

Similar expressions are obtained for curved beams by assembling the elastic statements as follows :

$$\frac{EI}{r_c^3}\overline{\underline{K}}\,\underset{\sim}{u} = nLr\,\overline{\underline{A}}\,\underset{\sim}{\bar{p}} + \rho W r_c t\,\overline{\underline{V}}\,\underset{\sim}{b} \quad . \tag{3.30}$$

Non-dimensionalising as before :

$$\hat{\underset{\sim}{u}} = \Lambda'(\underline{\underline{\bar{K}}}^{-1}\underline{\underline{\bar{A}}})\,\hat{\underset{\sim}{p}} + \Xi'(\underline{\underline{\bar{K}}}^{-1}\underline{\underline{\bar{V}}})\,\hat{\underset{\sim}{b}} \qquad (3.31)$$

where $\Lambda' = \Lambda\left[12\left[\frac{r}{t}\right]^3\left[1 + \frac{t}{2r}\right]^3\right]$; $\Xi' = \Xi\left[12\left[\frac{r}{t}\right]^2\left[1 + \frac{t}{2r}\right]^4\right]$.

The extra bracketed terms [ ], incorporate the influence of beam thickness t.

Non-dimensionalisation of the planar analysis in particular, offers significant economies in solution ; a 'small' library of dimensionless rods is sufficient to enable the analysis of a large variety of physical rods.

3.2.4 *Partitioned Equations*

For any nodal coordinate θ, it is possible to partition from the above dimensionless forms the i^{th} equation corresponding to the radial surface displacement :

$$\hat{u}_r = (\hat{\underset{\sim}{u}})_i = \Lambda(\underline{\underline{\bar{K}}}^{-1}\underline{\underline{\bar{A}}})_i\hat{\underset{\sim}{p}} + \Xi(\underline{\underline{\bar{K}}}^{-1}\underline{\underline{\bar{V}}})_i\hat{\underset{\sim}{b}}$$

writing $\langle L_r\rangle = \Lambda(\underline{\underline{\bar{K}}}^{-1}\underline{\underline{\bar{A}}})_i$; $\langle G_r\rangle = \Xi(\underline{\underline{\bar{K}}}^{-1}\underline{\underline{\bar{V}}})_i$

then $$\hat{u}_r = \langle L_r\rangle\,\hat{\underset{\sim}{p}} + \langle G_r\rangle\,\hat{\underset{\sim}{b}} \qquad (3.32)$$

The radial displacement slope $\frac{\partial \hat{u}_r}{\partial \theta}\left[= \hat{u}_r'\right]$ can be similarly obtained :

$$\hat{u}_r' = \langle L_r'\rangle\,\hat{\underset{\sim}{p}} + \langle G_r'\rangle\,\hat{\underset{\sim}{b}} \quad . \qquad (3.33)$$

These expressions form the basis of the elastic displacement description used in the remainder of this work.

3.3 System Discretisation

The dimensionless element expressions developed in the previous sections can be assembled into global matrix form to give the following system of equations:

$$\begin{bmatrix} 0 & 0 & \hat{n}_j^2 \\ 0 & 0 & \hat{m}_j^2 \\ \hat{e}_i^2 & \hat{d}_i^2 & \hat{r}_{ij}^2 \end{bmatrix} \begin{Bmatrix} \hat{\epsilon}^2 \\ \hat{\phi}^2 \\ \hat{P}_j^2 \end{Bmatrix} + \begin{bmatrix} 0 & 0 & \hat{n}_j^1 \\ 0 & 0 & \hat{m}_j^1 \\ \hat{e}_i^1 & \hat{d}_i^1 & \hat{r}_{ij}^1 \end{bmatrix} \begin{Bmatrix} \hat{\epsilon}^1 \\ \hat{\phi}^1 \\ \hat{P}_j^1 \end{Bmatrix} + \begin{Bmatrix} \hat{f} \\ \underset{\sim}{} \\ \hat{g}_i \end{Bmatrix} = 0 \qquad (3.34)$$

where the Reynolds equation expressions are given by :

$$\hat{r}_{ij}^k = \int_{\hat{\Omega}} \overline{W} \left[\hat{h}^3 (\hat{\alpha}\, N_i' N_j' + \hat{\beta} N_i N_j)\, \overline{N}^k + (2\dot{\overline{N}}^k (L_r)_j + s\overline{N}^k (L_r')_j) N_i \right] d\hat{\Omega}$$

$$\hat{e}_i^k = \int_{\hat{\Omega}} \overline{W} \left[-s\overline{N}^k \sin(\phi-\theta) - 2\dot{\overline{N}}^k \cos(\phi-\theta) \right] N_i \, d\hat{\Omega}$$

$$\hat{d}_i^k = \int_{\hat{\Omega}} \overline{W} \left[2\dot{\overline{N}}^k \hat{\epsilon} \sin(\phi-\theta) \right] N_i \, d\hat{\Omega}$$

$$\hat{g}_i = \int_{\hat{\Omega}} \overline{W} \left[(2\dot{\overline{N}}^k (G_r)_j + s\overline{N}^k (G_r')_j) N_i \right] \hat{b}_j^k \, d\hat{\Omega}$$

$$\hat{h} = 1 - \hat{\epsilon} \cos(\phi-\theta) + \hat{u}_r \quad .$$

The force balance terms are determined using :

$$\hat{n}_j^k = \int_{\hat{\Omega}} \overline{W} \left[\cos\theta N_j \overline{N}^k \right] d\hat{\Omega}$$

$$\hat{m}_j^k = \int_{\hat{\Omega}} \overline{W} \left[\sin\theta N_j \overline{N}^k \right] d\hat{\Omega}$$

$$\underset{\sim}{\hat{f}} = \int_{\hat{T}} \overline{W} \left[\overline{N}^k \underset{\sim}{\hat{f}}^k \right] d\hat{T}$$

where

$$\underset{\sim}{\hat{f}}^k = \langle \hat{f}_x^k, \hat{f}_y^k \rangle^T \; ; \; (L_r)_j = \langle L_r \rangle \; ; \; N_i' = dN_i/d\theta \; .$$

These time dependent equations are non-linear, reputably 'stiff'[83] and have moving internal boundaries. To require accurate economic solutions is particularly demanding of the solution technique.

One tempting scheme requiring little extra effort, is direct iteration within the time levels of equation (3.34). Such fixed-point iterations are however largely unsatisfactory[17,18,20], this being symtomatic of 'stiff' equations.

Techniques incorporating a stiff solution capability which in addition accommodate fluid-film boundary motion, are developed in the following Chapter.

CHAPTER FOUR

EQUATION SOLUTION

Numerical discretisation of the field equations results in two sets of algebraic equations of quite different nature :

- fluid-film equations ; a small set (<100) of non-linear 'stiff' equations involving moving internal boundaries and
- elasticity equations ; a large set of linear equations undergoing a multiplicity of loads.

In this Chapter, solution techniques separately tailored to each set of equations are developed; Newton-Raphson and Continuation procedures for the fluid, Sub-Structuring and Influence constructions for the structure.

Algorithmic details for the modelling of cavitation interface motion are developed. The work concludes with the verification of elasticity models and subsequent characterisation of elastic displacement behaviour.

Validation of fluid-film behaviour is performed in the following Chapter.

4.1 Fluid Film Solution

The early work of Benjamin[14] and the more recent approach of Rohde[37,68], demonstrated the usefulness of Newton-Raphson on obstinate EHL problems. With the realisation that these problems are 'stiff' and knowledge of requisite stiff solution techniques[84,86], namely :

- unconditionally stable discretisation
- Newton-Raphson solution of the resulting implicit forms

a framework, missing from the above works, is established for the development of stable fluid-film solutions.

4.1.1 *Non–Linear Equation Solution*

Having dealt with discretisation in the previous Chapter, we now focus attention on iterative Newton-Raphson (N-R) techniques and the attendant process of Continuation. Such procedures[89] offer the desirable feature of quadratic convergence/divergence, convergent behaviour of the N-R iteration being maintained through accurate initial guesses obtained via Continuation.

(a) Newton-Raphson (N-R) :

It is convenient firstly to re-express discretised fluid equations (3.34) in the following form :

$$\underset{\sim}{R}(\underset{\sim}{u}, \underset{\sim}{f}, \underset{\sim}{b}, s) = 0 \tag{4.1}$$

where

$\underset{\sim}{u} = <\hat{\epsilon}^2, \hat{\phi}^2, \hat{p}^2>^T$, $\underset{\sim}{f} = <\hat{f}_x{}^2, \hat{f}_y{}^2>^T$, $\underset{\sim}{b} = <\hat{b}_x{}^2, \hat{b}_y{}^2>^T$ and s, are all implicit functions of time. The N-R scheme can then be generated using a Taylor's expansion of $\underset{\sim}{R}$:

Suppose at some fixed time t, initial test point $\underset{\sim}{u}$ differs from the solution by $\Delta\underset{\sim}{u}$. If $\underset{\sim}{R}$ is sufficiently differentiable at $\underset{\sim}{u}$, then :

$$\underset{\sim}{R}(\underset{\sim}{u}+\Delta\underset{\sim}{u},\underset{\sim}{f},\underset{\sim}{b},s) = \underset{\sim}{R}(\underset{\sim}{u},\underset{\sim}{f},\underset{\sim}{b},s) + \frac{\partial \underset{\sim}{R}}{\partial \underset{\sim}{u}}\Delta\underset{\sim}{u} + 0(\Delta\underset{\sim}{u}^2) = 0 \quad .$$

Introducing jacobian $\underset{\sim}{J} = \dfrac{\partial \underset{\sim}{R}}{\partial \underset{\sim}{u}}$, a first order iterative scheme, the Newton-Raphson Method, can be constructed :

$$\left\| \begin{array}{l} \underset{\sim}{u}_{n+1}{}^t = \underset{\sim}{u}_n{}^t + \Delta\underset{\sim}{u}_n{}^t \quad \text{where} \\ \underset{\sim}{J}_n{}^t \Delta\underset{\sim}{u}_n{}^t = - \underset{\sim}{R}_n{}^t \end{array} \right\| \tag{4.2}$$

(subscript n denotes iteration level, superscript t denotes time level). Given initial guess $\underset{\sim}{u}_0^t$, iteration of a solution in the space domain (t fixed) can proceed to the desired accuracy, typically satisfying **both** :

$$\|\underset{\sim}{R}_n^t\| \leq 10^{-10} \quad \text{and} \quad \|\Delta\underset{\sim}{u}_n^t\| \leq 10^{-6}$$

where $\|\underset{\sim}{x}\| = \left[\sum_i x_i^2\right]^{\frac{1}{2}}$. The heart of such a scheme is the construction of jacobian $\underset{\sim}{J}$.

Jacobian Construction : Exact expressions for the jacobian can be determined by several methods. Rohde[37] developed expressions using Frechet derivatives[90] which, from a theoretical standpoint are particularly useful. However, in practice, a discretised jacobian can be simply obtained by differentiating equations (3.34) with respect to $\underset{\sim}{u}^2$ ($\underset{\sim}{u}^1 = <\hat{\epsilon}^1,\hat{\phi}^1,\hat{p}^1>^T$ does not enter into the calculations as it is fixed).

The matrix N-R expression (4.2) then becomes :

$$\begin{bmatrix} 0 & 0 & \hat{N}_j \\ 0 & 0 & \hat{M}_j \\ \hat{E}_i & \hat{D}_i & \hat{R}_{ij} \end{bmatrix}_n^t \begin{Bmatrix} \Delta\hat{\epsilon}^2 \\ \Delta\hat{\phi}^2 \\ \Delta\hat{p}_j^2 \end{Bmatrix}_n^t = -\underset{\sim}{R}_n^t \qquad (4.3)$$

where the Reynolds equation derivatives are given by :

$$\hat{R}_{ij} = \hat{r}_{ij}^{2} + \int_{\hat{\Omega}} \overline{W}\,\overline{N^2}\left[Q_i(L_r)_j\right] d\hat{\Omega}$$

$$\hat{E}_i = \hat{e}_i^{2} + \int_{\hat{\Omega}} \overline{W}\,\overline{N^2}\left[2\hat{\dot{\phi}}\sin(\phi-\theta)N_i - \cos(\phi-\theta)Q_i\right] d\hat{\Omega}$$

$$\hat{D}_i = \hat{d}_i^{2} + \int_{\hat{\Omega}} \overline{W}\,\overline{N^2}\left[(\hat{\epsilon}(2\hat{\dot{\phi}}-s)\cos(\phi-\theta) + 2\hat{\dot{\epsilon}}\sin(\phi-\theta))N_i + \hat{\epsilon}\sin(\phi-\theta)Q_i\right] d\hat{\Omega}$$

and $\quad Q_i = 3\hat{h}^2(\hat{\alpha}N_i'N_j' + \hat{\beta}N_iN_j)\overline{N}^k\hat{p}_j^{\,k}$

whilst force balance derivatives are given by :

$$\hat{N}_j = \hat{n}_j^{2} \quad ; \quad \hat{M}_j = \hat{m}_j^{2}$$

$\hat{n}_j^{2}$ and $\hat{m}_j^{2}$ as per (3.34).

Provided one retains information when constructing $\underset{\sim}{R}$, the additional computation required to determine $\underset{\sim}{J}$ is not large. Quasi-Newton updates of $\underset{\sim}{J}^{-1}$ offer avenues for further computational savings[89].

(b) **Continuation :**

The result of a successful set of N-R iterations is a solution $\underset{\sim}{u}_*^t$. An estimate of the solution at new time t + Δt is again determined using a Taylor's expansion of $\underset{\sim}{R}$:

$$\underset{\sim}{R}(\underset{\sim}{u} + \Delta\underset{\sim}{u}, \underset{\sim}{f} + \Delta\underset{\sim}{f}, \underset{\sim}{b} + \Delta\underset{\sim}{b}, s + \Delta s)^{t+1}$$

$$\simeq \underset{\sim}{R}(\underset{\sim}{u},\underset{\sim}{f},\underset{\sim}{b},s)^t + \frac{\partial \underset{\sim}{R}^t}{\partial \underset{\sim}{u}} \Delta\underset{\sim}{u} + \frac{\partial \underset{\sim}{R}^t}{\partial \underset{\sim}{f}} \Delta\underset{\sim}{f} + \frac{\partial \underset{\sim}{R}^t}{\partial \underset{\sim}{b}} \Delta\underset{\sim}{b} + \frac{\partial \underset{\sim}{R}^t}{\partial s} \Delta s = 0$$

Introducing jacobian $\underset{\sim}{J}_*^t$ at $\underset{\sim}{u}_*^t$, a first order continuation scheme, Euler's method, can be constructed :

$$\left\| \begin{array}{l} \underset{\sim}{u}_0^{t+1} = \underset{\sim}{u}_*^t + \Delta\underset{\sim}{u}^t \qquad \text{where} \\ \underset{\sim}{J}_*^t \Delta\underset{\sim}{u}^t = -\left[\frac{\partial \underset{\sim}{R}}{\partial \underset{\sim}{f}} \Delta\underset{\sim}{f} + \frac{\partial \underset{\sim}{R}}{\partial \underset{\sim}{b}} \Delta\underset{\sim}{b} + \frac{\partial \underset{\sim}{R}}{\partial s} \Delta s\right]^t \end{array} \right\| \qquad (4.4)$$

As $(\underset{\sim}{J}_*^t)^{-1}$ is known from the previous N-R iteration, $\underset{\sim}{u}_0^{t+1}$, the initial guess for the new N-R iterations can be determined very cheaply. Evaluating the bracketed derivatives above, gives :

$$\frac{\partial \underset{\sim}{R}}{\partial \underset{\sim}{f}} \Delta\underset{\sim}{f} = \begin{bmatrix} \hat{F}_{jk} \\ \underset{\sim}{0} \end{bmatrix} \Delta\hat{f}_k^2 \; ; \; \frac{\partial \underset{\sim}{R}}{\partial \underset{\sim}{b}} \Delta\underset{\sim}{b} = \begin{bmatrix} 0 \\ 0 \\ \hat{B}_{jk} \end{bmatrix} \Delta\hat{b}_k^2 \; ; \; \frac{\partial \underset{\sim}{R}}{\partial s} \Delta s = \begin{bmatrix} 0 \\ 0 \\ \hat{S}_j \end{bmatrix} \Delta\hat{s}^2$$

where $$\hat{F}_{jk} = \int_{\hat{T}} \overline{W}\,\overline{N}^2\,\delta_{jk}\,d\hat{T} = \frac{\Delta t}{2}\cdot\frac{2}{3}\delta_{jk}$$

$$\hat{B}_{jk} = \int_{\hat{\Omega}} \overline{W}\,[2\dot{\overline{N}}^2(G_r)_k + s\overline{N}^2(G_r')_k]\,N_j d\hat{\Omega}$$

$$\hat{S}_j = \int_{\hat{\Omega}} \overline{W}\,\overline{N}^2[-\hat{\epsilon}\sin(\phi-\theta) + \hat{u}'_r]\,N_j d\hat{\Omega}\ .$$

Interval Halving : In the course of this work, sufficiently accurate $\Delta\underset{\sim}{u}^t$ estimates were obtained using the influence of $\Delta\underset{\sim}{f}$ alone. This is a consequence of using interval halving, a procedure whereby N-R iterations deemed 'unsuccessful' (see T4.1) are re-commenced using halved step lengths.

Unfortunately, interval halving is not a panacea. Unduly short time-steps ($< \frac{1}{10}^0$) were found to lead to ill-conditioning and hence inaccuracy in solution. However, by incorporating suitable step-doubling mechanisms (T4.1), time step lengths attuned to the required solution accuracy are attained automatically, 5-10^0 crank-angles being typical.

Step halving	Step doubling
$\hat{h} < 0$ $\hat{\epsilon} < 0$ slow convergence (> 25 iterations)	rapid convergence (< 7 N-R iterations)

T4.1

The above processes can be seen in a broader context as follows : dividing equation (4.4) by Δt and taking the limit as $\Delta t \rightarrow 0$, gives :

$$\underset{\sim}{J}_{*}{}^{t}\dot{\underset{\sim}{u}}^{t} = -\left[\frac{\partial \underset{\sim}{R}}{\partial \underset{\sim}{f}}\dot{\underset{\sim}{f}} + \frac{\partial \underset{\sim}{R}}{\partial \underset{\sim}{b}}\dot{\underset{\sim}{b}} + \frac{\partial \underset{\sim}{R}}{\partial s}\dot{s}\right]^{t}$$

Thus, the continuation or prediction phase can be viewed as solving

$$\dot{\underset{\sim}{R}} = 0 \quad \forall t \tag{4.5}$$

whilst the N-R or correction phase solves (at fixed t) :

$$\underset{\sim}{R} = 0 \quad \forall \theta \tag{4.6}$$

By providing a set of initial conditions and iterating between these two procedures, a family of solutions $\underset{\sim}{u}^{t}$ are marched out in time parameter t, concluding when the required periodicity is achieved.

Overall, the process is fairly insensitive to initial conditions, any errors being typically damped-out within 180^{0} crank-angle.

4.1.2 *Cavitation Regions and Interfaces*

The predominant mode of bearing operation in this work is that of an oil film Ω_1 divided by regions of gas cavitation Ω_2 (F4.1).

The curved cavitation interfaces observed experimentally are however modelled by lines of constant θ,

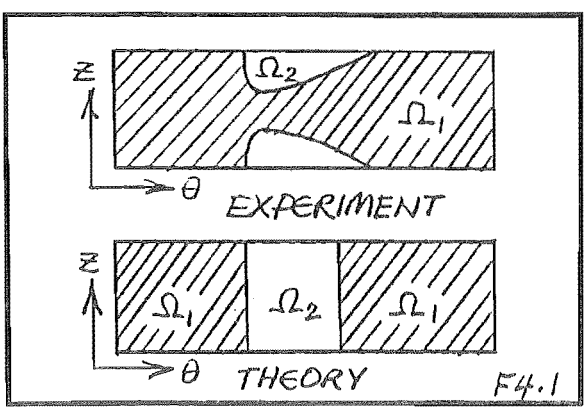

a consequence of the axial pressure dependence introduced in Section 3.1.1. Subsequently, interface movement or growth becomes a discrete process requiring the addition and removal of equations in the θ coordinate.

Within oil film Ω_1, small transient regions of 'vapour cavitation' Ω_3 may sporadically appear.

The processes of identification and growth of these different regions, each performed at every Newton-Raphson iteration, are now outlined.

(a) **Region Identification :**

Two regions need to be identified for the solution to proceed : regions Ω where Reynolds equation is valid, and regions Ω^c, where it is not. Using the definitions of Section 2.1.5

$$\Omega_1: p > 0 \; ; \; \Omega_2: p = 0 \; ; \; \Omega_3: p < 0$$

the following 'algorithm' was devised :

(i) Identify regions Ω_1 by a point-wise search of $\underset{\sim}{p}$. Include growth regions : any adjacent equation lying in Ω_2. Identify regions Ω_3 by a point-wise search of $\underset{\sim}{p}$.

(ii) Check regions Ω_3 for blocks larger than s_{crit}.

If $||\Omega_3|| \geq s_{crit}$

then $\Omega = \Omega_1 \; ; \; \Omega^c = \Omega_2 \cup \Omega_3$

else $\Omega = \Omega_1 \cup \Omega_3 \; ; \; \Omega^c = \Omega_2$

where $||\Omega||$ is the included angle of Ω, s_{crit} typically 60^0.

(iii) Identify growth regions Ω^* by locating equations in region Ω adjacent to regions Ω^c.

At this stage, a map of the regions will take the following form :

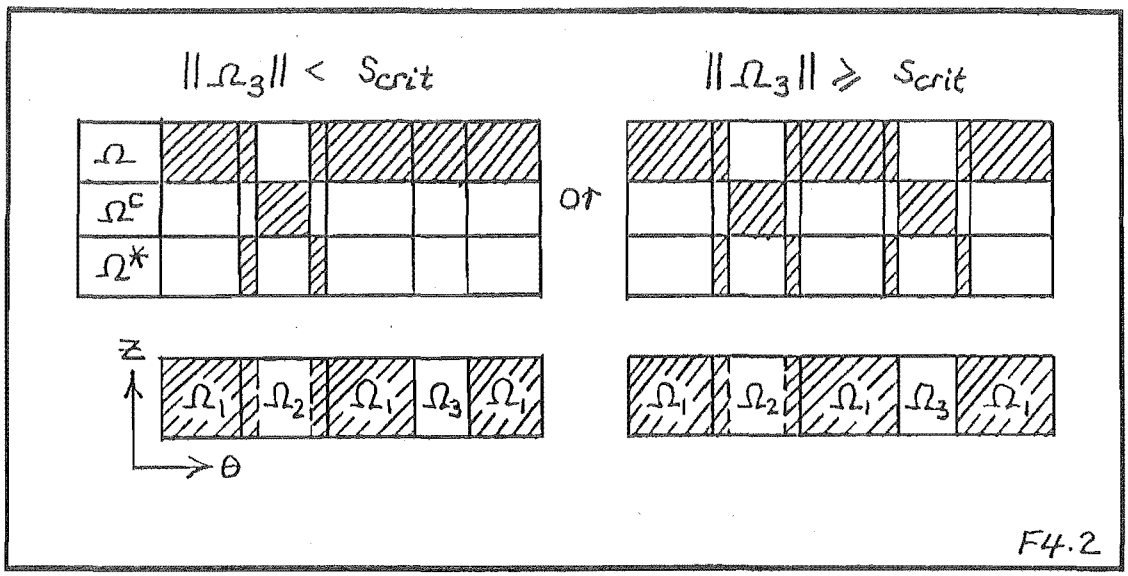

F4.2

The right-hand condition of F4.2 occurs only rarely and causes few problems. However, the left-hand condition requires special treatment when regions Ω_3 are active.

(b) **Negative Pressure Deactivation :**

Throughout this work, regions $\Omega_3 \subset \Omega$ are deactivated from the force balance and pressure-displacement relationships. Inclusion of these regions leads to strong interactions between Ω_3 and the pressure-displacement fields, significantly affecting journal locus. This was deemed 'un-physical' and on this basis deactivated. Thus, pressures within Ω_3 contribute only to the pressure induced flows of these regions.

A process of deactivation is performed as follows : if, on the successful termination of a series of N-R iterations active Ω_3 regions are present, then :

(i) the time interval is frozen

(ii) parameter ρ, a pressure multiplier, is introduced in regions Ω_3 of the force balance and pressure-displacement equations.

(iii) a family of ρ-solutions are 'marched-out', successively reducing ρ from one to zero, hence deactivating Ω_3

(iv) the time interval is incremented and ensuing time steps performed with ρ set to zero.

Although somewhat involved, large negative pressure magnitudes necessitated this step-wise deactivation so as to maintain stability.

Termination of Ω_3 regions is typically through degeneration; negative pressures revert to positive forms as conditions proceed. Durations in the order of 10^0 crank-angle are typically observed; Section 6.1.3a looks at this further.

(c) **Interface Growth :**

Having identified regions Ω, the governing equations can then be solved over domain Ω. As Ω and Ω^c are approximately equal in size, significant computational savings are achieved over standard Sommerfeld type solutions.

Partitioning the N-R equations (4.2) into growth equations ($\underset{\sim}{u}^* \epsilon \Omega^*$) and non-growth equations ($\underset{\sim}{u} \epsilon (\Omega - \Omega^*)$), one obtains the partitioned system equations and their solution ; respectively :

$$\begin{bmatrix} J_1 & J_2 \\ J_3 & J_4 \end{bmatrix}_n^t \begin{Bmatrix} \Delta \underset{\sim}{u} \\ \Delta \underset{\sim}{u}^* \end{Bmatrix}_n^t = - \begin{Bmatrix} \underset{\sim}{R}_1 \\ \underset{\sim}{R}_2 \end{Bmatrix}_n^t \; ; \; \begin{Bmatrix} \Delta \underset{\sim}{u} \\ \Delta \underset{\sim}{u}^* \end{Bmatrix}_n^t = - \begin{bmatrix} \mathcal{J}_1 & \mathcal{J}_2 \\ \mathcal{J}_3 & \mathcal{J}_4 \end{bmatrix}_n^t \begin{Bmatrix} \underset{\sim}{R}_1 \\ \underset{\sim}{R}_2 \end{Bmatrix}_n^t \tag{4.7}$$

Pressures $\underset{\sim}{u}^*$, resulting from the growth equations are then checked sequentially for positiveness :

$$u_i^* \geq p_{crit}$$

p_{crit} typically being $\frac{1}{2}\%$ of the maximum centre-line pressure of the previous converged time-step.

If the above inequality holds, then the growth equation associated with Δu_i^* is retained. If not, the growth equation is removed and the system equations re-solved. This can be achieved very simply through the following equality :

$$\begin{bmatrix} J_1 & J_2 \\ J_3 & J_4 \end{bmatrix} \cdot \begin{bmatrix} \mathcal{J}_1 & \mathcal{J}_2 \\ \mathcal{J}_3 & \mathcal{J}_4 \end{bmatrix} = \begin{bmatrix} I & 0 \\ 0 & I \end{bmatrix} \tag{4.8}$$

the first block of equations being manipulated to give :

$$J_1^{-1} = \mathcal{J}_1 - \mathcal{J}_2 . \mathcal{J}_4^{-1} . \mathcal{J}_3 \quad . \tag{4.9}$$

This is known as a Rank-One Update[89].

The process of checking and removal proceeds sequentially from regions of high pressure gradient to low pressure gradient until all equations in Ω^* are processed. This then completes the N-R iteration.

Currently the above procedures are performed exactly as described; matrix inversion and update. More efficient (complex) methods are available through the use of matrix factorisation modification[91].

4.1.3 *Numerical Details*

There are clearly a large number of 'hidden' numerical details in the procedures outlined thus far. This section details those critical to the implementation of this work.

(a) **Integration :**

The governing equations of the previous sections are all expressed in integral form. Evaluation is performed either numerically or analytically as follows :

Fluid–Film Equations : Reynolds equation expressions are integrated numerically using isoparametric transformations and Gaussian Quadrature[69]. This process can be represented element-wise as follows : (F4.3)

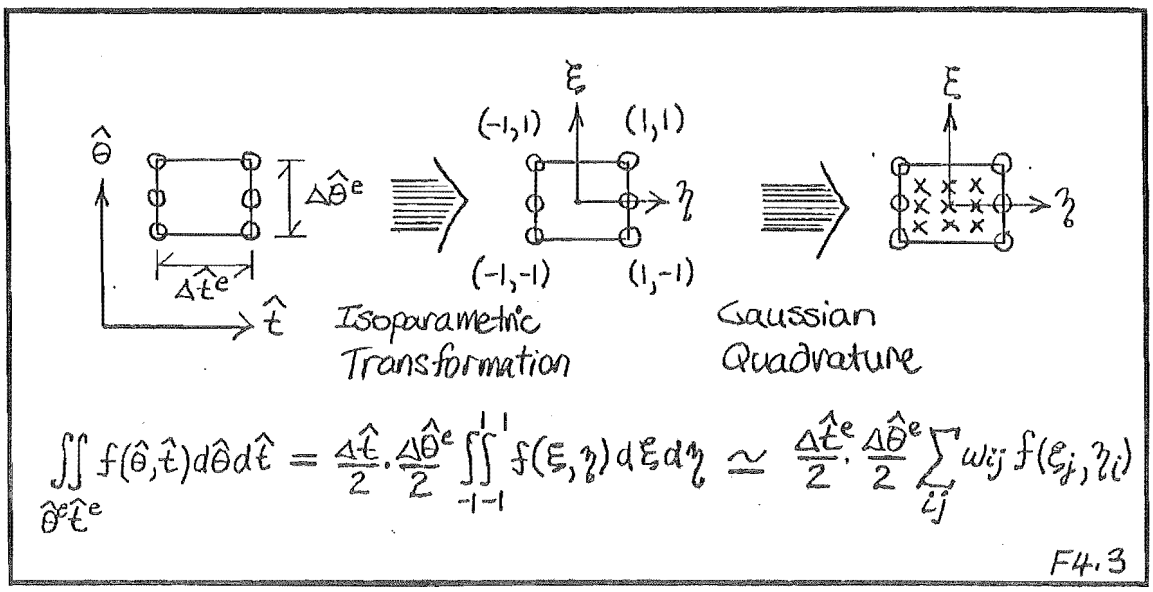

Throughout this work 3 x 3 quadrature rules were found to strike a good balance between accuracy and efficiency, both 2 x 2 and 4 x 4 rules having been tried.

Force Balance Equations : Force balance expressions are integrated analytically as follows : Rewriting equations (3.15)(3.16) in vector form :

$$\int_{\hat{\Omega}^e} \overline{W} \begin{Bmatrix} \cos\theta \\ \sin\theta \end{Bmatrix} N_j^e \overline{N}^k \, d\hat{\Omega}^e \, \hat{p}_j^k + \begin{Bmatrix} \hat{f}_x \\ \hat{f}_y \end{Bmatrix}^k \int_{\hat{T}^e} \overline{W} \overline{N}^k \, d\hat{T}^e = 0 \qquad (4.10)$$

the temporal integrations can be determined using :

$$\int_{\hat{T}^e} \overline{W} \overline{N}^k \, d\hat{T}^e = \frac{k\Delta\hat{t}^e}{6}$$

giving

$$\frac{\Delta\hat{t}^e}{2} \left[\frac{k}{3} \begin{Bmatrix} <A_x> \\ <A_y> \end{Bmatrix} \hat{p}^k + \frac{k}{3} \begin{Bmatrix} \hat{f}_x \\ \hat{f}_y \end{Bmatrix}^k \right] = 0 \qquad (4.11)$$

where

$$\begin{Bmatrix} <A_x> \\ <A_y> \end{Bmatrix} = \begin{bmatrix} \cos\theta_i & -\sin\theta_i \\ \sin\theta_i & \cos\theta_i \end{bmatrix} . \underset{\sim}{B} \; ; \; \underset{\sim}{B} = \int_{\theta^e} \begin{Bmatrix} \cos\theta^e \\ \sin\theta^e \end{Bmatrix} <N> d\theta^e$$

(θ_i : global angular element coordinate, θ^e : local angular coordinate ($\theta = \theta_i + \theta^e$)). All spatial integrations are thus contained in $\underset{\sim}{B}$ which can be conveniently re-constructed from W of Section 3.2.1b.

From the above treatments, it can be seen that in terms of integration, time and space dimensions behave as a single continuum. Within this continuum, the temporal mesh remains constant with respect to $\hat{\theta}$, allowing factor $\frac{\Delta\hat{t}^e}{2}$ to be dropped from both the Reynolds and force balance expressions.

(b) **Interpolation :**

The theory developed thus far has largely been independent of the shape or trial functions. The form these functions take and their accompanying meshes are as follows :

Spatial Trial Functions :

The spatial trial function N_i, used throughout this work is the quadratic Lagrangian element of F4.4.

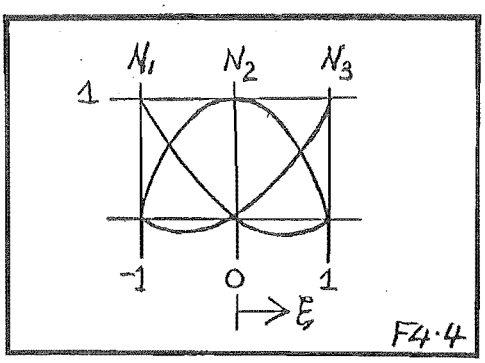

F4·4

This element is discouragingly inhomogeneous when used on coarse meshes : steadily loaded rigid bearing solutions can vary significantly as the load line is moved through an element. However, uniform circumferential meshes of around 36 elements have been found to be sufficiently fine to ensure homogeneity. (See Section 5.2.3b for further discussion).

Temporal Trial/ Weight Functions : $(\overline{N}^i, \overline{W})$. Earlier sections introduced linear Lagrangian functions (F4.5) as both trial and weighting functions of the temporal data. Using these functions, temporal mesh divisions of up to 10^0 crank-angle have been successfully tested in conjunction with interval halving.

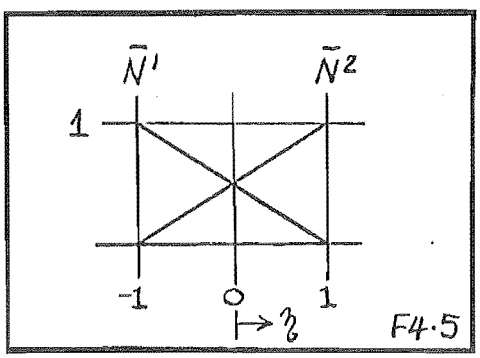

F4·5

Elastic Displacement Interpolation : Having chosen to integrate Reynolds' equation numerically, it becomes necessary to interpolate nodal elastic displacement data to obtain fluid-film Gauss point data. Fortunately, elastic and fluid-film meshes are continuously aligned, however, the form this interpolation

takes is found to be important.

Exact curved beam models posed no problems, interpolation being performed using the curved beam shape functions. The resulting displacement fields are necessarily smooth, a consequence of their analytic formulation.

Numerical elastic models are less amenable. Initially Gauss point displacements were determined using one-dimensional cubic Hermite interpolation of the requisite nodal data. However, the resulting displacement fields were not sufficiently smooth to be used; it would seem that *one–dimensional* Hermite interpolation is not a close enough approximation of the *two–dimensional* sub-parametric Hermite displacement variation. Instead, nodal u_r,u_r' data is interpolated individually using linear shape functions, sufficient smoothing being obtained this way.

Repeated interpolation is avoided by performing interpolation once, at program initialisation. Subsequent displacement calculations are performed entirely on Gauss point data.

Further discussion on elastic displacement continuity can be found in Sections 4.2.2, 5.3.2.

External Load Interpolation : At any given time, external loads $\hat{f}_x$,$\hat{f}_y$ are determined using cubic Hermite interpolation of nodal load data, typically supplied every 10^0 crank-angle. The additional nodal derivative data required by the Hermite procedure is generated using central difference approximations of the 'raw' load data.

4.2 Elasticity Solutions

This section presents the adaptations of some standard solution procedures of linear elasticity : Influence matrix constructions of exact beam theories; Sub-Structuring of Finite Element implementations.

Trial function selection and its ensuing effects on fluid-film equations are discussed.

Finally, sample elastic displacement fields are presented for radially point loaded structures, allowing dimensionless characterisation of elastic behaviour to be attempted.

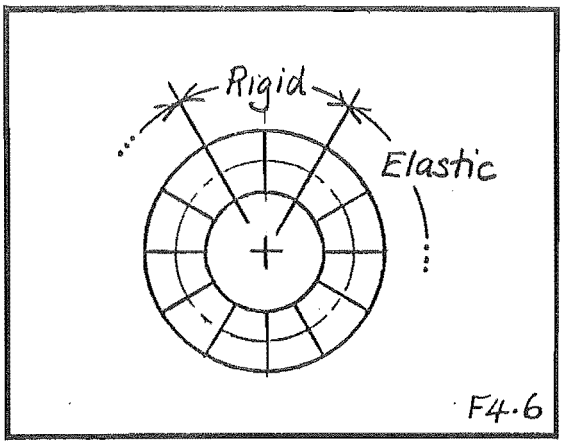

F4.6

4.2.1 *Curved Beams*

Elasticity models were initially constructed using rigid sectors and 'built-in' elastic sectors (F4.6). Careful restrictions on geometry allow smooth elastic solutions to be generated very frugally through an influence matrix construction.

(a) **Influence Construction :**

Using the exact curved beam element of Section 3.2.1 and uniform spatial meshes of constant rectangular cross-section, influence relationships are constructed as follows :

The elastic sector is firstly divided into two elements, the division falling on the first global element boundary. Nodal loads $\{F_r, F_\theta, M\}$ are then applied to the interface (a-b) and displacements $\{u_r, u_\theta, r_c\gamma\}_i$ determined at the required global positions (Gauss points) in the two elements. (F4.7).

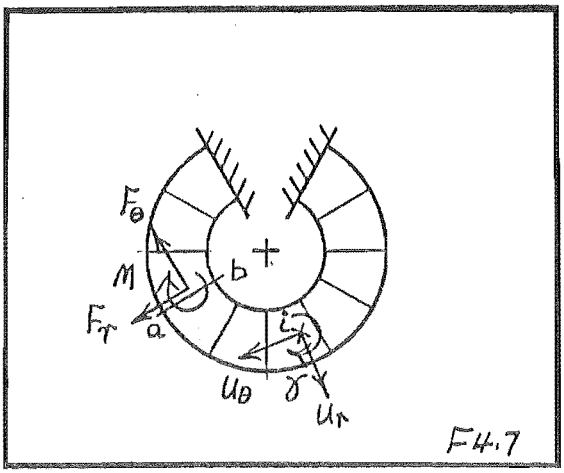

F4.7

This procedure is repeated with division a-b falling on successive global element boundaries, structural symmetry being used to afford further economies. The resulting influence relationship can be written as follows :

$$\underset{\sim}{u} = \frac{r_c^3}{EI}\underline{\bar{K}}^{-1}\,\underset{\sim}{f} \quad \text{where} \tag{3.19}$$

$\underline{\bar{K}}^{-1}$ is the global influence matrix, the other terms as per Section 3.2.1.

Global pressure/nodal-force relationships and body-force/nodal-force relationships are assembled in the usual F.E manner[69]. The required non-dimensional forms,

$$\hat{\underset{\sim}{u}} = \Lambda'(\underline{\bar{K}}^{-1}.\underline{\bar{A}})\hat{\underset{\sim}{p}} + \Xi'(\underline{\bar{K}}^{-1}.\underline{\bar{V}})\hat{\underset{\sim}{b}} \tag{3.31}$$

can then be assembled ready for partitioning.

(b) **Sample Results :**

Results for a 300^0 curved-beam model with radially applied nodal forces are presented in F4.8†.

In this figure, neutral-axis displacement fields u_r, u_r', u_θ are represented by separate families of curves. Successive curves in each family depict dimensionless displacement behaviour induced by radial force F_r applied sequentially around the beam nodes.

---

† Unless stated otherwise, curved beam models use thick beam theory (E/GK=3).

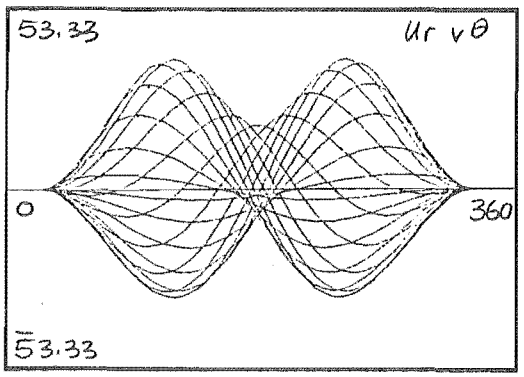

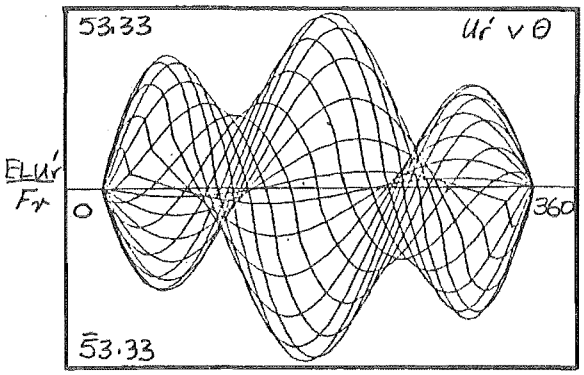

CURVED BEAM N-A DISPLACEMENTS

Elastic Sector	300°
Element Size	15°
t/r	0.5
E/GK	3.0

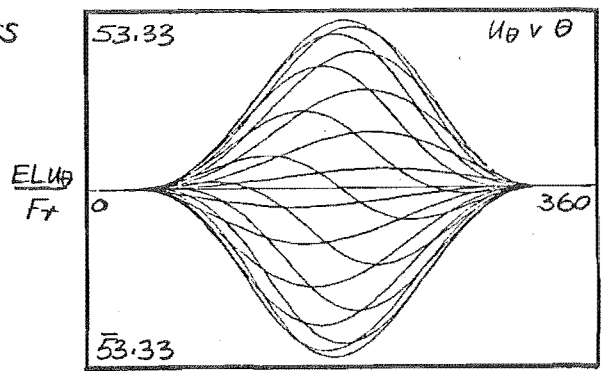

F4.8

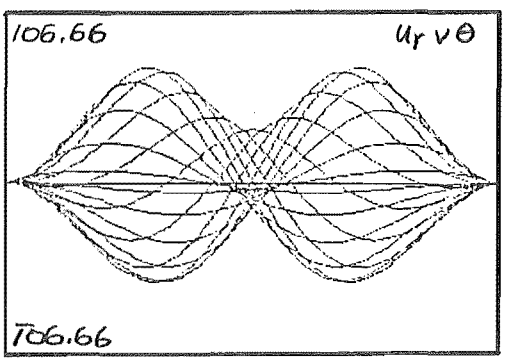

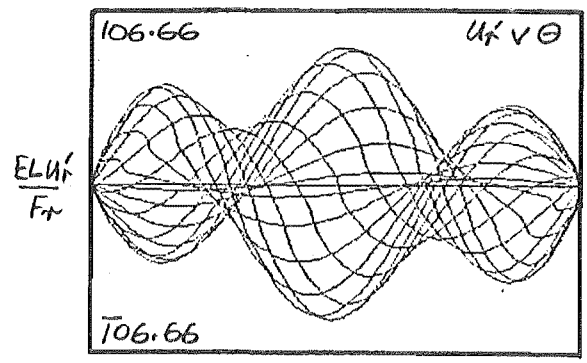

CURVED BEAM N-A DISPLACEMENTS

Elastic Sector	360°
Element Size	10°
t/r	0.5
E/GK	3.0

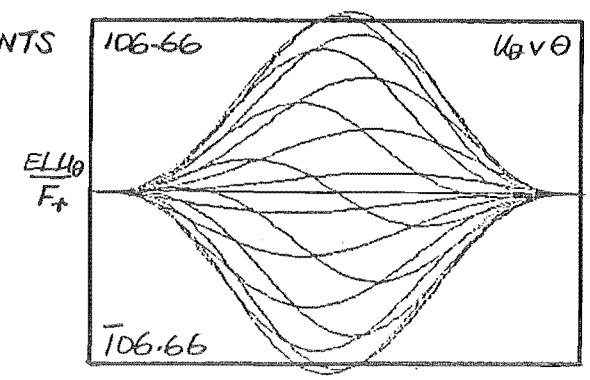

F4.9

One interesting feature characteristic of rings, is the 'geometric stiffening' of the structure as load moves towards the beam's line of symmetry. This is accompanied by a general 'pinching' of the ring structure (F4.10).

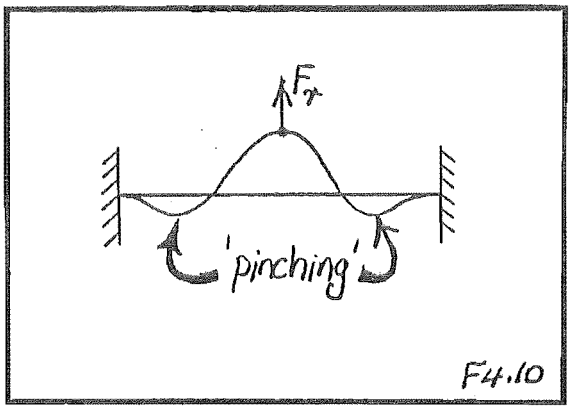

The behaviour of a 360^0 ring, presented in F4.9, is clearly very similar to the 300^0 ring of F4.8. The removal of the rigid neck approximately doubles deflection.

4.2.2 *Planar Finite Element Models*

To overcome geometrical inadequacies of rigid-elastic sector modelling, F.E plane-stress models of constant thickness were constructed.

These models have impaired continuity when compared to curved beams, requiring a judicious choice of displacement trial functions if successful operation of the fluid-film equations is to be achieved. Furthermore, to efficiently process multiple load cases (~ 600) at a small percentage of the total nodes (~ 10%), selective tailoring of standard solution procedures is required.

Steps undertaken to achieve these objectives are outlined in the following sections :

(a) Trial Functions

A variety of functions are used for different purposes in this work :

Displacement Trial Functions : (N_i) Subparametric cubic Hermite elements[69,92] incorporating quadratic Lagrangian geometry are deployed in the work presented.

This element uses a 12-term displacement polynomial in conjunction with an 8-term geometry polynomial. (F4.11). Implementation details can be found in Appendix A6.

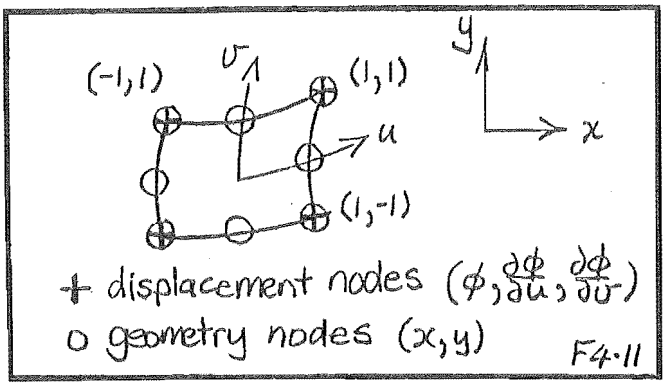

Earlier attempts to use simpler 8-noded isoparametric element solutions were unsuccessful; insufficient derivative continuity impeded the workings of the fluid-film equations. Deployment of the Hermite element, with its enhanced inter-element continuity, provided sufficient continuity for F.E analogues of the curved beam models to run successfully. However, convergence of the fluid-film model was impaired when compared to the equivalent curved beam solutions.

Clarification of the relationship between elastic field continuity and fluid-film equations clearly warrants further investigation, however it was considered beyond the scope of this work.

Pressure Trial Functions : (M_i). Pressure tractions are modelled using quadratic Lagrangian functions. These functions can be salvaged from the two-dimensional geometry functions (Appendix A6) by specifying the traction side[87].

Body–Force Trial Functions : ($\overline{M}_i$). Body forces are assumed to remain constant over each element, variation being element-wise. The applied body forces are then determined at the element centroids. Fine spatial meshes necessary for overall solution accuracy ensure suitable apportioning of these forces.

(b) **Sub-Structured Solutions :**

In this work, Sub-Structuring techniques[93] are used to 'reduce' the initial structure to that of a super-element :

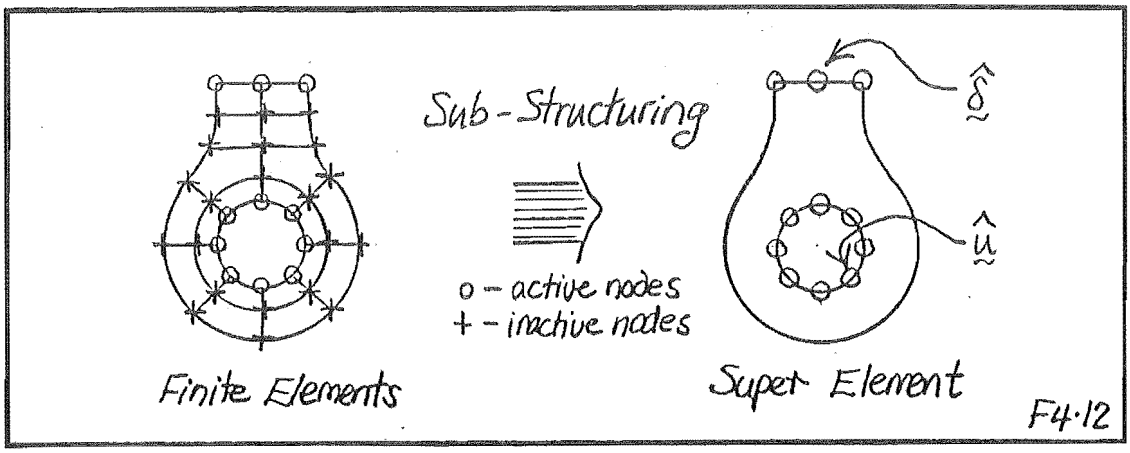

Redundant nodes are statically condensed from the structure during element assembly, a procedure performed automatically by Frontal-Solvers[87] and adapted for this work.

The resulting 'reduced equations' can then be partitioned to read :

$$\begin{bmatrix} \overline{K}_1 & \overline{K}_2 \\ \overline{K}_3 & \overline{K}_4 \end{bmatrix} \begin{Bmatrix} \hat{u} \\ \hat{\delta} \end{Bmatrix} = \Lambda \begin{bmatrix} \overline{A}_1 \\ \overline{A}_2 \end{bmatrix} \hat{p} + \Xi \begin{bmatrix} \overline{V}_1 \\ \overline{V}_2 \end{bmatrix} \hat{b} \qquad (4.12)$$

where $\hat{u}$ - active (retained) nodes

$\hat{\delta}$ - nodes with prescribed displacements.

This reduced stiffness relation is dense (non-sparse), not unlike relationships generated by Boundary Integral Methods[94]†.

The 'solution' for displacements $\hat{u}$ can be written as :

$$\hat{u} = \Lambda(\overline{K}_1^{-1}\overline{A}_1)\hat{p} + \Xi(\overline{K}_1^{-1}\overline{V}_1)\hat{b} - (\overline{K}_1^{-1}\overline{K}_2)\hat{\delta} \qquad (4.13)$$

---

† these would appear to have a promising future in EHL work.

whilst reactions $\hat{\underset{\sim}{r}}$ at prescribed displacements $\hat{\underset{\sim}{\delta}}$ are :

$$-\hat{\underset{\sim}{r}} = \Lambda(\overline{\underline{A}}_2-\overline{\underline{K}}_3\overline{\underline{K}}_1^{-1}\overline{\underline{A}}_1)\hat{\underset{\sim}{p}} + \Xi(\overline{\underline{V}}_2-\overline{\underline{K}}_3\overline{\underline{K}}_1^{-1}\overline{\underline{V}}_1)\hat{\underset{\sim}{b}} - (\overline{\underline{K}}_4-\overline{\underline{K}}_3\overline{\underline{K}}_1^{-1}\overline{\underline{K}}_2)\hat{\underset{\sim}{\delta}} \ . \qquad (4.14)$$

The efficiency of the above processes rely heavily on there being only a small percentage of retained nodes.

For rigid constraints, expression (4.13) reverts to the form presented in Section 3.2.3 :

$$\hat{\underset{\sim}{u}} = \Lambda(\overline{\underline{K}}_1^{-1}\overline{\underline{A}}_1)\hat{\underset{\sim}{p}} + \Xi(\overline{\underline{K}}_1^{-1}\overline{\underline{V}}_1)\hat{\underset{\sim}{b}} \ . \qquad (3.29)$$

(c) **Sample Results :**

As a companion to the earlier curved-beam results, centre-line (℄) and surface displacements for F.E curved-beams are presented in figures F4.13, F4.14 respectively. Nodal interpolation is via *one–dimensional* cubic Hermite polynomials. (See Section 4.1.3b).

For engineering purposes, curved-beam and F.E. ℄ displacement fields (F4.8, F4.13) can be considered to be identical. Surface F.E. displacements are however less amenable, u_r' beginning to exhibit undesirable behaviour about the applied loads. Fortunately, this behaviour occurs between nodes and is simply circumvented using linear interpolation of nodal u_r' data.

Most features of the curved beam model carry over into the planar big-end model of F4.15 : geometric stiffening becomes more pronounced, undesirable u_r' behaviour reappears and is once again circumvented using linear interpolation†. As expected, some discrepancy in behaviour is apparent about the palm-end of the rod, however by-and-large the full ring model of F4.9 compares favourably with

---

† linear interpolated surface displacements are presented.

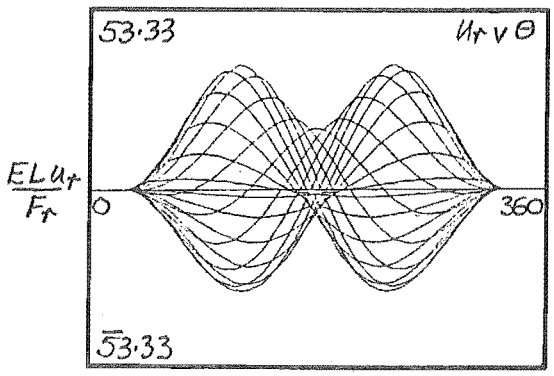

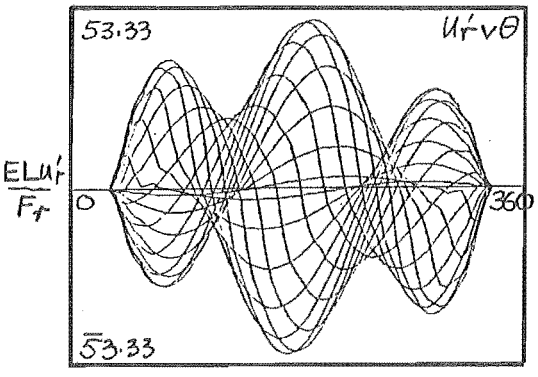

F·E CURVED BEAM (℄)

Elastic Sector 300°

Elements 20 x 2

t/r 0.5

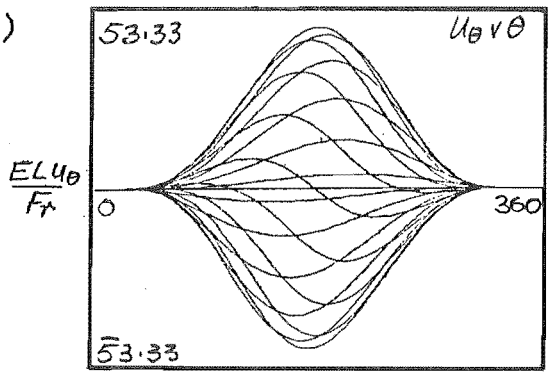

F4·13

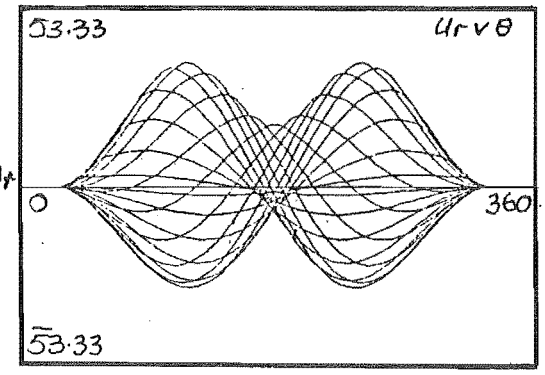

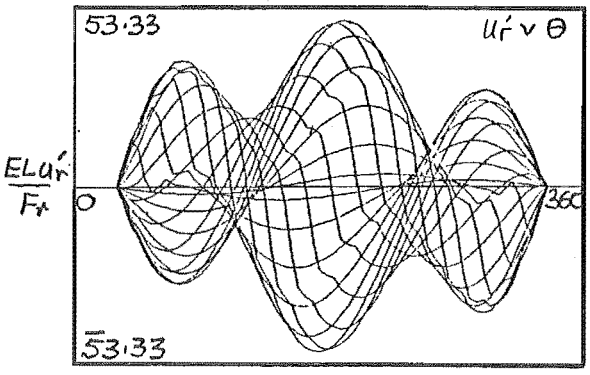

F.E CURVED BEAM (Surface)

Elastic Sector 300°

Elements 20x 2

t/r 0·5

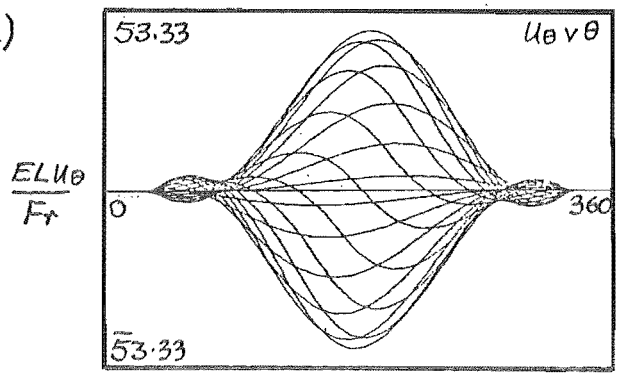

F4·14

the planar big-end of F4.15. The development of a curved beam model incorporating variable cross-sections may well be warranted.

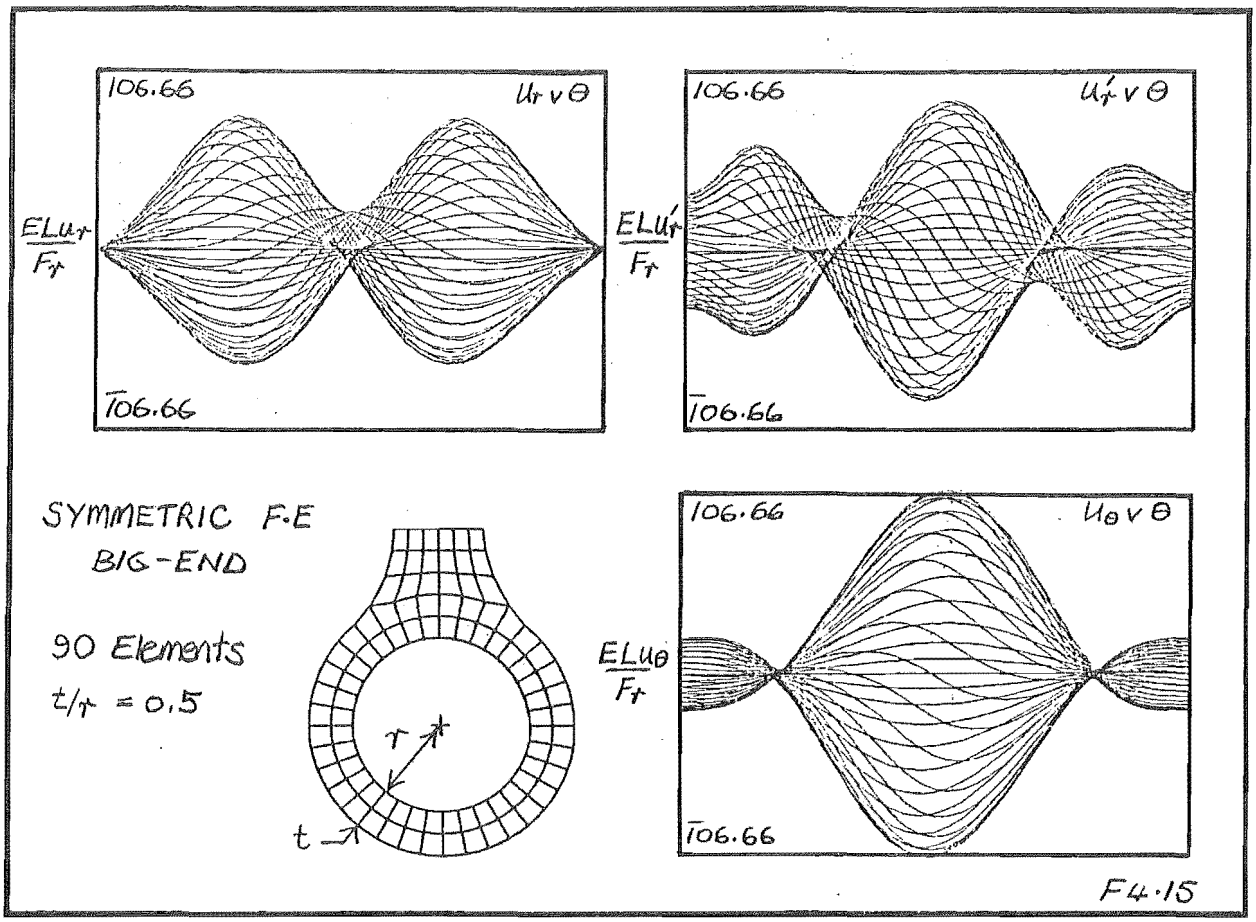

F4.15

(d) **Boundary Constraints :**

To complete this section, boundary constraints applied to the F.E. planar rod models are summarised in F4.16 :

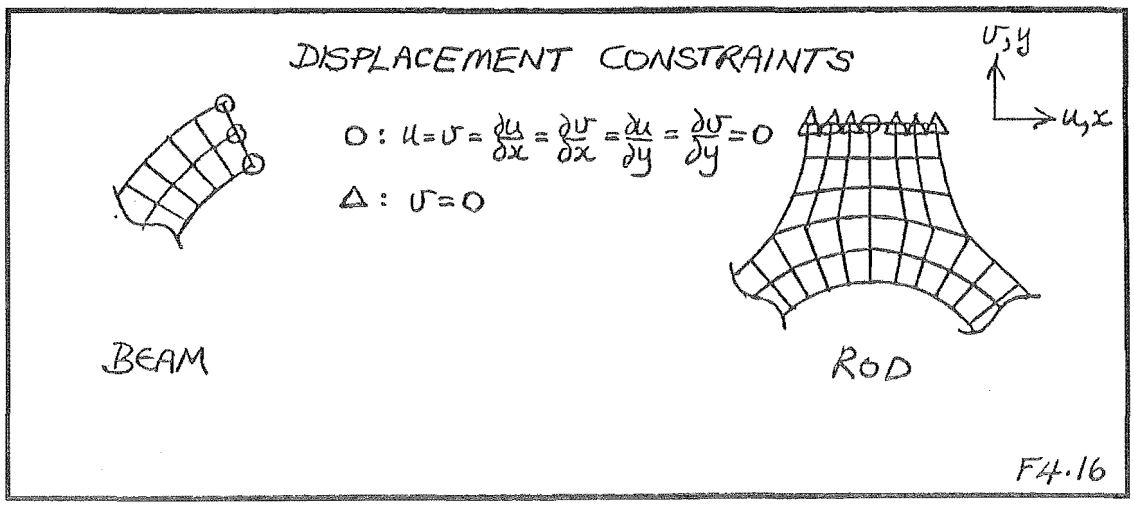

F4.16

4.2.3 *Dimensionless Elastic Behaviour*

A natural starting point for the characterisation of elastic behaviour is the curved-beam models of Section 3.2.1.

Taking the 360^0 ring of F4.9 and replacing dimensionless parameter $EL\,\frac{u}{F_r}$ by $\frac{EI}{r_c^3}\frac{u}{F_r}$, one finds that displacements accurate to within 10% can be accommodated on this single figure for the range of thickness :

$$0.4 < t/r < 0.6$$

Similarly, elastic sector size θ_s, can be incorporated to lesser accuracy using the additional multiplier $\left[\frac{360}{\theta_s}\right]^m$ where $300^0 < \theta_s < 360^0$, $m \simeq 4$ $(3 < m < 5)$.
These relationships are summarised in T4.2 as a series of multipliers for the $EL\,\frac{u}{F_r}$ ordinate (106.66) of F4.9.

Clearly, rigid sector size is as important as thickness ratio in determining elastic behaviour, although the above range of θ_s may be overstated.

θ_s \ t/r	0.40	0.45	0.50	0.55
360	1.728	1.291	1	0.797
340	1.375	1.027	0.796	0.634
320	1.079	0.806	0.624	0.498
300	0.833	0.623	0.482	0.384

T4.2

Planar F.E analyses (F4.15) suggest that, without attempting parameterisation of neck geometry, elastic behaviour is analogous to full-ring behaviour ($\theta_s = 360^0$). These similarities allow the full-ring model to form the basis of a dimensionless dynamic film-thickness estimate in Chapter Seven.

To complete this section, it is useful to present a single parameter characterisation of displacement behaviour :

$$0\left[\frac{u}{F_r}\right] = \frac{r_c^3}{EI} = \frac{12\left[\frac{r}{t}\right]^3\left[1 + \frac{t}{2r}\right]^3}{EL} \qquad (4.15)$$

With this characterisation it is possible to investigate the case of an infinitely thick housing, namely $t/r = \infty$:

$$0\left[\frac{u}{F_r}\right]_{\infty} = \frac{12\left[\frac{r}{t} + \frac{1}{2}\right]^3}{EL} = \frac{12}{EL}(\tfrac{1}{2})^3$$

In comparison, a typical housing $t/r = \frac{1}{2}$ gives :

$$0\left[\frac{u}{F_r}\right]_{\frac{1}{2}} = \frac{12}{EL}\left[\frac{10}{4}\right]^3$$

thus

$$0\left[\frac{u}{F_r}\right]_{\infty} / 0\left[\frac{u}{F_r}\right]_{\frac{1}{2}} = \left[\frac{2}{10}\right]^3 = 0.8\% \qquad (4.16)$$

Since journal deflection is dimensionally equivalent to infinitely thick housing deflection[8], (4.16) represents the ratio of journal to housing deflection; ample justification for the rigid journal treatment introduced in Section 2.1.4.

In closing this Chapter, it will be observed that the preceding work has largely involved the collection of various theoretical apparatus making up the big-end EHL problem. In the remaining Chapters we shift our attention to the verification of these techniques and their associated solutions in firstly a steady-state, then full dynamic environment.

CHAPTER FIVE

STEADY STATE SOLUTIONS

In the context of connecting-rod bearings, steady state solutions have little intrinsic value, moreover they have largely been responsible for the misconceptions present in dynamic work. Despite this, they do however provide a convenient means for the verification of the various solution techniques employed in this work.

This Chapter firstly uses the rigid model to verify parabolic pressure assumptions and mesh dependencies. Performance over a range of geometry and load are investigated. Selected elastic solutions are then reviewed from the literature, attention focusing on the work of Allen[17], Stafford[20], and Fantino[19]. Factors affecting oil-film sensitivity and multi-peak pressure behaviour are studied in detail. Finally, the performance of Fantino's bearing on both ring and housing geometries is presented over a broad range of load.

All results are generated on uniform meshes, solutions to the dynamic problem being delayed until Chapter Six.

Some background on the development of a steady state solution is a useful preliminary to the main body of this Chapter.

5.1 Steady Solution Development

In this work steady state results are determined as the limit of a dynamic solution under steady load: journal locus convergence is achieved through the decay of starting error transients to a steady state. This decay is load dependent; most rapid for high loadings, tediously slow at low load.

Such a solution procedure is then load based, the load vector being fixed in

magnitude and direction. In comparison, traditional steady state solutions are determined by fixing journal position, acquiring a pressure distribution and hence load vector. Without considerable load vector alteration, a direct comparison of solutions is difficult: modelling differences, most notably film boundary conditions for the rigid problem and elasticity models in the elastic case, lead unavoidably to discrepancies.

Bearing these points in mind, rigid then elastic steady state solutions are next presented.

5.2 Rigid Steady State Solutions

Several studies have implemented parabolic axial pressure approximations [11],[71], this section adds to that body of information on F.E. based approximations.

We firstly compare the parabolic axial pressure assumption against finite length solutions, then investigate the effects of quadratic pressure shape functions on breakdown boundary interpolation. General results over a range of loads, meshes and L/D ratios complete the section.

5.2.1 *Specific Cases : Axial pressure dependence*

Verification of axial pressure dependence is carried out against the half-Sommerfeld finite bearing solution of Hays [72]. In his work Hays presents axial and circumferential pressure distributions for a range of L/D, F5.1 presents results for L/D ratios of 1, $\frac{1}{2}$, $\frac{1}{4}$ at loads †associated with an eccentricity of 0.8 :

---

† the loads used are those presented by Cameron[43]

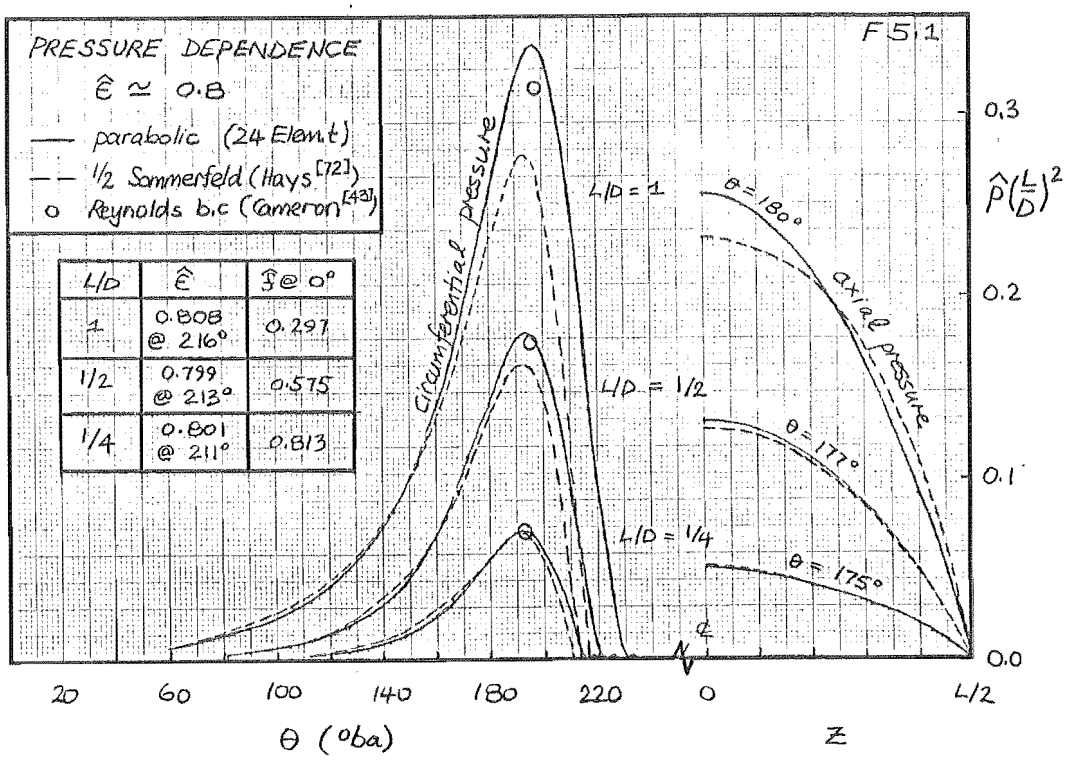

As can be expected, circumferential distributions differ, pressure being 'released' by the extra boundary flow of the half-Sommerfeld solution. Peak pressures and breakdown boundary positions are however quite close to the Reynolds boundary condition solutions given by Cameron[43].

Axial pressure distributions for the finite L=D solution show distinct centre-line pressure flattening leading to a lower load capacity in the parabolic approximation. This load carrying deficit, compensated by greater journal eccentricity, leads to higher peak pressures in the parabolic model.

At lower L/D ratios, the finite solution develops very parabolic axial profiles, flattening being much less pronounced. Under these conditions the parabolic model would seem very appropriate. Tests in Section 5.2.3 provide broader verification over a range of load, mesh size and L/D ratio.

5.2.2 *Breakdown Boundary Interpolation*

One of the unavoidable consequences of using quadratic pressure shape functions is the development of negative pressure at film rupture: consider for example a pressure distribution as it is moved across a mesh. In the region of film rupture three interpolation scenarios are possible as the various pressure shape functions come into play; F5.2 presents the possibilities :

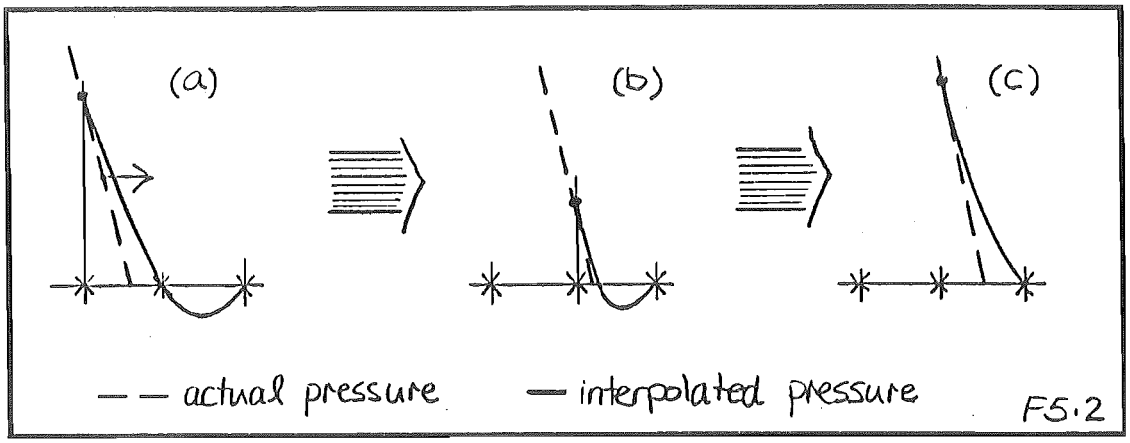

Because this behaviour occurs in a critical region of the oil-film, a region of high pressure gradients, solutions can develop an acute sensitivity to mesh. This sensitivity, explored further in the following section, can be overcome by mesh refinement or alternatively by a change to an homogeneous trial function (linear trial functions for example).

For convenience, negative pressures are not plotted in figures presented in this work, the exception being the extreme case of F5.5; in this figure, negative pressures represent less than 2% of the applied load.

5.2.3 *General Results*

Results covering L/D ratios of 1, ½, ¼, 0 (short bearing solution) and loads[43] associated with eccentricities 0.8, 0.9, 0.95, 0.97 are next presented. Two sets of solutions on both 24 and 36 element meshes are developed: variable-load fixed-direction solutions (Table T5.1) and fixed-load variable-direction solutions (Table T5.2).

TABLE 5.1 : **Fixed-Direction Variable-Load Results**

36 Elements																
L/D	0.0				0.25				0.50				1.0			
$\hat{\epsilon}$	0.97	0.95	0.90	0.80	0.97	0.95	0.90	0.80	0.97	0.95	0.90	0.80	0.97	0.95	0.90	0.80
$\hat{f}$	45.73	16.34	4.001	0.955	21.01	9.242	2.883	0.813	8.711	4.496	1.695	0.575	2.798	1.706	0.706	0.297
$\Delta\hat{\epsilon}$(%)	− .04	+ .05	− .03	− .03	+ .17	+ .03	+ .03	+ .11	+ .14	+ .07	0	− .12	+ .20	+ .60	+ .30	+ .30
$\Delta\hat{\varphi}$(deg)	− 0.2	+ 0.3	− 0.2	− 0.1	+ 0.4		− 0.2	+ 0.1	− 0.1		− 0.5	−0.7	− 0.4		− 0.4	− 0.2
$\Delta\hat{h}$(%)	+ 1.3	− 1.0	+ 0.3	+ 0.1	− 5.6	− 0.6	− 0.3	− 0.5	− 4.6	− 1.3	0	+ 0.5	− 8.0	− 12.	− 3.0	− 1.0
$\Delta\hat{p}$(%)	− 3.0	+ 3.0	− 0.7	− 0.1	− 4.0	− 5.0	− .3	+ 1.0	+6.0	+ 7.0	+ 6.0	+ 3.0	+ 25.	+ 27.	+ 15.	+ 7.0
					24 Elements											
$\Delta\hat{\epsilon}$(%)	− .01	− .03	− .02	− .04	+ .08	− .06	+ .04	+ .12	+ .10	+ .40	+ .03	− .05	+ .20	+ .80	+ .20	+ .20
$\Delta\hat{\varphi}$(deg)	− 0.5	− 0.2	+ 0.1	− 0.1	− 0.1		− 0.2	+ 0.2	− 0.2		− 0.5	− 0.4	− 0.3		− 0.6	+ 0.2
$\Delta\hat{h}$(%)	+ 0.3	+ 0.6	+ 0.2	+ 0.2	− 2.7	+ 1.2	− 0.4	− 0.5	−3.0	− 7.6	− 0.3	+ 0.2	− 8.0	−16.0	− 2.0	− 0.9
$\Delta\hat{p}$(%)	−17.0	− 2.0	− 2.0	− 0.6	− 9.0	− 6.0	− 2.0	+ 0.5	+ 3.0	+12.0	+ 4.0	+ 3.0	+16.0	+23.0	+13.0	+ 8.0

TABLE 5.2 : **Fixed-Load Variable-Direction Results** ($\hat{\epsilon}$ = 0.97)

36 Elements																
L/D	0.0				0.25				0.50				1.0			
$\Delta\theta^{\dagger}$	1/4	1/2	3/4	1	1/4	1/2	3/4	1	1/4	1/2	3/4	1	1/4	1/2	3/4	1
$\Delta\hat{\epsilon}$(%)	+ .01	+ .10	+ .02	0	− .13	− .12	− .18	0	+ .06	− .07	− .03	0	+ .01	+ .05	− .08	0
$\Delta\hat{\varphi}$(deg)	− .03	+ .50	+ .30	+ .01	− .45	− .56	− .43	+ .01	+ .37	− .12	− .13	+ .03	+ .10	+ .42	− .11	+ .07
$\Delta\hat{h}$(%)	− 0.3	− 3.3	− 0.7	0	+ 4.6	+ 4.2	+ 2.8	0	− 2.4	+ 2.4	+ 1.0	0	− 0.4	− 1.8	+ 2.9	0
$\Delta\hat{p}$(%)	− 0.1	+ 28.0	+ 5.0	− 0.1	− 2.2	− 1.6	+ 0.8	− 0.1	+ 6.0	+ 1.3	+ 3.2	− 0.1	− 1.1	+ 4.0	− 1.5	+ 0.1
					24 Elements											
$\Delta\hat{\epsilon}$(%)	+ .27	− .12	+ .02	0	+ .03	+ .30	− .70	0	0	+ .20	+ .20	0	− .06	+ .03	+ .30	+ .01
$\Delta\hat{\varphi}$(deg)	+ 1.8	+ .20	+ .60	+ .01	− .26	+ 1.2	+ .10	+ .03	− .30	+ .30	− .90	+ .04	− .30	− .30	+ .80	+ .10
$\Delta\hat{h}$(%)	− 9.0	+ 4.0	− 0.7	0	− 1.0	− 9.0	+ 0.7	0	0	− 6.0	− 7.0	0	+ 2.0	− 1.0	−10.0	− 0.4
$\Delta\hat{p}$(%)	+62.0	+10.0	+14.0	− 0.3	+ 5.0	+29.0	− 7.0	− .01	− 2.6	+ 18.	+ 8.0	− .02	+ 2.0	+ 11.0	+26.0	− .12

† $\Delta\theta$ ≡ Load shift in element units

(a) Fixed-direction Variable-Load Results :

Traditional fixed direction results are presented against the finite Reynolds boundary condition results given in Cameron[43], absolute percentage errors being recorded in T5.1.

Journal position and hence minimum film thickness are presented in F5.3(a) : Positional errors are quite small, $\Delta\hat{\epsilon} < 1\%$, $\Delta\hat{\phi} < 1^0$, there being similar errors on both meshes. These translate to maximum $\hat{h}_{min}$ errors of 10%.

The most conspicuous discrepancy in these results is the high eccentricity in the L=D case. This behaviour reflects the lower load carrying capacity of a parabolic profile at larger L/D ratios. A corresponding increase in peak pressure accompanies this trend (F5.3(c)), maximum pressure errors in the order of 20% occurring in the L=D case.

Finer meshes expectedly give better resolution of both peak pressure and breakdown boundary location, these points being consistently located to the closest nodal division on both meshes. Peak pressures are generally higher on the finer grid, the differences reducing with decreasing load and L/D ratio. Figure F5.4 presents sample distributions using $\hat{p}\left[\frac{L}{D}\right]^2$ as non-dimensional pressure.

There is little merit in pursuing further analysis of 'fixed-direction' mesh dependence; relative motion of mesh and load line can lead to much greater sensitivity.

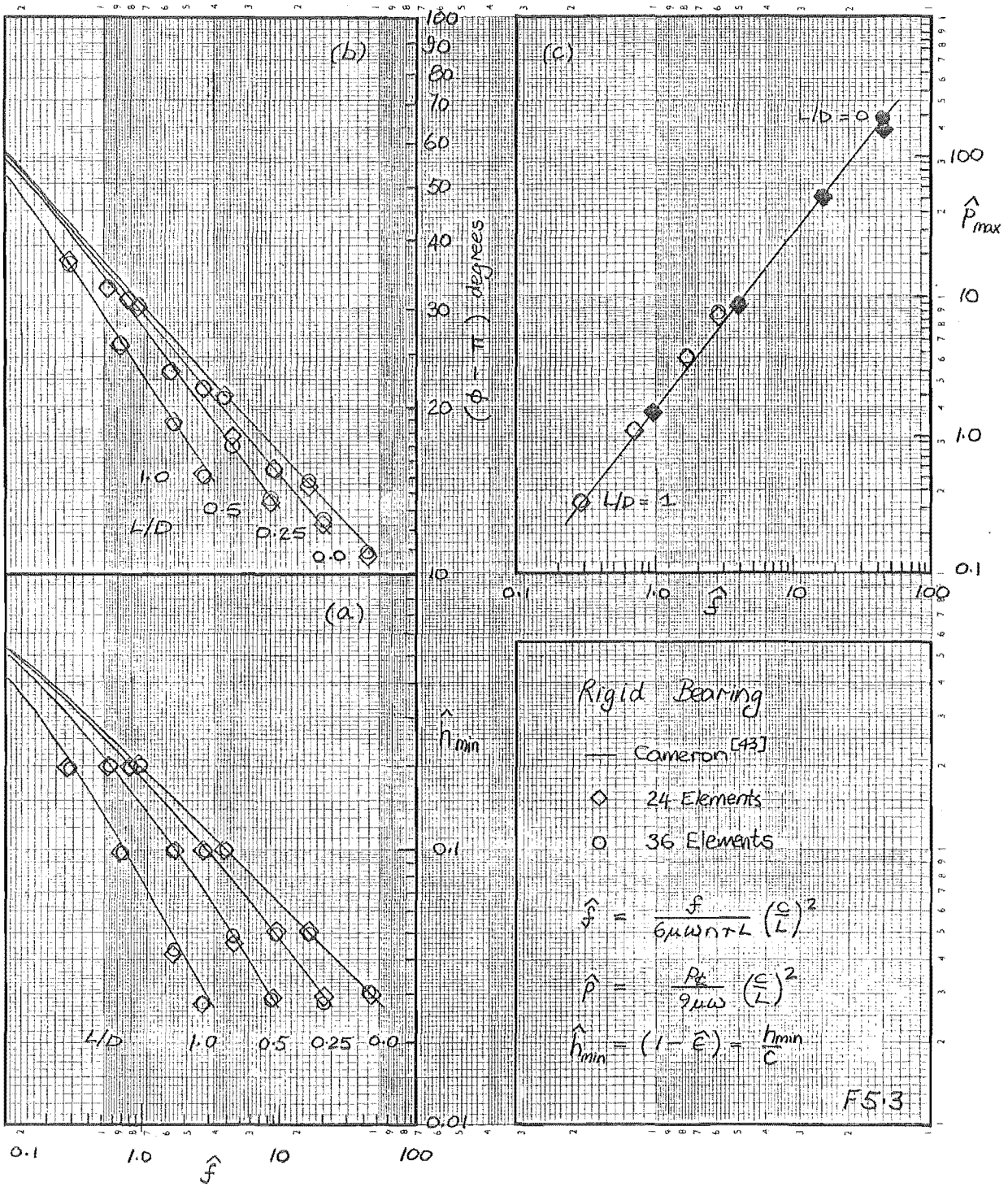
(b)
(a)
(c)
L/D
1.0
0.5
0.25
0.0
$(\phi - \pi)$ degrees
$\hat{h}_{min}$
$\hat{P}_{max}$
$\hat{f}$
L/D = 0
L/D = 1
Rigid Bearing
Cameron [43]
24 Elements
36 Elements
$\hat{f} = \frac{f}{6\mu\omega n r L}\left(\frac{c}{L}\right)^2$
$\hat{P} = \frac{P_{max}}{9\mu\omega}\left(\frac{c}{L}\right)^2$
$\hat{h}_{min} = (1-\epsilon) = \frac{h_{min}}{c}$
F5.3

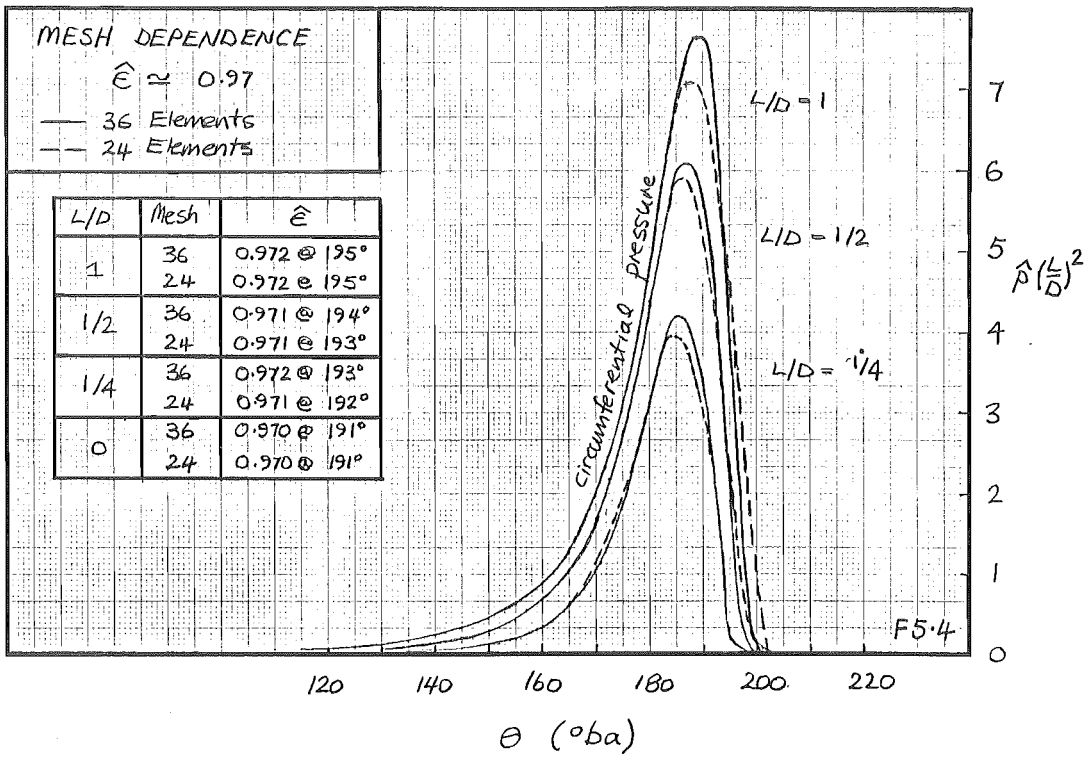

L/D	Mesh	$\hat{\epsilon}$
1	36	0.972 @ 195°
	24	0.972 @ 195°
1/2	36	0.971 @ 194°
	24	0.971 @ 193°
1/4	36	0.972 @ 193°
	24	0.971 @ 192°
0	36	0.970 @ 191°
	24	0.970 @ 191°

(b) **Variable-direction Fixed-Load Results :**

Mesh homogeneity as described in Section 4.1.3(b), can be tested by shifting the load line through an element: T5.2 presents percentage error deviations for $\frac{1}{4}, \frac{1}{2}, \frac{3}{4}$ and 1 element shifts at loads associated with the eccentricity 0.97.

Shifts of one element give an indication of the numerical accuracy obtainable on a given mesh: for 36 elements 0.1%, for 24 elements 1% on all parameters ($\Delta\hat{\epsilon}$, $\Delta\hat{\phi}$, $\Delta\hat{h}$, $\Delta\hat{p}$). Condition numbers for these solutions indicate approximately six digits of lost precision. This makes double precision arithmetic (8 byte reals) mandatory for all calculations.

For smaller shifts, journal positional errors are once again small: $\Delta\hat{\epsilon} < 1\%$, $\Delta\hat{\phi} < 2^0$, $\Delta\hat{h}_{min} < 10\%$ over both meshes. Peak pressures however show considerable deviation: On the finer mesh, accuracy is acceptable (10%) for all but the short bearing solution (L/D = 0). This solution has the highest non-dimensional pressures (26x the L=D solution) and hence gradients, severely limiting solution accuracy. This is more pronounced on the coarser 24 element mesh, rendering pressure solutions strictly exploratory for the tested L/D ratios.

Figure F5.5 shows the degree of pressure distribution distortion possible using quadratic shape functions. An additional feature peculiar to this loading, is the cusp at 165^0. The mechanism for this behaviour is once again quadratic interpolation of high gradient pressures on an inadequate mesh. It should be emphasised that this is 'worst-case' behaviour: highest load on a coarse mesh. Despite these misgivings, journal position and film thickness errors are still very acceptable.

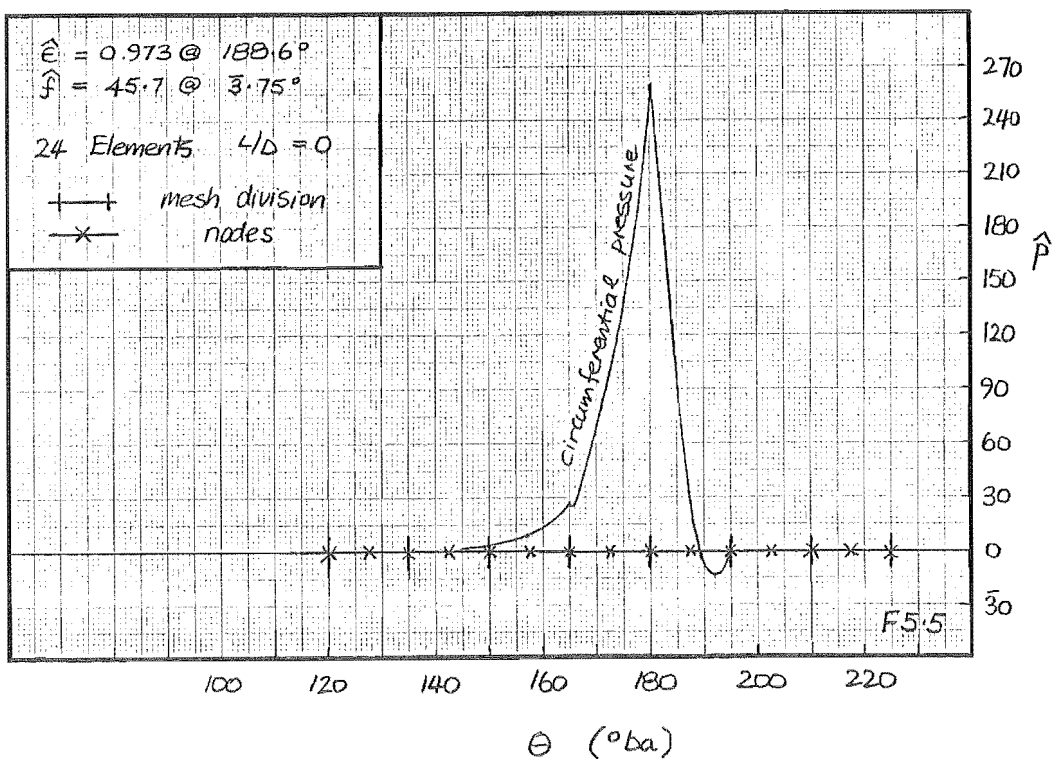

Summarising, the rigid steady state solutions of this section show the parabolic axial pressure assumption to be most appropriate for bearings of length-diameter ratios :

$$0 < L/D < \tfrac{1}{2}$$

whilst less suitable for $L/D > \frac{1}{2}$, it is much more accurate than the traditional 'short-bearing' approximation, $L/D = 0$.

In practice, circumferential pressure behaviour of the quadratic shape functions is more likely to cause problems; for work involving relative motion of mesh and load line, fine discretisations (10^0 b.a. maximum†) must be used if mesh and hence pressure homogeneity is to be maintained. However, accurate journal position can be computed quite confidently on coarser meshes.

We next look at specific elastic solutions.

5.3 Elastic Steady State Solutions

Two groups of elastic steady state solutions incorporating experimental and theoretical aspects are prominent in the literature: the work on housings of Fantino [19] and Frene[21] and that of Allen[17], Stafford[20] and Bozaci[22] on arcs. We look firstly at the theoretical work of Allen and Stafford then re-examine the bearing of Fantino.

5.3.1 *Arc Solutions*

Solutions to the rigid/elastic sector problem have been presented by Allen and Stafford. Both works use a constrained journal position, iteration being performed on the pressure vector and hence external load.

---

† b.a. ≡ bearing angle (circumferential)

(a) Allen :

The work of Allen is based on a finite length solution† incorporating Reynolds' boundary condition. This is in-turn coupled to *thin* inextensional beam theory, Allen incorrectly claiming the use of thick beam theory.

The resulting equations, valid only for steady state conditions, provide a surprisingly accurate solution verification: F5.6 and F5.7 show the results of Allen's[17] method and the current method for an inextensional 270^0 elastic/rigid sector.

Quantitatively, for F5.6 $\hat{\epsilon}$, $\hat{\phi}$, $\hat{h}$ and $\hat{u}$ are all within 1%, centre-line pressure $\hat{p}$ within 2% for the applied load given by Allen. The results in F5.7 are of similar accuracy. Considering the differences in solution techniques: journal position constraint; finite element verses finite differences; parabolic axial pressure distributions versus axial finite difference representations; mesh differences, agreement is exemplary.

(b) Stafford :

The results of Stafford continue along the rigid/elastic sector theme of Allen with some slight differences: Half-Sommerfeld rather than Reynolds boundary conditions are invoked; 8 noded isoparametric elastic elements†† replace curved beam theory.

Duplication of this work is made difficult by the difference in program solution modes: considerable iteration on external load vector is required to achieve the fixed journal position used by Stafford (T5.3).

---

† 64 x 8 grid

†† no indication of mesh is given

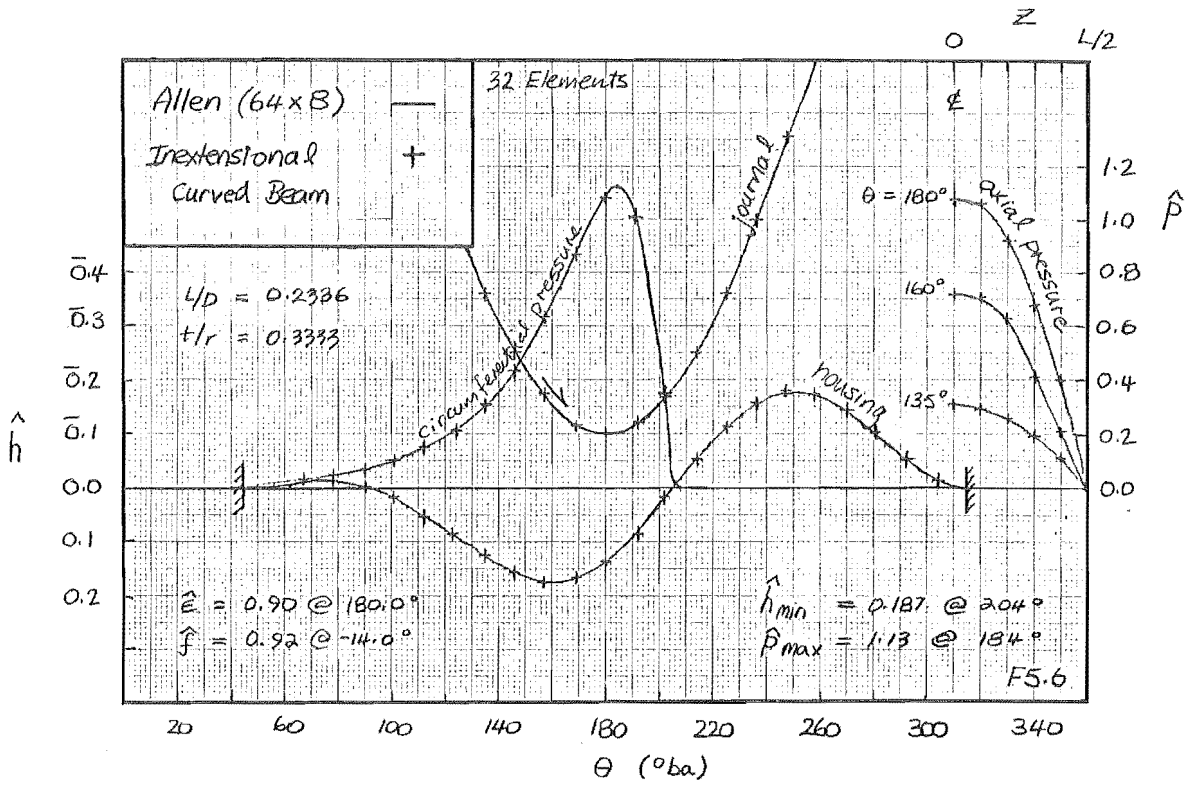
Allen (64×8)
Inextensional
Curved Beam
32 Elements
L/D = 0.2336
t/r = 0.3333
journal
circumferential pressure
housing
θ = 180°
160°
135°
axial pressure
ε̂ = 0.90 @ 180.0°
f̂ = 0.92 @ -14.0°
ĥmin = 0.187 @ 204°
p̂max = 1.13 @ 184°
F5.6
θ (°ba)
ĥ
p̂
Z
0
L/2
ℓ

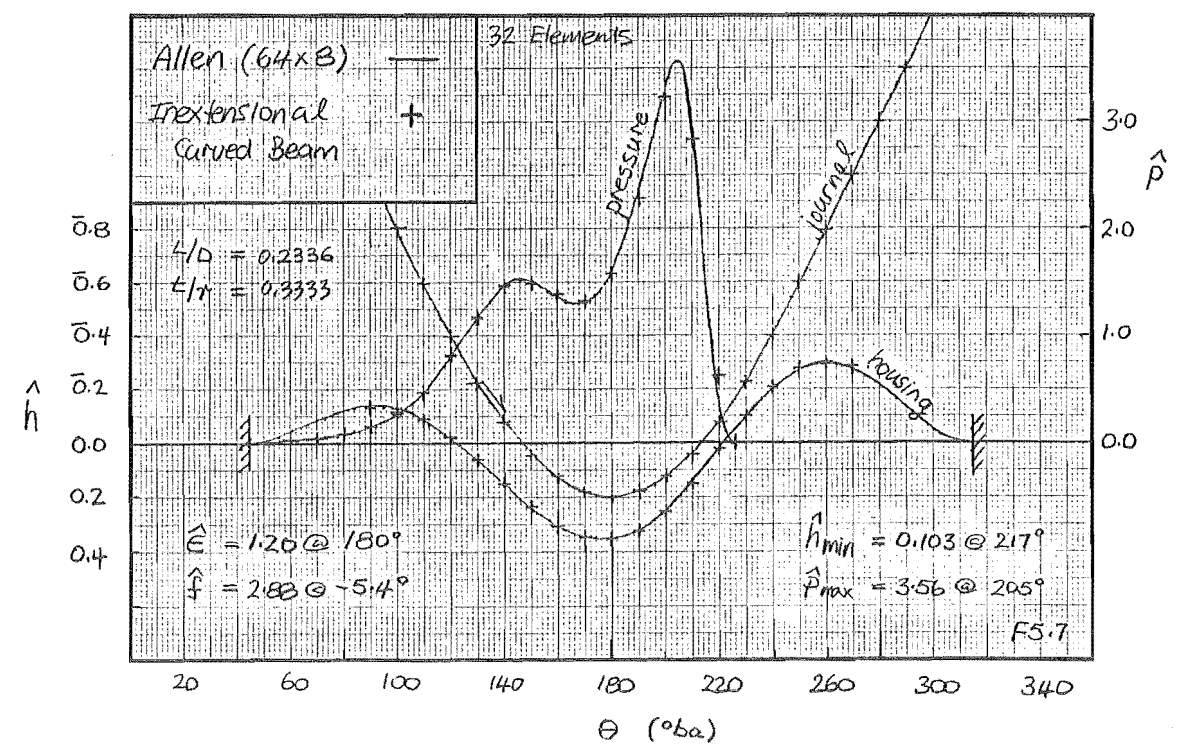
Allen (64×8)
Inextensional
Curved Beam
32 Elements
L/D = 0.2336
t/r = 0.3333
pressure
journal
housing
ε̂ = 1.20 @ 180°
f̂ = 2.88 @ -5.4°
ĥmin = 0.103 @ 217°
p̂max = 3.56 @ 205°
F5.7
θ (°ba)
ĥ
p̂

$\hat{\epsilon}$=1.3 @ 180^0	$\hat{f}$	$\hat{h}_{min}$	$\hat{p}_{max}$
Stafford	0.745 @ - 8.8^0	0.162 @ 230^0	0.800 @ 220^0
Inext.Beam	1.250 @ - 5.3^0	0.129 @ 236^0	1.319 @ 223^0
Thick Beam	0.760 @ - 7.2^0	0.173 @ 231^0	0.730 @ 216^0
Hermite Beam	0.778 @ - 7.2	0.174 @ 230^0	0.755 @ 216^0

T5.3

The results presented in F5.8 are for the most heavily loaded condition:
Case 1, $\hat{\epsilon}$ = 1.3 @ 180^0 of [20].

Considerable discrepancy between the results of Stafford and the inextensional 'Allen' model is apparent. Stafford claimed that this was due to different film boundary conditions, being under the impression that Allen was using thick beam theory. On comparison with actual thick beam results, it would seem that the major discrepancy is in the elasticity models, film boundary conditions being of secondary importance.

Results for an equivalent Hermite F.E beam (32 x 2 elements) are presented in F5.9. These results fall between those of Stafford and the thick curved beam, agreeing closely with the latter. Clearly oil-film sensitivity is sufficient to detect differences in elasticity model type. However, it is insufficient for these differences to create major discrepancies, at least not in this bearing.

In both Allen and Stafford's work, the development of doubly peaked pressure distributions is a consequence of housing 'wrap-around' in association

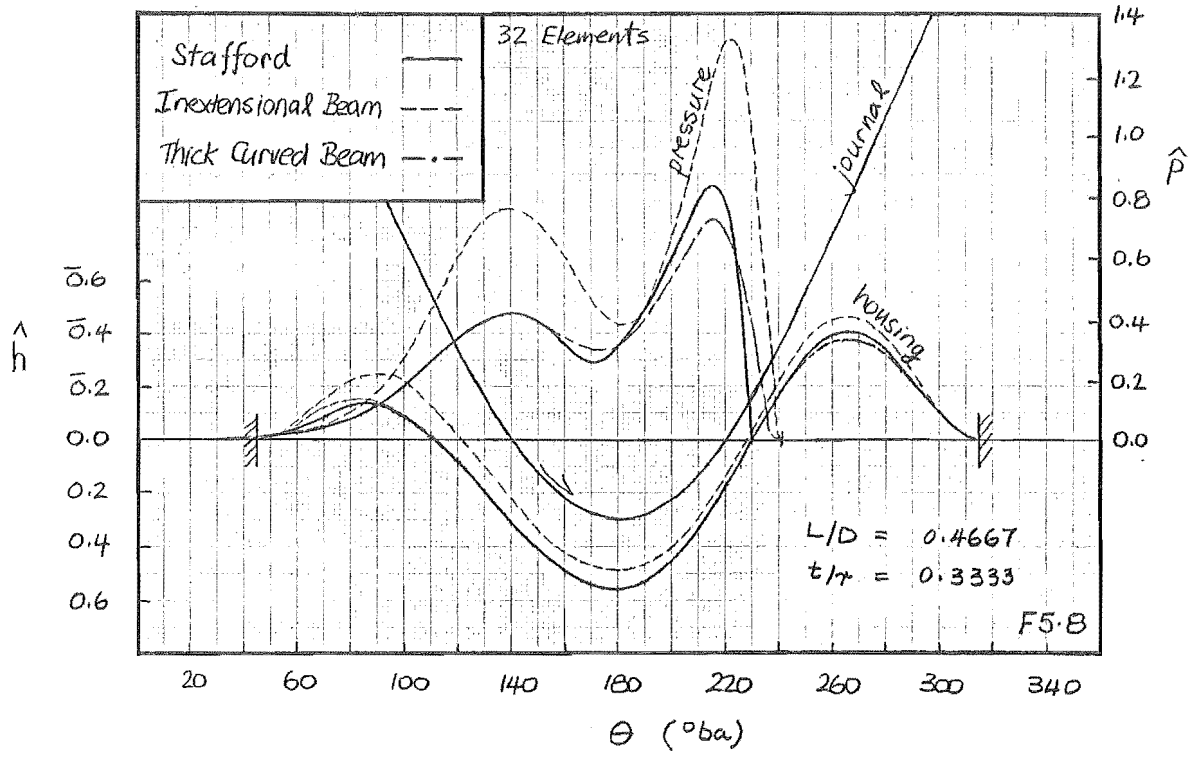
Stafford
Inextensional Beam
Thick Curved Beam
32 Elements
pressure
journal
housing
L/D = 0.4667
t/r = 0.3333
F5.8
ĥ
P̂
θ (°ba)
20
60
100
140
180
220
260
300
340
0.6
0.4
0.2
0.0
0.2
0.4
0.6
1.4
1.2
1.0
0.8
0.6
0.4
0.2
0.0

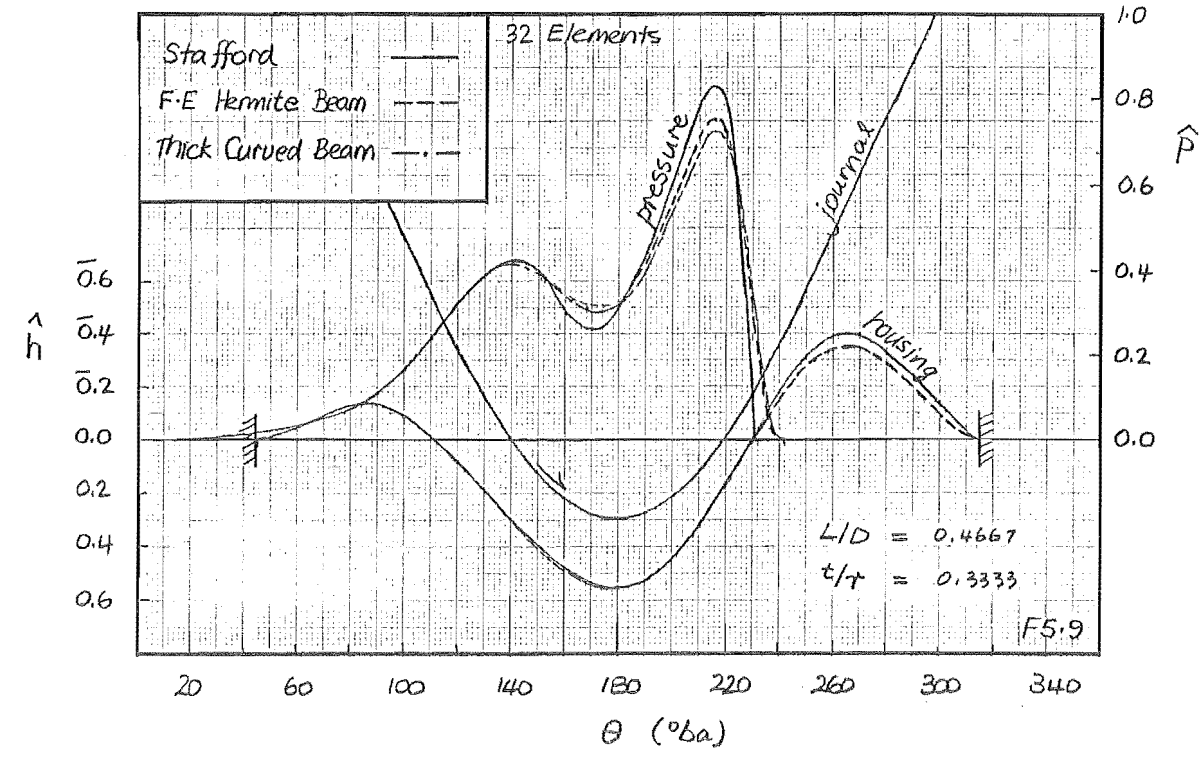
Stafford
F·E Hermite Beam
Thick Curved Beam
32 Elements
pressure
journal
housing
L/D = 0.4667
t/r = 0.3333
F5.9
ĥ
P̂
θ (°ba)
20
60
100
140
180
220
260
300
340
0.6
0.4
0.2
0.0
0.2
0.4
0.6
1.0
0.8
0.6
0.4
0.2
0.0

with curved-beam 'pinching' (F5.10). This behaviour induces an early film build-up and delayed film breakdown. Pressures developed at film inlet decay in the intervening 'wrap-around' region due to reduced constructive wedge action.

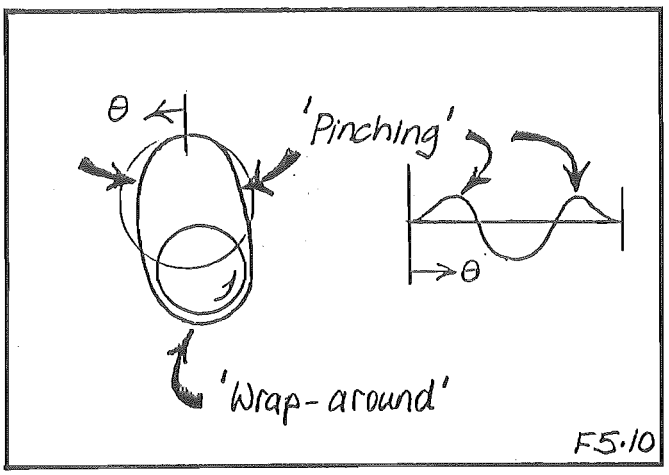

Pinching and wrap-around are then the identifying characteristics of ring EHL problems, dominating the film-thickness equation for anything but the lowest loads. The ramifications of this behaviour are investigated further in the following section under the more sensitive environment of Fantino's bearing.

5.3.2 *Housing Solutions*

When first presented, Fantino's housing solutions were quite controversial, the presence of oscillating pressure distributions causing some consternation[19]. Interpretation of these results was complicated by the use of coarse elasticity meshes and difficult, although realistic, geometry. (F5.11)

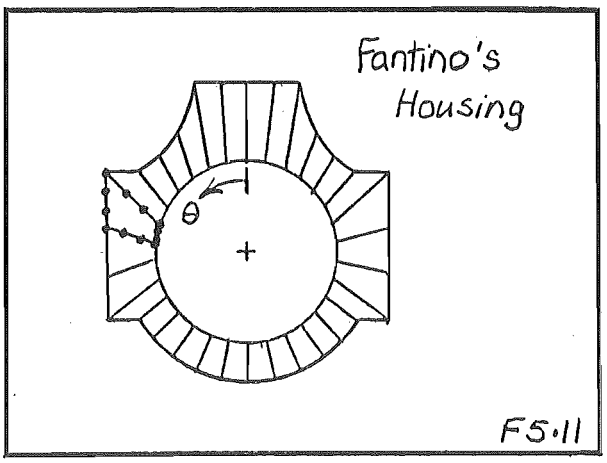

In this work, simple ring type geometries are instead used to re-evaluate Fantino's bearing. The question of multiple pressure peaks and their relationship to oil-film sensitivity, discretisation and displacement interpolation are investigated.

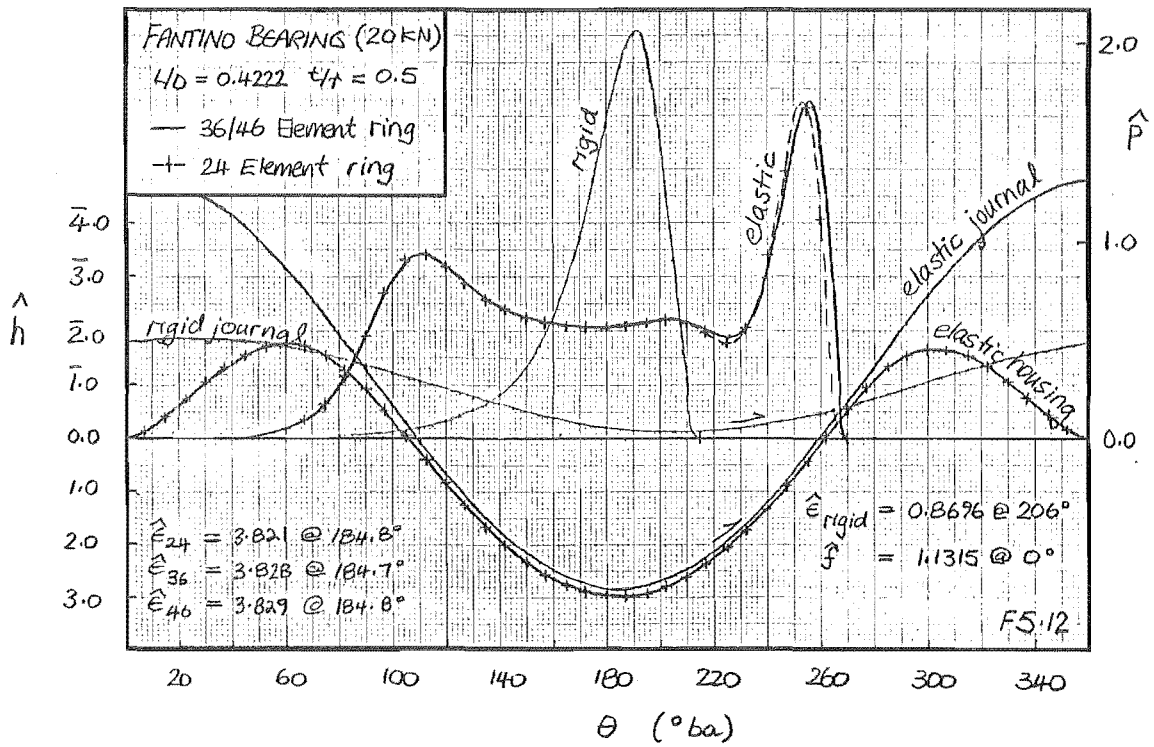
FANTINO BEARING (20 KN)
L/D = 0.4222 t/r = 0.5
— 36/46 Element ring
-+- 24 Element ring
rigid
elastic
elastic journal
rigid journal
elastic housing
$\hat{\varepsilon}_{24}$ = 3.821 @ 184.8°
$\hat{\varepsilon}_{36}$ = 3.818 @ 184.7°
$\hat{\varepsilon}_{46}$ = 3.829 @ 184.8°
$\hat{\varepsilon}_{rigid}$ = 0.8696 @ 206°
$\hat{f}$ = 1.1315 @ 0°
F5.12
$\hat{h}$
$\hat{P}$
θ (°ba)

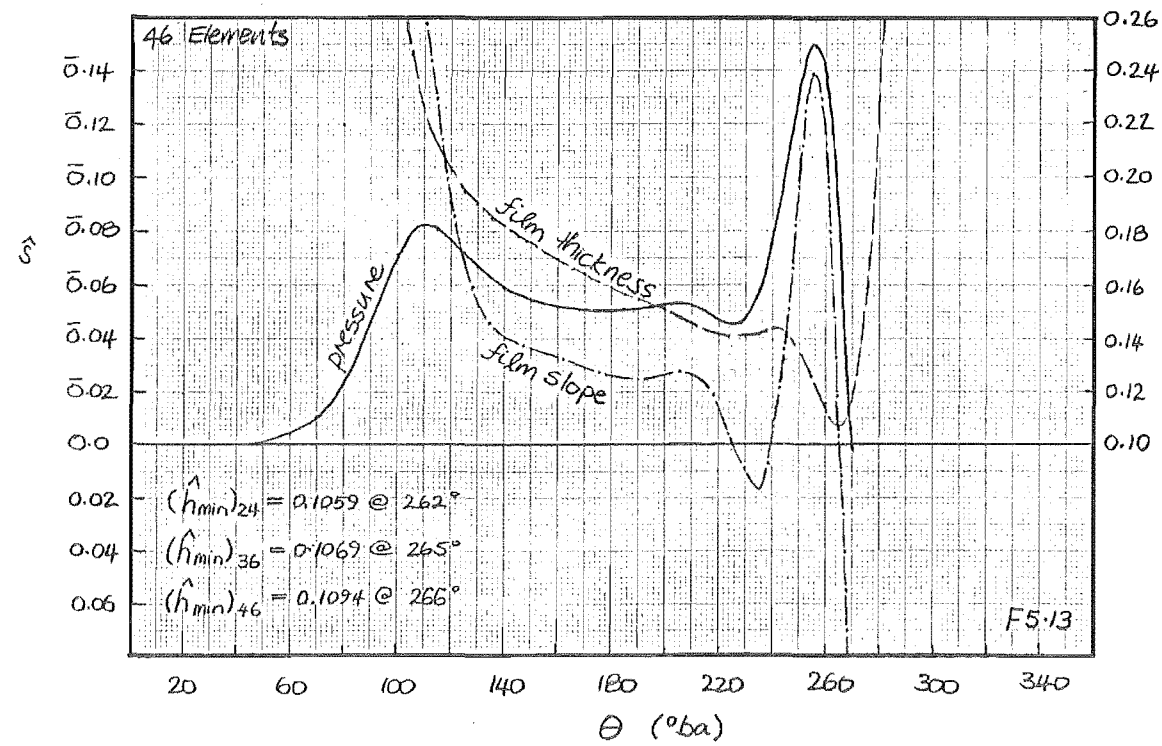
46 Elements
pressure
film thickness
film slope
$(\hat{h}_{min})_{24}$ = 0.1059 @ 262°
$(\hat{h}_{min})_{36}$ = 0.1069 @ 265°
$(\hat{h}_{min})_{46}$ = 0.1094 @ 266°
F5.13
$\hat{s}$
$\hat{h}$
θ (°ba)

(a) Multiple Pressure Peaks :

We firstly look at a ring under 20 kN loading: F5.12 shows the development of a third pressure peak, this extra peak corresponding closely with the film slope ($\hat{s}$) behaviour of F5.13. Circumferential mesh size clearly has little to do with its presence, results being very similar for 24, 36 and 46 elements.

For Fantino's bearing, triply peaked pressure distributions first appear at 15 kN and remain the predominate form through to the maximum tested load of 40 kN. Physically, the development of successive peaks can be explained as follows:

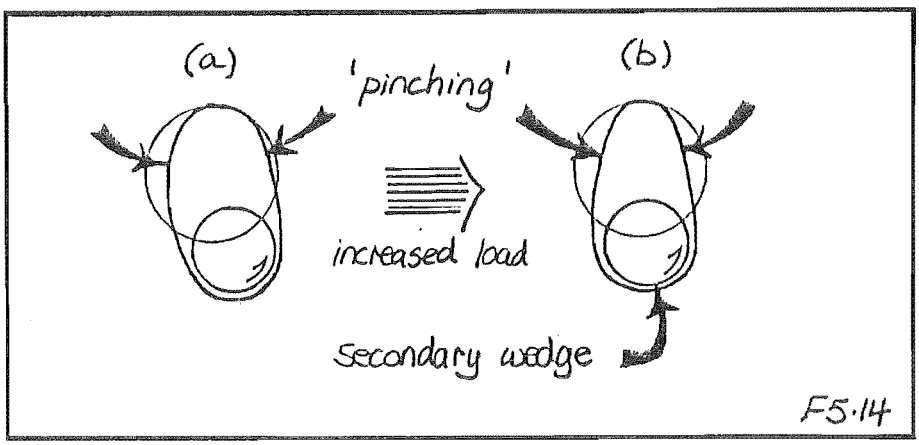

As observed in the previous section, a combination of wrap-around and pinching (F5.14a) produces broad doubly peaked pressure distributions, the left and right peaks of F5.12 being of this mechanism. In the intervening parallel film region, a weak secondary wedge develops (F5.14b): this is not the product of 'wobbly' housing distortion but is instead due to the *relative* interaction of surface curvatures, probably from the alteration of housing curvature through pinching. We will see later that with increased tensioning of the beam around the journal, secondary wedge effects can diminish under load.

Given these mechanisms, the development of multiple peaks is then largely dependent on oil-film sensitivity.

(b) **Film Sensitivity :**

For the steady state case, load capacity is generated through film 'wedge' action, hence it is pertinent to look at film slopes $\hat{s}$: $\left[\hat{s} = \frac{\partial \hat{h}}{\partial \theta}\right]$

The operating régime of Fantino's bearing is such that considerable housing wrap-around occurs, producing a large section of parallel oil-film. Film slope is then the difference of two terms of similar magnitude; the geometric and elastic slopes.

For the 20 kN case of F5.13, the resultant slope through this region is due to the third/fourth significant digit of the individual slope terms. In comparison, film-thickness is dependent on the second/third significant digit. Clearly any untoward behaviour in the third/fourth significant figures of the slope is likely to collapse the solution, inexactness in the fourth/fifth figure will lead to spurious solutions.

Two sources of such errors were observed, discretisation and elastic displacement interpolation :

Discretisation : For the curved beam model, both geometric and elastic slope are trigonometric functions; smoothness is implicit. Any errors present are then largely due to circumferential discretisation (F5.15); round-off is approximately in the tenth decimal place.

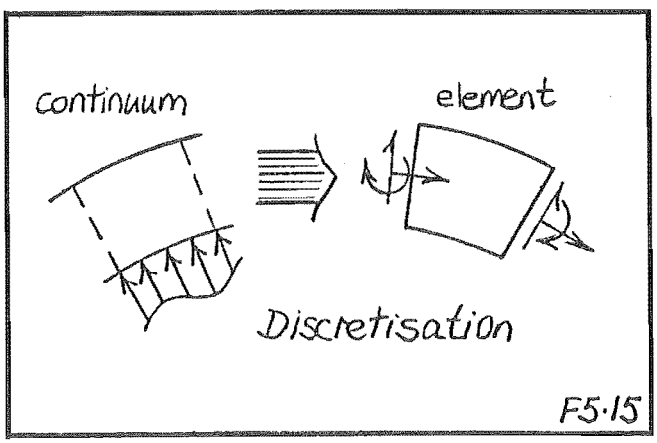

Unfortunately the errors of an inadequate discretisation are sufficient to induce spurious yet stable solutions, witness F5.16 at 40 kN.

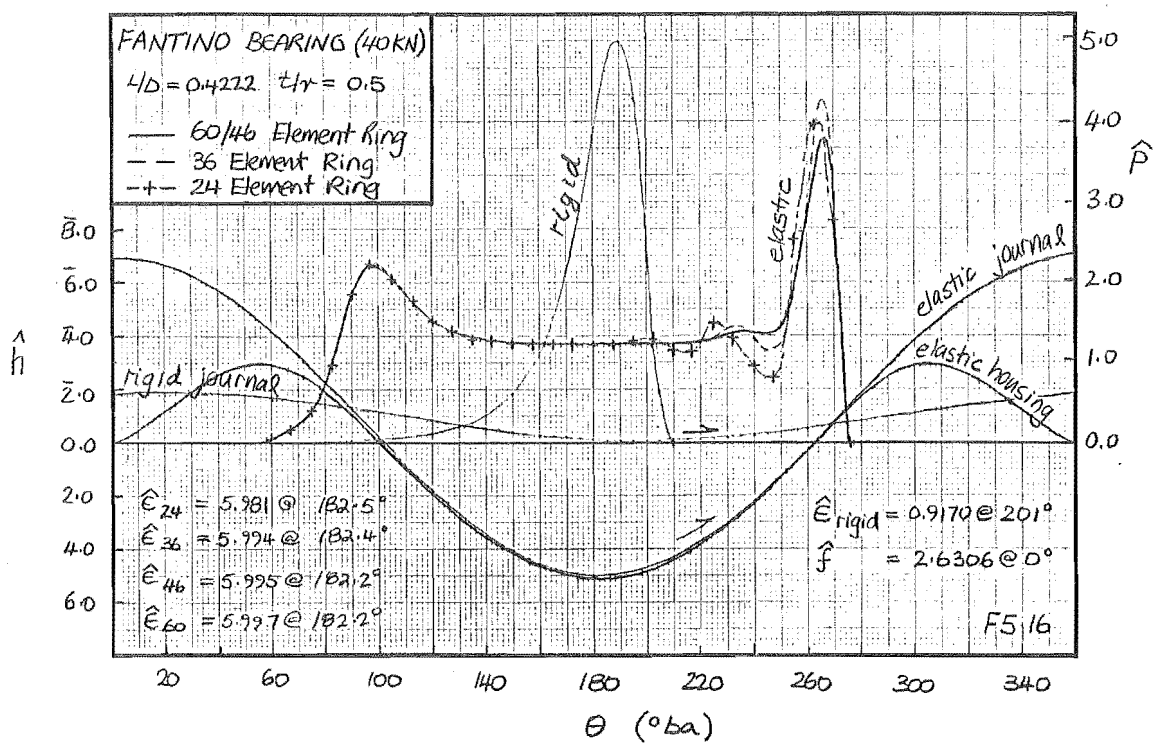
FANTINO BEARING (40KN)
L/D = 0.4222 t/r = 0.5
60/46 Element Ring
36 Element Ring
24 Element Ring
rigid
elastic
elastic journal
elastic housing
rigid journal
$\hat{\epsilon}_{24}$ = 5.981 @ 182.5°
$\hat{\epsilon}_{36}$ = 5.994 @ 182.4°
$\hat{\epsilon}_{46}$ = 5.995 @ 182.2°
$\hat{\epsilon}_{60}$ = 5.997 @ 182.2°
$\hat{\epsilon}_{rigid}$ = 0.9170 @ 201°
$\hat{f}$ = 2.6306 @ 0°
F5.16
$\hat{h}$
$\hat{P}$
θ (°ba)

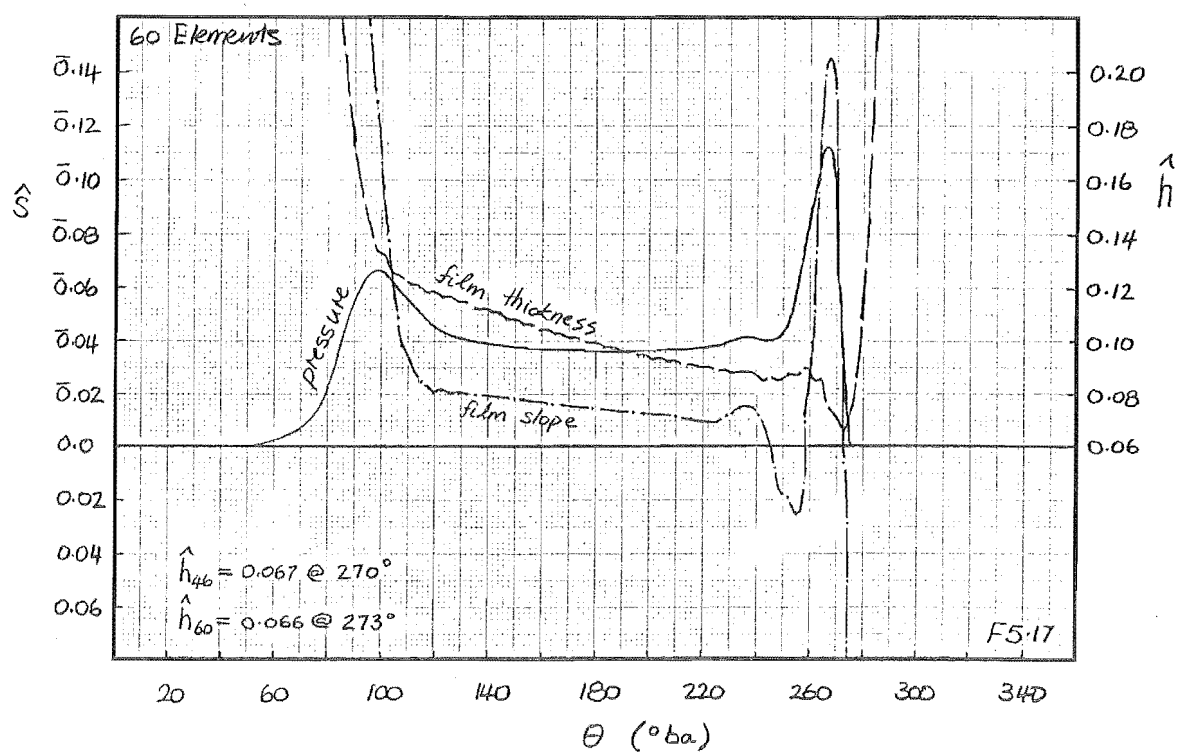
60 Elements
pressure
film thickness
film slope
$\hat{h}_{46}$ = 0.067 @ 270°
$\hat{h}_{60}$ = 0.066 @ 273°
F5.17
$\hat{s}$
$\hat{h}$
θ (°ba)

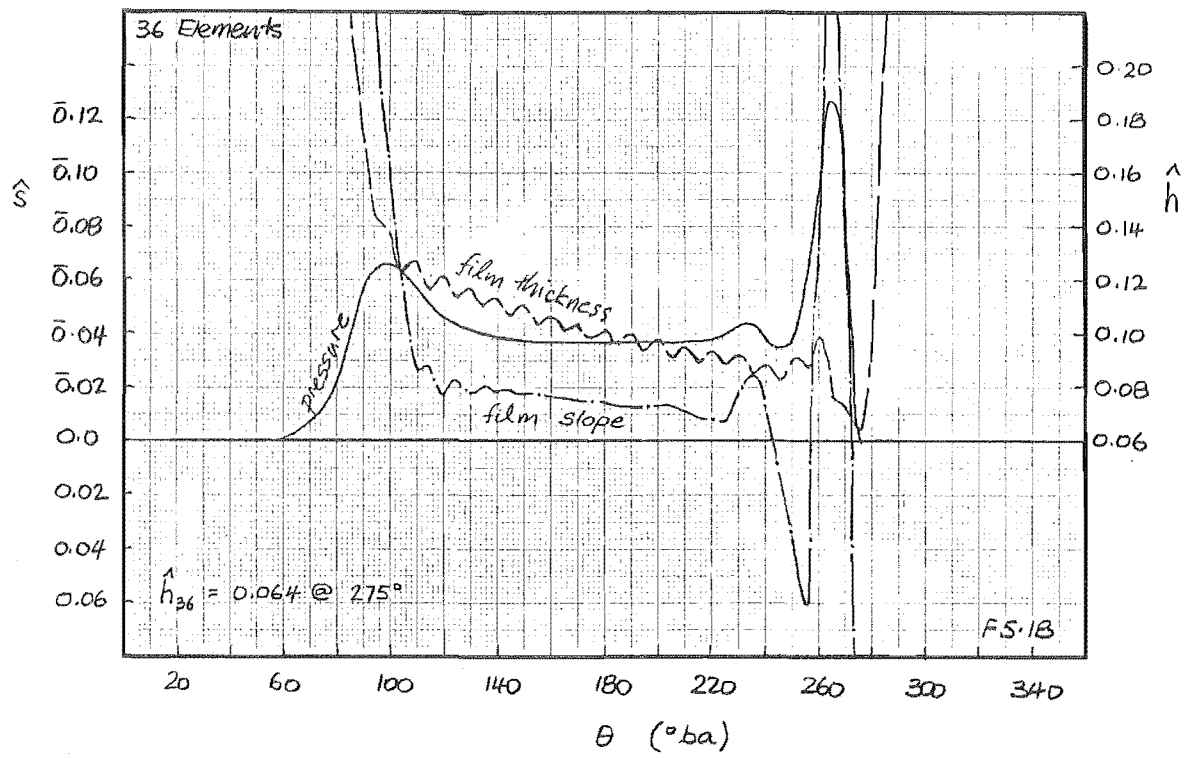
36 Elements
pressure
film thickness
film slope
$\hat{h}_{36}$ = 0.064 @ 275°
FS·18
$\bar{p}$
$\hat{h}$
θ (°ba)

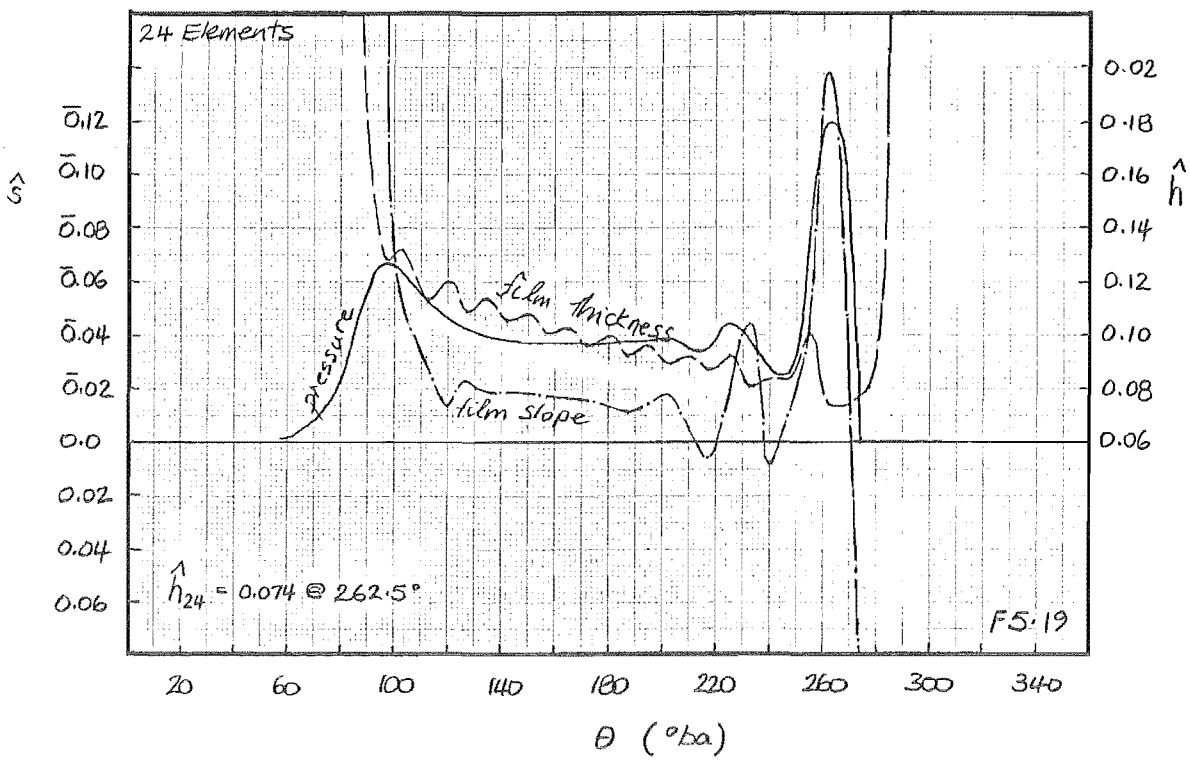
24 Elements
pressure
film thickness
film slope
$\hat{h}_{24}$ = 0.074 @ 262.5°
FS·19
$\bar{p}$
$\hat{h}$
θ (°ba)

Mesh frequency oscillations have appeared in film-thickness and film-slope behaviour: for the 60 and 46 element solutions (F5.17) oscillations are ineffectual, the 36 element solution (F5.18) not sufficiently affected to produce a majorly spurious solution whilst the 24 element solution (F5.19) is spurious.

Verification of mesh independence on significantly finer grids is clearly important if a converged solution is to be claimed.

Displacement Interpolation : To illustrate the effect of interpolation error, it is informative to induce elastic interpolation 'noise' in the 20 kN curved beam example and observe the results.

For this purpose, 10^0 nodal u_r,u_r' curved beam displacements are separately linearly interpolated onto 10^0 fluid element gauss points (F5.20). This introduces significant interpolation error as exact curved beam u_r,u_θ displacements are intimately coupled. The results are shown in F5.21 and F5.22, significant differences being apparent.

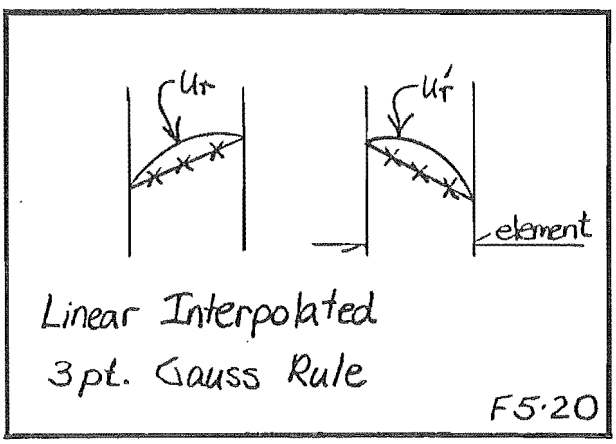

Oscillations are present in both slope and displacement fields, the level of 'noise' being sufficient to produce a spurious solution (c.f. F5.19 @ 40 kN). Displacement and slope fields have clearly become unsynchronised.

How well then does an Hermite F.E. ring fare given that the displacement fields are linearly interpolated to the Gauss Points? (See Section 4.1.3(b)).

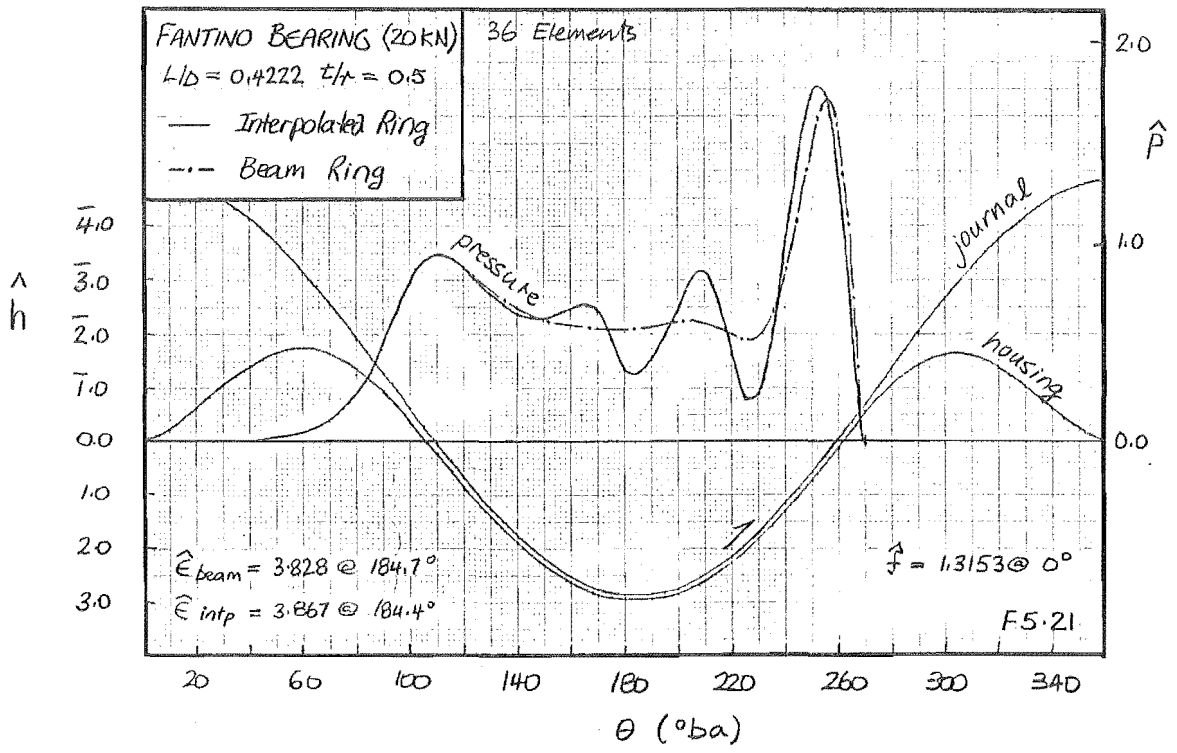
FANTINO BEARING (20 kN)
36 Elements
L/D = 0.4222 t/r = 0.5
Interpolated Ring
Beam Ring
pressure
journal
housing
$\hat{\epsilon}_{beam}$ = 3.828 @ 184.7°
$\hat{\epsilon}_{intp}$ = 3.867 @ 184.4°
$\hat{f}$ = 1.3153 @ 0°
F5.21
$\hat{h}$
$\hat{p}$
θ (°ba)

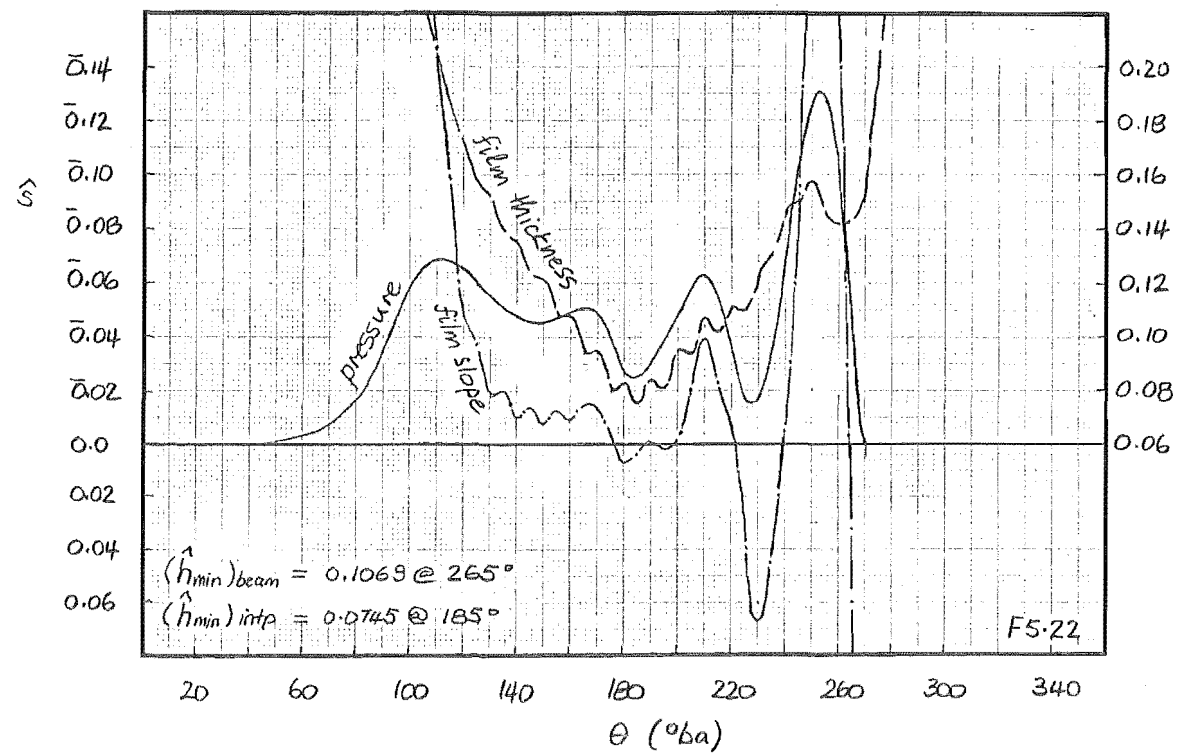
film thickness
pressure
film slope
$(\hat{h}_{min})_{beam}$ = 0.1069 @ 265°
$(\hat{h}_{min})_{intp}$ = 0.0745 @ 185°
F5.22
$\hat{s}$
$\hat{h}$
θ (°ba)

Interestingly the distinct tertiary pressure peak of the beam ring is not evident in the 20 kN F.E ring of F5.23, F5.24. Oscillations in slope and displacement are present at slightly lower levels than the interpolated beam results, amplitudes in the order of 0.5% of the displacement field being typical. This level of noise is sufficient to mask the development of the third pressure peak; slope behaviour alludes to third peak pressure mechanisms being present, the central peak being merged with the right-hand peak.

Very similar behaviour is exhibited by the F.E housing solution, F5.25 and F5.26 being at 20 kN. Again, no tertiary pressure peak is present although slope behaviour suggests the mechanism is present. The stiffer neck of the housing produces a pressure distribution of smaller included angle, overall displacement behaviour being reduced as evident from journal eccentricity.

Before concluding this section, some comment on noise attenuation is in order.

Noise Attenuation : It should be emphasised that both elastic displacement and slope are outwardly smooth in all the above solutions. Only when geometric terms are differenced does noise become apparent, levels being controllable for discretisation but unacceptably high for F.E interpolation. Alleviation of this noise problem is not altogether straight forward.

A 'quick-fix' would be to use more elastic F.E's. This however only shifts the problem to higher loads and increases computational burden. Indiscriminant smoothing, as shown by the interpolated curved beam results, can introduce a signature all of its own.

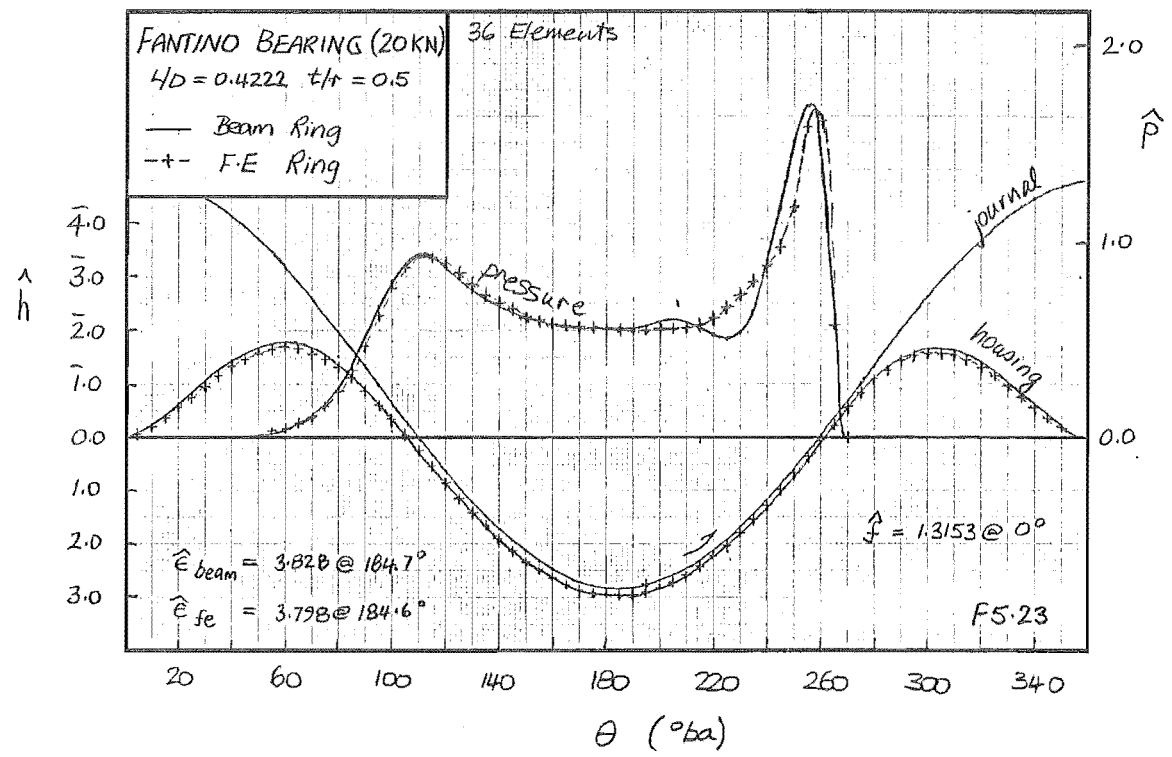
FANTINO BEARING (20 KN)
36 Elements
L/D = 0.4222 t/r = 0.5
Beam Ring
F.E Ring
pressure
journal
housing
$\hat{\epsilon}_{beam}$ = 3.828 @ 184.7°
$\hat{\epsilon}_{fe}$ = 3.798 @ 184.6°
$\hat{f}$ = 1.3153 @ 0°
F5.23
$\hat{h}$
$\hat{p}$
θ (°ba)

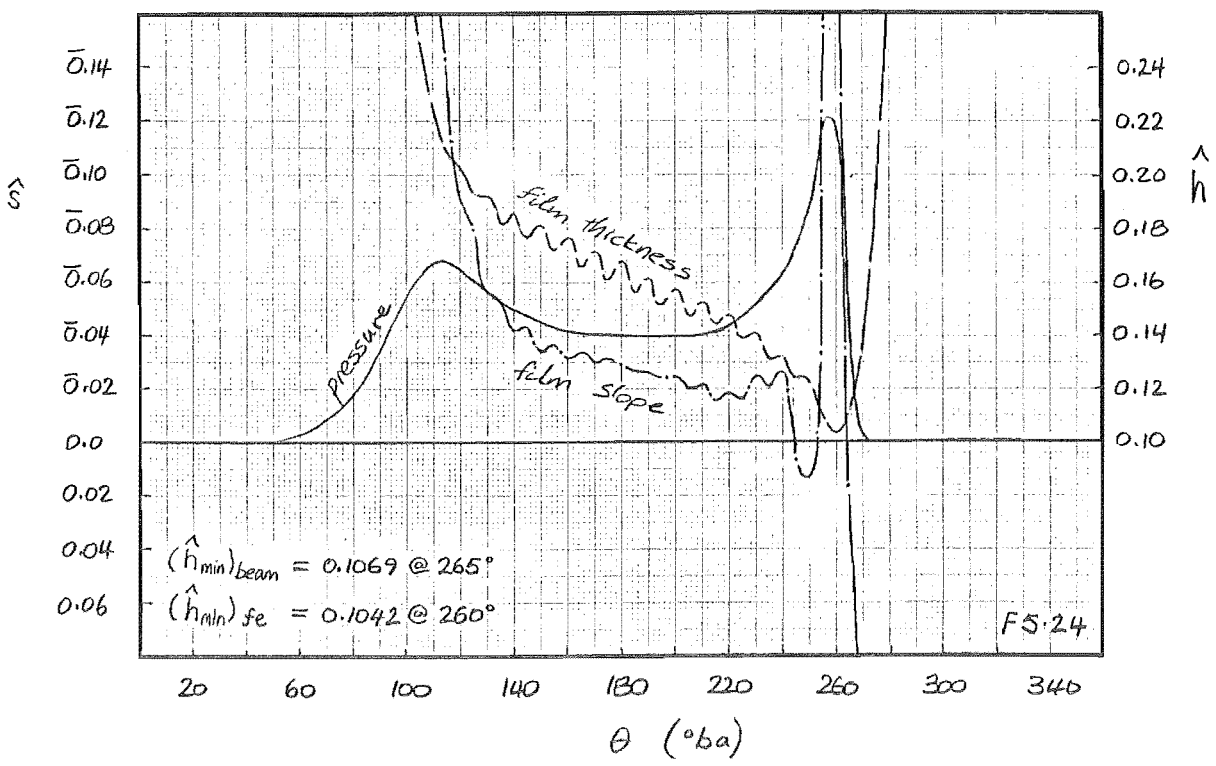
film thickness
pressure
film slope
$(\hat{h}_{min})_{beam}$ = 0.1069 @ 265°
$(\hat{h}_{min})_{fe}$ = 0.1042 @ 260°
F5.24
$\hat{s}$
$\hat{h}$
θ (°ba)

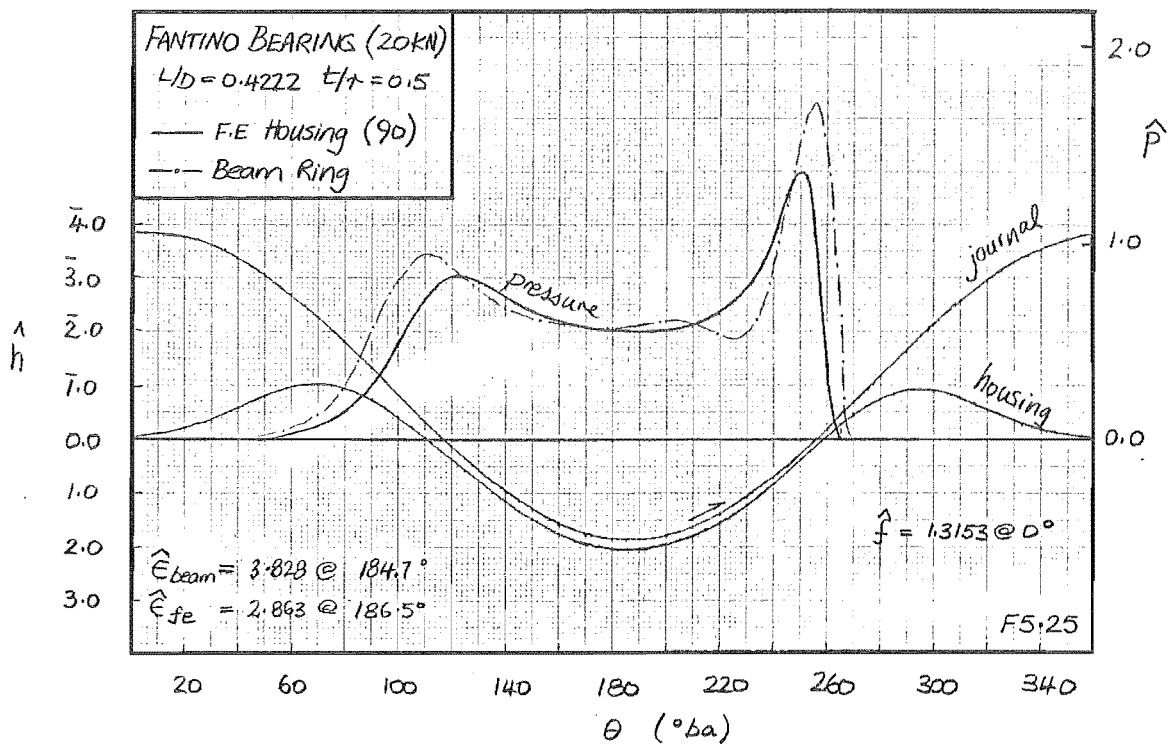
FANTINO BEARINGS (20KN)
L/D = 0.4222 t/r = 0.15
F.E Housing (90)
Beam Ring
pressure
journal
housing
$\hat{f}$ = 1.3153 @ 0°
$\hat{\epsilon}_{beam}$ = 3.828 @ 184.7°
$\hat{\epsilon}_{fe}$ = 2.863 @ 186.5°
F5.25
$\hat{h}$
$\hat{p}$
θ (°ba)

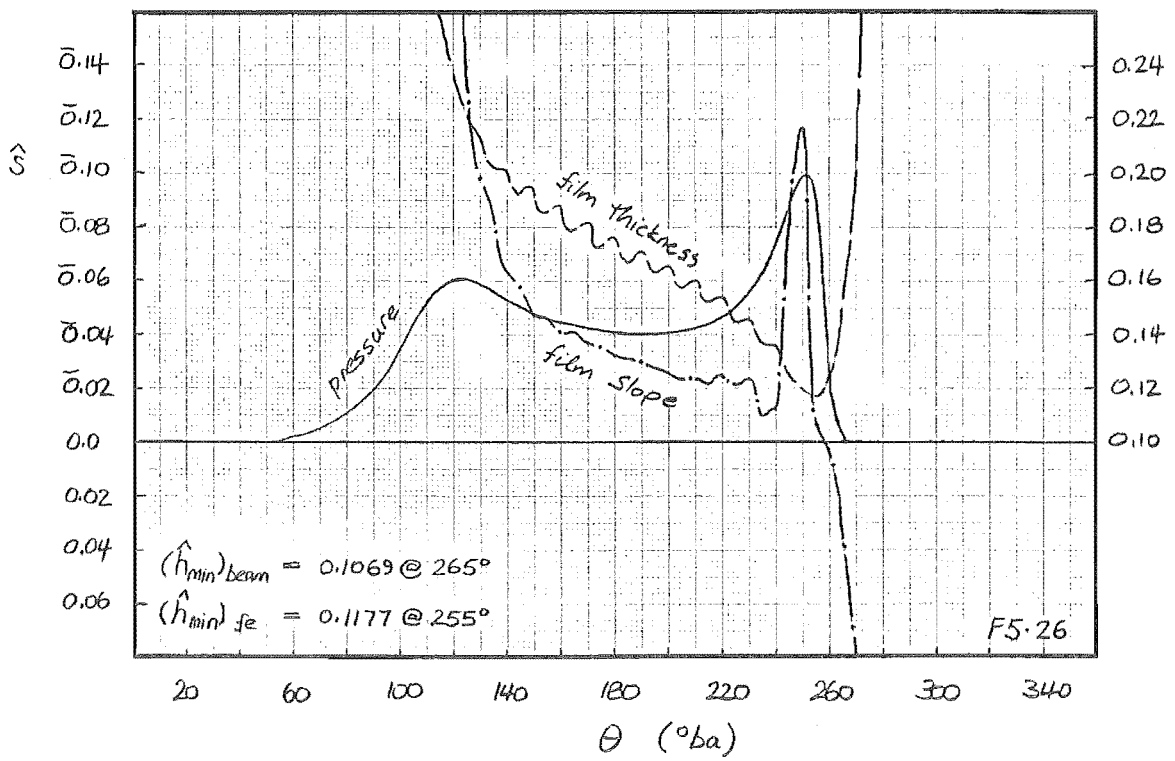
film thickness
pressure
film slope
$(\hat{h}_{min})_{beam}$ = 0.1069 @ 265°
$(\hat{h}_{min})_{fe}$ = 0.1177 @ 255°
F5.26
$\hat{s}$
$\hat{h}$
θ (°ba)

The only really satisfactory solution is the use of smooth shape functions *within* the elastic variational principle. The use in this work of Hermite polynomials is a first attempt in this direction, unfortunately thwarted by the use of external linear nodal interpolation. Further effort directed towards extracting the exact interpolation may elicit the required outcome, otherwise even higher continuity elastic trial functions will need to be devised.

(c) **Load Dependence :**

Performance maps for Fantinos bearing over a range of load are provided in F5.27. Elastic trends are similar to those reported by Fantino; reduced film-thickness, pressure and attitude angle; increased eccentricity over the rigid solution.

F.E. results indicate sensible behaviour despite increased noise levels, ring solutions showing good agreement. Housing solutions are generally consistent with increased structural stiffness: reduced eccentricity, increased film-thickness. Peak pressure does not however fit this pattern: reduced primary pinching from stiffer neck geometry reduces the peak pressures.

What is not apparent from this figure is the low load-convergence limit of the F.E solutions.

Convergence Limit : From preceding sections, it should be apparent that the steadily loaded ring problem becomes increasingly ill-conditioned with load; 'wrap-around' decreases wedge action, in the limit becoming swamped by elastic 'noise'. At this point, the N-R solution technique undergoes a dramatic solution collapse :

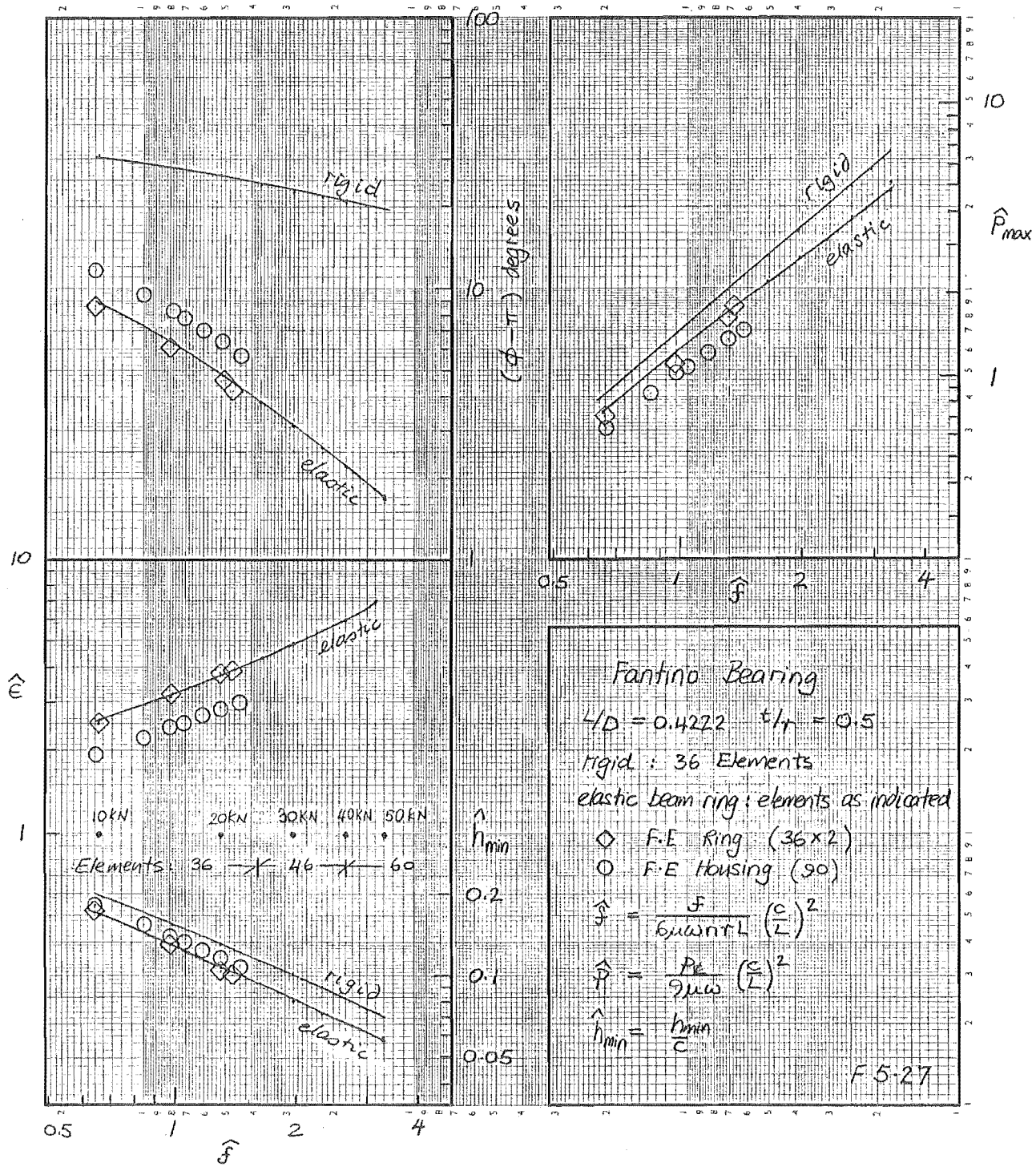
rigid
elastic
$(\phi - \pi)$ degrees
$\hat{\epsilon}$
$\hat{f}$
$\hat{P}_{max}$
$\hat{h}_{min}$
10KN
20KN
30KN
40KN
50KN
Elements: 36 46 60
Fantino Bearing
L/D = 0.4222 t/r = 0.5
rigid : 36 Elements
elastic beam ring : elements as indicated
◇ F.E Ring (36×2)
○ F.E Housing (90)
$\hat{f} = \frac{f}{6\mu\omega n r L}\left(\frac{c}{L}\right)^2$
$\hat{P} = \frac{Pc}{9\mu\omega}\left(\frac{c}{L}\right)^2$
$\hat{h}_{min} = \frac{h_{min}}{c}$
F 5-27

For curved beams and rigid bearings, stable convergent solutions were obtained for loads greatly in excess of the design load; F5.16 at 40 kN is a case in point. For these solutions, discretisation noise was not found to be a problem. For the equivalent F.E rings, this was not however the case.

As low as 21 kN, unstable oscillatory journal motion occurs, leading to solution collapse; lack of load carrying wedge terms is compensated by the development of unstable dynamic journal action. Stable load limit then gives some measure of the noise level tolerated by the bearing solution; the observably higher noise levels in the F.E solutions lead to their early demise.

So, what can be concluded about Fantino's bearing?

Given the reluctance of current procedures to converge on F.E geometries, it is difficult to comment on the strong oscillatory pressure behaviour observed by Fantino. What can be said with certainty is that the generic ring solution ($t/r = 0.5$) exhibits diminishing triple peak behaviour to very high loads. Non-uniform geometry in the form of bolt flanges may provide sources for further geometry related peaks, however numerical inadequacies, in particular the insidious side effects of a coarse elastic discretisation, can lead to many more.

Extension of Fantino's problem to a full parameterisation was considered but rejected; the steady state problem is inefficiently solved by the current program and is by-and-large pathological. Effort was instead directed to the more relevant dynamic problem.

CHAPTER SIX

DYNAMIC SOLUTIONS

The dynamic solutions of this Chapter focus on the Ruston and Hornsby (R-H) bearing presented by Campbell[6]. Other bearings could well have formed this basis, however the sheer quantity of experimental and theoretical literature associated with this bearing make it the *de facto* standard big-end test case.

This Chapter firstly uses inertial loadings to develop an understanding of the fundamental film mechanisms; ring solutions are used to illustrate basic bearing performance, the additional features of the elastic bearing being thoroughly explored. These ring solutions are then ratified against full housing solutions. The influence of engine speed on performance, is investigated on both elastic geometries.

The second portion of this Chapter extends loading to incorporate gas forces. Solutions to rigid, ring and housing geometries are presented with an emphasis on verification : the parabolic rigid solution against state-of-the-art finite length solutions; curved beam solutions against full housing solutions. Finally, a detailed comparison is made between these theoretical solutions and *in situ* film measurements made by Butcher[34].

6.1 Inertial Load : Ruston-Hornsby

Dynamic big-end bearing loading is fundamentally that of the inertial con-rod components, at least this is the case when gas loading is less than five times the inertial loading[96]. It is therefore of considerable interest to look at the bearings response to such loadings.

6.1.1 *Load Diagram*

The inertial load diagram used for the Ruston-Hornsby, is the lumped mass one of F6.1. This diagram differs slightly from the inertial loop of Campbell's[6] gas diagram, the R-H engine having a supercharged cycle.

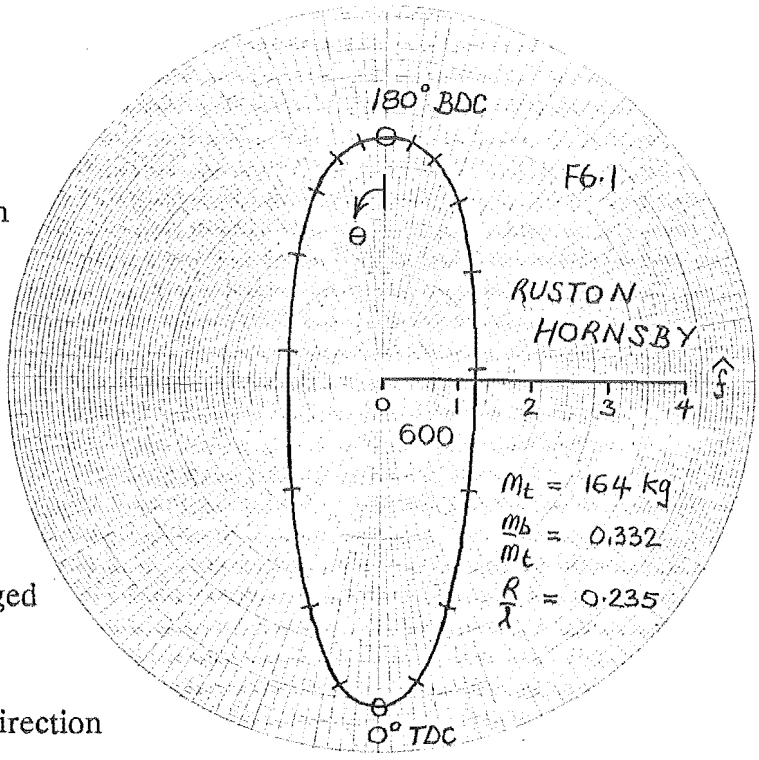

Rate of change of load direction ($\dot{\psi}$) and magnitude ($\dot{f}$) are presented in F6.2, these temporal variations being useful in interpreting locus behaviour.

Before looking at the effects of elasticity, it is worth reviewing the basic performance of the rigid bearing.

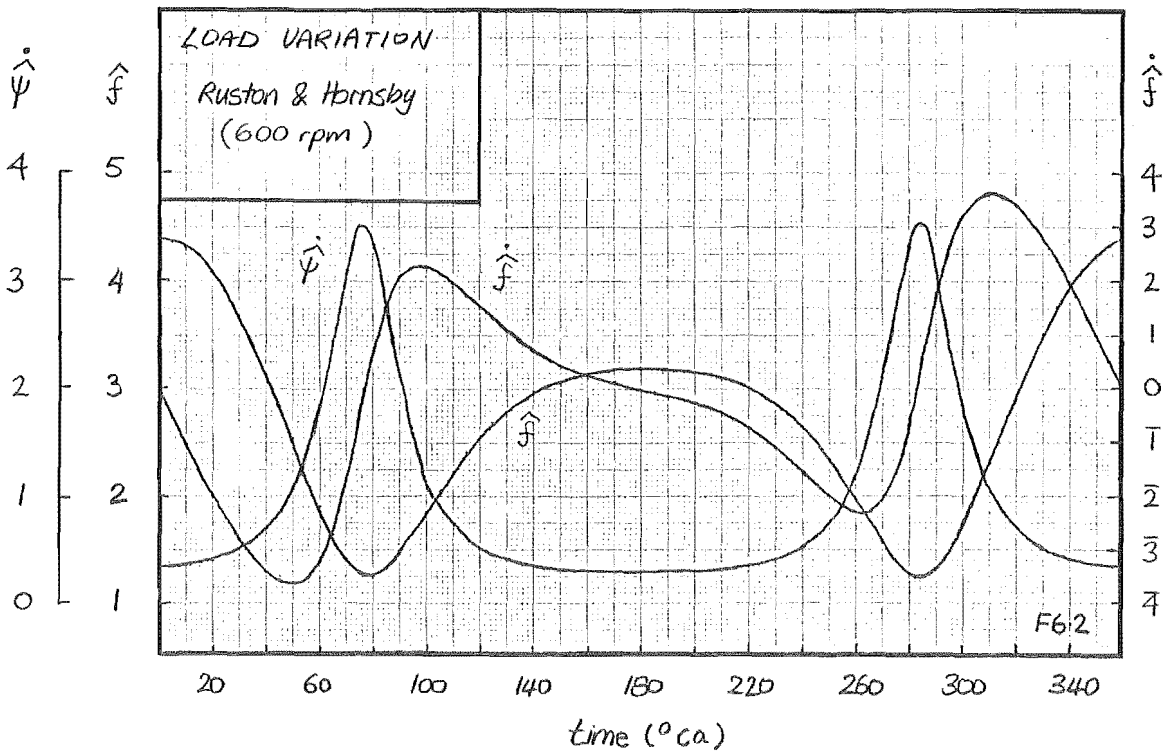

6.1.2 *Rigid Bearing Solutions*

In this work 'dynamic performance' is taken to be characterised by :

$$\hat{h}_{min} \; ; \; \hat{p}_{max} \; ; \; \hat{\underset{\sim}{\epsilon}}$$

These parameters are just a small subset of the available information; friction forces, flow losses and bearing surface stains/stresses are also available. Figures F6.3, F6.4 show this 'dynamic-performance' over the full 600 rpm R-H load cycle.

It is useful to try and isolate cause-and-effect relationships between performance and load.

(a) **Causal Relationships :**

Dynamic performance of an elastic bearing is characterised by the reaction of the five forcing terms in Reynolds equation (3.14), namely :

$$\hat{q} = \left[2(\hat{\dot{u}}_r - \hat{\dot{\epsilon}}\cos(\phi-\theta) + \hat{\epsilon}\hat{\dot{\phi}}\sin(\phi-\theta)) + s\left[\frac{\partial \hat{u}_r}{\partial \theta} - \hat{\epsilon}\sin(\phi-\theta)\right]\right] \qquad (6.1)$$

to the two external load terms $\hat{f}_x$, $\hat{f}_y$.

For a rigid bearing these five terms reduce to three, their dimensionless forms characterised by the terms 'squeeze' $\hat{s}$ and 'wedge' $\hat{w}$ as follows :

$$\text{squeeze} \; : \; \hat{\dot{\epsilon}}$$

$$\text{wedge} \; : \; \hat{\epsilon}(\hat{\dot{\phi}} - s/2)$$

Variation of these measures throughout the load cycle is outlined in F6.5. Not surprisingly, wedge action dominates :

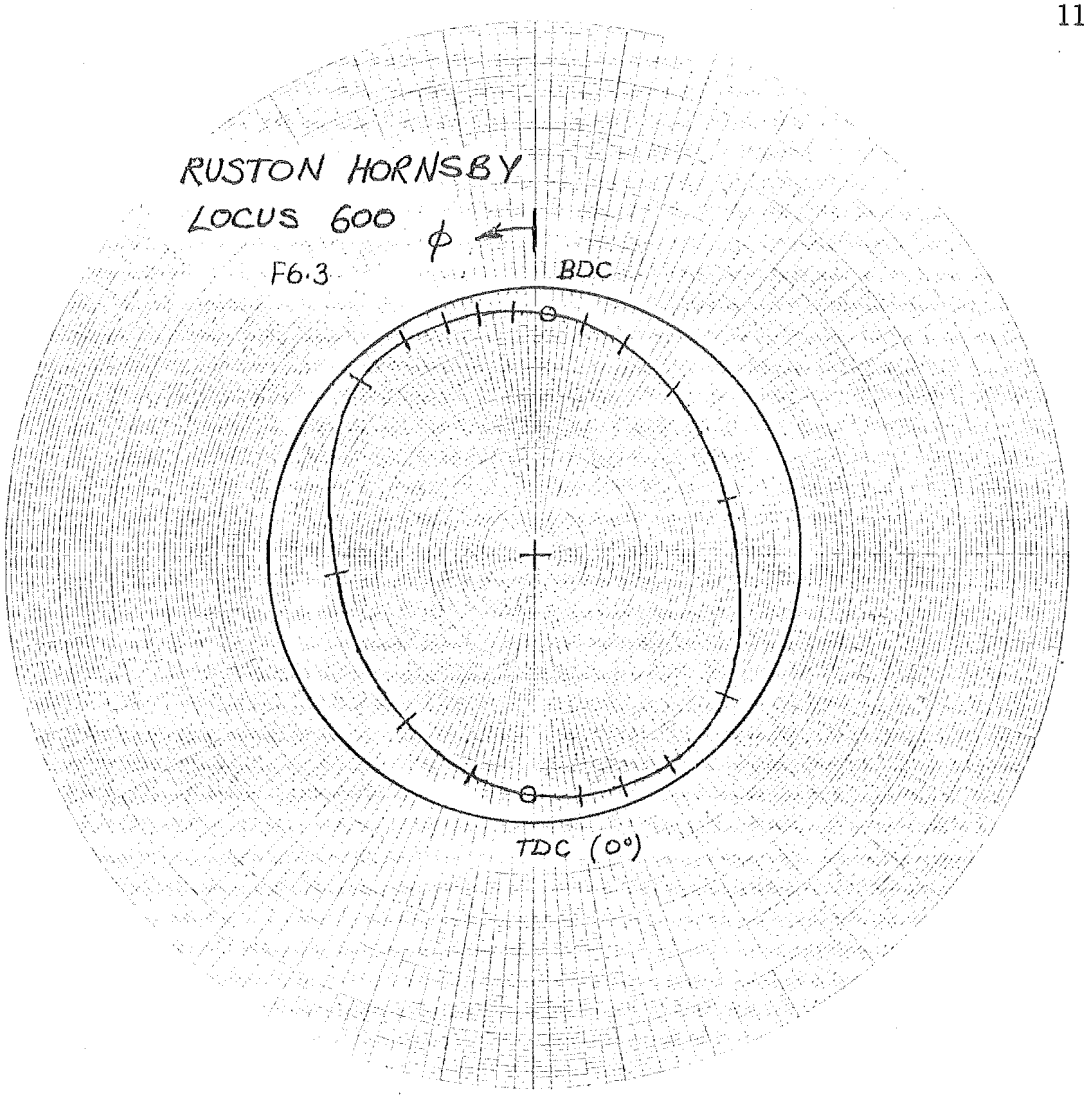
RUSTON HORNSBY
LOCUS 600
F6.3
ϕ
BDC
TDC (0°)

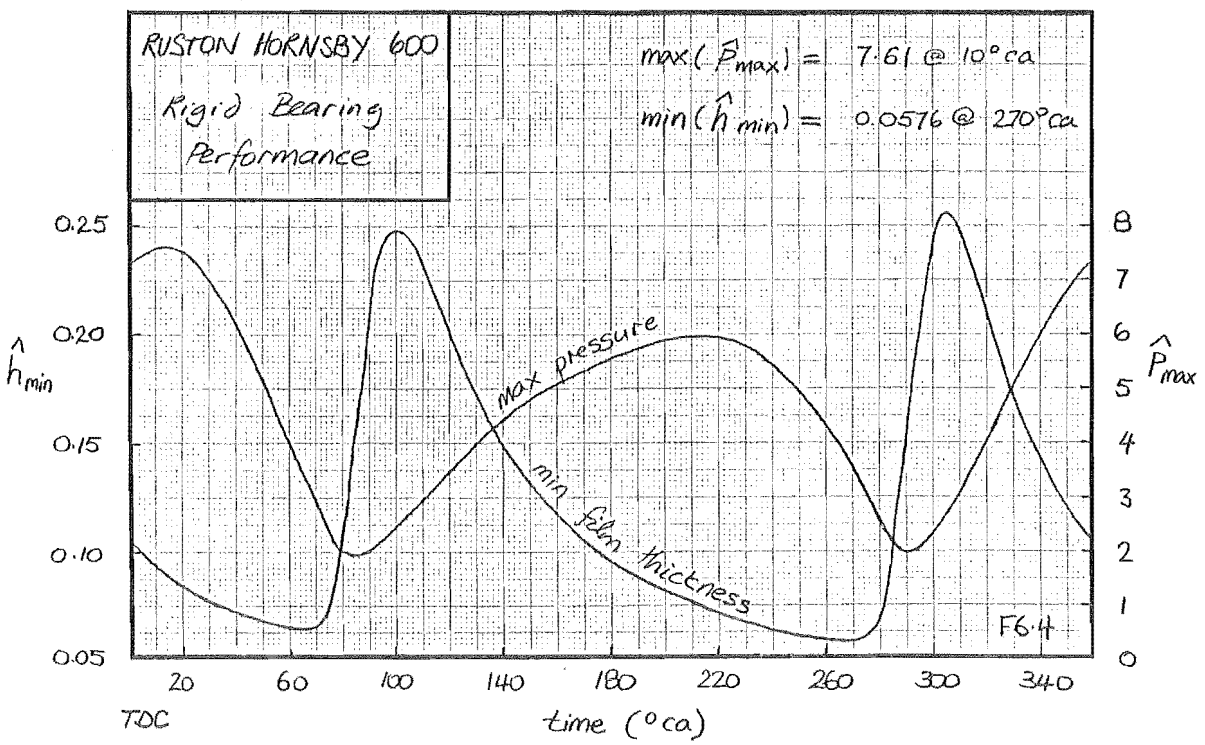
RUSTON HORNSBY 600
Rigid Bearing
Performance
max(P̂max) = 7.61 @ 10°ca
min(ĥmin) = 0.0576 @ 270°ca
max pressure
min film thickness
F6.4
ĥmin
P̂max
0.25
0.20
0.15
0.10
0.05
8
7
6
5
4
3
2
1
0
20
60
100
140
180
220
260
300
340
TDC
time (°ca)

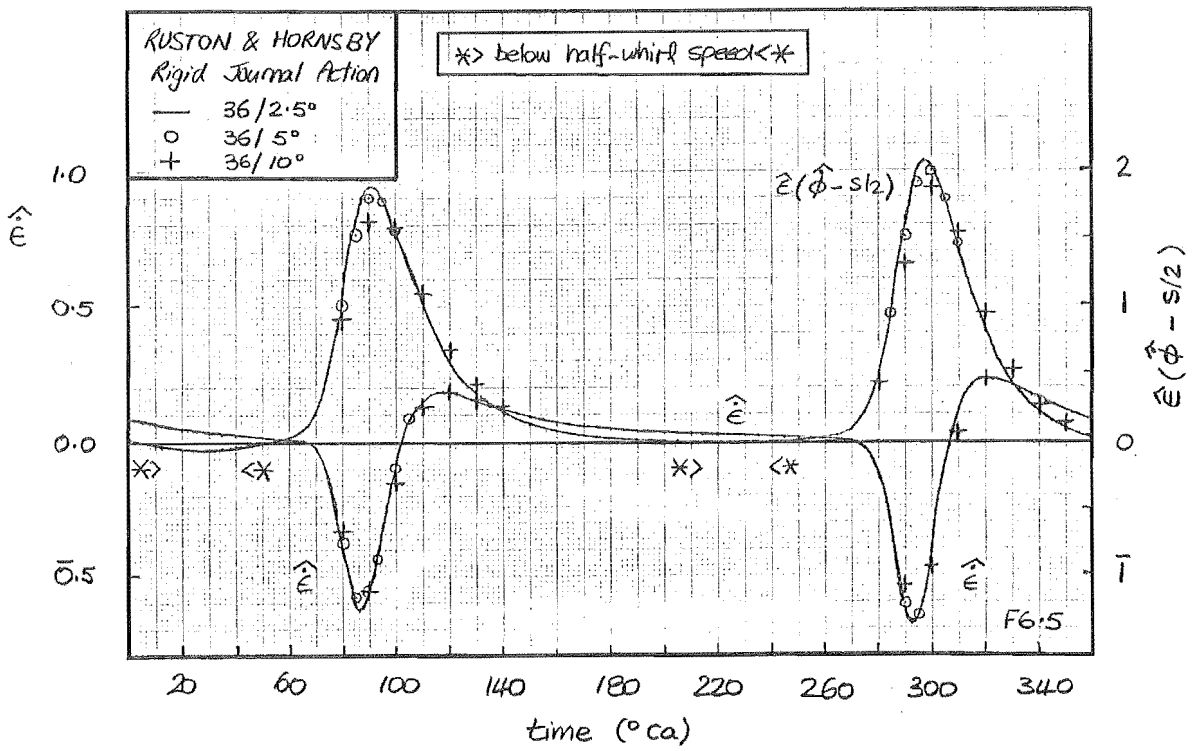

Radial motion is restricted to O(c), angular motion to much larger O(r). As shown by F6.4, the predominant film-thickness form is strongly influenced by wedge velocity $\hat{\epsilon}(\hat{\dot{\phi}} - s/2)$, this velocity being in response to the 'sweep' velocity of the external load diagram ($\hat{\dot{\psi}}$, F6.2).

During periods of low whirl velocity, most notably around TDC and BDC†, squeeze action becomes influential; at half-whirl speed ($\hat{\dot{\phi}} \equiv s/2$) it is the only term. It is the unfortunate consequence of geometry that during these periods external load is maximised, minimum film-thickness is then determined by the zero squeeze condition :

$$\hat{\dot{\epsilon}} = 0 \; ; \; \min \left(\hat{\dot{\phi}} - s/2\right) ,$$

load being carried by the remaining wedge terms. This invariably occurs around

---

† TDC : top dead centre (0°ca); BDC : bottom dead centre (180°ca)

270^0ca for a rigid bearing, although these conditions need not be similar in an elastic bearing.

A strong relationship also exists between maximum film pressure (F6.4) and external load magnitude (F6.2), load being integrated pressure. Maximum pressures are developed around TDC and BDC, TDC pressures being slightly higher.

An overview of the various spatial film contributions throughout the load cycle is presented in F6.6 : the inner arc represents pressures; centre arc, wedge action; the outer arc, squeeze action. Shading respectively represents positive pressures, constructive wedge action ($\hat{\varepsilon}(\hat{\dot{\phi}}$-s/2)sin($\theta$-$\phi$)) and closing film squeeze velocity ($\hat{\dot{\varepsilon}}$cos(θ-ϕ)). Half-whirl speeds, predominant film action and resulting pressure are all available on this figure.

We now look at how the major parameters are affected firstly by temporal step length, then spatial meshing.

(b) **Temporal Mesh :**

Results of varying time meshes on a fixed 36 element spatial mesh are presented in F6.7. Fine meshes $(36/2.5^0)^{\dagger}$ can be seen to lead to 'lumpy' pressure behaviour, the mesh homogeneity problems of Section 5.2.2 resurfacing. These oscillations are of sufficiently small amplitude (< 2%) not to affect film-thickness.

Coarser meshes are not significantly different in either film-thickness or pressure, however the $36/10^0$ mesh does provide a smoother pressure behaviour. A slight trend towards thicker minimum films is apparent on the coarser meshes.

---

† $36/2.5^0 \equiv$ 36 spatial elements, 2.5^0ca temporal elements

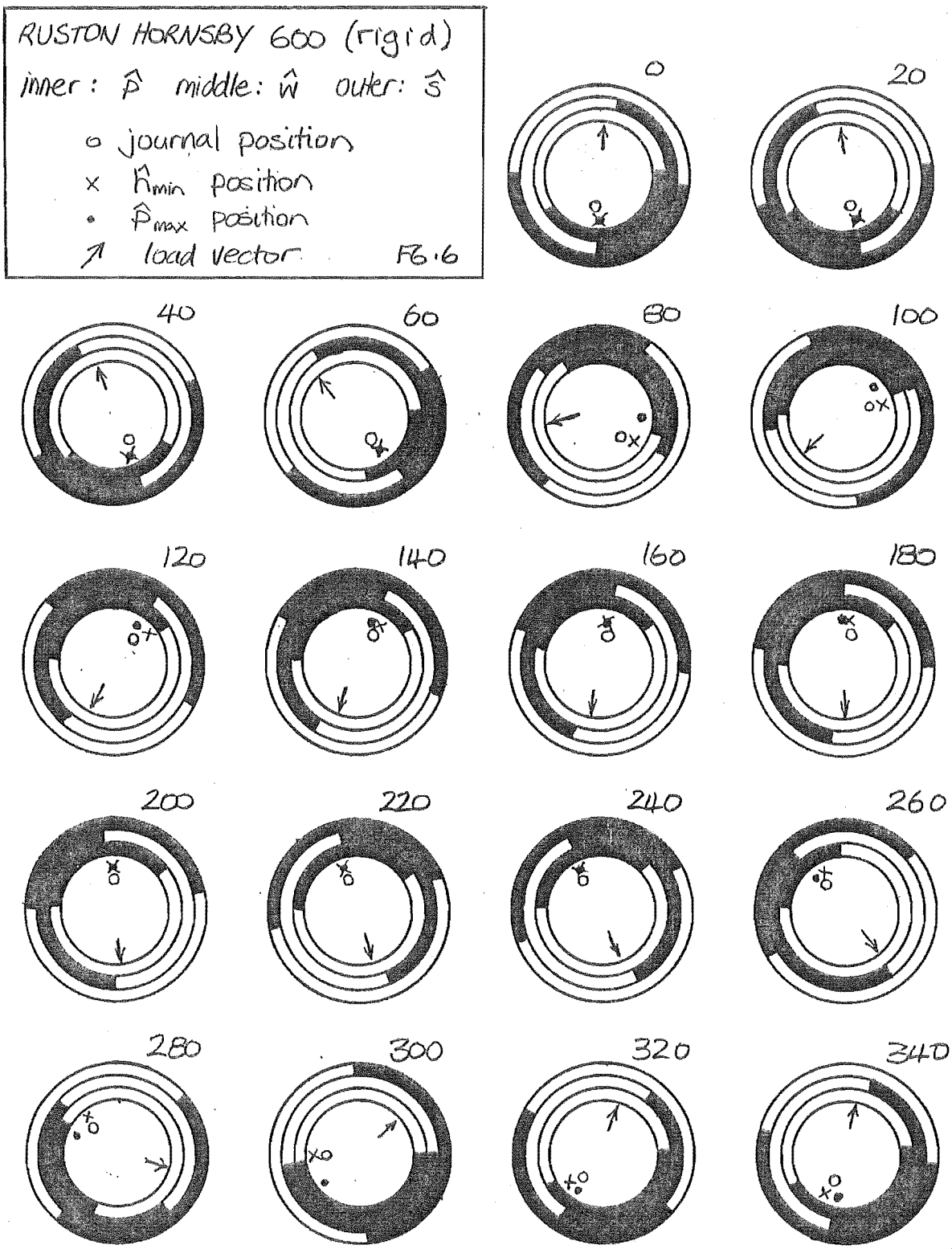
RUSTON HORNSBY 600 (rigid)
inner: $\hat{p}$ middle: $\hat{w}$ outer: $\hat{s}$
o journal position
× $\hat{h}_{min}$ position
• $\hat{p}_{max}$ position
↗ load vector
0
20
40
60
80
100
120
140
160
180
200
220
240
260
280
300
320
340

FG·6

Journal squeeze and wedge velocities are presented in the previous figure, F6.5. Little perceptible difference is apparent in $\hat{\dot{\epsilon}}$ over all three meshes ; differences in $\hat{\epsilon}(\hat{\dot{\phi}} - s/2)$ are most notable on the $36/10^0$ mesh. This corresponds closely with the film-thickness differences encountered at 90^0 and 300^0 crank-angle.

Overall, the three time meshes produce quite satisfactory results, coarser meshes sacrificing resolution but not accuracy to any great extent. Spatial/temporal mesh matching would seem to be a desirable, although difficult feature to implement ; temporal interval halving, although never invoked by the rigid model, would complicate such an implementation.

(c) Spatial Mesh :

Results for various spatial meshes are presented in F6.8. Base curve $46/5^0$ shows smooth pressure behaviour throughout the load cycle, film thickness being equally well controlled.

As spatial mesh coarsens, maximum pressure behaviour again becomes lumpy : for the $24/5^0$ solutions, amplitudes < 6% ; $36/5^0$ meshes, amplitudes < 2% (only two perceptible lumps at around 200^0ca). Despite this lumpy behaviour, film thickness remains largely unaffected, moreover $\max(\hat{p}_{max})$ and $\min(\hat{h}_{min})$ correspond closely with the $46/5^0$ solution.

The affect of mesh variation on temporal components $\hat{\dot{\epsilon}}$ and $\hat{\epsilon}(\hat{\dot{\phi}} - s/2)$, was found to be negligible.

Absolute verification of the rigid bearing model against other R-H solutions is delayed until Section 6.2.2 on gas loadings and the generalised inertial loadings of Chapter Seven. At this stage, it is probably sufficient to say that a close correspondence was found to exist.

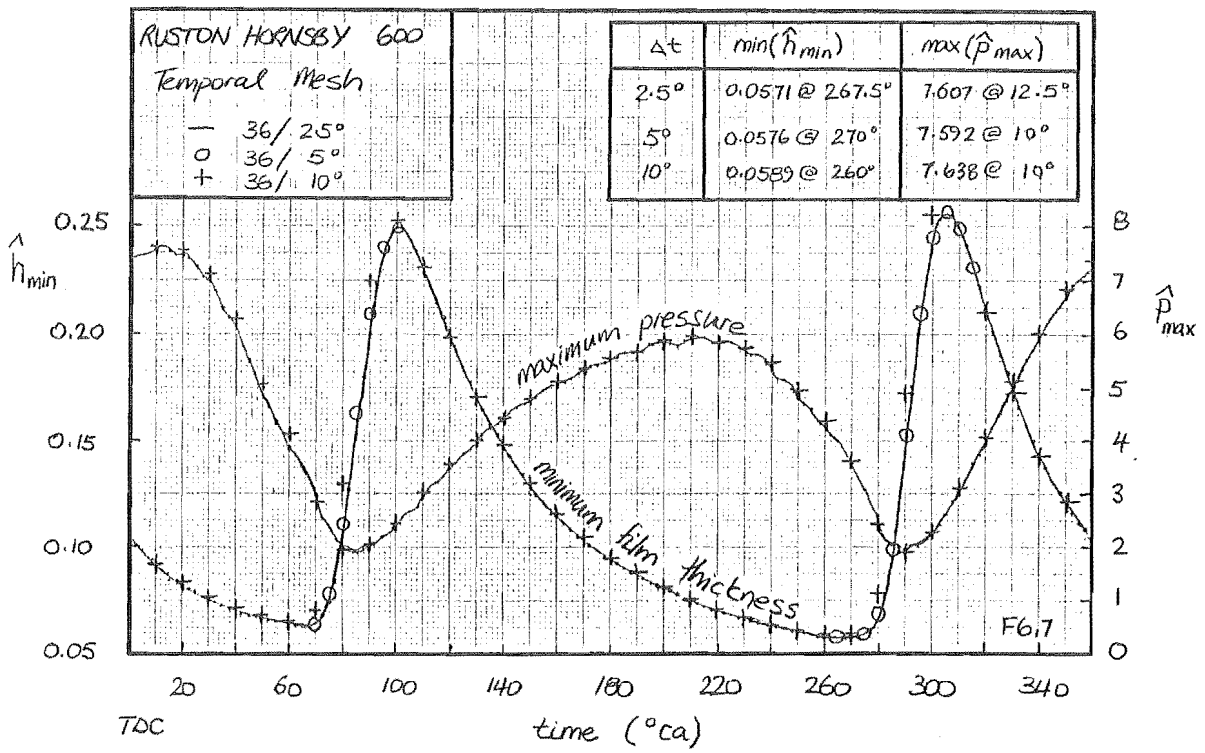
RUSTON HORNSBY 600
Temporal Mesh
— 36/ 25°
o 36/ 5°
+ 36/ 10°
Δt | min(ĥmin) | max(p̂max)
2.5° | 0.0571 @ 267.5° | 7.607 @ 12.5°
5° | 0.0576 @ 270° | 7.592 @ 10°
10° | 0.0589 @ 260° | 7.638 @ 10°
maximum pressure
minimum film thickness
F6.7
ĥmin
p̂max
TDC
time (°ca)

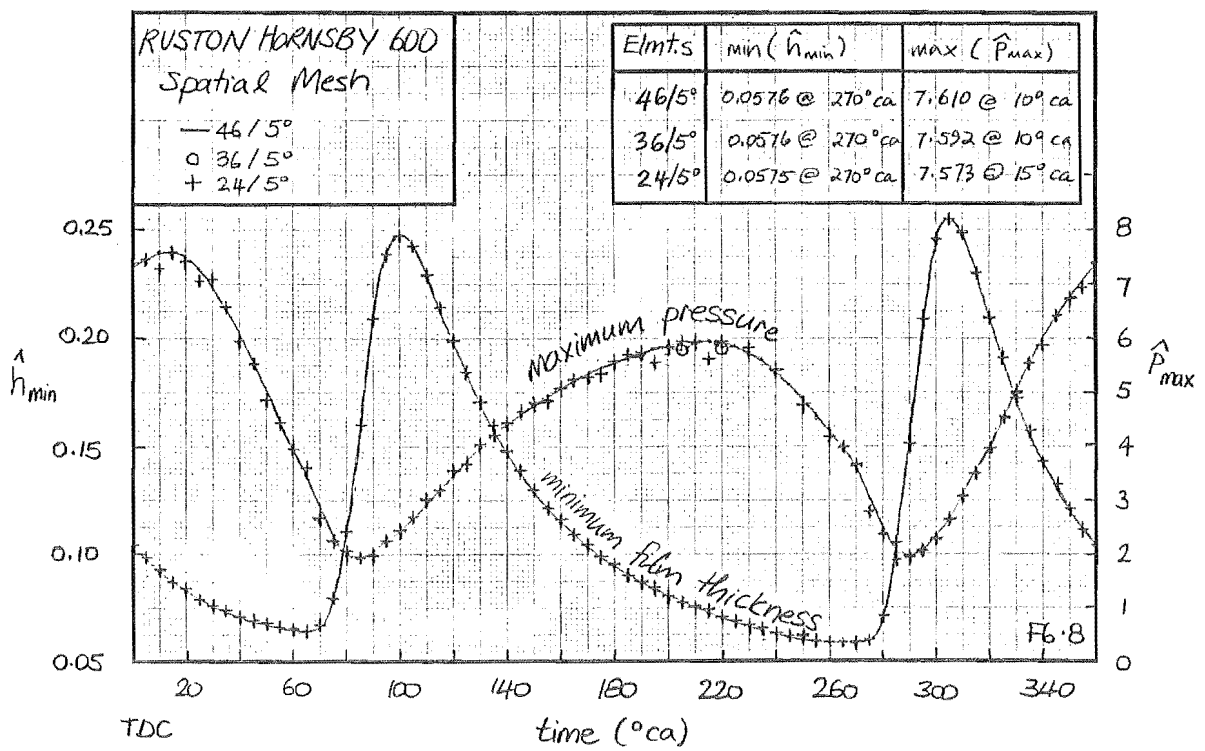
RUSTON HORNSBY 600
Spatial Mesh
— 46/5°
o 36/5°
+ 24/5°
Elmts | min(ĥmin) | max(p̂max)
46/5° | 0.0576 @ 270°ca | 7.610 @ 10°ca
36/5° | 0.0576 @ 270°ca | 7.592 @ 10°ca
24/5° | 0.0575 @ 270°ca | 7.573 @ 15°ca
maximum pressure
minimum film thickness
F6.8
ĥmin
p̂max
TDC
time (°ca)

6.1.3 *Elastic Ring Solutions*

Characterisation of elastic bearing performance is developed through an extension of the rigid bearing wedge and squeeze concepts introduced in Section 6.1.2 : we firstly re-categorise rigid squeeze and rigid wedge terms as journal squeeze and wedge action, thus :

- journal squeeze $\hat{\dot{\epsilon}}$
- journal wedge $\hat{\epsilon}(\hat{\dot{\phi}} - s/2)$,

whilst terms associated with the housing are categorised as elastic squeeze and wedge :

- elastic squeeze $\hat{\dot{u}}_r$
- elastic wedge $\frac{s}{2}\hat{u}'_r$.

These can in turn be broken down into squeeze and wedge actions due to elastic pressure and body-force displacements. The interplay of these six actions, all being comparable measures of their respective forcing terms in equation (6.1), determine the overall response of the elastic bearing to the dynamic load.

This section looks at this response using curved-beam ring solutions, firstly at 600 rpm then through the speed range of the R-H engine. It is completed with a look at discretisation. Housing solutions are investigated in Section 6.1.4.

(a) Ring Solutions : 600 rpm

As companions to the earlier rigid solutions, F6.9 and F6.10 contrast elastic bearing performance against that of the 600 rpm rigid bearing. This solution is based on a 360^0 curved-beam ring (t/r = 0.5) of 36 spatial elements and a 5^0ca nominal time step.

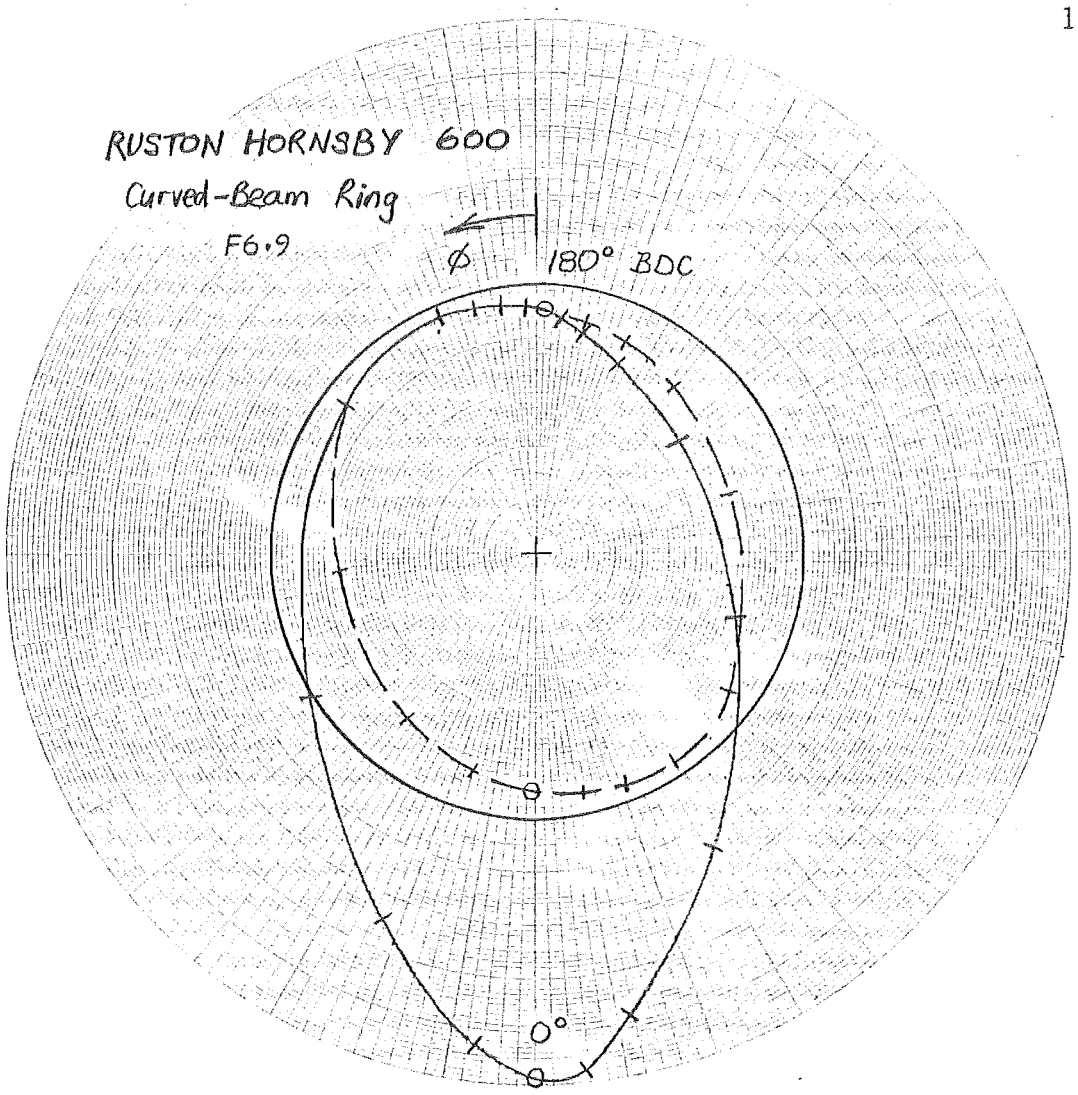
RUSTON HORNSBY 600
Curved-Beam Ring
F6.9
φ
180° BDC
0°

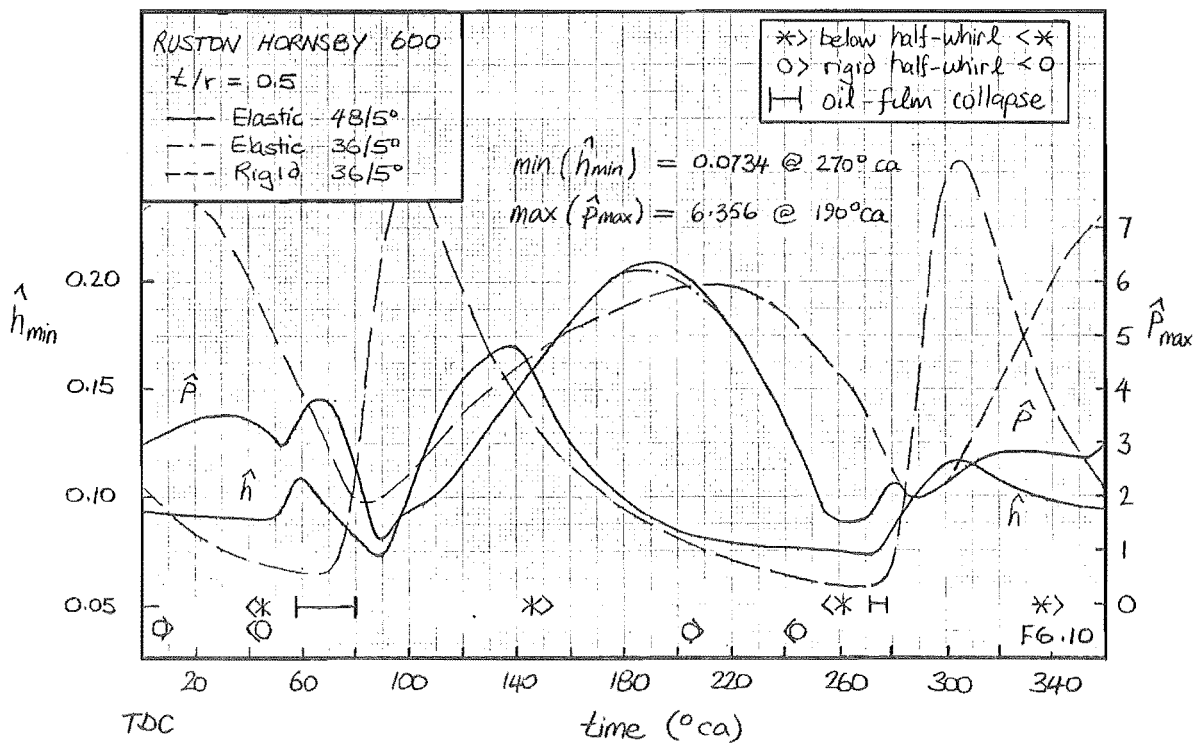
RUSTON HORNSBY 600
ℓ/r = 0.5
Elastic 48/5°
Elastic 36/5°
Rigid 36/5°
> below half-whirl <
O> rigid half-whirl <O
oil-film collapse
min (ĥmin) = 0.0734 @ 270° ca
max (p̂max) = 6.356 @ 190°ca
ĥmin
p̂max
0.20
0.15
0.10
0.05
7
6
5
4
3
2
1
0
20
60
100
140
180
220
260
300
340
TDC
time (°ca)
F6.10

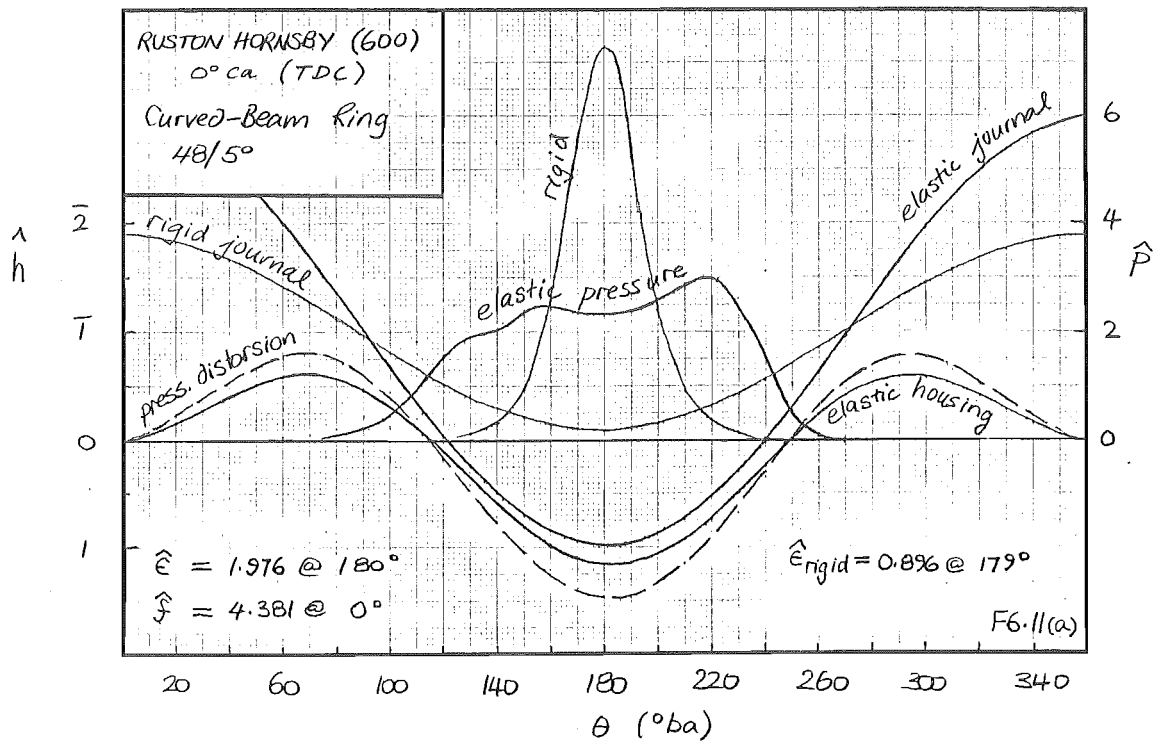
RUSTON HORNSBY (600)
0° ca. (TDC)
Curved-Beam Ring
48/5°
rigid
elastic journal
rigid journal
elastic pressure
press. distorsion
elastic housing
$\hat{\epsilon} = 1.976$ @ 180°
$\hat{\mathcal{F}} = 4.381$ @ 0°
$\hat{\epsilon}_{rigid} = 0.896$ @ 179°
F6.11(a)
$\hat{h}$
$\hat{P}$
θ (°ba)

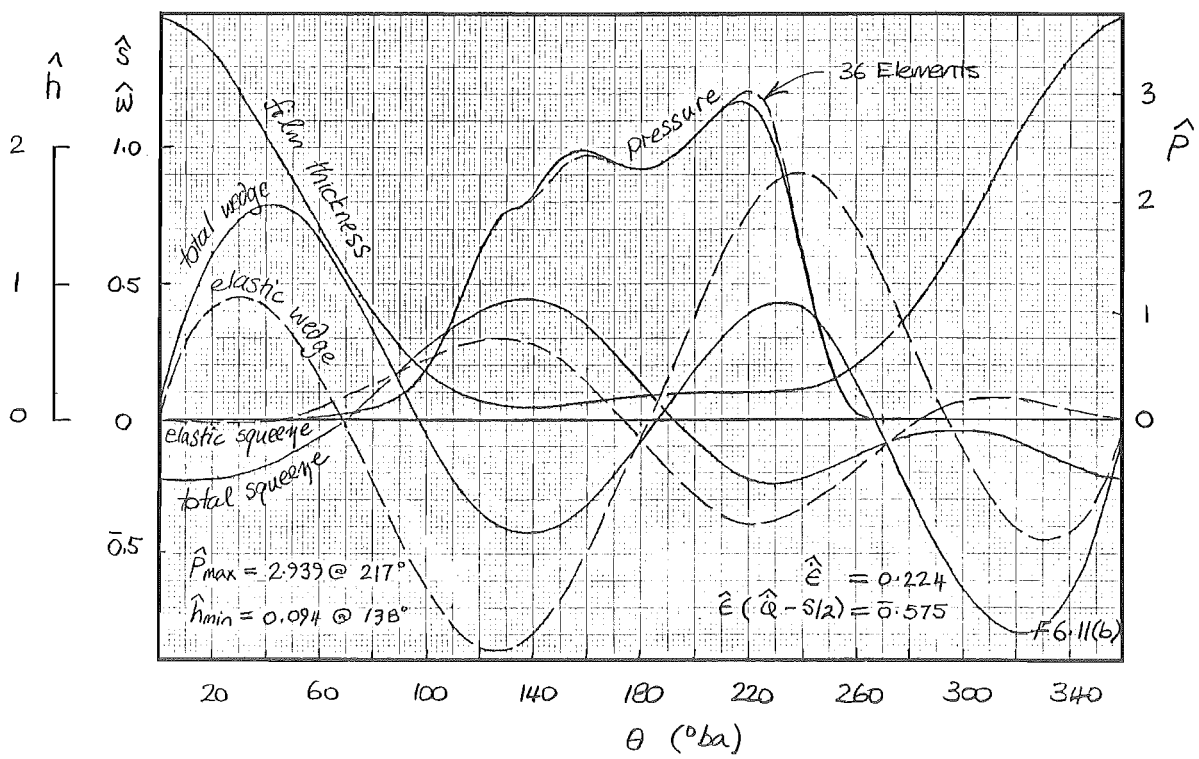
$\hat{h}$
$\hat{S}$ $\hat{W}$
$\hat{P}$
film thickness
pressure
36 Elements
total wedge
elastic wedge
elastic squeeze
total squeeze
$\hat{P}_{max} = 2.939$ @ 217°
$\hat{h}_{min} = 0.094$ @ 138°
$\hat{\epsilon} = 0.224$
$\hat{\epsilon}\,(\hat{Q} - S/2) = \bar{0}.575$
F6.11(b)
θ (°ba)

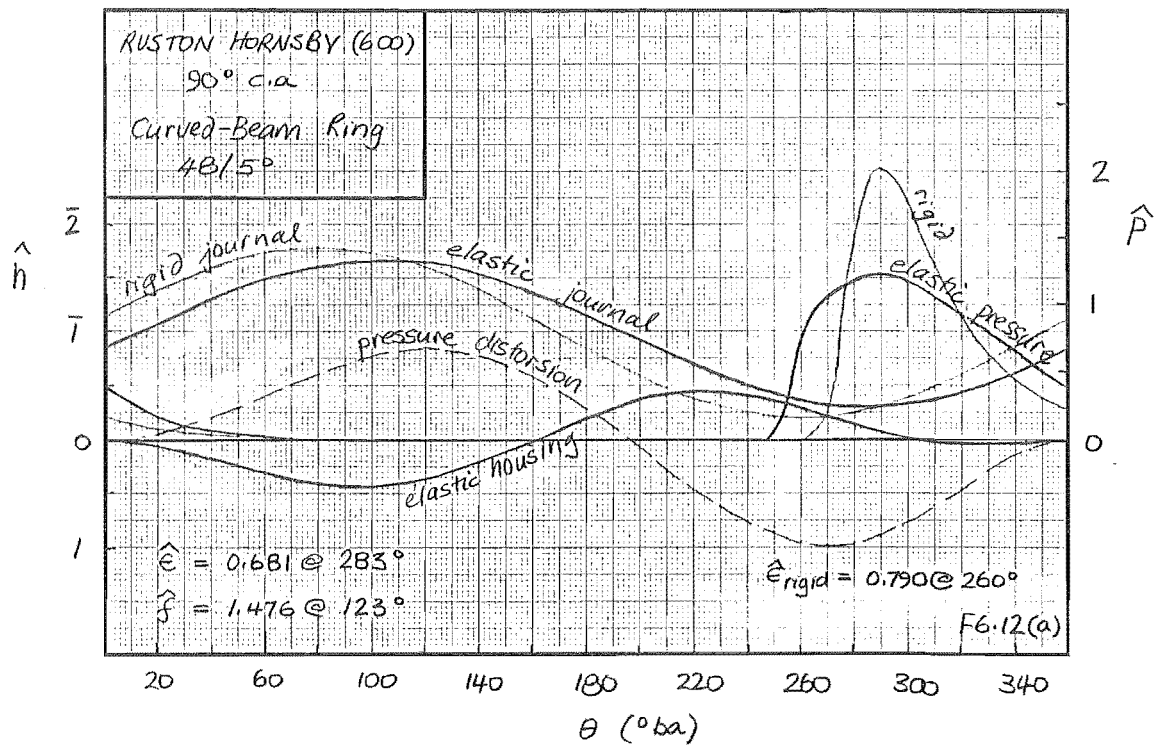
RUSTON HORNSBY (600)
90° c.a
Curved-Beam Ring
48/5°
rigid journal
elastic journal
pressure distortion
elastic housing
rigid
elastic pressure
$\hat{\epsilon}$ = 0.681 @ 283°
$\hat{f}$ = 1.476 @ 123°
$\hat{\epsilon}_{rigid}$ = 0.790 @ 260°
F6.12(a)
$\hat{h}$
$\hat{P}$
θ (°ba)

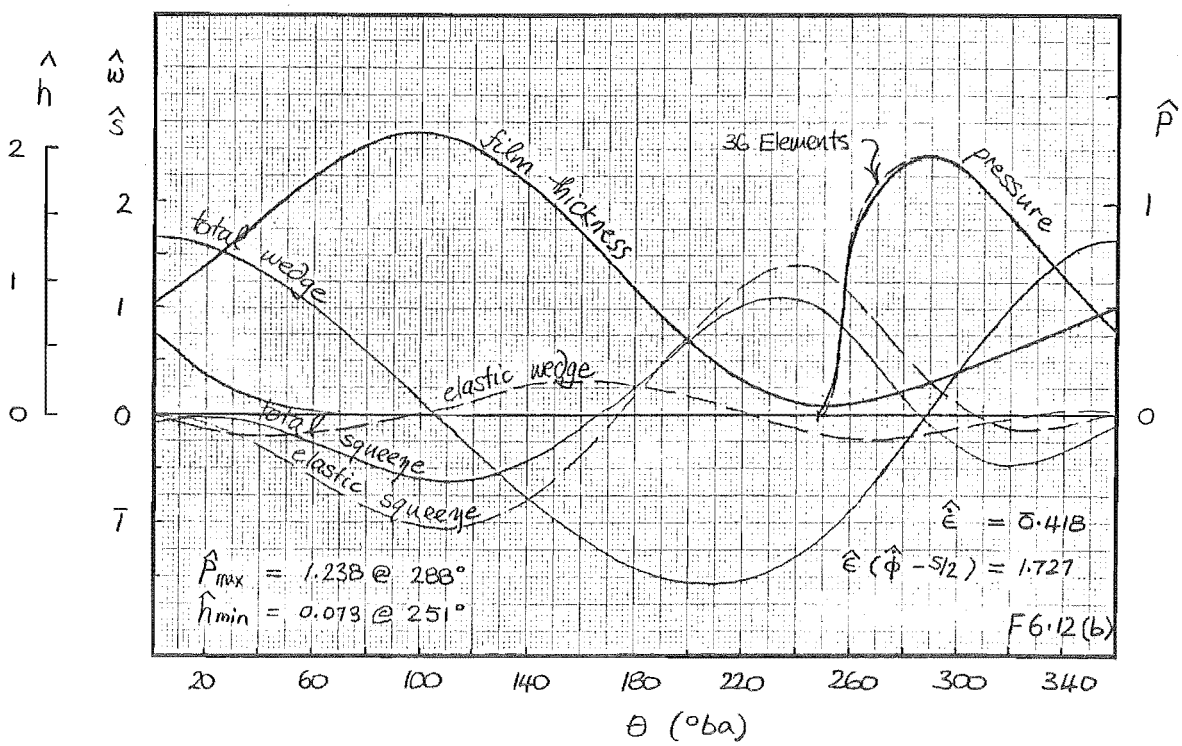
$\hat{h}$
$\hat{w}$ $\hat{s}$
$\hat{P}$
film thickness
total wedge
elastic wedge
total squeeze
elastic squeeze
36 Elements
pressure
$\hat{P}_{max}$ = 1.238 @ 288°
$\hat{h}_{min}$ = 0.073 @ 251°
$\hat{\epsilon}$ = 0.418
$\hat{\epsilon}(\hat{\phi} - S/2)$ = 1.727
F6.12(b)
θ (°ba)

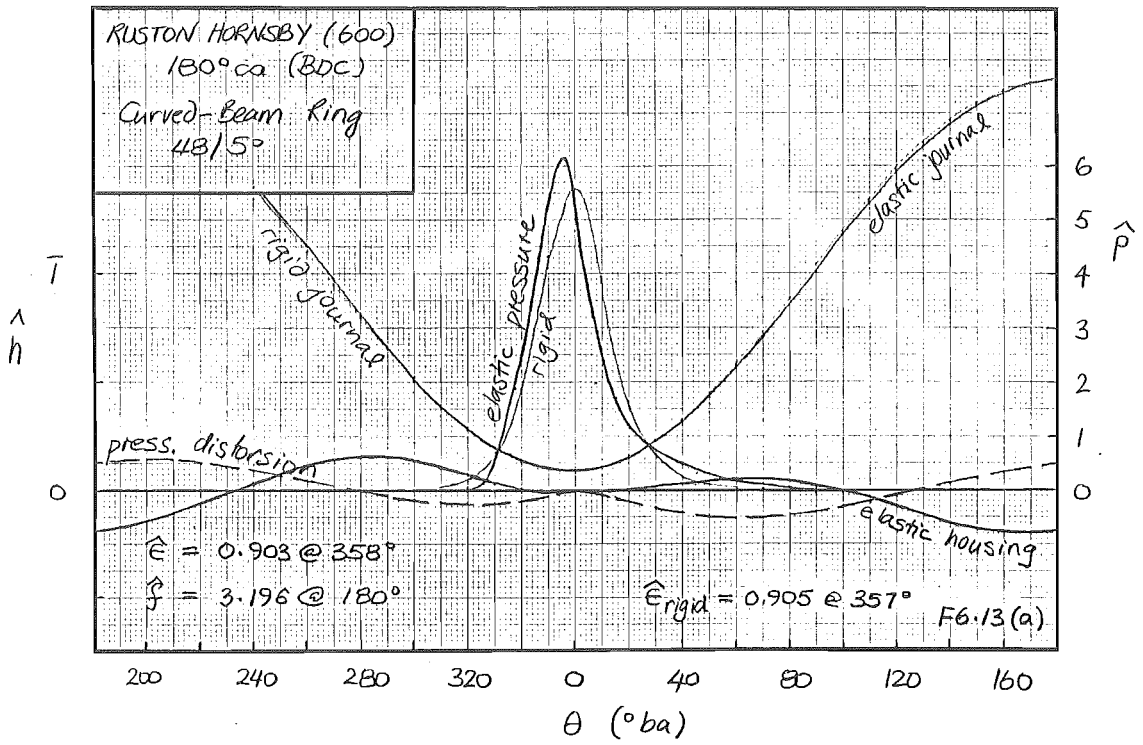
RUSTON HORNSBY (1600)
180° ca (BDC)
Curved-Beam Ring
48/5°
rigid journal
elastic pressure
rigid
elastic journal
press. distorsion
elastic housing
$\hat{\epsilon}$ = 0.903 @ 358°
$\hat{f}$ = 3.196 @ 180°
$\hat{\epsilon}_{rigid}$ = 0.905 @ 357°
F6.13(a)
$\bar{l}$
$\hat{h}$
$\hat{P}$
θ (°ba)

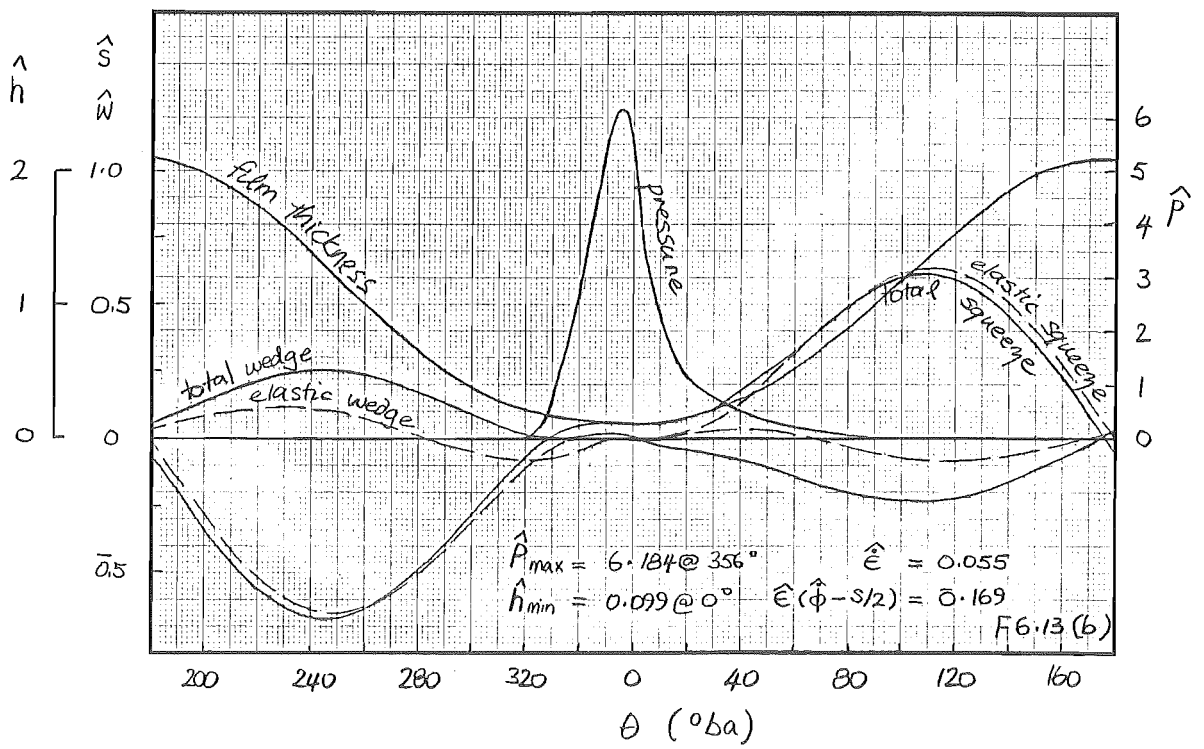
$\hat{h}$
$\hat{S}$
$\hat{W}$
film thickness
pressure
total wedge
elastic wedge
total
elastic squeeze
$\hat{P}_{max}$ = 6.184 @ 356°
$\hat{h}_{min}$ = 0.099 @ 0°
$\hat{\epsilon}$ = 0.055
$\hat{\epsilon}(\hat{\phi}-S/2)$ = 0.169
F6.13(b)
$\hat{P}$
θ (°ba)

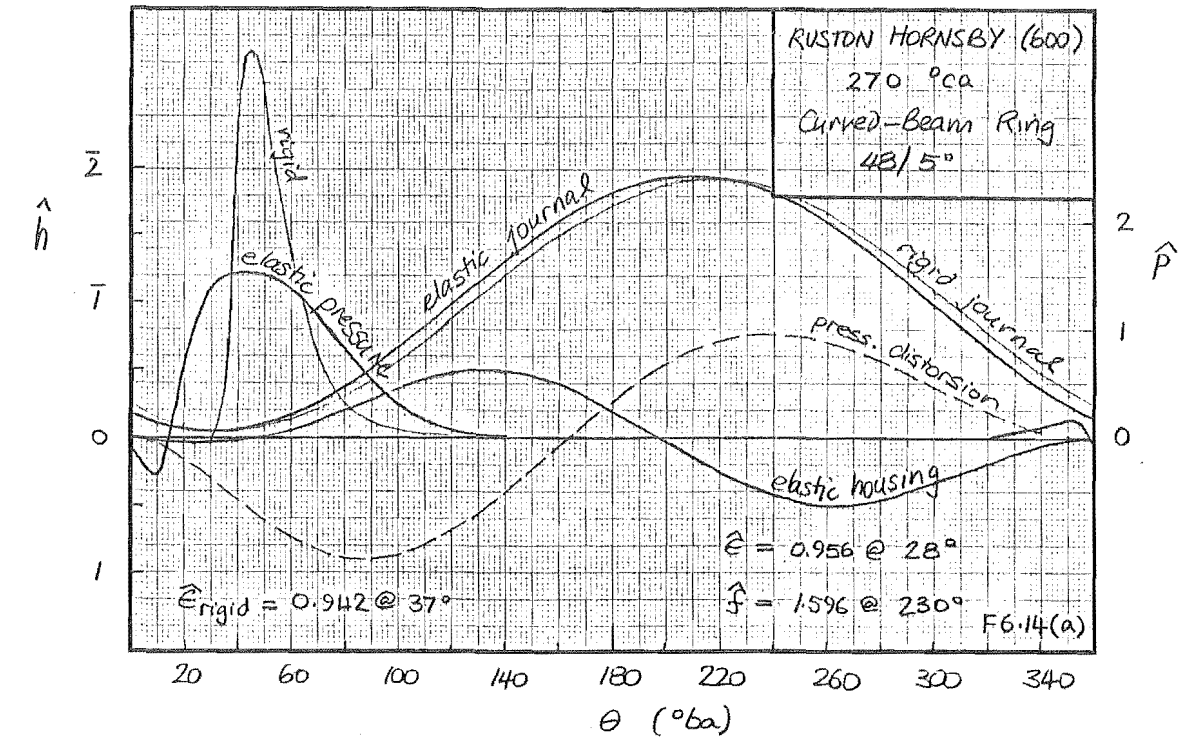
RUSTON HORNSBY (600)
270 °ca
Curved-Beam Ring
48/5"
rigid
elastic pressure
elastic journal
rigid journal
press. distortion
elastic housing
$\hat{\epsilon}$ = 0.956 @ 28°
$\hat{\epsilon}_{rigid}$ = 0.942 @ 37°
$\hat{f}$ = 1.596 @ 230°
F6.14(a)
$\hat{h}$
$\hat{P}$
θ (°ba)

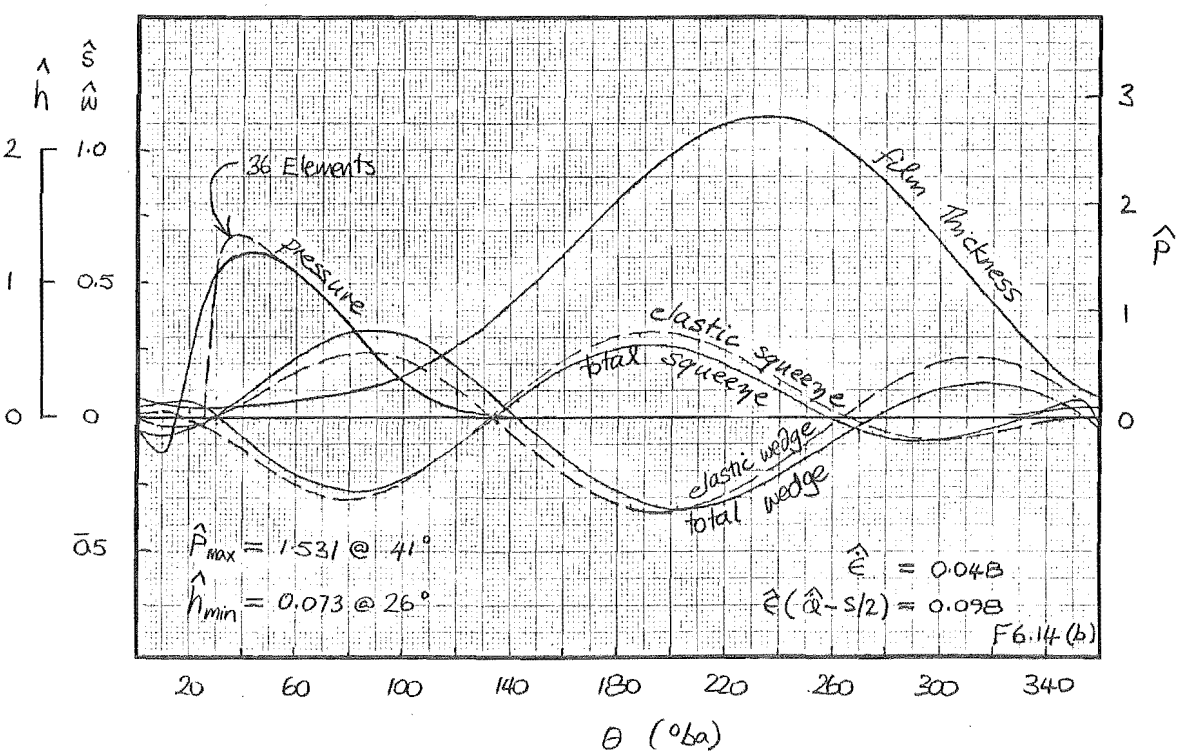
$\hat{h}$
$\hat{s}$
$\hat{w}$
$\hat{P}$
36 Elements
Pressure
film Thickness
elastic squeeze
total squeeze
elastic wedge
total wedge
$\hat{P}_{max}$ = 1.531 @ 41°
$\hat{h}_{min}$ = 0.073 @ 26°
$\hat{\epsilon}$ = 0.048
$\hat{\epsilon}(\hat{a}-s/2)$ = 0.098
F6.14(b)
θ (°ba)

Four additional sets of figures capture the salient features of the elastic cycle : F6.11, maximum distorsion at TDC (0^0ca); F6.12, minimum film pressure at 90^0ca; F6.13, maximum film pressure at BDC (180^0ca); F6.14, minimum film thickness and film collapse at 270^0ca. The first of each pair of figures, (a), give circumferential pressure and surface behaviour, the second, (b), presents the various film mechanisms : total squeeze ($\hat{\dot{\epsilon}}\cos(\theta-\phi) - \hat{\dot{u}}_r$) and total wedge ($\hat{\epsilon}(\hat{\dot{\phi}} - s/2)\sin(\theta-\phi) - \frac{s}{2}\hat{u}_r'$) action; elastic squeeze ($-\hat{\dot{u}}_r$) and elastic wedge ($-\frac{s}{2}\hat{u}_r'$) action; film-thickness and pressure.

Marked differences between rigid and elastic solutions have appeared, our investigation into these differences begins with elastic journal action.

Journal Action : Journal action in the elastic bearing is presented in F6.15. The basic rigid forms (F6.5) have clearly been influenced by cap deflection.

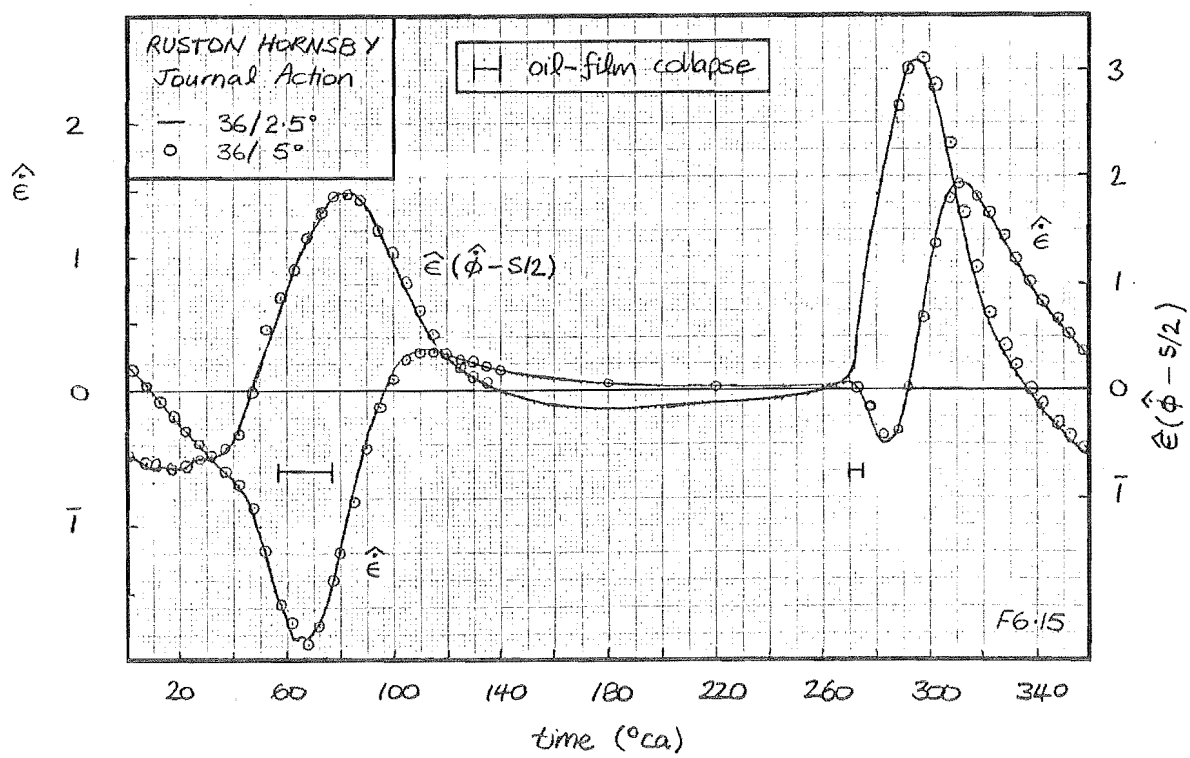

As journal locus traverses the rigid clearance circle, journal action increases markedly : peak squeeze action is increased 400%; peak wedge action by 150%. Increased clearance from housing deflection allows much higher velocities to be attained.

However, overall the journal spends more time below half-whirl speed than its rigid counterpart, journal squeeze action making a greater contribution to film action.

Housing Action : Elastic housing actions, depicted in F6.11b-14b consist of two components : elastic pressure actions and elastic body-force action. To illustrate the development of these elastic components, F6.16 outlines the various distorsions with crank angle : The outer ring represents body-force distorsion; middle ring, pressure distorsion; the inner ring, total distorsion. Shaded sections represent outward (positive) deflections. Body-force vector along with journal and peak pressure position are depicted in the central circle.

The dominance of body-force deflection through a large portion of the cycle graphically illustrates the error of earlier works in excluding its effects : deflected forms 120^0ca either side of BDC are predominantly due to this term, body-forces contributing significantly to ring flexure. Only when the body-force is directed into the ring's neck (60^0 ca either side of TDC) and pressure acts into the cap does pressure distorsion become influential.

It should be noted that there is no elastic equivalent to journal half-whirl speed; the elastic components are continuously present throughout the load cycle.

Total Film Action : We have looked at journal and housing action in isolation, however it is total film action, the sum of journal, pressure and body-force actions that determine bearing performance.

RUSTON HORNSBY 600 (Ring)
Elastic Distorsion
inner: total middle: $\hat{p}$ outer: $\hat{b}$

o journal position
• $\hat{p}_{max}$ position
↑ body-force

F6.16

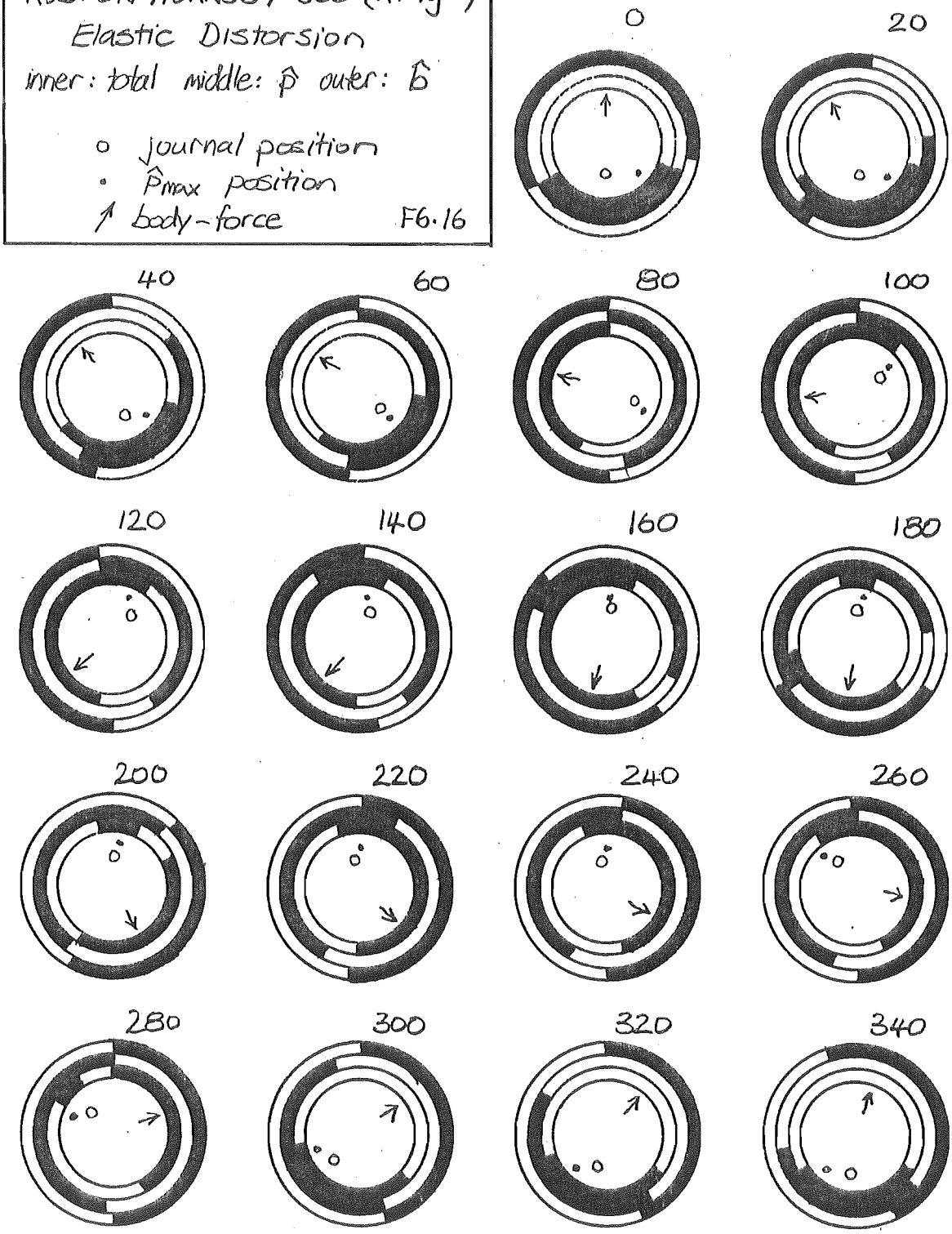

The interplay of the six film actions and the resulting ascendent forms are summarised in F6.18 at 20^0ca intervals : The inner arc represents film pressure; centre arc, total wedge action; outer arc, total squeeze action. Film actions are as defined previously (Section 6.1.3a). Load vector along with journal, peak pressure and minimum film-thickness positions are presented in the central circle. In addition, the major contributions from wedge and squeeze action are categorised by a ratio in the central circle thus :

$$x{:}y \quad x,y \epsilon \{j,b,p\}$$

x represents the largest wedge term : j for journal, p for pressure, b for body-force ; y represents the largest squeeze term. The only symbol remaining undefined is the hatched shading associated with film collapse (negative pressures).

Comparison of elastic and rigid figures (F6.6, F6.18) reveal significant changes in wedge and squeeze phenomena, the overall picture being far more complex than the cosine/sine relationships of the rigid bearing. Owing to this complexity, it was felt a full description of the various mechanisms was warranted. This was aided considerably by the observations of Section 6.1.3b. We start this description at BDC with the journal in the ring neck : (F6.9,.10,.16,.18 are pertinent to this discussion).

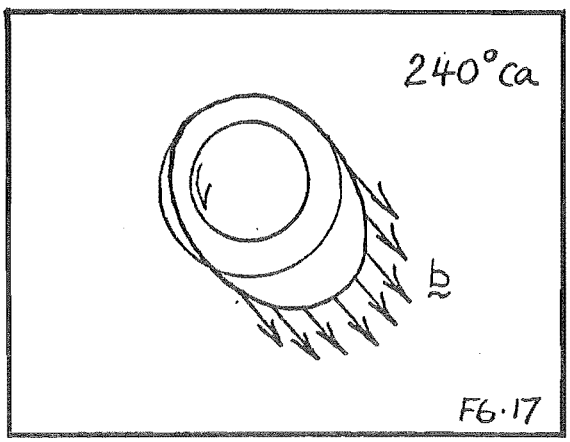

F6·17

At this point in the cycle body-force actions dominate, firstly through squeeze then, from 220-270^0ca, through wedge action; this second period of wedge (F6.17) is responsible for the noticeably thickened minimum film-thickness in the elastic

RUSTON HORNSBY 600 (Ring)
inner: $\hat{p}$ middle: $\hat{w}$ outer: $\hat{s}$

o journal position
× $\hat{h}_{min}$ position
• $\hat{p}_{max}$ position
↗ load vector

F6.18

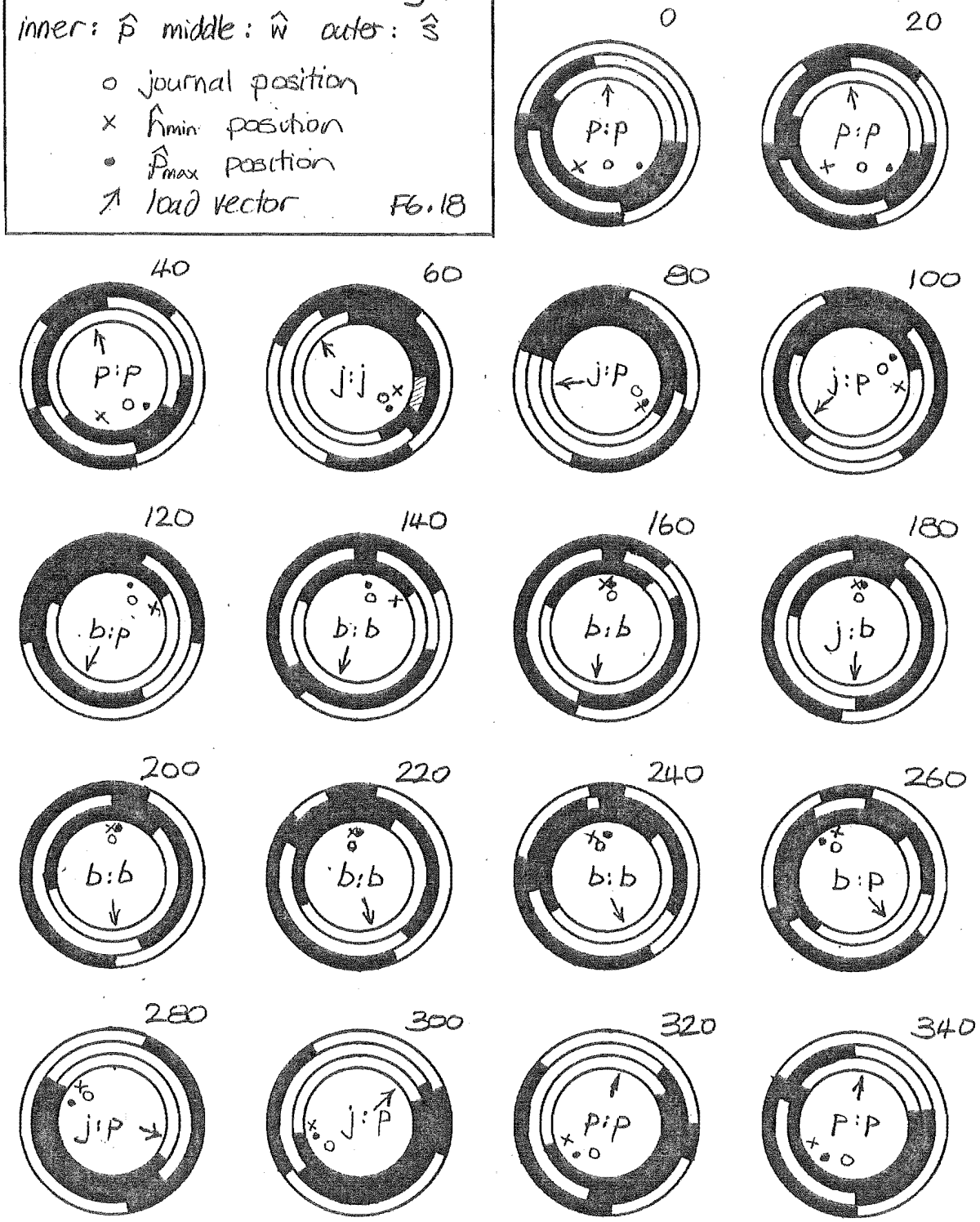

bearing (27%). The associated reduction in peak pressure indicates the strong beneficial effect body-force has on load capacity. During the latter stages of this period (240-270^{0}ca), elastic discontinuity of the neck restraint fragments wedge action, inducing a short film collapse at 270^{0}ca (F6.14); this is the subject of discussion in the following section.

Journal wedge action then increases dramatically; by 280^{0}ca it has become the dominant term. However, by 300^{0}ca the effects of pressure distorsion begin to be felt : as journal locus extends beyond the rigid clearance circle and approaches TDC, wedge action undergoes a transition from being journal dominated to being pressure dominated; peak pressures and minimum film thickness decrease substantially on the rigid solution. Ascending pressure squeeze action makes a strong contribution by 350^{0}ca, significantly thickening the oil-film through 10-40^{0}ca compared to the rigid solution. Elastic actions are generally much stronger during these periods than their rigid bearing counterparts.

Through the next 100^{0}ca, journal motion back into the clearance circle becomes influential : beginning at around 50^{0}ca, journal wedge action firstly supplements pressure squeeze action, then comes to dominate film action through to 120^{0}ca; detrimental journal squeeze action during this period (60-80^{0}ca) collapses the oil-film for a second period.

Finally, through the remaining crank angles (140-180^{0}ca) body-force squeeze action dominates; films get thinner and pressures increase, symptoms of reduced load carrying capacity.

The details surrounding the periods of film breakdown are of some interest.

Oil–Film Collapse : Two periods of negative film pressure were observed during the 600 rpm load cycle: a very short period, 0.001 seconds (5^{0}ca) at 270^{0}ca and a longer period, 0.005 seconds beginning at 60^{0}ca. The first breakdown was shown in F6.14, the second sequence in F6.19.

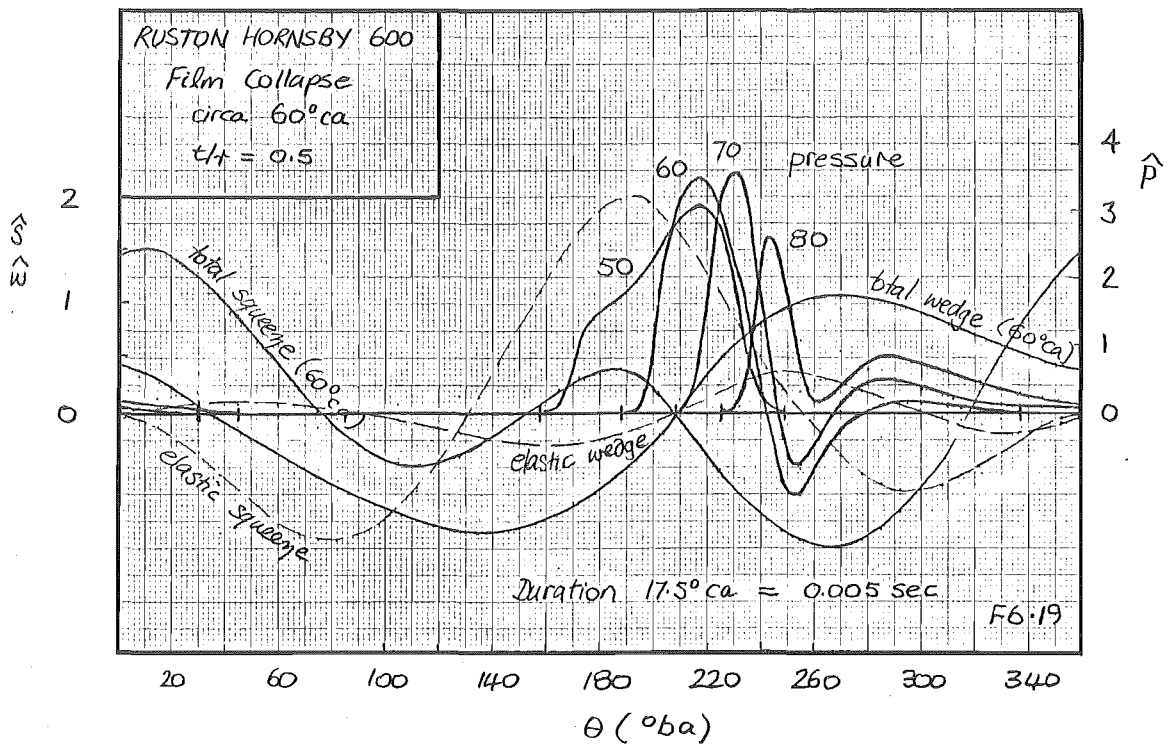

Elastic slopes associated with the neck constraint induce the first film breakdown at 270°ca; this disruption does not occur in a full elastic housing, it is purely a consequence of a discontinuous 'elastic' neck.

The second period of disruption is induced by elastic locus distorsion : negative squeeze action of the journal retreating into the neck of the rod, collapses the oil-film. Although this collapse mechanism is available in the rigid model, not a single case was observed; locus distorsion is an integral part of this condition. It should be noted that a similar but quite separate disruption is experienced during gas loading; the physical existence and experimental evidence of such collapses are discussed in Section 6.2.3a.

Before leaving the 600 rpm solutions, the pathological case of zero body-force is briefly presented.

Body–Forces : The current work differs from previous elastic works through the inclusion of deflections due to the body-forces of con-rod motion. It is interesting to observe the effects of neglecting this influence, witness figures F6.20, F6.21.

Locus behaviour indicates that body-forces significantly stiffen the big-end ring perpendicular to the con-rod centre-line. The resulting minimum film thickness and maximum pressure forms are significantly altered : $\min(\hat{h}_{min})$ is reduced by 50%, $\max(\hat{p}_{max})$ increased by 60%; journal wedge velocity *never* drops below half-whirl speed. Clearly this body-force cannot be neglected from either a phenomenological or load consistency standpoint. More important however, are the serious questions raised about experimental testing procedures.

Many bearing test-rigs are only dynamic in that they apply a time-varying load; dynamic body-force is usually completely neglected. The NEL work of Cooke[97] is a case in point. As we have seen, the oil-film régime generated under such conditions is quite dissimilar from that in the con-rod, results consequently having little meaning within the con-rod context : a comprehensive review of experimental test-rig procedures would seem to be well overdue.

(b) **Ring Solutions : Variable Speed**

In an attempt to unravel the various mechanisms affecting elastic performance, a sequence of solutions† were developed at increasing engine revolutions : 200 and 400 rpm, the previous 600 rpm solution (F6.9) and finally one at 700 rpm. These results are presented in F6.23 - F6.28, the balance being contained in Appendix A7.

Through this sequence it is possible to trace the development of the various film mechanisms. However, before tackling this, an overview of the basic performance trends is presented.

---

† the same curved-beam model was used as in the 600 rpm case.

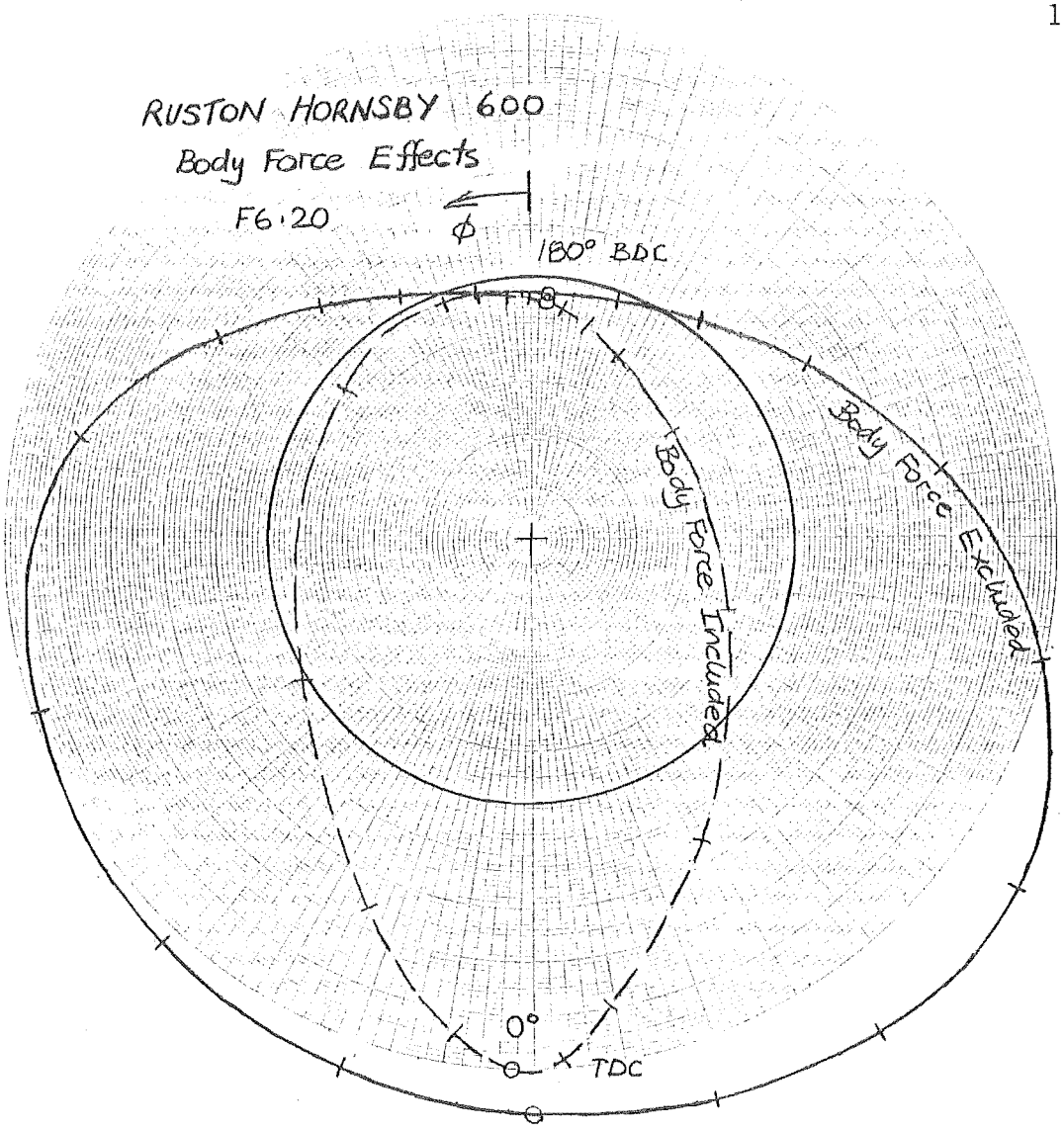
RUSTON HORNSBY 600
Body Force Effects
F6.20
φ
180° BDC
Body Force Included
Body Force Excluded
0°
TDC

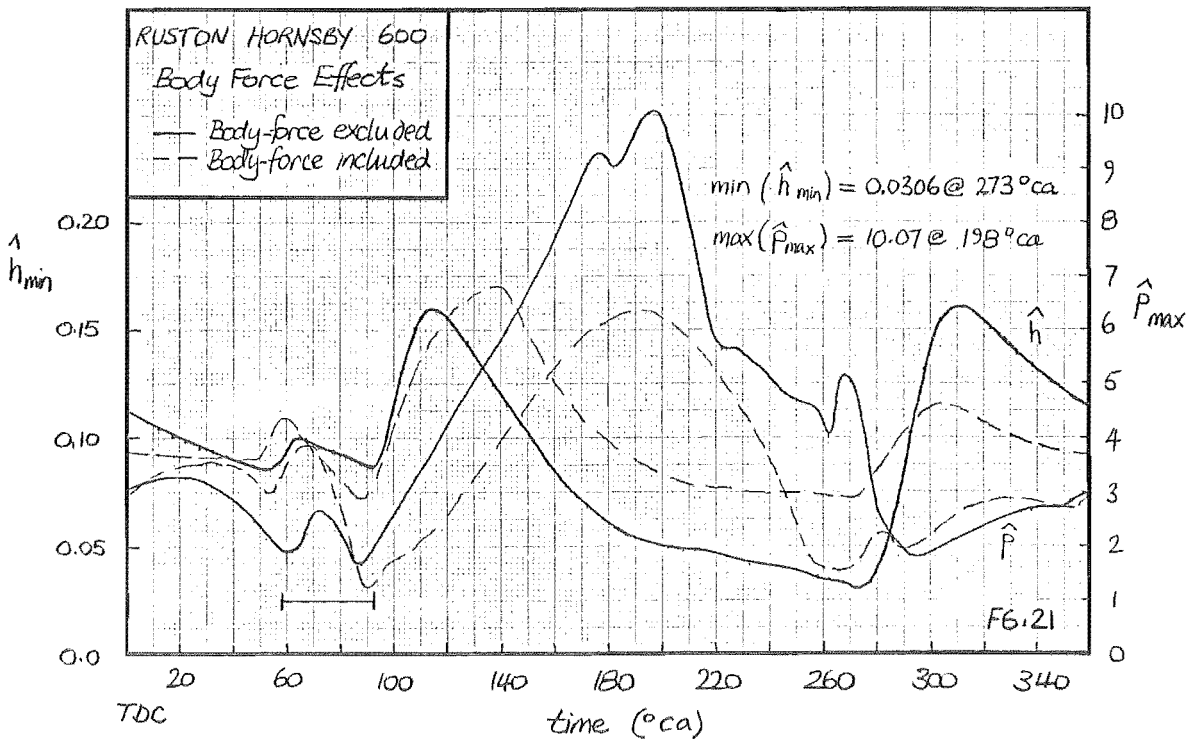
RUSTON HORNSBY 600
Body Force Effects
Body-force excluded
Body-force included
min (ĥ min) = 0.0306 @ 273°ca
max (P̂max) = 10.07 @ 198°ca
ĥ
P̂
F6.21
ĥmin
P̂max
0.20
0.15
0.10
0.05
0.0
10
9
8
7
6
5
4
3
2
1
0
20
60
100
140
180
220
260
300
340
TDC
time (°ca)

Performance Trends : Significant positional shifts in minimum film thickness and maximum pressure occur through the operational speed range of the Ruston-Hornsby : For the first 600 rpm, min($\hat{h}_{min}$) is located in the neck of the rod; *circa* 30^{0}ba, 270^{0}ca. This is not significantly different from the rigid bearing. A thickening trend in minimum film accompanies the speed increase, a product of strong body-force wedge action.

However, by 700 rpm this condition has shifted into the rod cap; *circa* 125^{0}ba, 345^{0}ca. A significantly reduced film thickness is then determined by elastic pressure action, a quite different mechanism from that in the rigid bearing : F6.22 indicates the gravity of the shift and in particular, its greater sensitivity to load. This film thinning condition has serious design consequences and is the subject of further investigation in Chapter Seven.

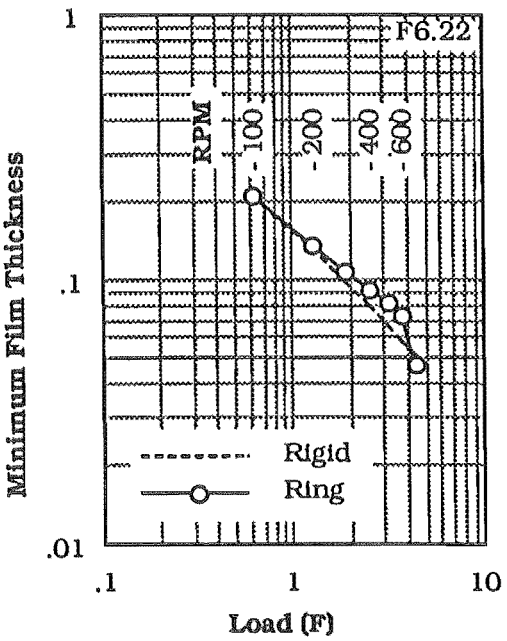

A similar shift is observed in maximum film pressure but at much lower revolutions : below 400 rpm, max($\hat{p}_{max}$) develops in the cap at around TDC; in the rigid bearing this condition occurs here at all speeds. However, by 400 rpm, cap distorsion reduces this peak pressure such that the BDC condition becomes critical; rigid results are then a poor indicator of max($\hat{p}_{max}$) behaviour.

Some influence of speed variation on film collapse is also apparent : sufficient locus distorsion is present by 400 rpm to induce a 60^{0}ca film-collapse, its duration increasing thereafter. By 700 rpm, this collapse shows noticeable mesh sensitivity; part (c) of this section investigates this further.

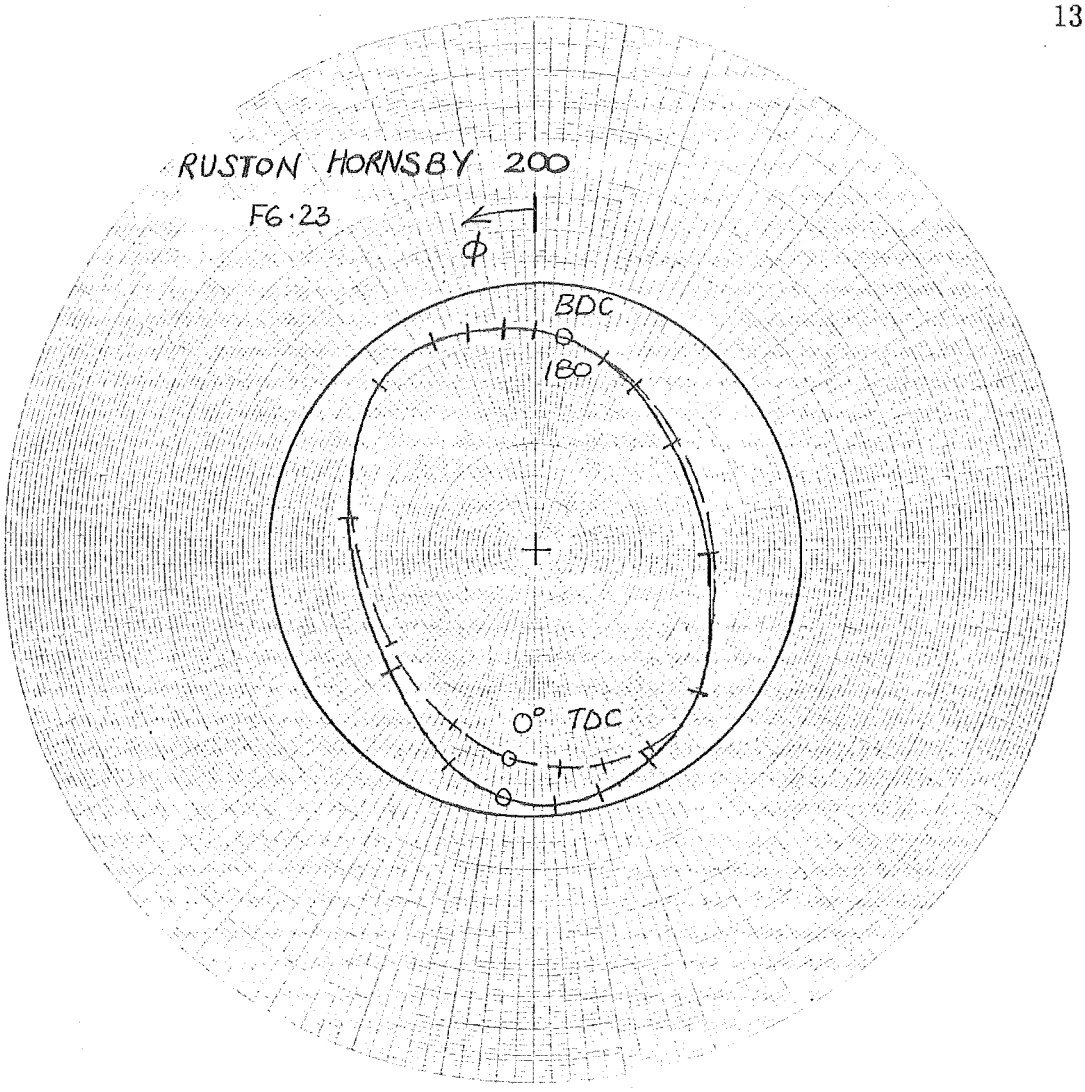
RUSTON HORNSBY 200
FG·23
φ
BDC
180
0° TDC

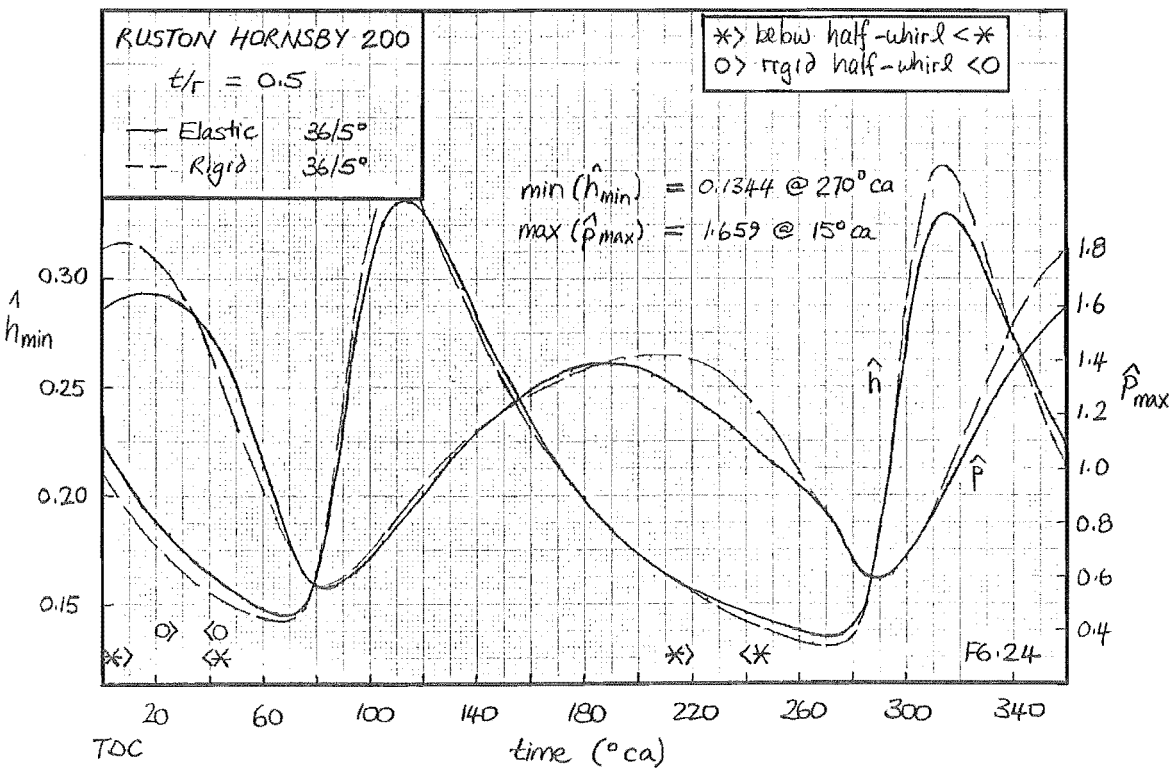
RUSTON HORNSBY 200
t/r = 0.5
Elastic 36/5°
Rigid 36/5°
> below half-whirl <
O> rigid half-whirl <O
min (ĥmin) = 0.1344 @ 270° ca
max (p̂max) = 1.659 @ 15° ca
ĥmin
p̂max
ĥ
p̂
0.30
0.25
0.20
0.15
1.8
1.6
1.4
1.2
1.0
0.8
0.6
0.4
20
60
100
140
180
220
260
300
340
TDC
time (° ca)
FG·24

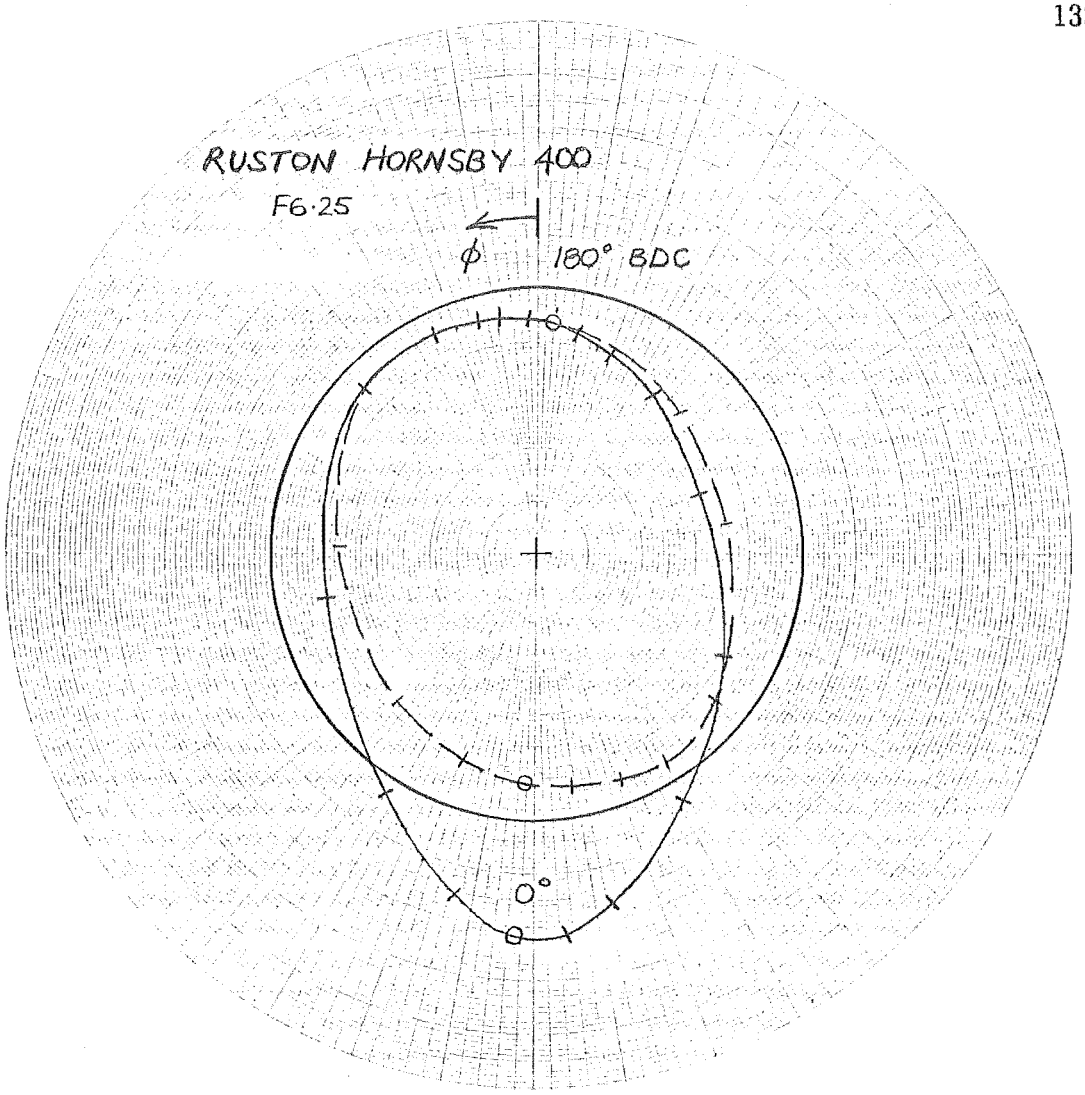
RUSTON HORNSBY 400
F6·25
φ
180° BDC
0°

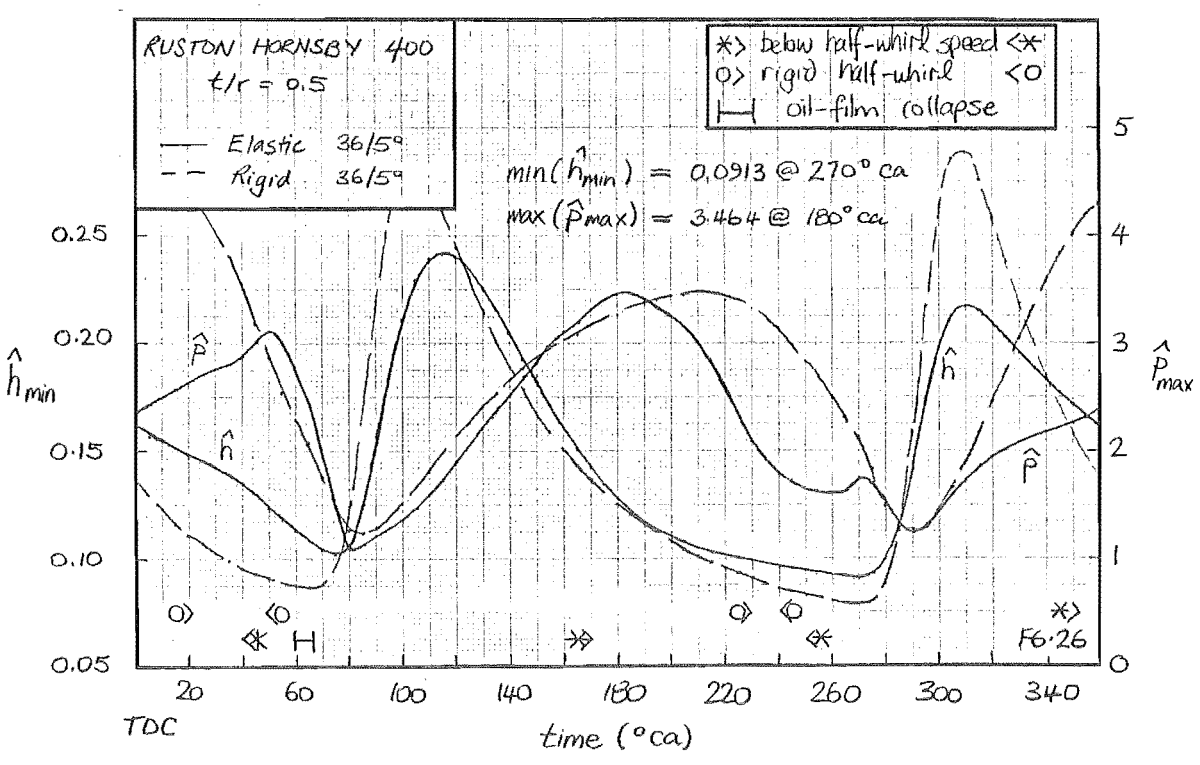
RUSTON HORNSBY 400
t/r = 0.5
Elastic 36/5°
Rigid 36/5°
> below half-whirl speed <
O> rigid half-whirl <O
oil-film collapse
min(ĥmin) = 0.0913 @ 270° ca
max(p̂max) = 3.464 @ 180° ca
ĥmin
p̂max
ĥ
p̂
0.25
0.20
0.15
0.10
0.05
5
4
3
2
1
0
20
60
100
140
180
220
260
300
340
TDC
time (°ca)
F6·26

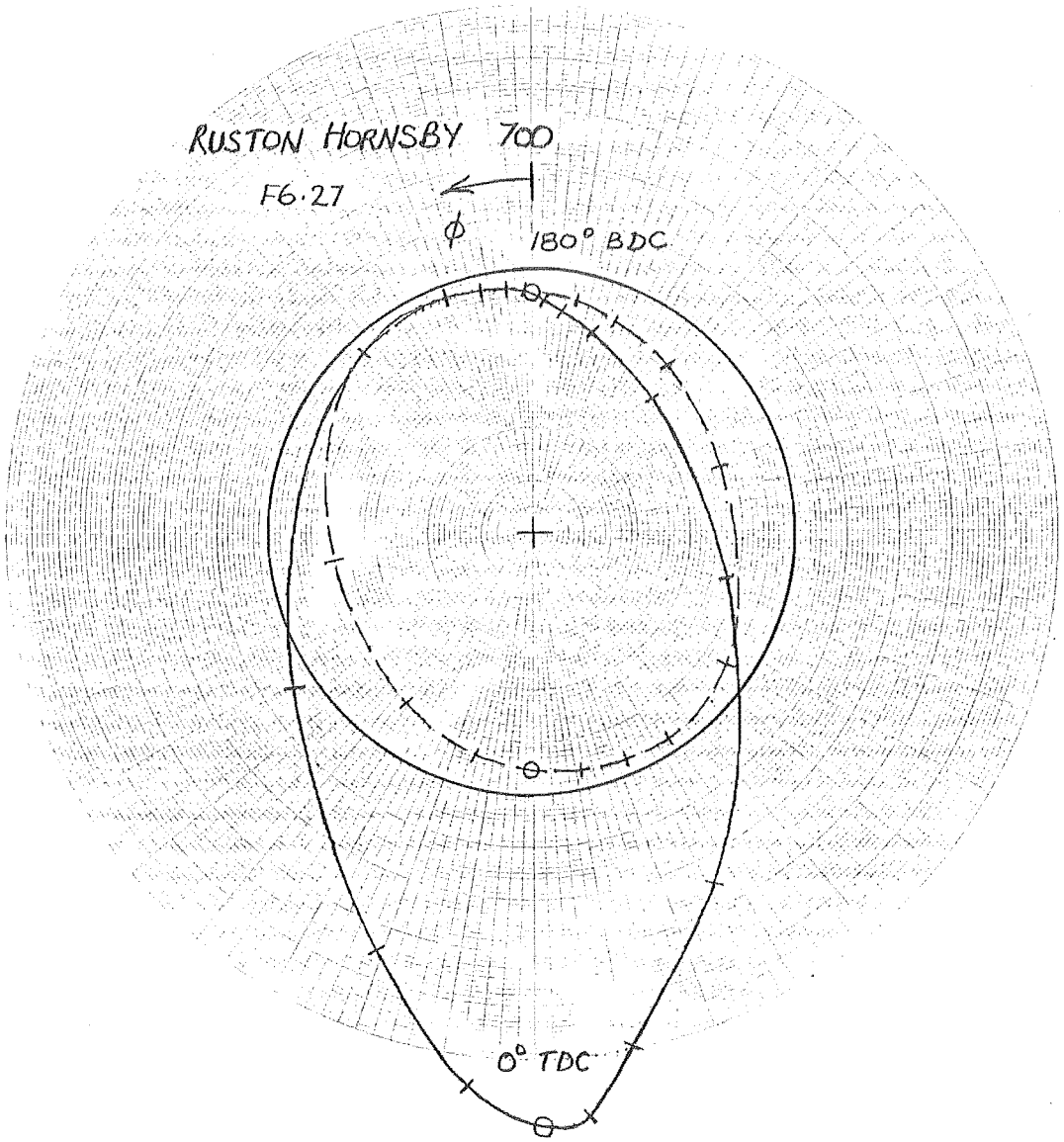
RUSTON HORNSBY 700
F6.27
φ
180° BDC
0° TDC

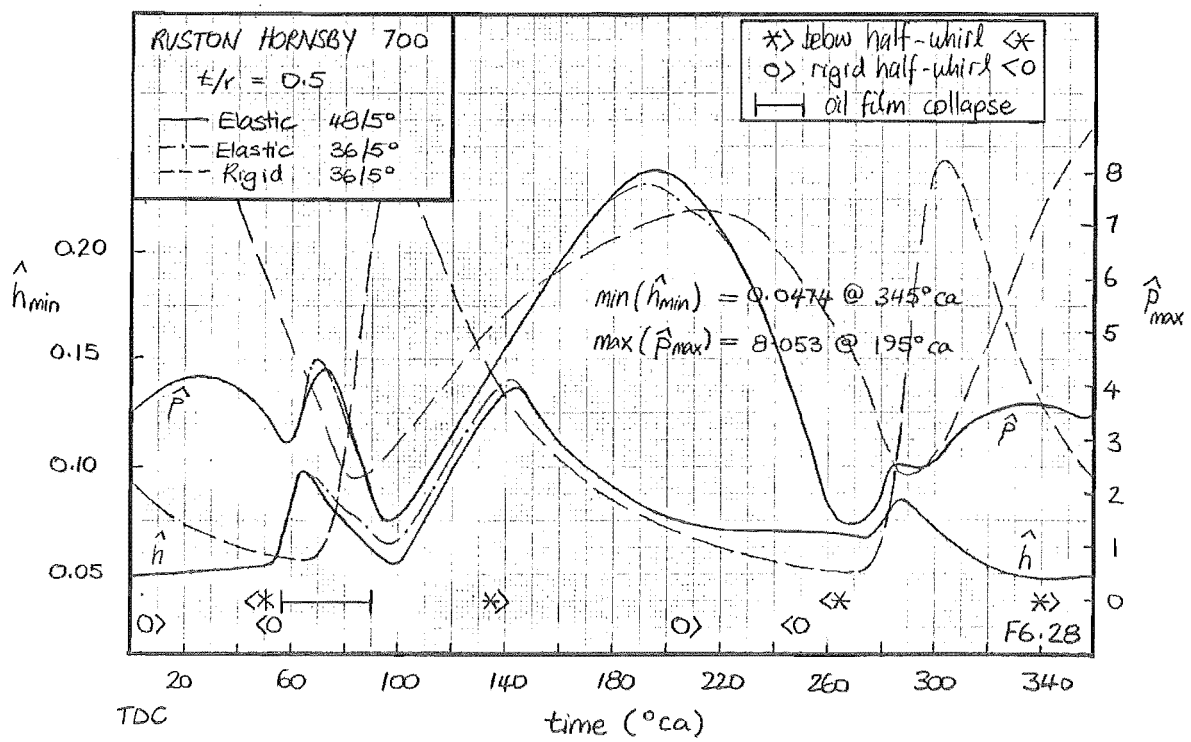
RUSTON HORNSBY 700
t/r = 0.5
Elastic 48/5°
Elastic 36/5°
Rigid 36/5°
> below half-whirl <
O> rigid half-whirl <O
oil film collapse
min(ĥmin) = 0.0474 @ 345°ca
max(p̂max) = 8.053 @ 195°ca
ĥmin
p̂max
p̂
ĥ
0.20
0.15
0.10
0.05
8
7
6
5
4
3
2
1
0
O>
<*
*>
<O
O>
<O
<*
*>
F6.28
20
60
100
140
180
220
260
300
340
TDC
time (°ca)

Clearly the picture presented by these elastic results is complex, however amidst this complexity two invariant features can be identified; distorted elastic form and dominant film action.

Distorted Elastic Form : Pressure distorsion, body-force distorsion and the resulting total distorsion have, at all speeds, very similar forms. (See Appendix A7). Moreover, two separate periods of influence can be identified : from 70^0ca through to 290^0ca, distorsion is dominated by body-forces; the remaining period is dominated by pressure distorsion (F6.29).

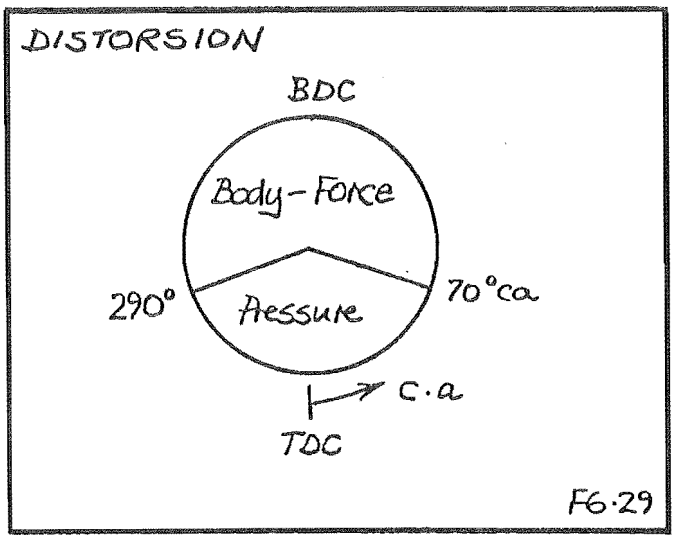

This behaviour is not entirely unexpected. The consistency enforced between external load and body-force (Section 2.2.2) automatically maintains a balance between integrated film pressure and body-force loadings. The corresponding deflections are consequently balanced throughout the speed range.

Dominant Film Action : To a surprising extent, dominant film action is also largely invariant with engine speed : F6.30 shows the various periods of wedge $\hat{w}$ and squeeze $\hat{s}$ and their respective transition angles.

Within each period, dominant film action is determined by the ratio of journal to elastic action; one would expect elastic action to be closely aligned with the distorted forms of F6.29 : the actual breakdown is given in F6.31, F6.32.

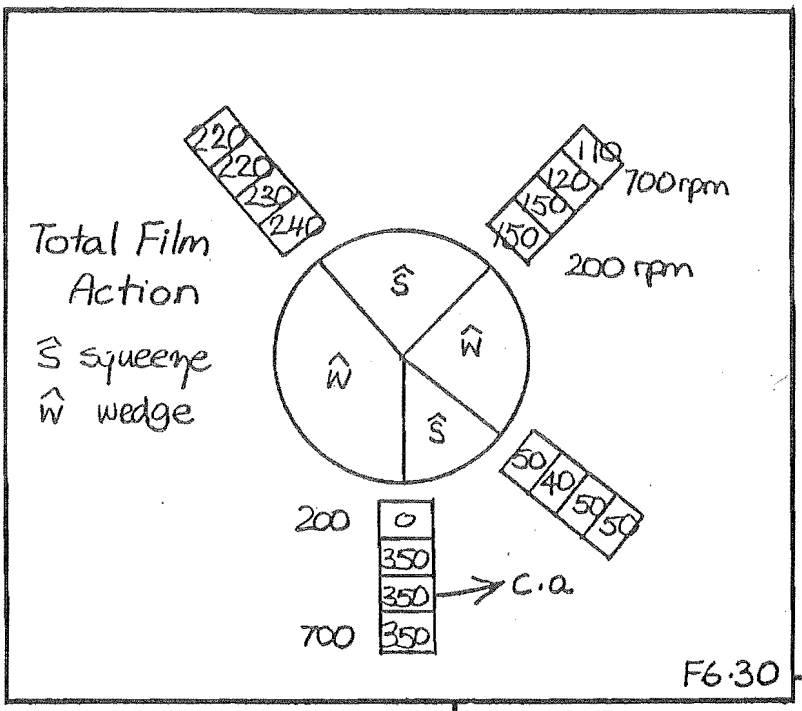

F6·30

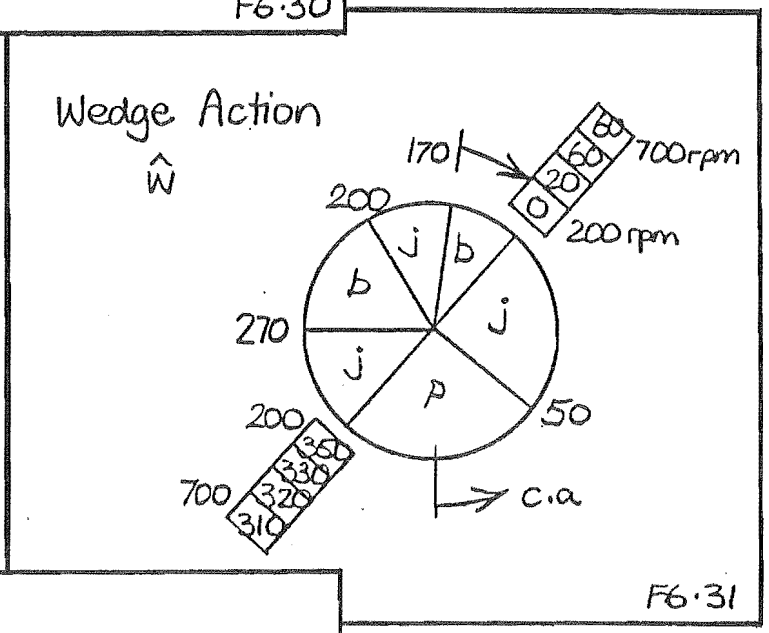

F6·31

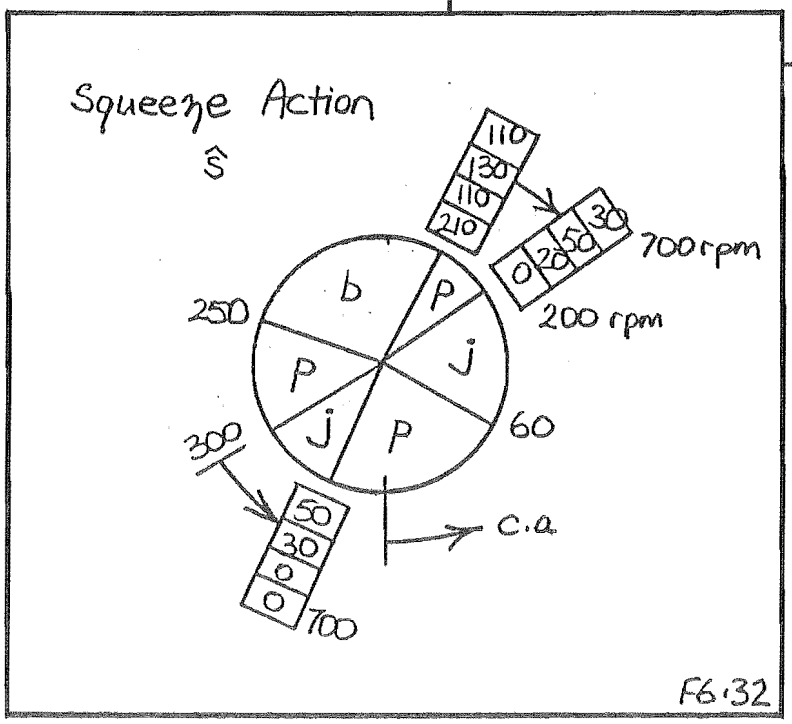

F6·32

In contrast to total film action, wedge and squeeze components show considerable variation in transition points. It is the variation of transition points at this level which determines the speed dependent performance shifts; interpretation of the 600 rpm result of Section 6.1.3a was from these figures. We forgo a full description of the remaining speeds; they are either simple extensions or subsets of the 600 rpm solution, focusing instead on discretisation.

(c) Discretisation :

Mesh dependence featured strongly in our discussion of dynamic rigid bearings. However, this proved to be much less of a problem in the elastic bearings.

The lumpiness associated with rigid peak pressures was not seen in the curved-beam bearing : lower pressure gradients in the elastic problem are less demanding of the pressure trial functions. Temporal mesh variation was found to have negligible effect on locus shape and velocity (F6.15), as well as on film-thickness and pressure.

Experience from the elastic steady state problem suggested that plausible, yet erroneous solutions may be generated through an inadequate discretisation. Fortunately, this concern was unfounded in the dynamic problem : F6.10 presented a 600 rpm verification on a considerably finer mesh(48 versus 36 elements), locus differences being so small as to not warrant plotting. Peak pressures during neck traversal are the only results to be outwardly affected; finer mesh provides a better resolution of displacements about the neck discontinuity.

Neck effects are again seen at 700 rpm (F6.28). However, the interaction of mesh and the 60^0ca film collapse is of greater concern; changes in film-thickness can be seen to propagate forward in time. This interaction indicates a need for a more sophisticated cavitation model, particularly under conditions of significant film fragmentation. However, despite this carry-over,

performance measures remain unaffected : journal locus remains unchanged; $\min(\hat{h}_{min})$ is sufficiently distant to be unaffected; $\max(\hat{p}_{max})$ is altered only by the previously discussed neck effects.

Overall, the sensitivity to discretisation observed in the steady-state bearing was not present to anywhere near the same extent in the dynamic elastic model, at least not in the Ruston-Hornsby bearing.

6.1.4 *Elastic Housing Solutions*

To complete this section on inertial loadings, we briefly investigate housing solutions using the Hermite elastic element of Section 4.2.2. Detailed comparisons with previous rigid and curved-beam solutions are delayed until the gas loaded sections of this Chapter.

However to begin, we look at a verification of the Hermite element using the previous ring geometry.

(a) **Hermite Ring Solution :**

Performance of a 400 rpm Hermite ring is presented in F6.33 and F6.34, comparison being drawn against the previous 400 rpm curved-beam ring. Both solutions use a 36 element circumferential mesh, two elements deep for the Hermite ring; temporal mesh is nominally 5^0ca.

The main differences are confined to peak pressure behaviour about BDC : boundary conditions at the neck restraint (Section 4.2.2d) are sufficiently different for some discrepancy to arise. Otherwise the cycles are reassuringly similar; this could not be said of the housing solutions.

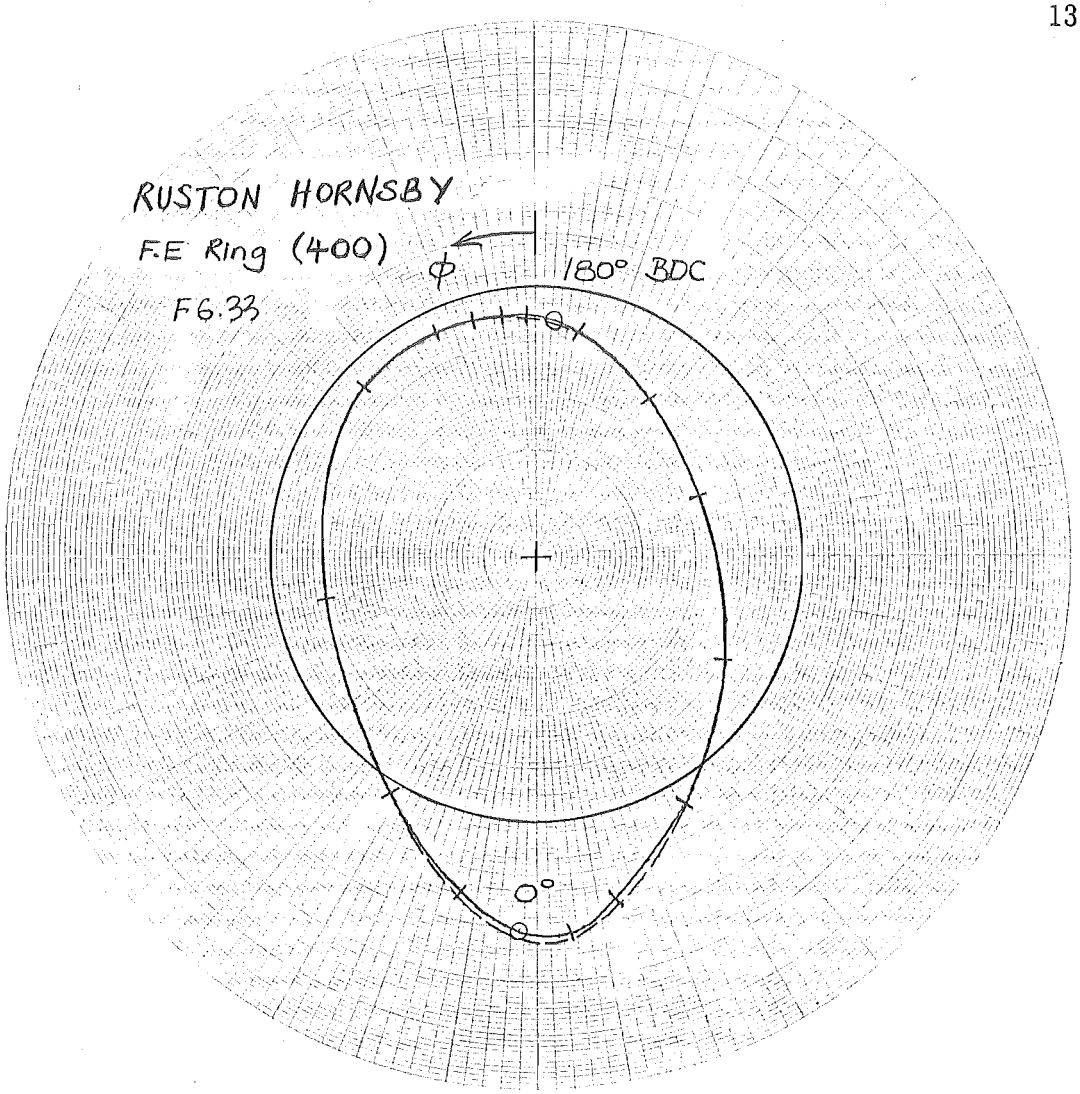
RUSTON HORNSBY
F.E Ring (400)
F6.33
φ
180° BDC
0°

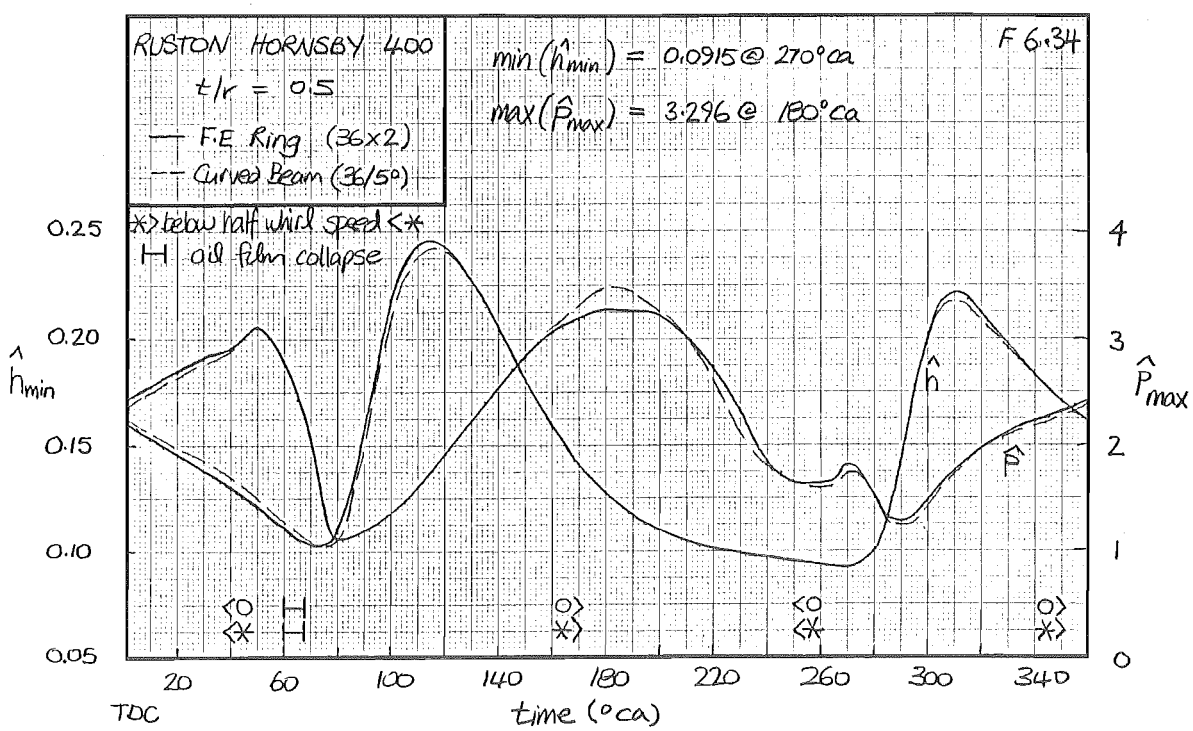
RUSTON HORNSBY 400
t/r = 0.5
— F.E Ring (36x2)
-- Curved Beam (36/5°)
min (ĥmin) = 0.0915 @ 270°ca
max (P̂max) = 3.296 @ 180°ca
F 6.34
> below half whirl speed <
H oil film collapse
ĥmin
P̂max
ĥ
P̂
0.25
0.20
0.15
0.10
0.05
4
3
2
1
0
20
60
100
140
180
220
260
300
340
TDC
time (°ca)

(b) **Hermite Housing Solution :**

A full dynamic housing solution is presented in figures F6.35-F6.38, geometry being that described in Section 4.2.2 (90 elements, t/r = 0.5). Here a 36 element spatial mesh and 5^0ca nominal time step are in force.

The stiffening effect of the neck is immediately apparent through reduced locus distorsion about TDC; less conspicuous is the shorter 60^0ca film collapse due to weaker journal action, subsequent film conditions developing earlier as a consequence.

Removal of the discontinuous neck constraint can be seen to have several beneficial side effects : elastic squeeze action in the neck region is increased, reducing peak pressures and thickening the oil-film about BDC; the fragmented wedge action and associated film collapse of 270^0ca disappear.

Probably the most striking change is the noticeably thicker oil-film around TDC : journal wedge action, the major contributor through $280\text{-}300^0$ca, undergoes destructive pressure squeeze action during this period; this action is less destructive in the case of the stiffer housing. Subsequent periods benefit significantly from this initial thickening and through the continuing influence of the stiffer geometry; film performance through these angles would seem to be as sensitive to elastic geometry as it was to the load (speed) variations of Section 6.1.3(b).

Overall, major shifts in our ring performance measures have not occurred; $\min(\hat{h}_{min})$ is slightly thinner but still positioned at around 270^0ca; $\max(\hat{p}_{max})$ is at BDC although reduced 30% in magnitude compared to the ring solution. Ring solutions could thus be concluded as giving good $\min(\hat{h}_{min})$ measurements of the housing condition, but only a qualitative assessment of housing peak pressures.

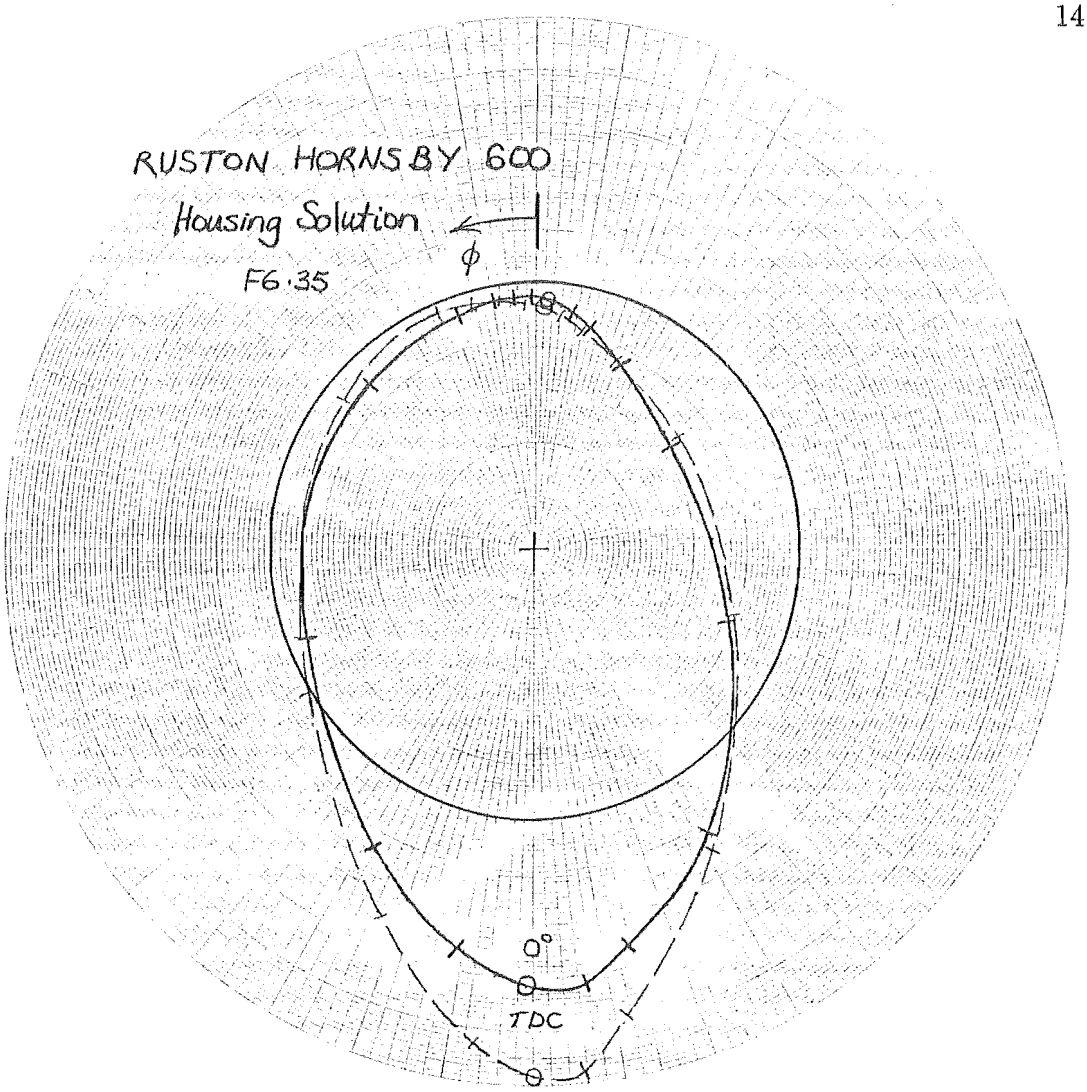
RUSTON HORNSBY 600
Housing Solution
F6.35
φ
0°
TDC

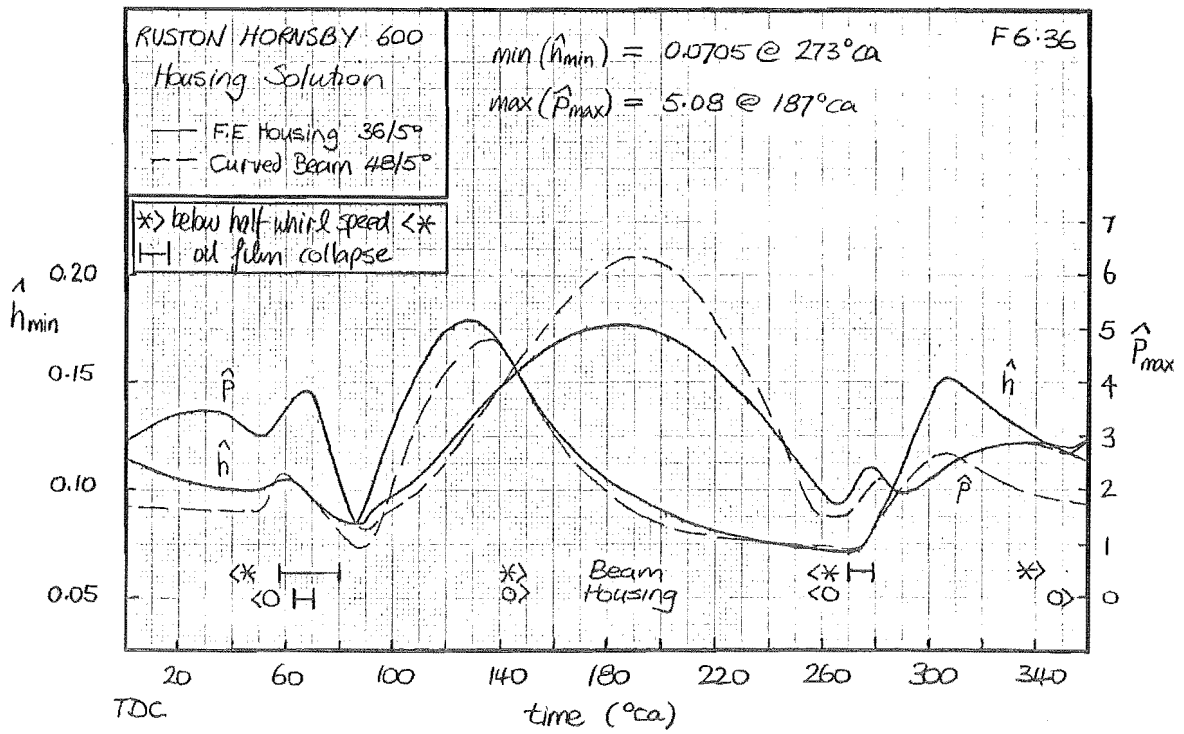
RUSTON HORNSBY 600
Housing Solution
F.E Housing 36/5°
Curved Beam 48/5°
<* below half whirl speed *>
H oil film collapse
min (ĥmin) = 0.0705 @ 273°ca
max (P̂max) = 5.08 @ 187°ca
F6.36
ĥmin
P̂max
0.20
0.15
0.10
0.05
7
6
5
4
3
2
1
0
P̂
ĥ
Beam
Housing
20
60
100
140
180
220
260
300
340
TDC
time (°ca)

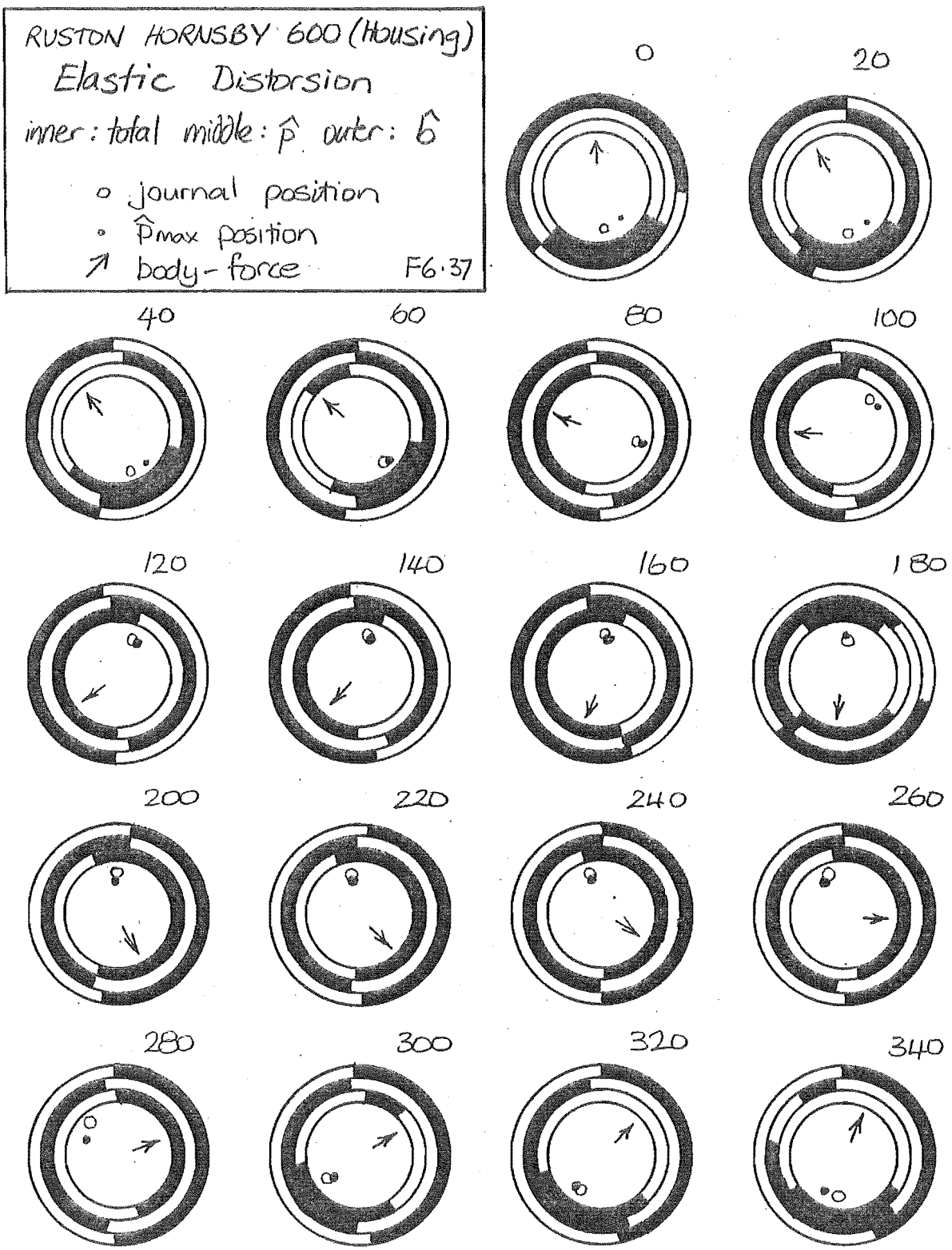
RUSTON HORNSBY 600 (Housing)
Elastic Distorsion
inner: total middle: p̂ outer: b̂
o journal position
• p̂max position
↗ body-force
F6.37
0
20
40
60
80
100
120
140
160
180
200
220
240
260
280
300
320
340

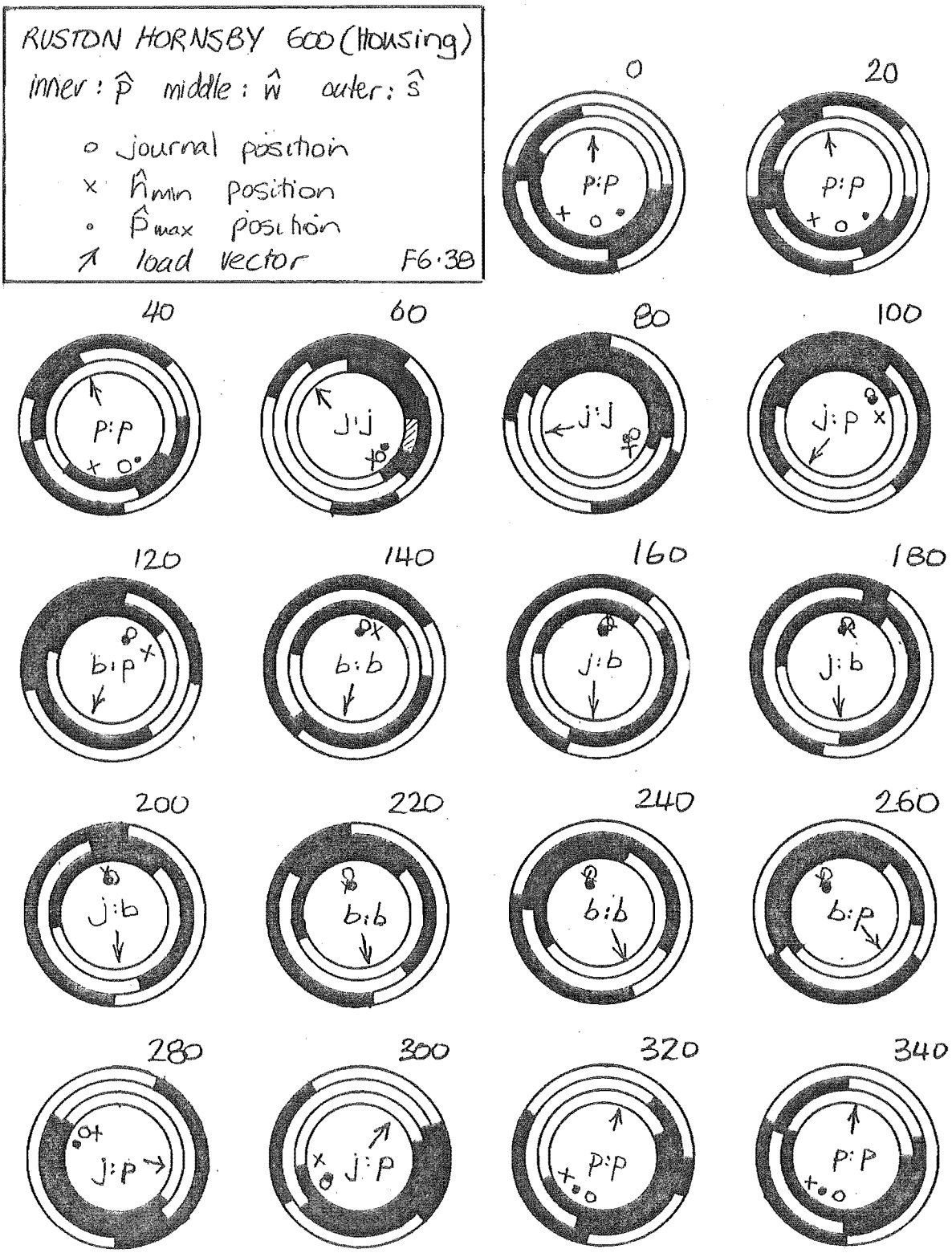
RUSTON HORNSBY 600 (Housing)
inner : $\hat{p}$ middle : $\hat{w}$ outer : $\hat{s}$
o journal position
× $\hat{h}_{min}$ position
• $\hat{p}_{max}$ position
↗ load vector
F6·38
0
20
40
60
80
100
120
140
160
180
200
220
240
260
280
300
320
340
P:P
J:J
J:P
b:P
b:b
J:b

(c) Speed Dependent Performance :

Neither of the Hermite solutions deviate significantly in film-thickness performance from the 600 rpm curved beam solution, nor over the remaining speed range (F6.39). Moreover, the discrepancy in load convergence limit observed in the various steady-state models is not as marked in the dynamic elastic solutions : curved beam solutions converge to 700 rpm; housing solutions to 600 rpm; Hermite ring solutions to 500 rpm.

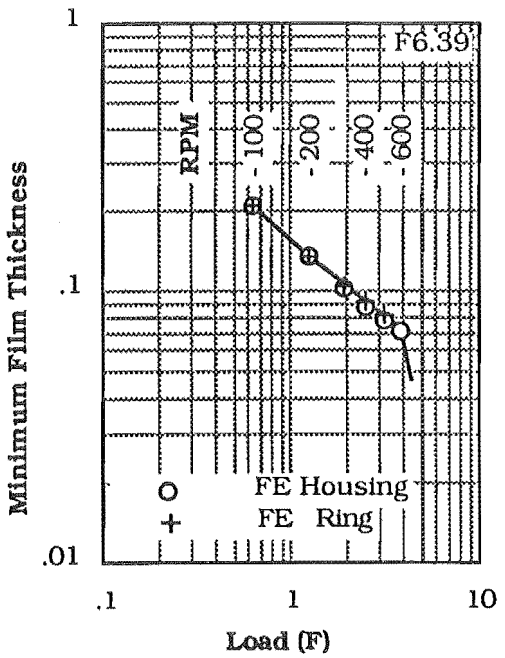

Once again this reflects the reduced sensitivity of the dynamic Ruston-Hornsby problem, in this case towards the linearly interpolated Hermite element (c.f. Section 5.3.2(c)).

The associated solution breakdowns occur at around 340^0ca ($\min(\hat{h}_{min})$) in the curved-beam model and at 70^0ca in the Hermite solution. The specific mechanisms of these failures currently remain undetermined; symptoms are typically a total reluctance of the solution scheme to step forward in time.

We next look at how the various Ruston-Hornsby models fare under gas loading.

6.2 Gas Load : Ruston-Hornsby

In the sections that follow, performance of the gas loaded rigid, ring and housing models are investigated. This work culminates with a comparison between these theoretical solutions and actual experimental measurements.

However, before proceeding, we take a brief look at the load diagram itself.

6.2.1 *Load Diagram*

The gas loaded R-H diagram[6] takes the form of F6.40. Here the inertial portion differs from the lumped-mass inertia diagram (F6.1) through the engine being supercharged : inertial load at TDC is decreased (5%); at BDC it is increased (6%). Peak gas load is approximately 1.5 times the maximum inertial load, its application beginning at about 300^{0}ca, maximum load being reached 70^{0}ca later.

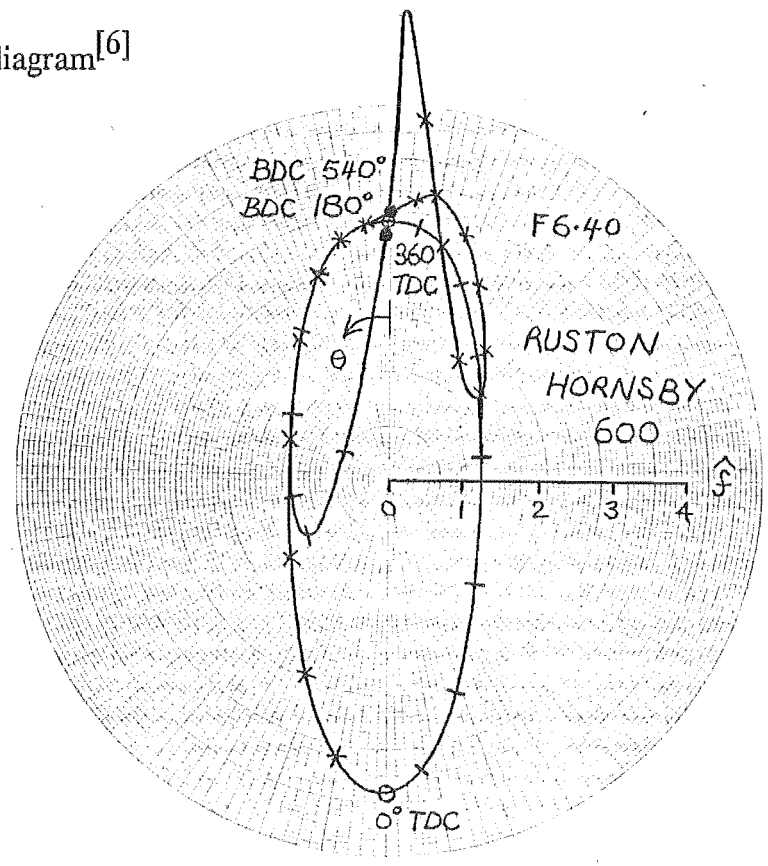

6.2.2 *Rigid Bearing Solutions*

The results for the gas loaded rigid bearing are presented in F6.41, F6.42. These are developed on a 36 element spatial mesh using a 5^{0}ca time step.

Maximum pressure behaviour is again lumpy through the high whirl

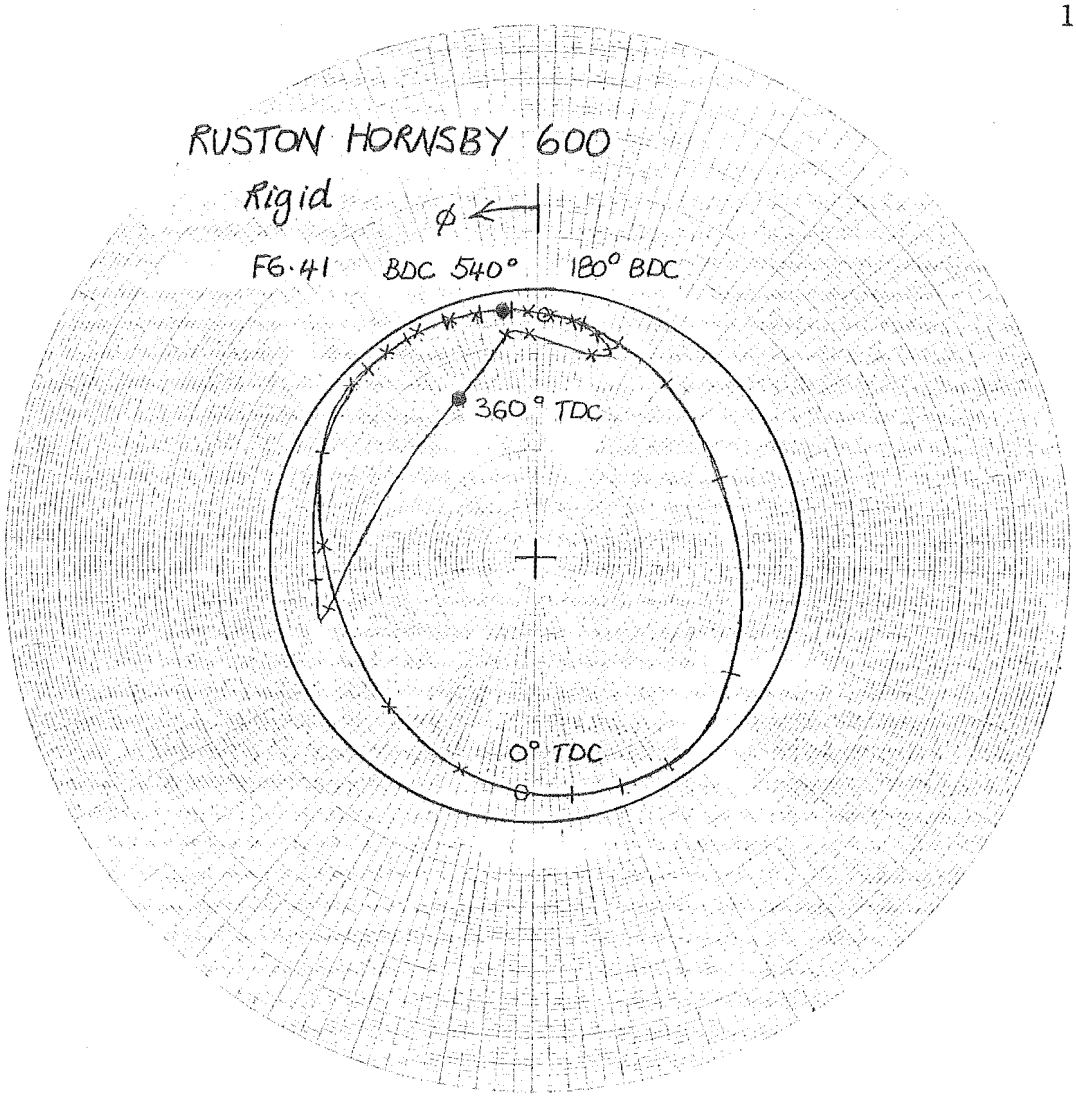
RUSTON HORNSBY 600
Rigid
φ
F6·41
BDC 540°
180° BDC
360° TDC
0° TDC

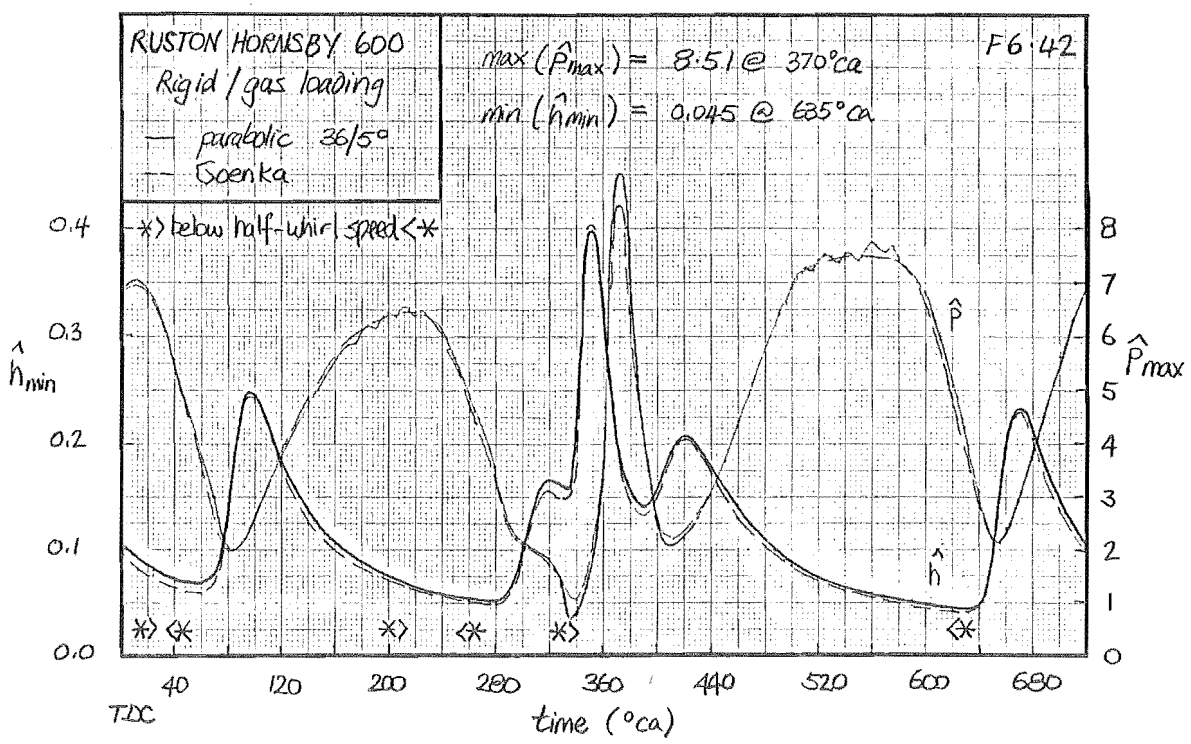
RUSTON HORNSBY 600
Rigid / gas loading
— parabolic 36/5°
-- Goenka
max (P̂max) = 8·51 @ 370°ca
min (ĥmin) = 0.045 @ 635°ca
F6·42
> below half-whirl speed <
0.4
0.3
0.2
0.1
0.0
ĥmin
8
7
6
5
4
3
2
1
0
P̂max
P̂
ĥ
40
120
200
280
360
440
520
600
680
TDC
time (°ca)

regions, mesh homogeneity problems resurfacing. Despite this, minimum film thickness behaviour is smooth, $\min(\hat{h}_{min})$ occurring in the inertial portion of the cycle close to one of the six half-whirl speed conditions.

Also shown in F6.42 is the finite length solution of Goenka[98], extracted from a review paper of Martin[23]: the parabolic axial pressure model generates slightly thicker films, Goenka obtaining :

$$\min(\hat{h}_{min}) = 0.042 \; ; \; \max(\hat{p}_{max}) = 8.46$$

Maximum film pressures are also pleasingly close throughout the cycle. It would seem that the combination of centre circumferential oil-groove and short geometry (L/D = 0.28125) are particularly well served by the parabolic pressure model.

Of greater interest however, are the elastic solutions.

6.2.3 *Elastic Bearing Solutions*

Two elastic gas loaded solutions were investigated in this work; a 360^0 curved-beam solution and an Hermite housing solution. We look firstly at the beam solution.

(a) Curved-Beam Solution :

The 360^0 beam solution is presented in F6.43, F6.44 on a 36 element spatial mesh and nominally 5^0ca time step. It is useful to divide this solution into inertial and gas loaded portions :

Inertial loading features through crank angles 560-280^0ca; half-whirl speeds, 60^0ca film collapse, peak pressure forms and locus are all largely unchanged from the previous inertial solution (F6.9, F6.10). Only film-thickness response around TDC is noticeably affected; a sensitivity to load through these crank angles was noted in the inertial solutions of Section 6.1.3(b). Positionally $\min(\hat{h}_{min})$ is

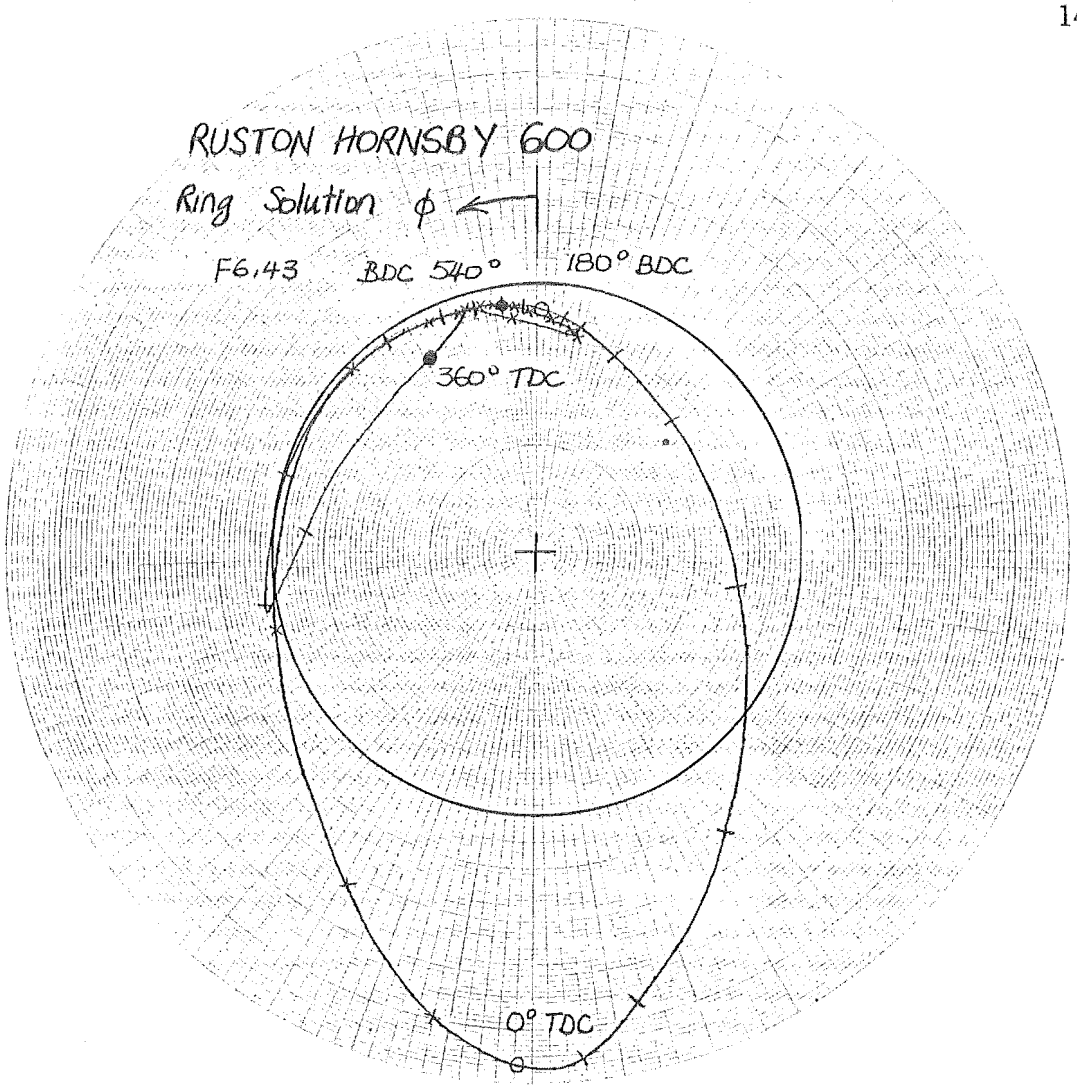
RUSTON HORNSBY 600
Ring Solution ϕ
F6.43
BDC 540°
180° BDC
360° TDC
0° TDC

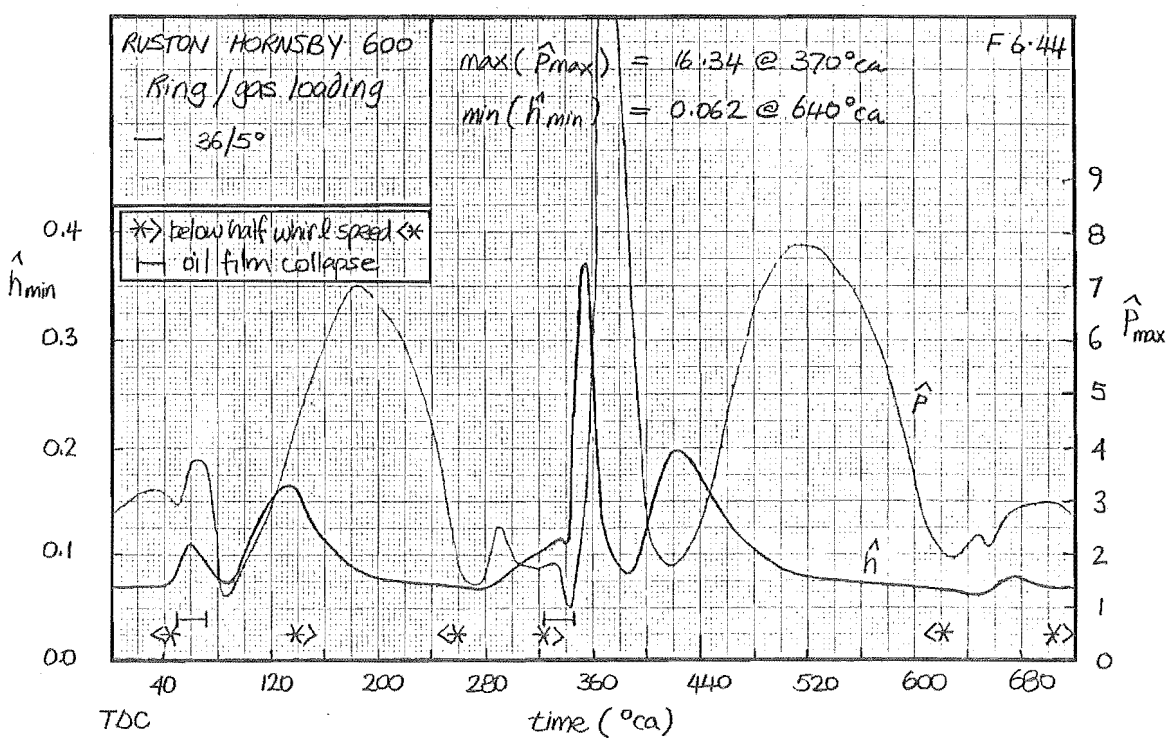
RUSTON HORNSBY 600
Ring / gas loading
36/5°
max(P̂max) = 16.34 @ 370°ca
min(ĥmin) = 0.062 @ 640°ca
F 6·44
below half whirl speed
oil film collapse
ĥmin
P̂max
P̂
ĥ
0.0
0.1
0.2
0.3
0.4
0
1
2
3
4
5
6
7
8
9
40
120
200
280
360
440
520
600
680
TDC
time (°ca)

unaffected at 630^{0}ca (270^{0}ca in F6.10) although reduced 14% in magnitude over the inertial solution; previous gas loaded film history is mainly responsible here, significant gas forces still being present at 540^{0}ca.

During the remaining gas portion of the cycle, peak pressure and minimum film thickness forms are very similar to the rigid solution : peak pressures rise markedly above those of the rigid model in response to the elastic discontinuity of the neck restraint. However, the most interesting difference is the appearance of an additional film collapse.

Gas Induced Film Collapse : At the point of gas locus reversal (320^{0}ca) an additional film collapse appears at a spatial angle of 90^{0}ba (See F6.47). Although of similar duration (18^{0}ca) and mechanism to the 60^{0}ca collapse, it is much stronger in magnitude; higher negative pressures are developed. It is not present in the rigid bearing.

It would be easy to dismiss this and the earlier 60^{0}ca collapse as being inconsequential; the associated oil-film conditions are admittedly simplistic. However, the strong attendant journal action cannot be ignored, such mechanisms having been implicated in the cavitation erosion of dynamically loaded bearings[53]. Elastic analyses clearly offer useful additional insight into such cases. Unfortunately, much of the associated data is commercially sensitive and consequently unavailable in the open literature.

(b) Housing Solutions :

The Hermite housing solution is presented in F6.45 and F6.46, again using 36 spatial elements and a 5^{0}ca nominal time step length.

Performance shifts between ring and housing solutions mirror those observed in the inertially loaded bearing : increased elastic stiffness is reflected in locus and $\hat{h}_{min}$ behaviour around TDC; min($\hat{h}_{min}$) remains largely unaffected in

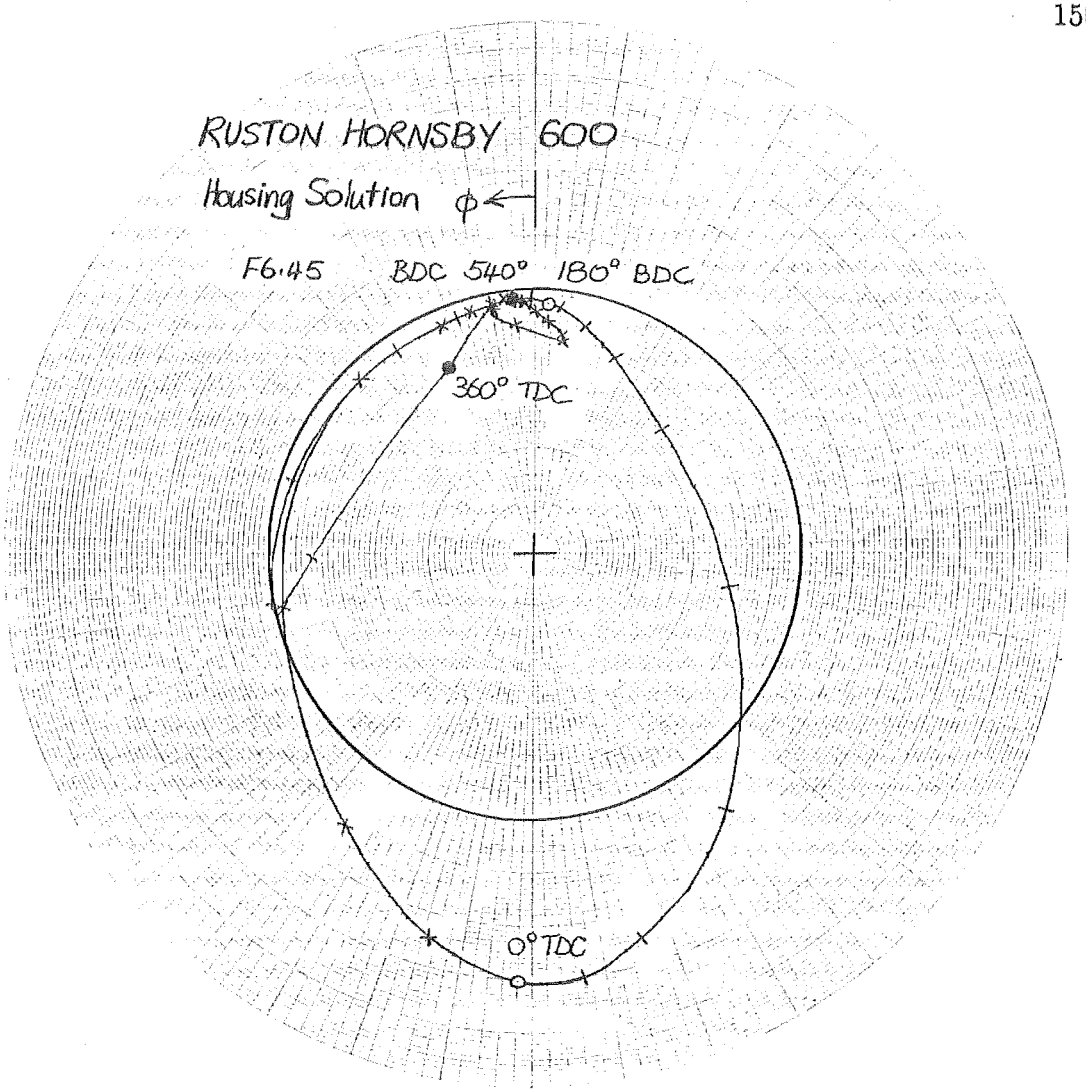
RUSTON HORNSBY 600
Housing Solution
F6.45
BDC 540° 180° BDC
360° TDC
0° TDC

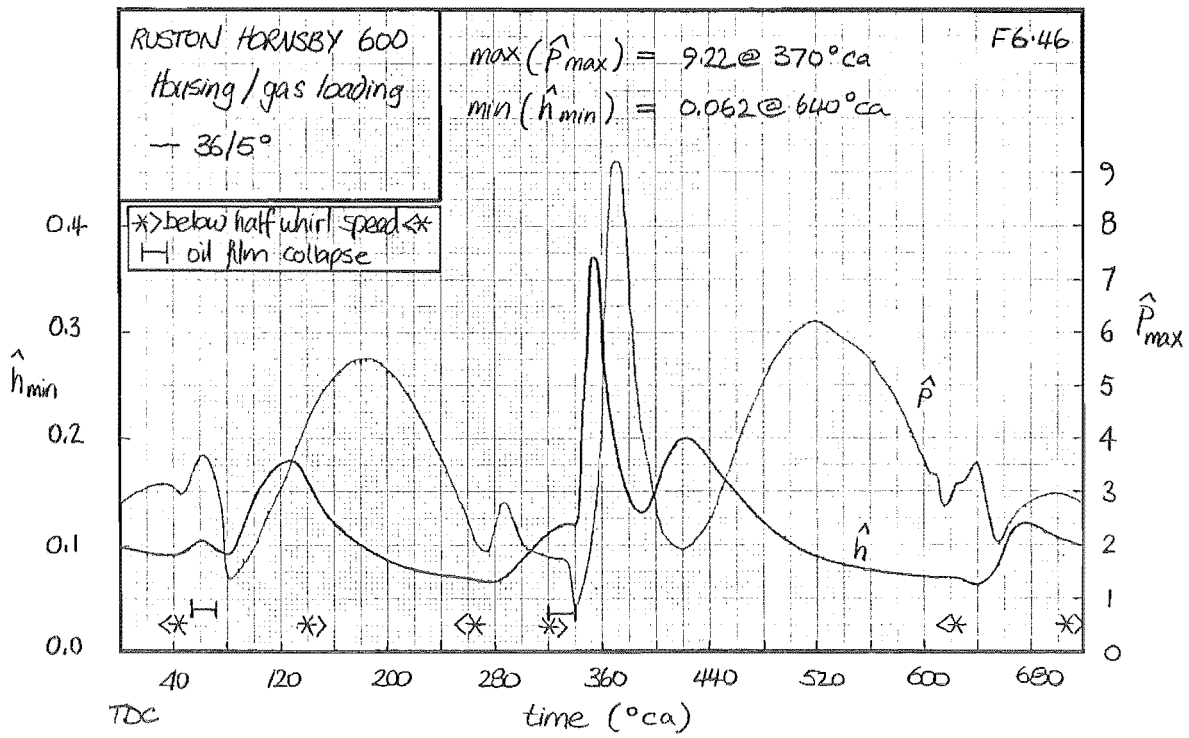
RUSTON HORNSBY 600
Housing / gas loading
— 36/5°
max (P̂max) = 9.22 @ 370° ca
min (ĥmin) = 0.062 @ 640° ca
F6.46
> below half whirl speed <
⊢ oil film collapse
ĥmin
P̂max
P̂
ĥ
0.4
0.3
0.2
0.1
0.0
9
8
7
6
5
4
3
2
1
0
40
120
200
280
360
440
520
600
680
TDC
time (°ca)

either magnitude or position; the 60°ca film collapse survives the geometry change as does the gas induced collapse at 320°ca.

Peak pressures during gas loading are reduced to rigid bearing level by the removal of the neck discontinuity; in fact the rigid model provides a good estimate of $\max(\hat{p}_{max})$. Other pressures formed in the neck region (180°ca, 520°ca) are similarly reduced.

A direct comparison of ring and housing solutions throughout the load cycle is provided in F6.47. Here film-thickness and pressure are presented every 30°ca. Development of pressure oscillations in the housing solution at 630°ca indicates that this model has about reached its convergence limit.

Overall, the closeness of ring and housing solutions at this detailed level, confirms the usefulness of the ring solution in assessing minimum film thickness and in particular that of $\min(\hat{h}_{min})$.

6.2.4 *Experimental Results*

Evidence from a variety of experimental bearings indicates appreciable elastic distorsion under dynamic loading[34,35,36]: observed back clearance† is greater than diametral clearance. This would seem to have intimidated theoretical workers from producing detailed comparisons with experimental results; it is not for lack of experimental material: Butcher[34] published *in situ* film-thickness measurements of the R-H bearing under dynamic load: Cooke[97] at NEL has studied the R-H bearing in a rigid bearing simulator.

(a) Cooke's Work :

Cooke's work involved the dynamic measurement of pressure, journal locus and oil-flows under varying geometry. Unfortunately, this was performed in a

---

† maximum film-thickness

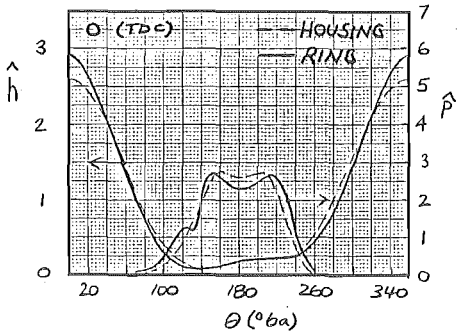
0 (TDC)
HOUSING
RING
ĥ
P̂
θ (°ba)

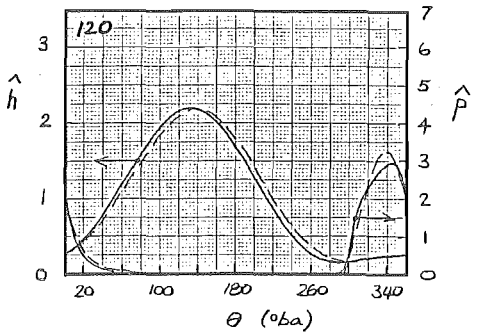
120
ĥ
P̂
θ (°ba)

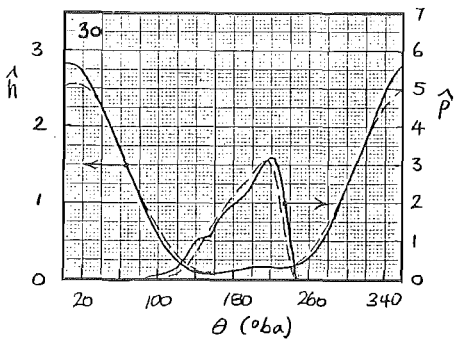
30
ĥ
P̂
θ (°ba)

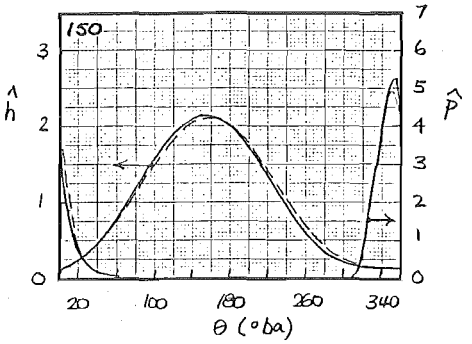
150
ĥ
P̂
θ (°ba)

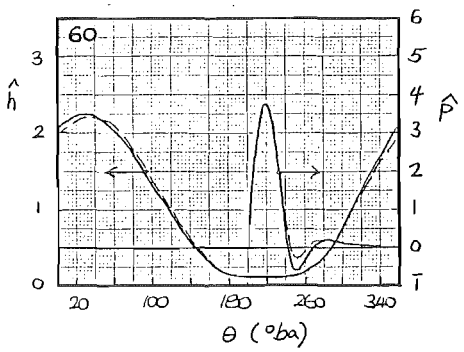
60
ĥ
P̂
θ (°ba)

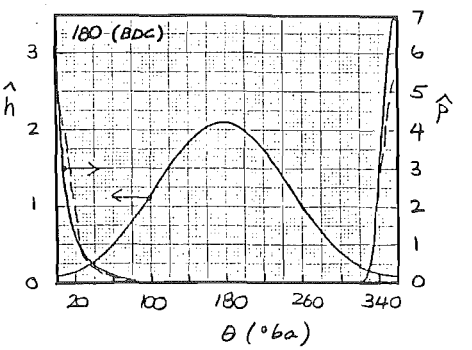
180 (BDC)
ĥ
P̂
θ (°ba)

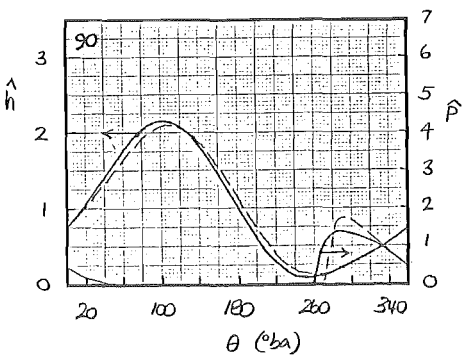
90
ĥ
P̂
θ (°ba)

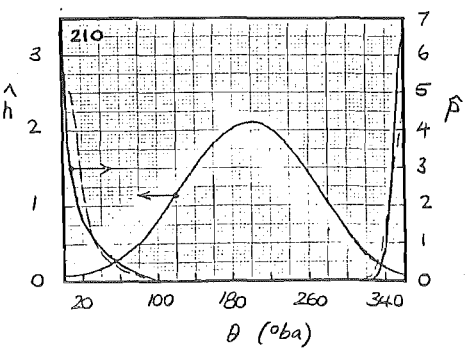
210
ĥ
P̂
θ (°ba)

F6.47

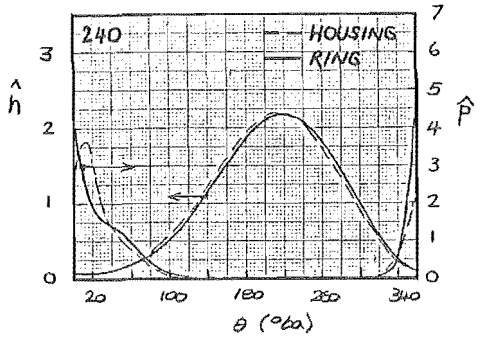
240
HOUSING
RING
ĥ
p̂
θ (°ba)

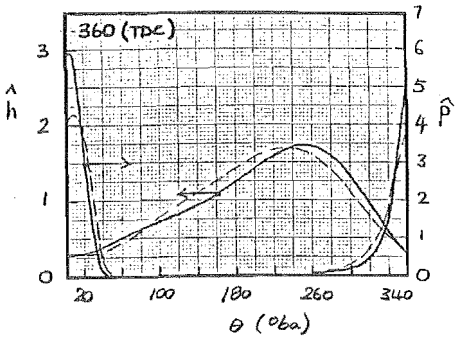
360 (TDC)
ĥ
p̂
θ (°ba)

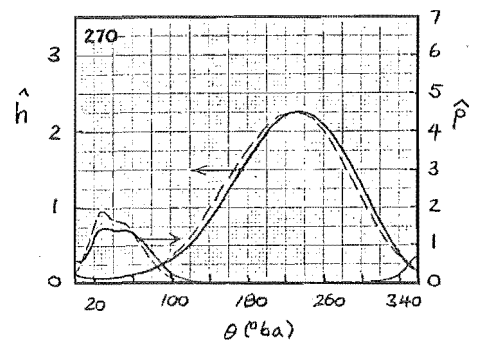
270
ĥ
p̂
θ (°ba)

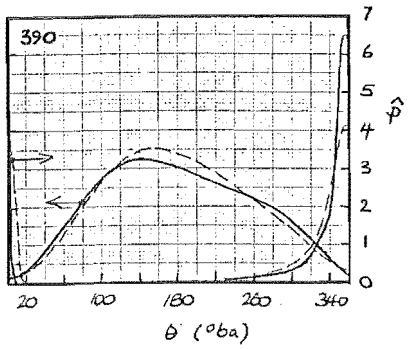
390
p̂
θ (°ba)

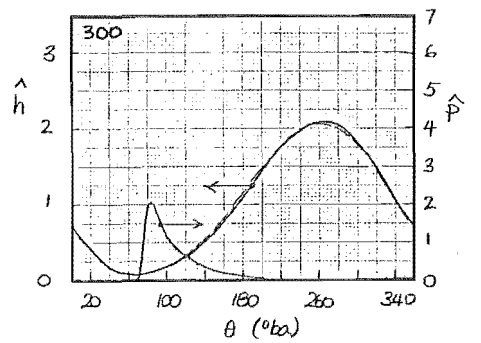
300
ĥ
p̂
θ (°ba)

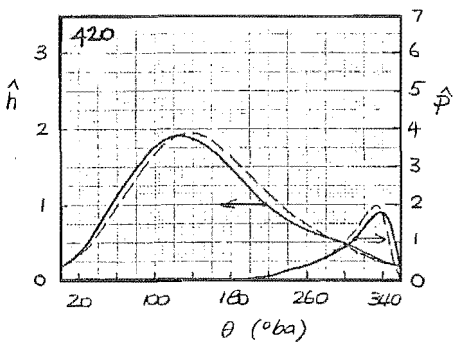
420
ĥ
p̂
θ (°ba)

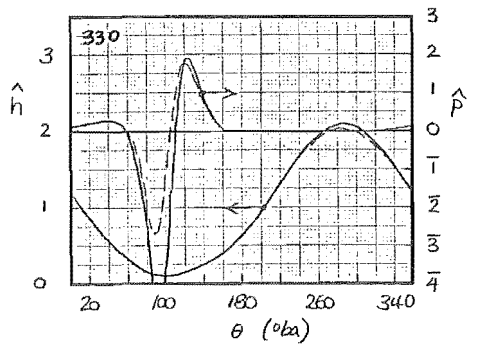
330
ĥ
p̂
θ (°ba)

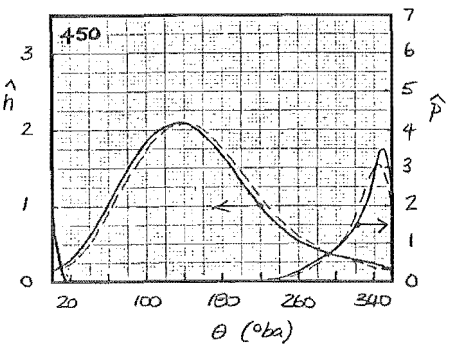
450
ĥ
p̂
θ (°ba)

F6.47 cont.

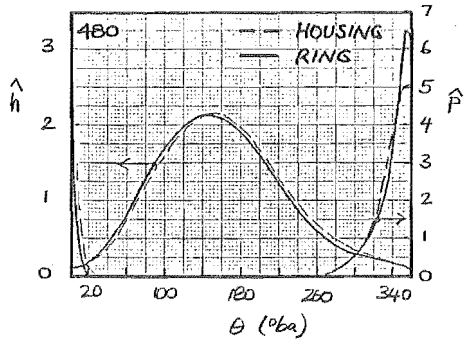
480
HOUSING
RING
$\hat{h}$
$\hat{p}$
θ (°ba)

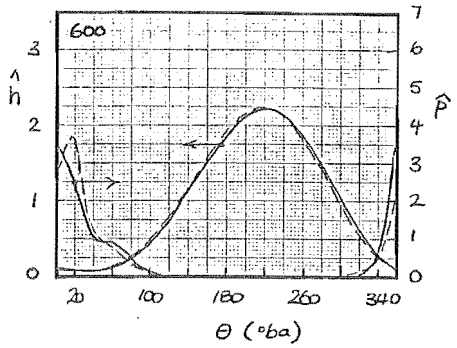
600
$\hat{h}$
$\hat{p}$
θ (°ba)

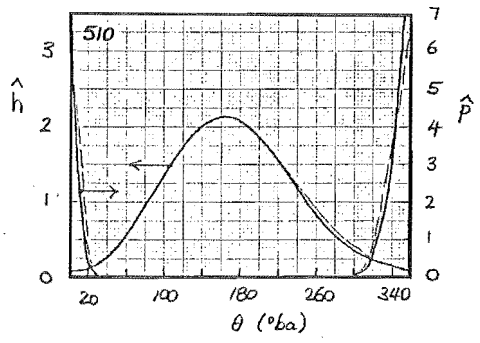
510
$\hat{h}$
$\hat{p}$
θ (°ba)

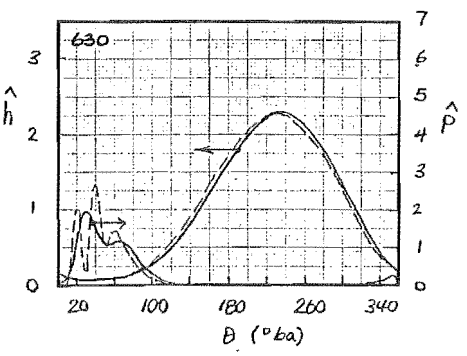
630
$\hat{h}$
$\hat{p}$
θ (°ba)

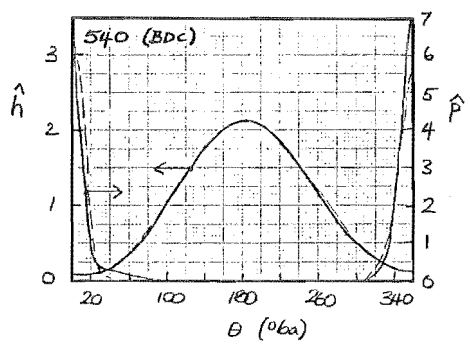
540 (BDC)
$\hat{h}$
$\hat{p}$
θ (°ba)

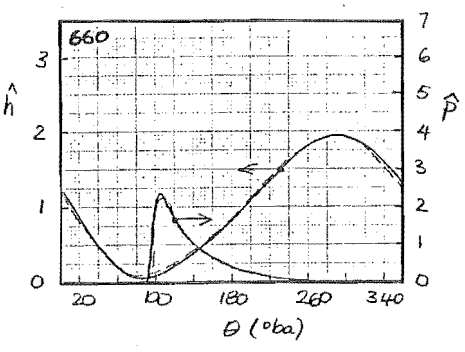
660
$\hat{h}$
$\hat{p}$
θ (°ba)

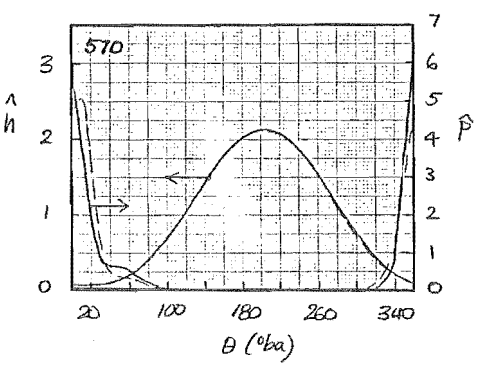
570
$\hat{h}$
$\hat{p}$
θ (°ba)

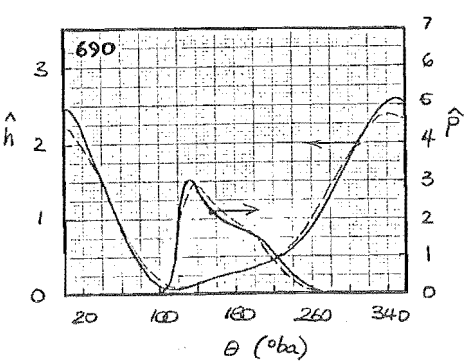
690
$\hat{h}$
$\hat{p}$
θ (°ba)

F6.47 cont.

'massive' test housing and consequently has little relevance to the current elastic con-rod problem; the quality of these results do however beg theoretical investigation by future workers.

(b) Butcher's Work :

Butcher's *in situ* film-thickness measurements are however particularly valuable : dynamic film-thickness was measured with capacitance probes at six spatial points (51^0, 111^0, 171^0, 231^0, 291, 351^0ba), the probes positioned in the centre circumferential groove of the R-H rod.

Butcher expresses certain reservations about the work, in particular the probes, situated in the bearing shell, are unsupported by the oil-groove. Several further reservations should also be expressed : journal and housing ovality were unmeasured; gas load unmonitored. Moreover, there are synchronisation effects in the results : probe measurements were not performed simultaneously; at any given crank angle, the various probe measurements are from different load cycles. Gas load variability thus enters into these measurements.

Bearing these points in mind, the results of the rigid solution, Hermite housing solution and Butcher's experimental work are gathered together in F6.48 : Circumferential variations in film-thickness and pressure are shown every 30^0ca for the full gas cycle. An absolute accuracy of ± 0.03 $\hat{\text{h}}$ (± 0.0001") is claimed for the capacitive probes, however the 360^0ca result would indicate that repeatability is only of the order of 0.15 $\hat{\text{h}}$.

For crank angles 570-90^0ca, the period of journal traversal through the cap, elastic models show a marked improvement in film-thickness prediction over the rigid model. This improvement is exemplified by the TDC result; here back clearance corresponds closely with measured clearance, wrap-around also shows good correlation.

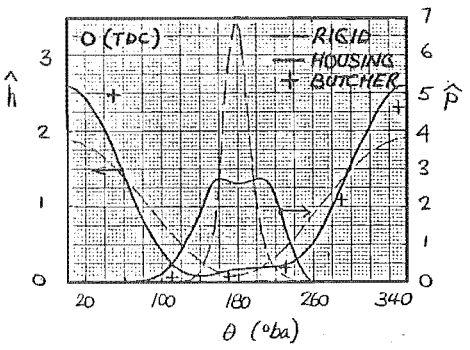
0 (TDC)
RIGID
HOUSING
BUTCHER
ĥ
p̂
θ (°ba)

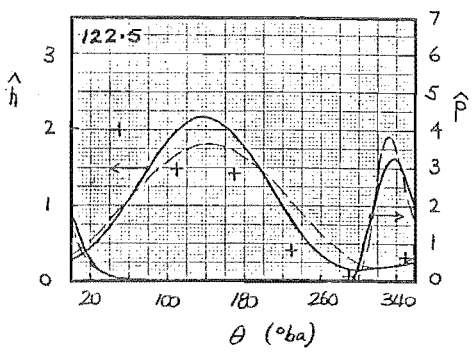
122·5
ĥ
p̂
θ (°ba)

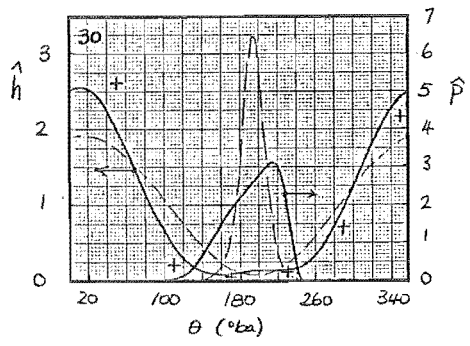
30
ĥ
p̂
θ (°ba)

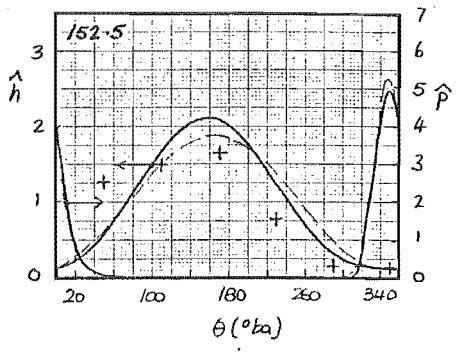
152·5
ĥ
p̂
θ (°ba)

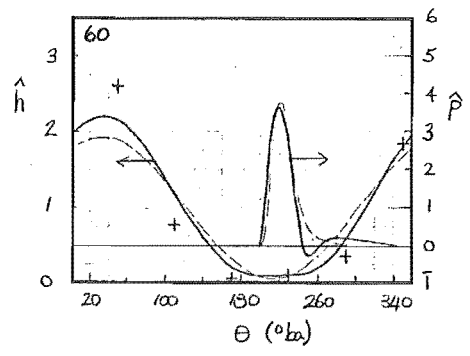
60
ĥ
p̂
θ (°ba)

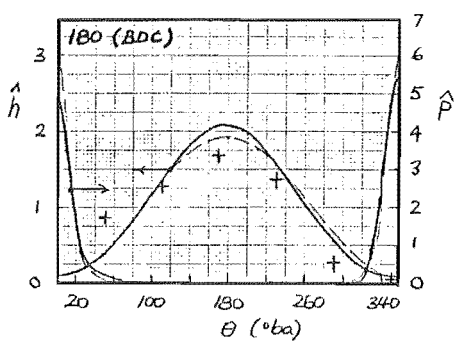
180 (BDC)
ĥ
p̂
θ (°ba)

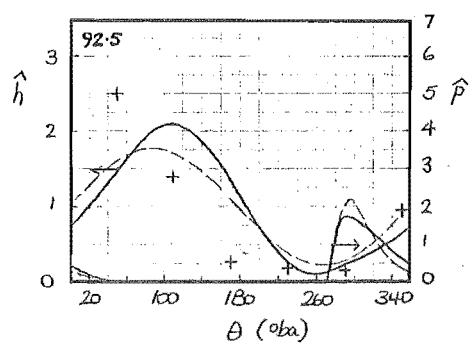
92·5
ĥ
p̂
θ (°ba)

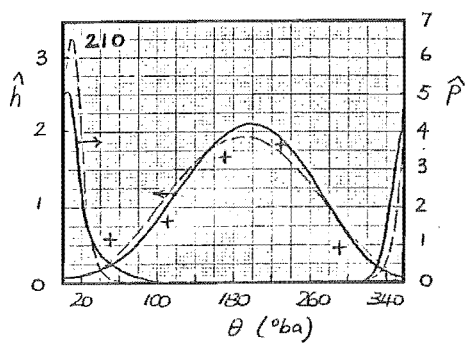
210
ĥ
p̂
θ (°ba)

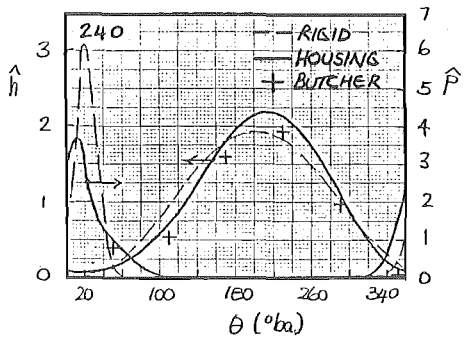
240
RIGID
HOUSING
BUTCHER
$\hat{h}$
$\hat{P}$
θ (°ba)

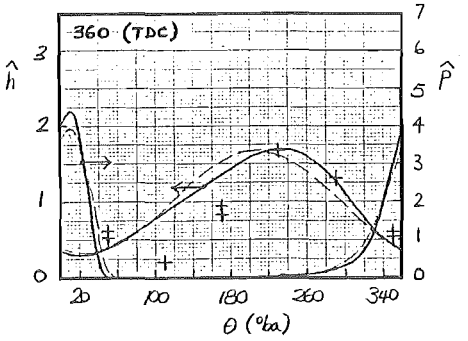
360 (TDC)
$\hat{h}$
$\hat{P}$
θ (°ba)

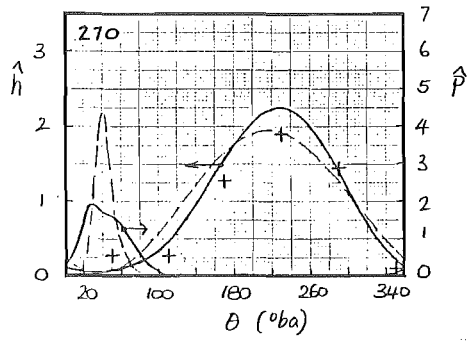
270
$\hat{h}$
$\hat{P}$
θ (°ba)

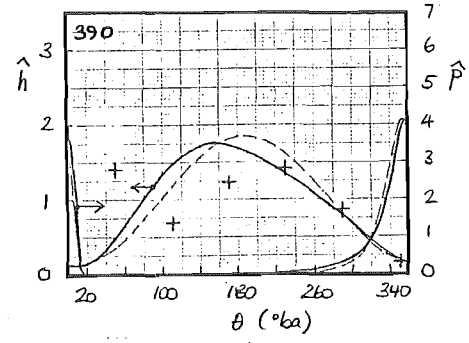
390
$\hat{h}$
$\hat{P}$
θ (°ba)

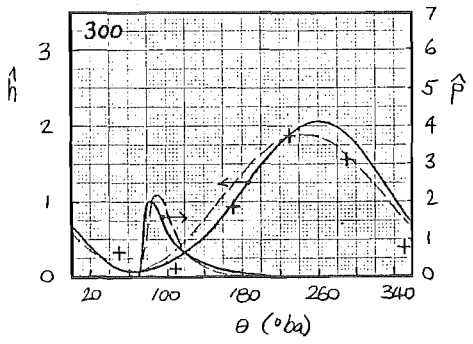
300
$\hat{h}$
$\hat{P}$
θ (°ba)

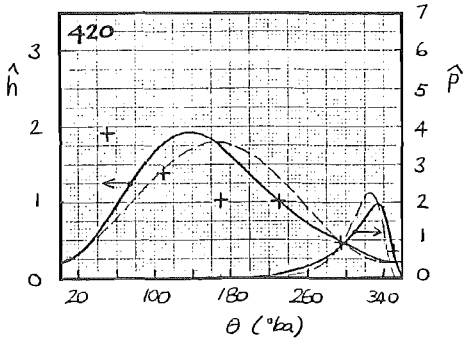
420
$\hat{h}$
$\hat{P}$
θ (°ba)

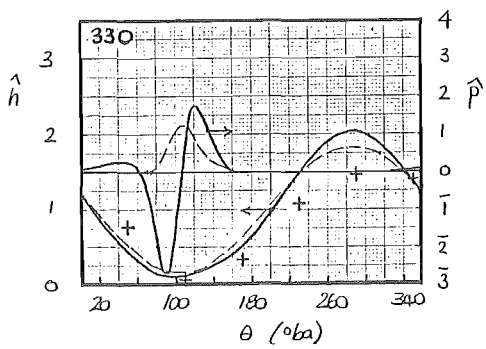
330
$\hat{h}$
$\hat{P}$
θ (°ba)

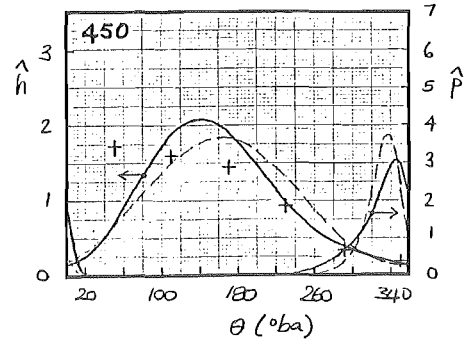
450
$\hat{h}$
$\hat{P}$
θ (°ba)

F6.48 cont.

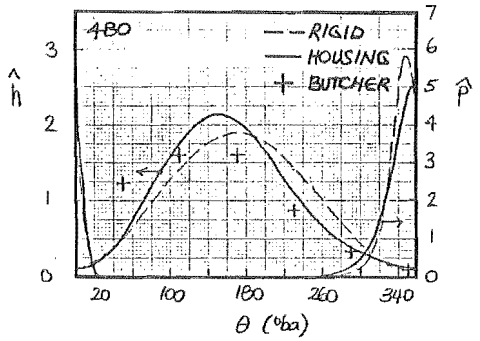
480
RIGID
HOUSING
BUTCHER
$\hat{h}$
$\hat{P}$
θ (°ba)

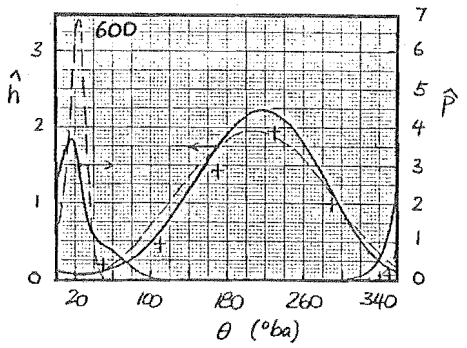
600
$\hat{h}$
$\hat{P}$
θ (°ba)

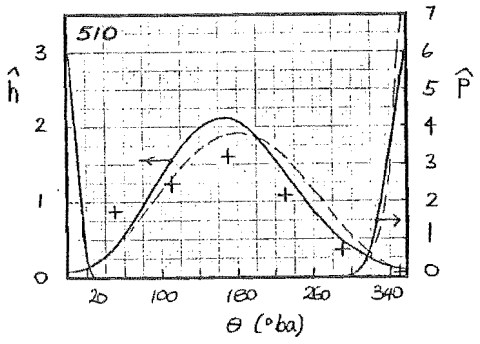
510
$\hat{h}$
$\hat{P}$
θ (°ba)

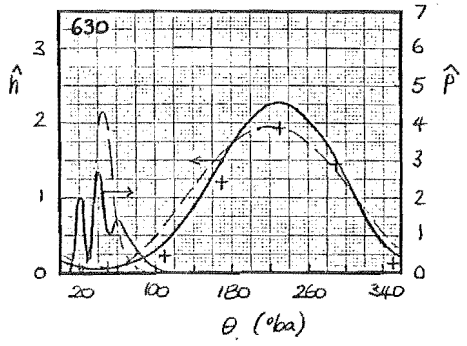
630
$\hat{h}$
$\hat{P}$
θ (°ba)

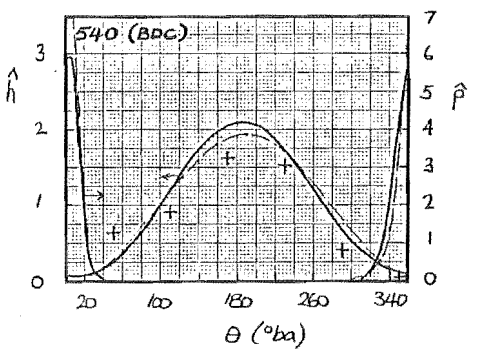
540 (BDC)
$\hat{h}$
$\hat{P}$
θ (°ba)

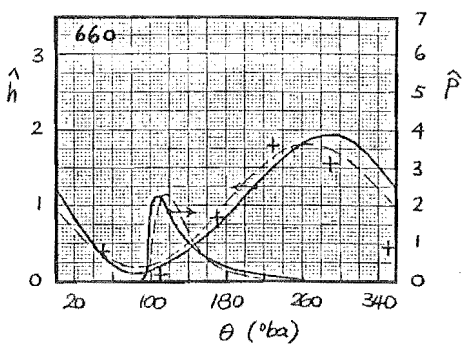
660
$\hat{h}$
$\hat{P}$
θ (°ba)

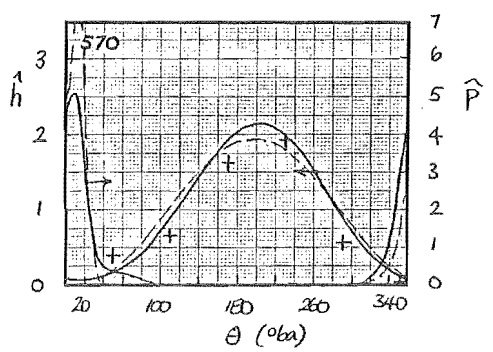
570
$\hat{h}$
$\hat{P}$
θ (°ba)

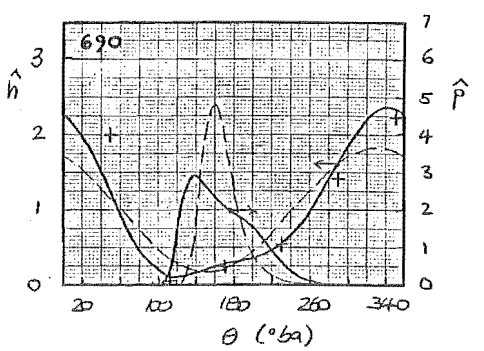
690
$\hat{h}$
$\hat{P}$
θ (°ba)

F6.48 cont.

From 90^{0}ca through to 160^{0}ca poor correspondence of both rigid and elastic solutions is evident. However, from 180^{0}ca through to 330^{0}ca, elastic film-thickness again shows good correlation, better than the rigid counterpart.

Poor correspondence is evident through the remaining gas loaded portions of the cycle (360-540^{0}ca) although the rigid solution shows equally poor correspondence. This portion of the cycle is open to the greatest variability; probe measurements can be from different gas cycles.

In general measured results indicate greater film asymmetry about the rod centre-line than predicted by theory, this asymmetry being present throughout the load cycle. Comparison of actual and theoretical geometries (F6.49) shows one possible source : oil-film pressure acts at the bearing centre whilst the reacting big-end portion of the body-force acts at the centre of mass; any difference in these centres produces a dynamic couple on the big-end promoting asymmetric distorsion.

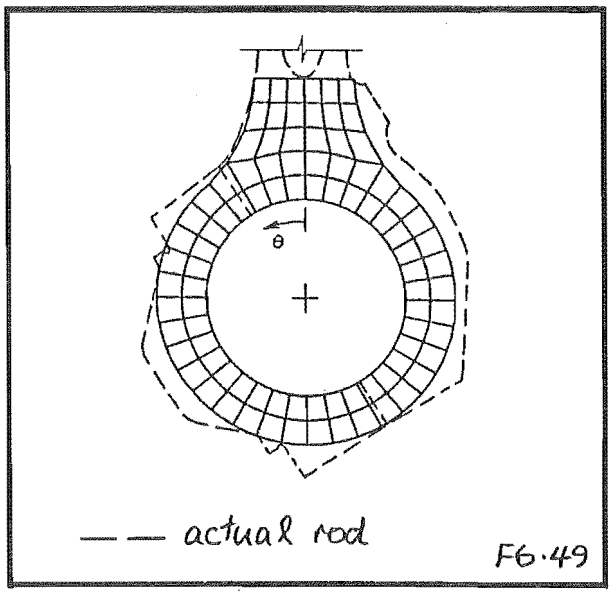

Clearly, assessment of overall agreement depends on where ones bias lies : it is probably fair to say that the elastic solution represents an encouraging improvement over the rigid solution, particularly during journal traversal of the con-rod cap. It is also clear that there are several periods where neither solution is representative of the experimental measurements.

Given the state of current theoretical tools, a new experimental program is probably overdue : rod stiffness could be determined statically to ascertain asymmetries; dynamic strain measurements to determine housing motion. A

series of motored film-thickness measurements would alone provide valuable new insight into this complex problem.

From the evidence amassed in this Chapter, a sequence of similarities can be constructed : experimental film-thickness measurements show encouraging correlation with theoretical gas loaded predictions; theoretical gas loaded film-thickness can be accurately assessed from inertial loaded solutions; film-thickness behaviour of inertially loaded housings is very similar to the inertially loaded ring solutions. It would seem then that, regarding $\min(\hat{h}_{min})$, inertial ring solutions could form the basis of an accurate performance assessment. This and the associated non-dimensionalisation are the subject of the following Chapter.

With regard to oil-film pressure however, ring solutions will not suffice : the rigid solution is sufficient for determining $\max(\hat{p}_{max})$ during gas loading however, a full housing solution is necessary for the inertial variations.

CHAPTER SEVEN

NON-DIMENSIONAL FILM THICKNESS ASSESSMENT

Both designer and researcher have a common need for bearing performance parameterisation: the designer in determining optimal geometries; the researcher in establishing *modus operandi.*

Until now, 'tuning' of bearings has in this work been performed intuitively; load variation through journal speed; stiffness variation through housing thickness. However, the difficulty encountered in just establishing elastic solutions, in particular for the bearing of Fantino[24], motivated such a parameterisation.

Several parameterisations of rigid bearing performance are available in the literature. In 1967 an important paper was published on big-end bearing design by Martin and Booker[96]. The basic thesis of this work was that provided peak firing load was less than five times the peak inertial load, minimum film-thickness could in general be predicted by considering inertial load alone. This, as shown in the previous Chapter, also holds in elastic bearings.

The result of Martin's assumptions was a simple design chart based on a short-bearing approximation. This approximation was later removed in a further simplified chart by Lloyd[99].

In the following sections we trace the development of a chart similar to Lloyd's, but in an elastic environment; F7.1 gathers together the various non-dimensional components.

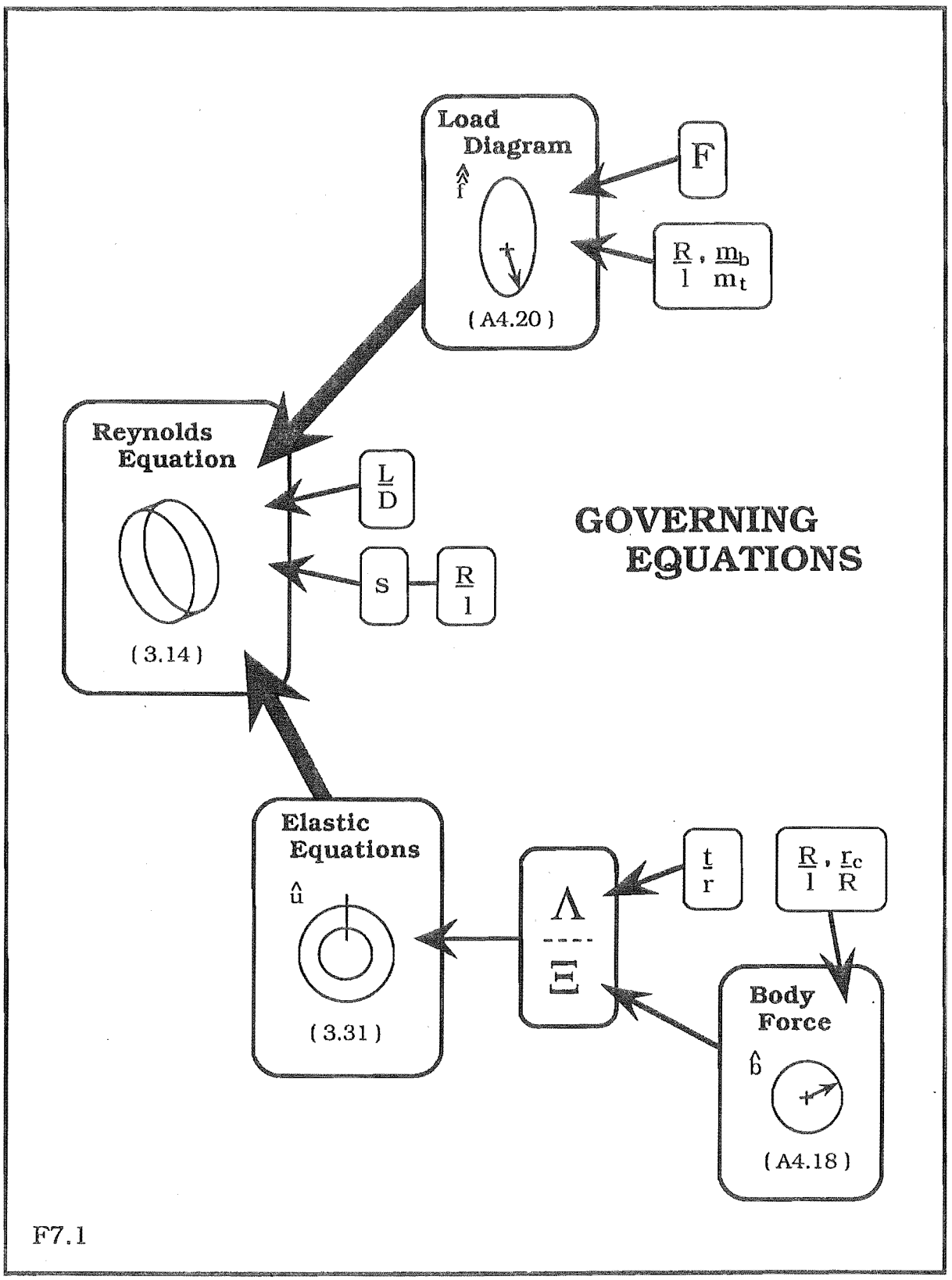
Load Diagram
F
R/l , m_b/m_t
(A4.20)
Reynolds Equation
L/D
S
R/l
(3.14)
GOVERNING EQUATIONS
Elastic Equations
(3.31)
Λ
Ξ
t/r
R/l , r_c/R
Body Force
(A4.18)

F7.1

7.1 Load Diagram

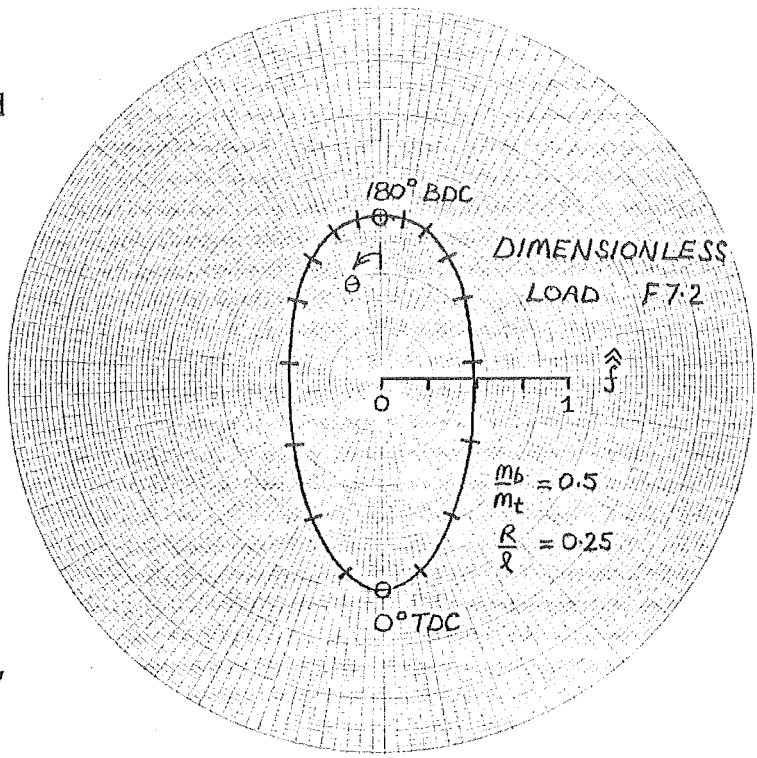

The dimensionless load diagram used in this work is the one of F7.2. This diagram is based on a fixed crank-radius to con-rod length of 1:4 and equal big (m_b) and little-end ($m_\ell + m_p$) masses. Both Martin and Lloyd have shown these two parameters to be of secondary importance in determining the load diagram compared to dimensionless load F: for any particular bearing we have from Appendix A4(g) :

$$\hat{\underset{\sim}{f}} = F\,\hat{\hat{\underset{\sim}{f}}} \qquad \text{(A4.19)}$$

where

$$F = \frac{m_t}{6}\frac{\omega R}{\mu n L r}\left[\frac{c}{L}\right]^2 . \qquad (7.1)$$

$$m_t = (m_b + m_\ell + m_p) \ .$$

This load number is different from that used by Lloyd; it is rooted in short, rather than long bearing theory. This will be seen to have several benefits.

7.2 Rigid Bearing Results

The rigid bearing performance diagram for the parabolic pressure model is given in F7.3. These results are based on a 36 element spatial mesh, 5^0 ca time step.

RIGID DATA

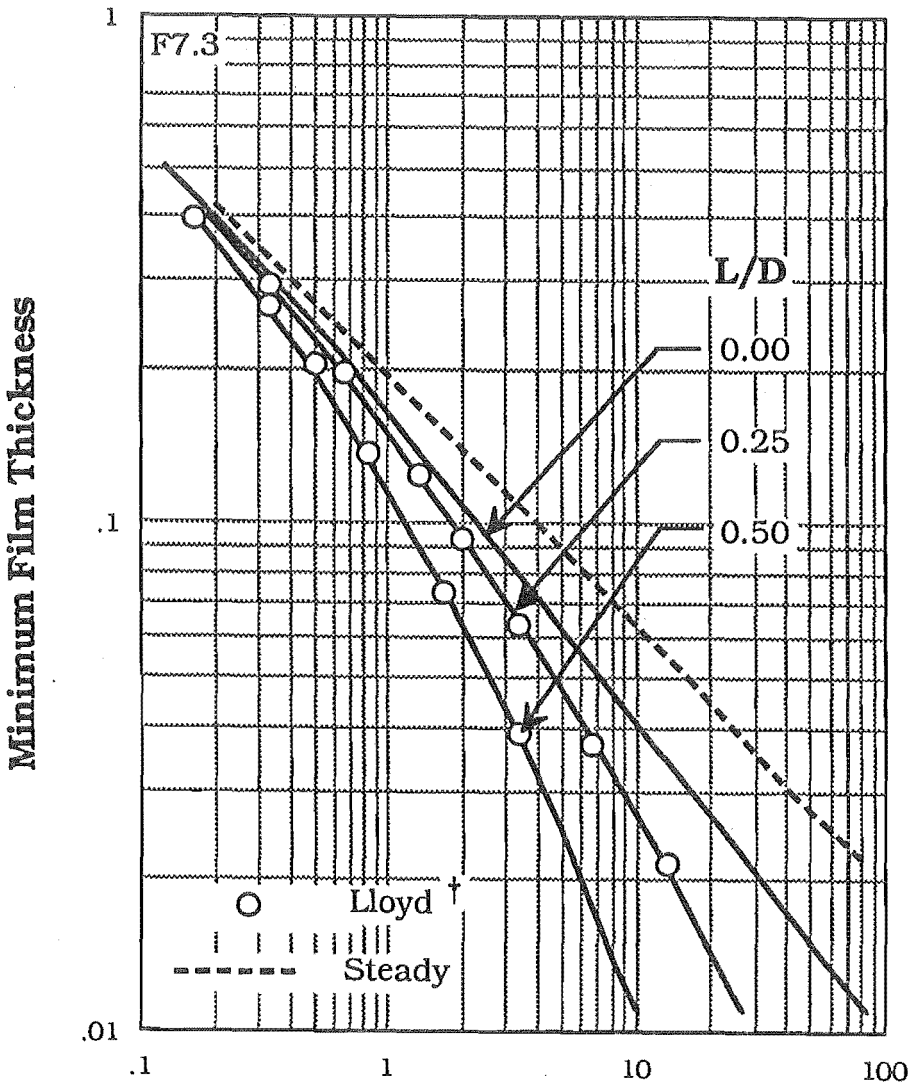

† The 0.25 L/D results are interpolated

Also shown are the finite length results of Lloyd and *steady–state* short bearing performance. Once again, the parabolic axial pressure assumption closely matches the finite dynamic solutions of Lloyd. It is also of interest to note the 'straight line' behaviour of the short bearing solution (L/D = 0). This relationship, not directly available in Lloyd's non-dimensionalisation, was determined to be :

$$\hat{h}_{min}\Big|_{L/D=0} = 0.159\ F^{-0.594};\ r^2 = 0.999^{\dagger}$$

It represents an upper bound to dynamic film thickness over all L/D ratios. Poorer although still quite acceptable fits were obtained for the remaining L/D ratios :

$$\hat{h}_{min}\Big|_{L/D=\frac{1}{4}} = 0.140\ F^{-0.729}\ ;\ r^2 = 0.993$$

$$\hat{h}_{min}\Big|_{L/D=\frac{1}{2}} = 0.102\ F^{-0.891}\ ;\ r^2 = 0.989\ .$$

In comparison, short *steady–state* performance is as follows :

$$\hat{h}_{min}\Big|_{L/D=0} = 0.194\ F^{-0.494}\ ;\ r^2 = 1.000$$

Of greater interest however, are the elastic solutions.

---

† r is the correlation coefficient

7.3 Elastic Bearing Results

At first appearance, non-dimensionalisation of the elastic bearing would seem a pointless task; the addition of two major elastic parameters, Λ and Ξ, each varying with engine speed, leads to considerable complexity. Fortunately, it is fairly easily shown that Λ, Ξ and F are interrelated in a much simpler fashion.

7.3.1 *Primary Parameters*

Two primary elastic parameters were first isolated in Section 3.2.3.

- Λ flexibility due to pressure
- Ξ flexibility due to body-force.

For curved beams, these can be expressed as :

$$\Lambda = \frac{24\mu\omega}{E}\left[\frac{L}{D}\right]^2\left[\frac{r}{c}\right]^3 \frac{nL}{W}.\ 12\left[\frac{r}{t}\right]^3 (1 + t/2r)^3 \qquad (7.2)$$

$$= \frac{6\mu\omega}{E}\ \frac{nr^4}{I}\left[\frac{L}{c}\right]^3 (1 + t/2r)^3\ , \qquad (7.3)$$

where I is the second moment of area of the beam about the N-A.

$$\Xi = \frac{\rho'}{E}(\omega r)^2\left[\frac{r}{c}\right]\left[\frac{R}{r}\right]\ \cdot\ 12\left[\frac{r}{t}\right]^2(1 + t/2r)^4\ . \qquad (7.4)$$

These can be related to non-dimensional load F as follows :

Based on the assumption that big-end mass m_b is a ring of internal radius r, thickness t and width W, we can write :

$$m_b = 4\pi\rho' r^3\ \frac{W}{D}\frac{t}{r}(1 + t/2r)\ , \qquad (7.5)$$

here adjusted density ρ' is determined as per Appendix A4(f). After some manipulation (7.1, 7.2 and 7.4) it is possible to show that :

$$\Xi = \Lambda F \frac{m_b}{m_t}/2\pi \tag{7.6}$$

This amounts to exchanging Ξ for $\frac{m_b}{m_t}$ in our non-dimensional parameter set; it offers significant advantages since $\frac{m_b}{m_t}$ typically varies from 0.3-0.6 whilst Ξ varies with engine speed.

To achieve consistent body-force loadings we set $\frac{m_b}{m_t}$ in-line with that used in the load diagram :

$$\frac{m_b}{m_t} = 0.5$$

The influence of this parameter on performance is investigated further in Section 7.3.2(a).

(a) **Performance Curves : $\frac{m_b}{m_t} = 0.5$**

Our non-dimensionalisation now incorporates just three major parameters : L/D, F and Λ. General elastic performance can now be presented as a series of rigid style charts at various flexibilities Λ : F7.4 shows curves for Λ = 1, 5, 10, 20 over a range of load and L/D ratio. These solutions are developed on a 36 element circumferential mesh using a 5^0 ca time step.

Probably the most general observation to be made is that bearing flexibility diminishes the L/D performance distinction ; circumferential pressure flows decrease with distortion as indicated by the shift towards the short bearing model.

At any particular flexibility, performance is very similar to that encountered in Chapter Six : film-thickness is increased over the rigid solution while the point of minimum film thickness remains in the proximity of the rod neck. As this

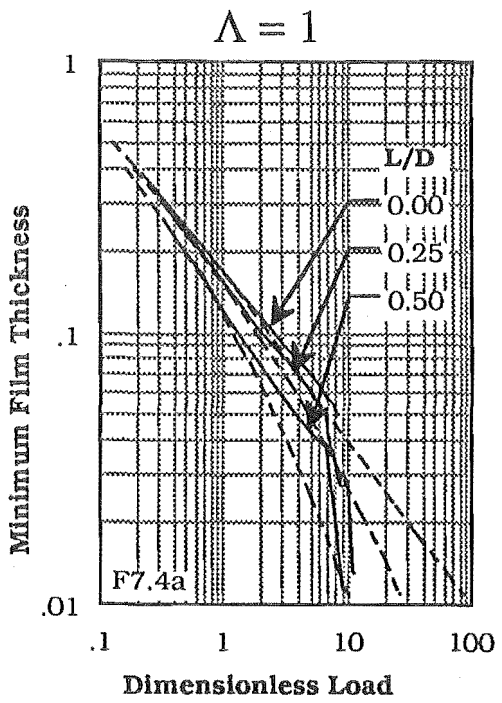
Λ = 1
Minimum Film Thickness
1
.1
.01
L/D
0.00
0.25
0.50
F7.4a
.1
1
10
100
Dimensionless Load

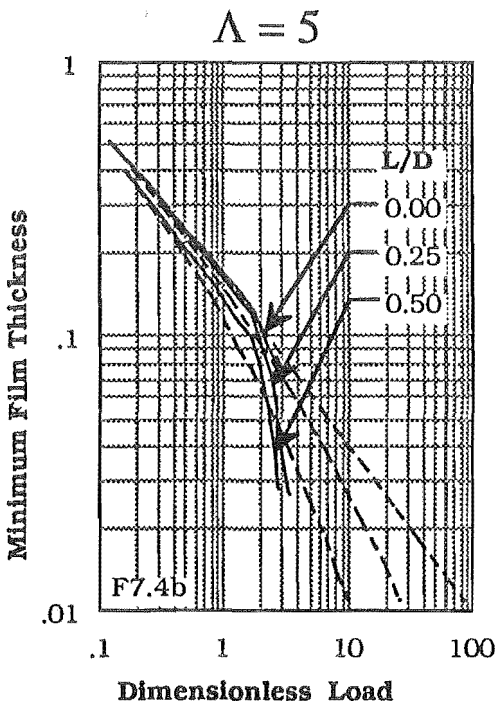
Λ = 5
Minimum Film Thickness
1
.1
.01
L/D
0.00
0.25
0.50
F7.4b
.1
1
10
100
Dimensionless Load

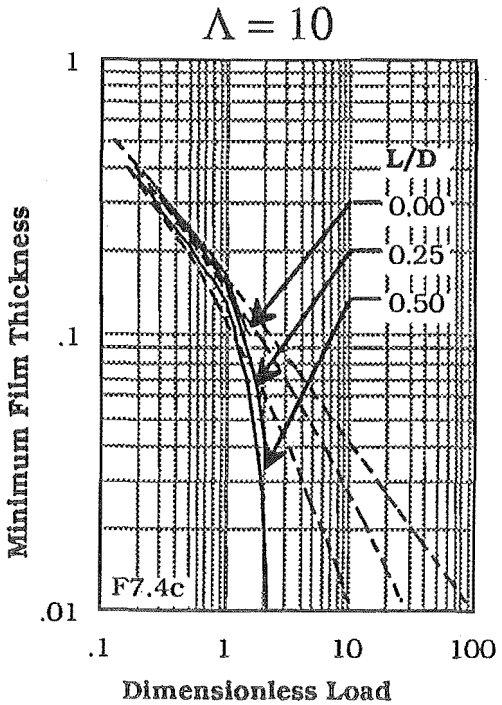
Λ = 10
Minimum Film Thickness
1
.1
.01
L/D
0.00
0.25
0.50
F7.4c
.1
1
10
100
Dimensionless Load

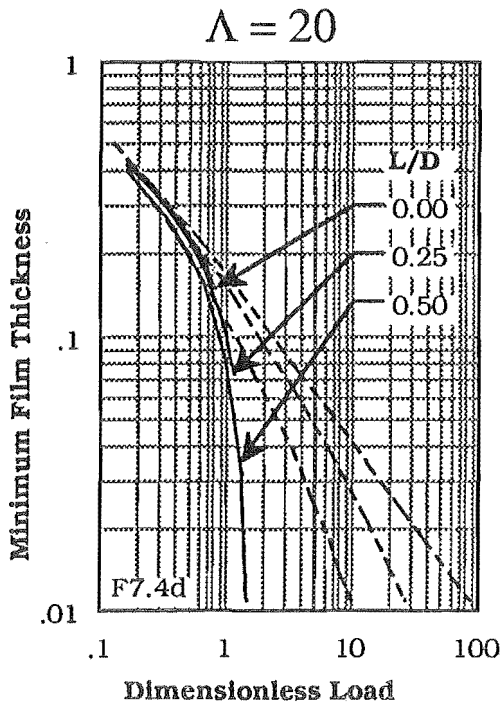
Λ = 20
Minimum Film Thickness
1
.1
.01
L/D
0.00
0.25
0.50
F7.4d
.1
1
10
100
Dimensionless Load

point moves out of the neck, a rapid film-thickness reduction occurs, this transition developing at lower loads as flexibility increases.

Prior to transition, bearing operation is more amicable than the rigid bearing ; thicker films are developed with lower sensitivity to load. Post transition behaviour is more hostile ; reduced film thickness with a greater load sensitivity.

Clearly, the point at which this transition occurs is important.

(b) **Transition Point Determination :**

In the previous Chapter we observed transition as a shift from neck based minimum films to cap based minimum films. In the non-dimensionalised bearing the situation is slightly more complicated :

At higher flexibilities ($\Lambda > 5$) transition occurs as in the Ruston and Hornsby case; the minimum film shifts from being at 270^0 ca (20^0 ba) to around 0^0ca (~ 120^0 ba). However, at lower flexibilities ($\Lambda = 1$) the shift is to 90^0 ca (260^0 ba). Plotting this transition load as a function of flexibility gives F7.5, the different mechanism of $\Lambda = 1$ standing out from the $\Lambda > 1$ data. The latter points can be seen to closely obey a relationship of the form :

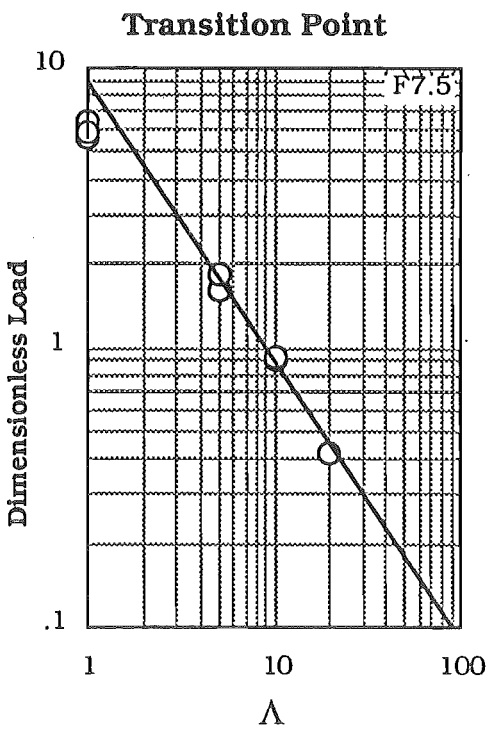

$$\Delta = \Lambda F = 9 \tag{7.7}$$

The simplicity of this relationship at first came as a surprise, however its interpretation is really quite plain : Λ is a measure of flexibility, F a measure of total dynamic load (pressure) ; the product Δ, is a measure of dynamic bearing deflection due to pressure. The above relationship thus states that when non-dimensional pressure deflection reaches nine, a transition in operating régime occurs. Bearing performance is then much more sensitive to load and elastic geometry.

For the current work we treat the $\Lambda = 1$ mechanism as if it were a $\Delta=9$ condition : future investigations could determine its influence and extent.

7.3.2 *Secondary Parameters*

Four secondary parameters are involved in our non-dimensionalisation. We look at each in turn.

(a) Lumped Mass Ratio : $\frac{m_b}{m_t}$

In the preceding charts, $\frac{m_b}{m_t}$ was set such that big-end and total little-end masses were equal. It is interesting to observe the effects of altering this ratio : Ξ is changed according to equation (7.6); load diagram according to Appendix A4†. Figure F7.6 shows results for ratios of $\frac{1}{3}$ and $\frac{2}{3}$ (L/D = 0.25, Λ = 5).

---

† The load diagram is altered to maintain a consistent body force.

The small overall changes in minimum film-thickness performance illustrate the secondary nature of this variation : a reduced big-end mass thickens the minimum oil-film and delays the transition of the cap condition.

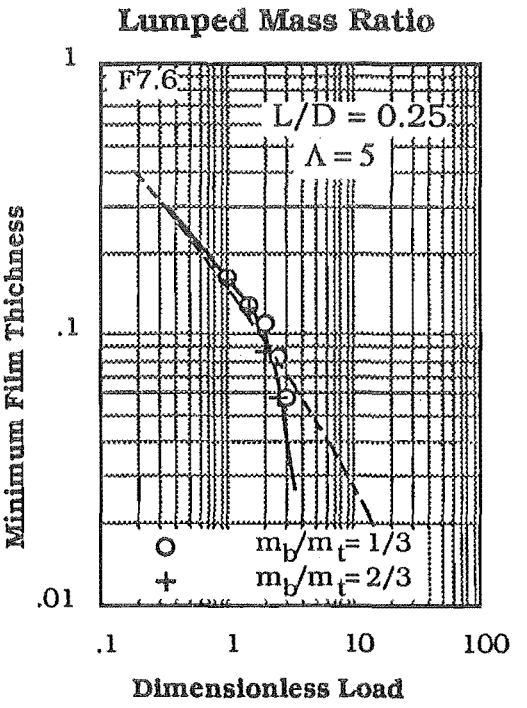

(b) Obliquity Ratio : R/ℓ

Obliquity ratio is quite a permeating influence. It is a secondary effect in the load diagram and body force; it also appears in Reynolds equation through speed modifier s. Figure F7.7 illustrates its influence on minimum film thickness.

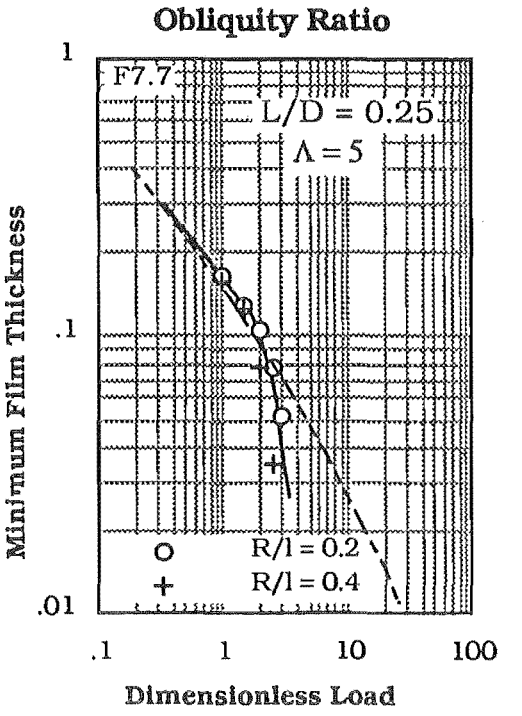

Pre-transition solutions are hardly altered : min($\hat{h}_{min}$) occurs at around 270^0 ca where the effects of R/ℓ are not felt - this is the reason why rigid bearing analyses are so insensitive to obliquity.

Post-transition changes are on a par with L/D changes, min ($\hat{h}_{min}$) occurring close to TDC where R/ℓ effects are greatest : films thicken with reduced obliquity; transition points remain unchanged. Much of this change can

be attributed to increased journal speed : changing R/ℓ from 0.2 to 0.4 causes a speed and consequent load increase of 17% $\left[\frac{1.4}{1.2}\right]$ at TDC.

(c) **Internal Elastic Parameters :**

Two elastic parameters are required internally by the elasticity model : t/r is used in the implementation of beam theory; $\frac{r_c}{R}$ to determine the position of the centroid through which the body-force acts.

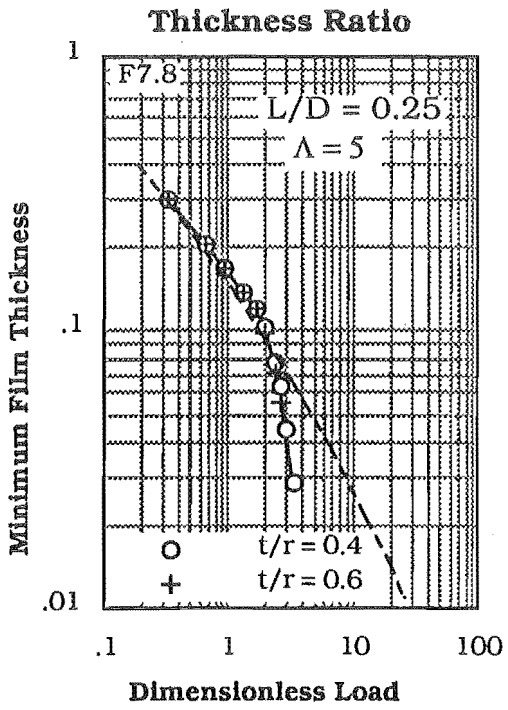

As noted in Section 4.2.3, internal dependence of thick beam behaviour on t/r is very weak : tests varying t/r from 0.4 to 0.6 in the L/D = $\frac{1}{4}$, Λ = 5 bearing (F7.8) produced little discernible difference. The major influence of this parameter is accounted for in Λ and F; all remaining dimensionless solutions use t/r = $\frac{1}{2}$.

The second parameter is somewhat more arbitrarily chosen to be 0.8 : the R-H rod is 0.7; Fantino's rod is 0.8. Figure F7.9 shows results at 0.6 and 1.0 for L/D = $\frac{1}{4}$, Λ = 5; very weak internal dependence is indicated, the major influence of this parameter being felt through dimensionless load F.

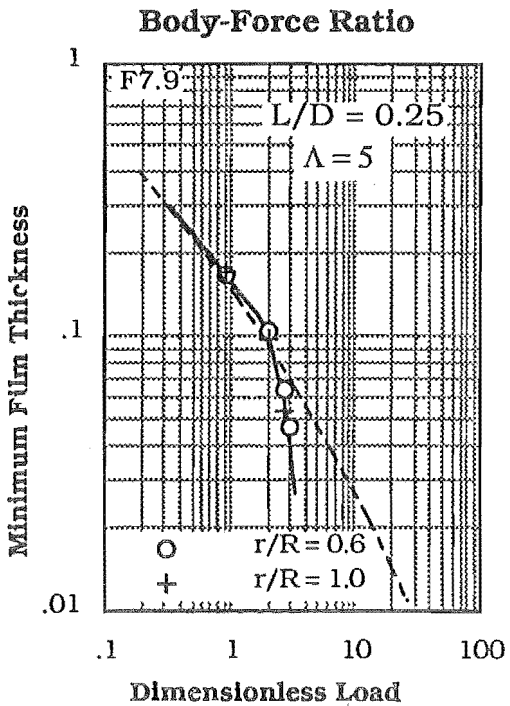

7.3.3 *Controlling Geometric Terms*

From the charts and deflection measures of the previous sections, a picture of elastic bearing performance has begun to emerge :

Two primary parameters, load F and flexibility Λ, have been seen to dominate elastic bearing performance. Both these parameters are dynamic, being functions of journal speed. They can thus vary several orders of magnitude during engine operation.

For a reasonably flexible bearing ($\Lambda > 1$), length-diameter ratio is relegated to a secondary effect along with lumped mass ratio, various internal elastic effects and obliquity†. All these secondary parameters are geometric quantities and consequently static; in a first approximation they can be neglected.

It is useful then to look at a breakdown of the two dominant parameters to determine the major geometric influences on elastic bearing performance.

Taking expressions (7.1), (7.2) and (7.7) and assuming the total rod/piston mass is proportional to the big-end mass, it is possible to extract the following proportionalities :

$$\Lambda \quad \alpha \quad \frac{r_c^3}{EI}\frac{\mu\omega rnL^3}{c^3}$$

$$F \quad \alpha \quad \rho tWr_c \frac{\omega Rc^2}{\mu nrL^3}$$

$$\Delta \quad \alpha \quad \frac{1}{c}\frac{\rho\omega^2 R}{E}\frac{r_c^4}{k^2} \qquad \text{where}$$

r_c is the section centroidal radius, k the radius of gyration of the section about r_c.

---

† post-transition obliquity effects are assumed to be incorporated by altering load.

For convenience assume k α t[†] and $r_c \simeq r$; Table T7.1 then gives the power relationships for the various proportionalities :

parameter	F	Λ	Δ
μ	-1	+1	0
E	0	-1	-1
ρ	+1	0	+1
ω	+1	+1	+2
R	+1	0	+1
W/n	+1	-1	0
c	+2	-3	-1
t	+1	-3	-2
L	-3	+3	0
r	0	+4	+4
k	0	-2	-2

T7.1

It is reassuring that t and ω behave as intuition would dictate; t weakly increasing load but strongly reducing flexibility; ω increasing load and flexibility but being detrimental to deflection. Of particular note are parameters c, t and L : any variation towards improved performance from a rigid perspective (lowering F) has a detrimental effect on flexibility.

The strongest elasticity determinator however is journal/housing radius, r^4 : Clearly from an elastic standpoint journal radius should be kept to the minimum dictated by crankshaft stress considerations. This is contrary to what one would expect from a specific loading basis; it comes about through housing flexibility being proportional to r_c^3.

---

† true for simple solid sections

As a case study for these observations, we next look at the troublesome bearing of Fantino.

7.3.4 *Case Study : Fantino's Bearing*

Two studies are presented in this section : a verification of chart determinations against actual bearing calculations and a study of non-dimensional parameter manipulation from a design standpoint.

However, before beginning it is useful to illustrate the disparity between the dimensionless parameters of Fantino's bearing and the Ruston and Hornsby bearing of Chapter Six : Table T7.2 presents the data; Appendix A8 contains the calculations :

	F	Λ	Δ
Ruston and Hornsby (600)	3.8	2.6	10
Fantino (5500)	1.6	31.3	49

T7.2

In comparison to the Ruston-Hornsby bearing, Fantino's bearing is lightly loaded but extremely flexible. From a rigid bearing perspective one would not expect problems, the bearing being so lowly loaded, however problems it definitely has.

(a) Chart Verification :

From the deflection measures developed in previous sections, transition would be expected to occur at a lowly 2500 rpm. Operation is consequently mainly in the post-transition régime with all the attendant problems of oil-film fragmentation.

Performance under 'exact', rather than chart conditions is presented in F7.10 : transition is observed to occur between 2500 and 3000 rpm, this corresponding to Δ = 10-15 ; convergence is maintained through to 4000 rpm or Δ = 23. The mesh used is the usual 36 spatial elements, 5^0 ca setup.

Chart results are presented in T7.3 at speeds roughly corresponding to flexibilities of 5, 10 and 20.

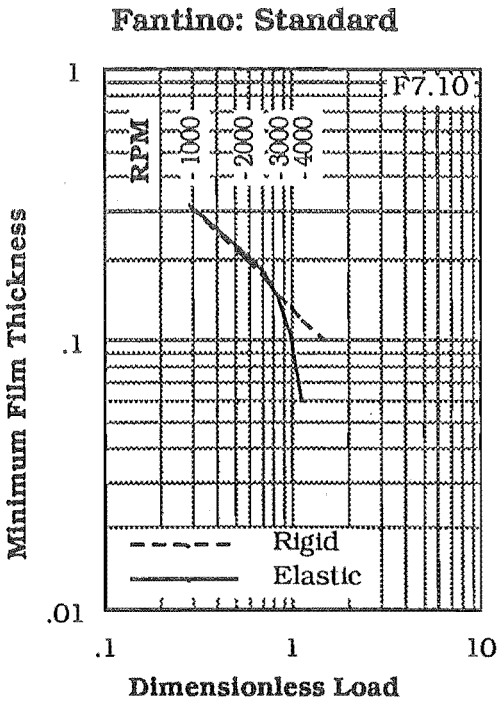

ω	F	Λ	$\hat{h}_{min}$ (exact)	$\hat{h}_{min}$ (chart)
1000	0.286	5.68	0.317	~ 0.30
2000	0.571	11.37	0.208	~ 0.20
3500	0.999	19.89	0.104	~ 0.10

T7.3

These preliminary results look particularly encouraging although further testing over a greater range of geometries would probably be prudent. It is with some confidence then, that we can look at a simple design problem.

(b) Primary Parameter Manipulation :

Given the disparity between flexibility and load in Fantino's bearing, the question arises as to whether we can affect performance gains by trading off flexibility with load. Table T7.4 presents some possibilities (Appendix A8 contains the calculations).

Case	F	Λ	Δ	$\hat{h}_{min}$
Standard (5500)	1.6	31	50	-
0.89 r	1.7	21	35	~ 0.01
1.22 k	1.6	20	32	~ 0.01
0.89r,1.22k	1.7	13	22	~ 0.03

T7.4

The strength of radius variation is clearly apparent; a reduction in journal radius of 11% produces a similar effect to a 22% increase in the radius of gyration. (k is assumed to be obtained without an increase in rod mass). By combining both changes it is possible to obtain conditions within the bounds of current computational experience ($\Delta < 20$).

Performance of this stiffened design (r = 0.024m, t = 0.0165m) under 'exact' as opposed to chart conditions is shown in F7.11 ; a full description of the 5000 rpm solution is given in F7.12, 7.13. Whilst small film-thickness reductions have occurred in pre-transition behaviour, substantial improvements in post-transition behaviour have accrued : transition occurs at around Δ = 12 (4000 rpm); solution convergence is to 5500 rpm; minimum film-thickness has about doubled.

Correspondence with chart solutions is again close : at $\Lambda \simeq 5$ (2000 rpm) the chart gives 0.2 as opposed to 0.182; at $\Lambda \simeq 10$ (4500 rpm) a chart result

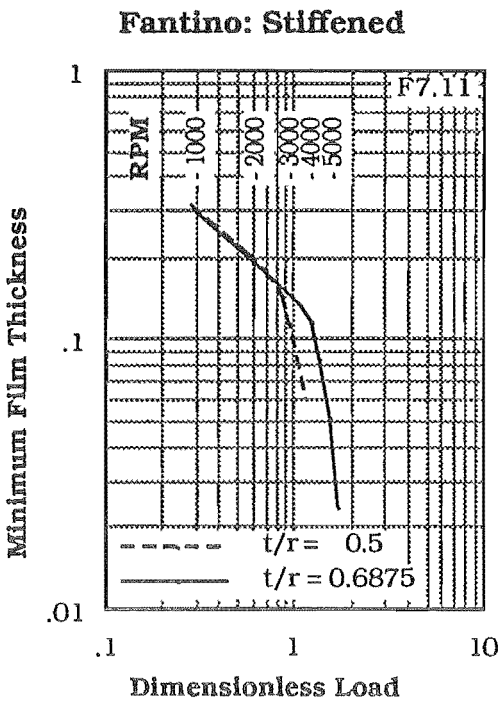

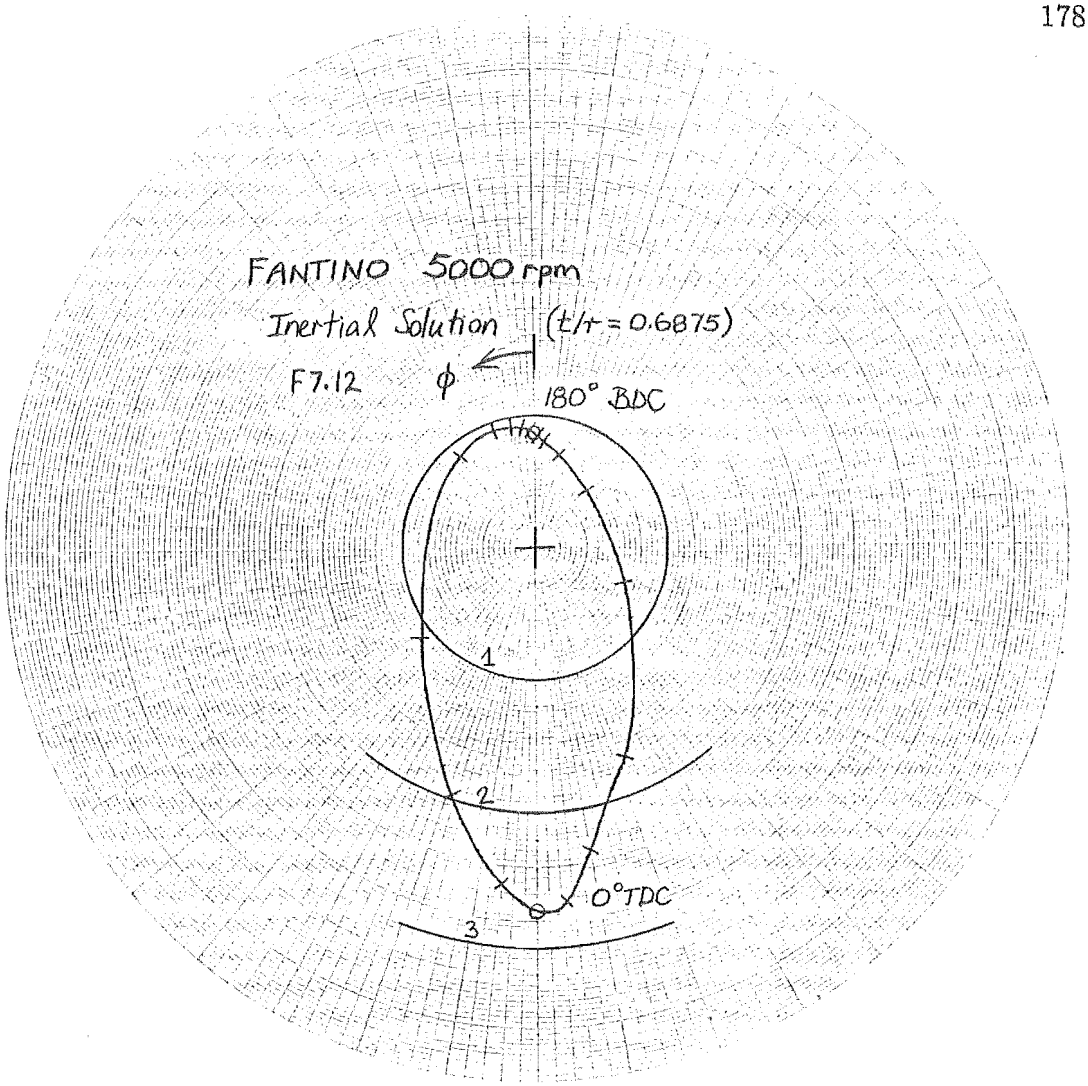
FANTINO 5000 rpm
Inertial Solution (t/r = 0.6875)
F7.12
ϕ
180° BDC
0°TDC
1
2
3

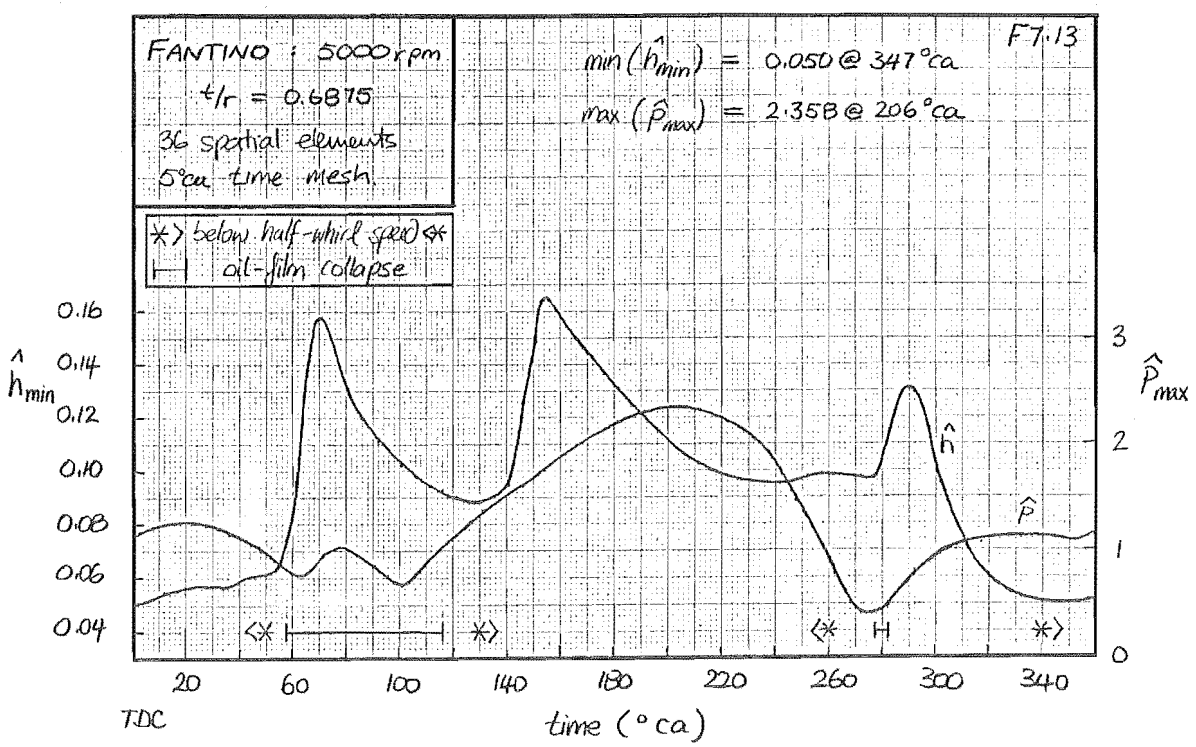
FANTINO ; 5000 rpm
t/r = 0.6875
36 spatial elements
5°ca time mesh
min (ĥmin) = 0.050 @ 347°ca
max (P̂max) = 2.358 @ 206°ca
F7.13
⟨* below half-whirl speed *⟩
oil-film collapse
ĥmin
P̂max
ĥ
P̂
0.16
0.14
0.12
0.10
0.08
0.06
0.04
3
2
1
0
20
60
100
140
180
220
260
300
340
TDC
time (°ca)

of 0.08 is obtained compared to an 'exact' solution of 0.084.

Finally, results of ± 20% change in radial bearing clearance (c) at 5000 rpm are presented in T7.5.

c	$\hat{h}_{min}$	$\hat{h}'_{min} = \hat{h}_{min}\,(c/c')$
0.8c′	0.072	0.057
c′	0.050	0.050
1.2c′	0.039	0.047

T7.5

These trends are in-keeping with those observed in rigid bearings[100] : increased clearance reduces absolute film thickness.

Summarising, this case study illustrates the usefulness of extending the rigid bearing non-dimensionalisation to incorporate primary elastic effects : film mechanism transitions, dynamic minimum film-thickness and the interplay of the major elastic geometric influences would seem to be sufficiently well portrayed to make this a useful design tool; testing on further bearing geometries will prove its worth.

Additional design charts (F7.4) at intermediate flexibilities are needed for a useful coverage of engine speed ranges.

CHAPTER EIGHT

CONCLUSION

This thesis has embraced the elastohydrodynamic analysis, solution and verification of the dynamic big-end bearing in the aim of providing design level information of distorted bearing performance.

Reynolds' equation has firstly been re-examined in light of surface displacements. A comprehensive evaluation of its application in various con-rod reference frames has resulted in a clarified schema for the EHL big-end problem. Consistent modelling of the con-rod was found to require the inclusion of elasticity body-forces; these additional body-forces provide significant stiffening of the big-end eye under dynamic load. All current models were found to be in someway deficient in this respect.

Combining uniform axial film-thickness assumptions with parabolic pressure profiles, an approximate hydrodynamic model was constructed : use of the parabolic axial profile was subsequently vindicated for bearings of $L/D < \frac{1}{2}$ in both rigid and elastic environments. An elastohydrodynamic extension of the problem was achieved by coupling either curved-beam or planar Finite Element housing models to the previous hydrodynamic equations.

The curved-beam approach proved instrumental in providing bench mark solutions for the F.E. elasticity implementation : the role of discretisation and surface displacement interpolation errors were highlighted in the steady-state problem; F.E housing solutions were found to be inferior to their curved-beam counterparts, increased residual errors restricting convergence at higher load.

For the dynamic problem, ring, housing and experimental works were drawn together to provide a comprehensive verification of dynamic elastic bearing behaviour. Journal action in the elastic bearing was found to be much greater

than in the rigid bearing due to housing distortion. This increased action leads to intense oil-film collapses, likened in this work to vapour cavitation : journal motion from the distorted con-rod cap back into the rod neck and rapid journal action during gas load reversal produced short duration oil-film collapses ; elastic housing discontinuities were also observed to induce such collapses. These mechanisms have not been previously observed in theoretical solutions; they were not present in the equivalent rigid bearing analyses.

Strong similarities in film-thickness behaviour were observed between experimental and the present elastic housing solutions. These similarities extended to the inertial curved-beam solutions, allowing a quite general non-dimensional characterisation of minimum film-thickness to be performed. With this characterisation, two minimum film régimes were identified : one in which the minimum film is located in the rod neck and a second in which the minimum film is located in the con-rod cap.

The first régime is characterised by a thickening of minimum films over their rigid bearing counterparts; this mechanism dominates at low load. The second régime is characterised by thinner minimum films and an increased sensitivity to load and elastic geometry; this phenomena occurs at higher loads. Non-dimensionalisation of the associated transition point, along with bearing flexibility and load, enabled quantitative tribological measures of elastic geometry to be developed. This characterisation provides useful new insight into con-rod design, something that has hitherto been based on intuition; it also marks the completion of this work.

8.1 Future Work

Extension of the present study should focus on an improved treatment of vapour cavitation and the incorporation of axial deformation effects. The work of Brewe[55] and Bayada[101] provide a lead for the former effects; Oh's

analysis[29] for the latter effects.

Advancement on either of these fronts will require a concomitant improvement in solution techniques. The present Newton-Raphson procedures are too slow for such extensions : the rigid Ruston and Hornsby gas loaded analysis requires around one hour of CPU†; the elastic equivalent takes four hours of CPU. A logical extension would be the use of rank two Quasi-Newton Methods[89]. These algorithms would provide faster implementations of the present N-R approach without sacrificing its robustness : currently, time stepping rarely drops below 2.5^0 ca, even for gas loaded elastic solutions; less than ten solution iterations are typically required at any given time step.

On the experimental front, initiation of new programs are desperately needed : major misconceptions are present in current test-rig procedures, a rigid bearing paradigm pervading much of the thinking and consequent hardware of experimentalists. Attention would instead be better focused on obtaining controlled *in situ* film measurements.

---

† Digital MicroVax II

REFERENCES

[1] Gordon, J.E. *The New Science of Strong Materials*, Princeton University Press (1976).

[2] Dowson, D., Higginson, G.R. *Elasto–hydrodynamic Lubrication - The Fundamentals of Roller and Gear Lubrication.* Pergamon Press (1966).

[3] Hamrock, B.J., Dowson, D. *Ball Bearing Lubrication - The EHD Lubrication of Elliptical Contacts.* Wiley and Sons (1981).

[4] Reynolds, O. *On the Theory of Lubrication and its Application to Mr Beauchamp Towers' experiments, including an experimental determination of the viscosity of Olive Oil.* Papers on Mechanical and Physical Subjects by O. Reynolds. (Reprints). Volume II p.228. Cambridge Univ. Press 1901.

[5] Carl, T.E. *An Experimental Investigation of a Cylindrical Journal Bearing under Constant and Sinusoidal Loading.* Proc. Inst. Mech. Engrs. Lubrication and Wear 2nd Conv. 1964.

[6] Campbell, J. Love, P.P., Martin, F.A., Rafique,S.O. *Bearings for Reciprocating Machinery: A review of the Present State of Theoretical, Experimental and Service Knowledge.* Proc. Instn. Mech. Engrs., 1967-68, 182(3A), *51.*

[7] Higginson, G.R. *The Theoretical Effects of Elastic Deformation of the Bearing Liner on Journal Bearing Performance.* Proc. Instn. Mech. Engrs., 1965-66 180(3B), 31.

[8] O'Donoghue, J., Brighton, D.K., Hooke, C.J.K. *The Effect of Elastic Distorsions on Journal Bearing Performance.* Trans ASME 1967, 89 (Series F), 409.

[9] Hooke, C.J., Brighton, D.K., O'Donoghue, J.P. *The Effect of Elastic Distorsion on the Performance of Thin Shell Bearings.* Proc. Instn. Mech. Engrs., 1966-67, 181(3B) 63; also discussion p.163.

[10] Brighton, D.K., Hooke, C.J., O'Donoghue, J.P. *The Theoretical and Experimental Investigation of the Effect of Elastic Distorsions on the Performance of Journal Bearings.* Proc. Instn. Mech. Engrs., 1967-68, 182(3N), 192.

[11] O'Donoghue, J.P., Koch, P.R., Hooke, C.J. *Approximate Short Bearing Analysis and Experimental Results obtained using Plastic Bearing Liners.* Proc. Instn. Mech. Engrs., 1969-70, 184(3L), 190; also discussion p.227.

[12] Conway, H.D., Lee, H.C. *The Analysis of the Lubrication of a Flexible Journal Bearing.* Trans. ASME 1975, 97 (Series F), 599.

[13] Conway, H.D., Lee, H.C. *The Lubrication of Short Flexible Journal Bearings.* Trans. ASME 1977, 99 (Series F), 376.

[14] Benjamin, M., Castelli, V. *A Theoretical Investigation of Compliant Surface Journal Bearings.* Trans. ASME 1971, 93 (Series F), 191.

[15] Chandrawat, H.N., Sinhasan, R. *A Study of Steady State and Transient Performance Characteristics of a Flexible Shell Journal Bearing.* Trib. Int. 1988, 21(3), 137.

[16] Ibrahim, S., McCallion, H. *Elastic Distorsion of Journal Bearing Housings.* Proc. Instn. Mech. Engrs., 1967-68, 182(3N), 13.

[17] Allen, D.G. *A Theoretical Investigation of the Effects of Housing Distorsion on Journal Bearing Performance.* Ph.D Thesis, University of Nottingham, 1972.

[18] Oh, K.P., Huebner, K.H. *Solution of the Elastohydrodynamic Finite Journal Bearing Problem.* Trans. ASME, 1973, 95 (Series F), 343.

[19] Fantino, B., Frene, J., Du Parquet, J. *Elastic Con–Rod Bearing with Piezoviscous Lubricant : Analysis of the Steady–State Characteristics.* Trans. ASME 1979, 101 (Series F), 190; also discussion p.198.

[20] Stafford, A., Henshell, R., Dudley, B. *Finite Element Analysis of Problems in EHD Lubrication.* EHD and Related Topics, 5th Leeds-Lyon Symp. on Trib., 1978, II (iv), 35.

[21] Frene, J., Desailly, R., Fantino, B. *Hydrodynamics of an Elastic Con–Rod Bearing : Comparison of Theoretical and Experimental Results.* EHD and Related Topics, 5th Leeds-Lyon Symp. on Trib., 1978, IX (iii), 329.

[22] Bozaci, A., Dudley, B.R., Middleton, V., Allen, D.G. *Steady Load Performance of a Journal Bearing with an Elastic Housing.* EHD and Related Topics, 5th Leeds-Lyon Symp. on Trib., 1978, IX (ii), 320.

[23] Martin, F. *Developments in Engine Bearing Design.* Trib. Int. 1983, 16(3), 147.

[24] Fantino, B., Godet, M., Frene, J. *Dynamic Behaviour of an Elastic Con–Rod Bearing – Theoretical Study.* SAE trans. 1983. SAE 830307.

[25] Fantino, B., Frene, J. *Comparison of Dynamic Behaviour of Elastic Con–Rod Bearing in both Petrol and Diesel Engines.* Trans. ASME J. Trib. 1985, 107(1), 87.

[26] Fantino, B., Frene, J., du Parquet, J. *Viscosity Effects on the Dynamic Characteristics of an Elastic Engine Bearing.* SAE trans. 1985. SAE 852074.

[27] Smith, E.H. *EHL in Dynamically Loaded Journal Bearings.* Mechanisms and Surface Distress. 12th Leeds-Lyon Symp. on Trib. 1985, XIII(iii), 375.

[28] LaBouff, G.A., Booker, J.F. *Dynamically Loaded Journal Bearings : Finite Element Treatment for Rigid and Elastic Surfaces.* Trans. ASME J. Trib. 1985, 107(4), 505.

[29] Oh, K.P., Goenka, P.K. *The EHD Solution of Journal Bearings under Dynamic Load.* Trans. ASME J. Trib. 1985, 107(3), 389.

[30] Goenka, P.K., Oh, K.P. *An Optimal Short Bearing Theory for EHD Solutions of Journal Bearings.* Trans. ASME J. Trib. 1986, 108(2), 294.

[31] Goenka, P.K., Oh, K.P. *An Optimal Connecting Rod Design Study – A Lubrication Viewpoint.* Trans. ASME J. Trib. 1986, 108(3), 487.

[32] van der Tempel,L, Moes, H., Bosma, R. *Numerical Simulation of Dynamically Loaded Flexible Short Journal Bearings.* Trans ASME J. Trib. 1985, 107(3), 396.

[33] van der Tempel, L., Moes, H., Bosma, R. *Starvation in Dynamically Loaded Flexible Short Journal Bearings.* Trans ASME J. Trib. 1985, 107(3), 516.

[34] Butcher, A.E. *Developments in the Measurement of Oil Film Thickness in Dynamically Loaded Bearings.* Proc. Instn. Mech. Engrs. 1967-68, 182(3G), 105.

[35] Hiruma, M., Furuhama, S. *Measurement of the Journal Locus in the Con–Rod Big–End Bearing of an Automobile Gasoline Engine.* Trans ASME 1973, 95 (Series F), 249.

[36] Goodwin, G., Holmes, R. *On the Continuous Monitoring of Oil–film Thickness in an Engine Bearing.* Proc. Instn. Mech. Engrs. 1978, 192(1978), 371.

[37] Rohde, S.M., Oh, K.P. *A Unified Treatment of Thick and Thin film EHD Problems using Higher Order Element Methods.* Proc. R. Soc. Lond. 1975, 343(A), 315.

[38] Oh, K.P. *The Numerical Solution of Dynamically Loaded EHD Contact as a Nonlinear Complementarity Problem.* Trans ASME J. Trib. 1984, 106(1), 88.

[39] Kostreva, M.M. *Elasto–Hydrodynamic Lubrication : A Non–linear Complementarity Problem.* Int. J. Num. Meth. in Fluids 1984, V4, 377.

[40] Lubrecht, A.A., Breukink, G.A., Moes, H., ten Napel, W.E., Bosma, R. *Solving Reynolds Equation for EHL Line Contacts by Application of Multi–grid Method* – Fluid Film Lub., Osborne Reynolds Cent. 13th Leeds-Lyon Symp. 1986, VI(i), 175.

[41] Chittenden, R.J., Dowson, D., Sheldrake, N.P., Taylor, C.M. *The Use of Multi–level Adaptive Techniques for EHL Line Contact Analysis.* Fluid Film Lubn., Osborne Reynolds Cent. 13th Leeds-Lyon Symp. 1986, VI(ii), 183.

[42] Berthe, D., Godet, M. *A More General Form of Reynolds' Equation – Application to Rough Surfaces.* Wear (1973), 27, 345-357.

[43] Cameron, A. *Principles of Lubrication.* Longmans Green and Co. Ltd. (1966).

[44] Batchelor, J. *An Introduction to Fluid Dynamics.* Cambridge University Press (1967).

[45] Sokolnikoff, I., Redheffer, R. *Mathematics of Physics and Modern Engineering,* 2nd edition. McGraw-Hill Int. (1966).

[46] Fantino, B. *Influence des defauts de forme et des deformations elastiques des surfaces en lubrification hydrodynamique sous charges statiques et dynamiques.* Thése de Docteur d'Etat ès Sciences, 1981, Université Claude Bernard Lyon I.

[47] Lloyd, T., Horsnell, R., McCallion, H. *Investigation into the Performance of Dynamically Loaded Journal Bearings : Theory.* Proc. Instn. Mech. Engrs. 1966, 181(3B) 1.

[48] Dowson, D., Taylor, C. *Fundamental Aspects of Cavitation in Bearings.* Cavitation and Related Phenomena in Lub. Proc. of 1st Leeds-Lyon Symp. on Trib.. 1974, I(iii), 15.

[49] Jacobson, B., Hamrock, B. *High Speed Motion Picture Camera Experiments of Cavitation in Dynamically Loaded Journal Bearings.* Trans. ASME J. Trib., 1983, **105(3)**, 446.

[50] Elrod, H., Adams, M. *A Computer Program for Cavitation and Starvation Problems.* Cavitation and Related Phenomena in Lub. 1st Leeds-Lyon Syp. on Trib., 1974, **II(ii)**, 37.

[51] Elrod, H. *A Cavitation Algorithm.* Trans. ASME J. Trib., 1981, 103(3), 350.

[52] Rohde, S., McAllister, G. *A Variational Formulation for a Class of Free Boundary Problems in Hydrodynamic Lubrication.* Int. J. Eng. Sci., 1975, **13**, 841.

[53] Wilson, R. *Cavitation Damage in Plain Bearings.* Cavitation and Related Phenomena in Lub. 1st Leeds-Lyon Symp. on Trib., 1974, **VII(i)**, 177. (Also discussion).

[54] Martin, F., Garner, D., Adams, D. *Hydrodynamic Aspects of Fatigue in Plain Journal Bearings.* Trans. ASME J. Trib., 1981, **103(1)**, 150.

[55] Brewe, D.E. *Theoretical Modelling of the Vapour Cavitation in Dynamically Loaded Journal Bearings.* Trans. ASME J. Trib., 1986, **108(4)**, 628.

[56] Webster, W., Coffell, R., Alfaro, D. *3–D Finite Element Analysis of a High Speed Diesel Engine Con–Rod.* SAE Trans., 1983, SAE 831322.

[57] Yoo, Y., Haug, E., Choi, K. *Shape Optimal Design of an Engine Con–Rod.* Trans. ASME J. Mech., Transm, Design, 1984, 106(3), 415.

[58] Carlson, B., Ruff, J. *New Considerations in Con–Rod Design.* SAE Trans., 1983, SAE 831323.

[59] Spikes, R., Robinson, S. *Engine Bearing Design up–to–date.* Tribology-Key to the Efficient Engine, 1982, Instn. Mech. Engrs. Conf. Pub. C1/82.

[60] Lai, W., Rubin, D., Krempl, E. *Introduction to Continuum Mechanics.* Pergamon Press Inc. (1974).

[61] Craven, A., Holmes, R. *The Vibration of Engine Crankshafts – A Fast Numerical Solution.* Int. J. Num. Meth. Eng., 1972, 5, 17.

[62] Davis, R., Henshell, R., Warburton, G. *Constant Curvative Beam Finite Elements for in–plane Vibration.* J.S.V., 1972, 25(4), 561.

[63] Fettahlioglu, O., Mayers, J. *Consistent Treatment of External Deformations for the Bending of Arches, Curved Beams and Rings.* Trans. ASME, 1977, 99 (Series J), 2.

[64] Fettahlioglu, O., Toridis, T. *Elastic–Plastic Analysis of Curved Structures Subjected to Static and Dynamic Loads.* Trans. ASME, 1976, 98 (Series J), 126, 98 (Series J), 198.

[65] Hahn, H. *Dynamically Loaded Journal Bearings of Finite Length.* Proc. Instn. Mech. Engrs. 'Lub. and Wear', 1957, 100.

[66] Horsnell, R., McCallion, H. *Prediction of Some Journal Bearing Characteristics under Static and Dynamic Loading.* Proc. Instn. Mech. Engrs. 'Lubrication and Wear Conv,', 1963, 126.

[67] Booker, J., Shu, C. *Finite Element Analysis of Transient EHD Lubrication.* Dev. in Num. and Exp. Methods Applied to Trib. 10th Leeds-Lyon Symp. on Trib., 1983, 157.

[68] Rohde, S., Wicker, D., Booker, J. *EHD Squeeze Films : Effects of Viscoelasticity and Fluctuating Load.* Trans. ASME, 1979, 101 (Series F), 74.

[69] Zienkiewicz, O.C. *The Finite Element Method.* 3rd Edition, McGraw-Hill (1977).

[70] Finlayson, B.A. *The Method of Weighted Residuals and Variational Principles.* V87 Mathematics in Science and Engineering, Academic Press (1972).

[71] Rohde, S., Li, D. *A Generalised Short Bearing Theory.* Trans. ASME, 1980, 102 (Series F), 278.

[72] Hays, D. *A Variational Approach to Lubrication Problems and the Solution of the Finite Journal Bearing.* Trans. ASME, 1959, 81 (Series D), 13.

[73] Tanner, R.I., *The Estimation of Bearing Loads using Galerkin's Method.* Int. J. Mech. Sci., 1961, 3 (1961), 13.

[74] Reddi, M. *F.E. Solution of the Incompressible Lubrication Problem.* Trans. ASME, 1969, 91 (Series F), 524.

[75] Reddi, M., Chu, T. *F.E. Solution of Steady–State Compressible Lubrication Problem.* Trans. ASME, 1970, 92 (Series F), 495.

[76] Allan, T. *Application of F.E. Analysis to Hydrodynamic and Externally Pressurised Pocket Bearings.* Wear, 19 (1972), 169.

[77] Booker, J., Huebner, K. *Application of F.E.M. to Lubrication: An Engineering Approach.* Trans. ASME, 1972 94 (Series F), 313.

[78] Taylor, C., O'Callaghan, J. *A Numerical Solution of EHL Problem using F.E.* J. Mech. Eng. Sci., 14 (1972), 229.

[79] Wu, S., Oden, J. *A Note on Some Mathematical Studies on EHD Lubrication.* Int. J. Eng. Sci., 1987, 25 (6), 681.

[80] Douglas, J. Dupont, J. *A Galerkin Method for a Non–linear Direchlet Problem.* Math. of Compt., 29 (1975), 687.

[81] Cimatti, G. *On the Existence of Solutions for the Fundermental Problem of Hydrodynamic Lubrication.* Int. J. Eng. Sci., 17 (1979), 701.

[82] Kostreva, M.M. *Pressure Spikes and Stability Considerations in EHL Models.* Trans. ASME J. Trib., 1984, 106 (3), 386.

[83] Shu, C.F. *Transient EHL Analysis by F.E.M.* Ph.D thesis, Cornell University, 1981.

[84] Lambert, J.D. *Computational Methods in Ordinary Differential Equations.* Wiley and Sons (1973).

[85] Argyris, J., Vas, L., Willam, K. *Higher Order Methods for Transient Diffusion Analysis.* Compt. Methds. App. Mech. Eng., 12 (1977), 243.

[86] Gear, C.W. *Numerical Initial Value Problems in Ordinary Differential Equations.* Prentice-Hall (1971).

[87] Cheung, Y., Yeo, M. *A Practical Introduction to F.E. Analysis.* Pitman (1979).

[88] Szabo, B., Lee, G. *Derivation of Stiffness Matrices for Problems in Plane Elasticity by Galerkin's Method.* Int. J. Num. Meth. Eng., 1 (1969), 301.

[89] Fletcher, R. *Practical Methods of Optimisation.* Vol. 1 and 2. Wiley (1981).

[90] Milne, R.D. *Applied Functional Analysis – An Introductory Treatment.* Pitman (1980).

[91] Gill, P., Murray, W., Saunders, M. *Methods for Computing and Modifying LDV Factors of a Matrix.* Math. of Compt., 29 (1975), 1051.

[92] Norrie, D., De Vries, G. *An Introduction to F.E. Analysis.* Academic Press (1978).

[93] Cook, R.D. *Concepts and Applications of F.E Analysis.* 2nd Edition. Wiley and Sons (1981).

[94] Brebbia, C., Telles, J., Wrobel, L. *Boundary Element Techniques : Theory and Applications in Engineering.* Springer Verlag (1984).

[95] Timoshenko, S. *Strength of Materials : Part 1 Elementary.* 3rd Edition. D. Van Nostrand Co. (1955).

[96] Martin, F.A., Booker, J.F. *Influence of Engine Inertia Forces on Minimum Film Thickness in Con–Rod Big–End Bearings.* Proc. Instn. Mech. Engrs., 1966-67, **181 (1)**, 749.

[97] Cooke, W.L. *Performance of Dynamically Loaded Journal Bearings.* Parts 1 and 2, Dept. of Industry, National Engineering Laboratory. NEL Report No. 683 and 688 (1983).

[98] Goenka, P.K. *Dynamically Loaded Journal Bearings : Finite Element Method Analysis.* Trans. ASME J. Trib.. 1984, **106 (4)**, 429.

[99] Lloyd, T., McCallion, H. *A Computer Program for the Design of Reciprocating Engine Bearings.* Computers in Internal Combustion Engine Design Symp. Instn. Mech. Engrs., 1968, Paper 20, p.201.

[100] Lloyd, T., Horsnell, R., McCallion, H. *An Investigation into the Performance of Dynamically Loaded Journal Bearings : Design Study.* Proc. Instn. Mech. Engrs., 1966, **181 (3B)**, 28.

[101] Bayada, G. *Variational Formulation and Associated Algorithm for the Starved Finite Journal Bearing.* Trans. ASME, 1983, J. Lub. Tech. **105(3)**, 453.

APPENDIX A1

SPATIAL FILM DERIVATIVE

Equation (2.7) is a re-organisation of the classical material derivative formula[60] :

$$\frac{Dh}{Dt} = \frac{\partial h}{\partial t} + \underset{\sim}{\nabla} h.\underset{\sim}{V}$$

This expresses material film derivate $\frac{Dh}{Dt}$ (the time rate of change of a quantity at a material particle) in terms of the spatial derivative $\frac{\partial h}{\partial t}$ (the time rate of change of the quantity at a fixed spatial coordinate) and convective velocity $\underset{\sim}{\nabla} h.\underset{\sim}{V}$. (The influence of the material point and spatial frame moving with relative velocity $\underset{\sim}{V}$).

If a reference frame is chosen such that neither surface has spatial movement, then spatial derivative $\frac{\partial h}{\partial t}$ is zero and the problem steady-state.

Material derivative $\frac{Dh}{Dt}$ is the spatial velocity one would observe if $\underset{\sim}{V} = 0$, for then $\frac{Dh}{Dt} = \frac{\partial h}{\partial t}$. This amounts to the velocity of a material point when moving with the material frame.

In all cases, the material point in question is the one coincident with the spatial coordinate.

APPENDIX A2

FRICTION TRACTIONS

For an incompressible Newtonian fluid, surface friction tractions are determined using[44]:

$$\tau_{r\theta} = 2\mu e_{r\theta} \; ; \; e_{r\theta} = \tfrac{1}{2}\left[r \frac{\partial}{\partial r}\left[\frac{v_\theta}{r}\right] + \frac{1}{r}\frac{\partial v_r}{\partial \theta}\right] \qquad \text{(A2.1)}$$

For thin viscous shear films of negligible curvature, one obtains :

$$\tau_{r\theta} = \mu \frac{\partial v_\theta}{\partial r} \qquad \text{(A2.2)}$$

which upon substitution of film velocity (2.2) becomes :

$$\tau_{r\theta} = \mu\left[\frac{1}{2\mu r}\frac{\partial p}{\partial \theta}(2r - h_1 - h_2) + \frac{v_{\theta_2} - v_{\theta_1}}{h_2 - h_1}\right] \qquad \text{(A2.3)}$$

From Section 2.1.2d and 2.3.1 we obtain :

$$v_{\theta_2} - v_{\theta_1} = -\omega rs[1 + 0(\tfrac{c}{r})]$$

Thus, at the journal surface $r = h_1$, we obtain :

$$\tau_{r\theta}\big|_{h_1} = -\left[\frac{h}{2}\frac{1}{r}\frac{\partial p}{\partial \theta} + \frac{\mu\omega rs}{h}\right] \qquad \text{(A2.4)}$$

The total friction force ff on the journal is given by :

$$ff = -\iint_{\theta z} \tau_{r\theta}|_{h_1} \, r d\theta dz \quad (+ve \text{ anti-clock}) \tag{A2.5}$$

Discretisation : Taking the discretised expressions of Section 3.1.1 :

$$p \simeq \tilde{p}^e = g(z) N_i^e(\theta) \tilde{p}_i^e \; ; \; g(z) = \left[1 - \left[\frac{2z}{L}\right]^2\right]$$

friction force becomes :

$$ff = \iint_{\theta z} \left[\frac{h}{2} \frac{g}{r} \frac{\partial N_i^e}{\partial \theta} \tilde{p}_i^e + \frac{\mu \omega r s}{h}\right] r d\theta dz \tag{A2.6}$$

Integrating the axial (z) terms and non-dimensionalising according to Section 3.1.3 gives :

$$\hat{ff} = \frac{c}{r}\left[\frac{D}{L}\right]^2 \tfrac{1}{2} \int \left[\left[\frac{L}{D}\right]^2 \hat{h} \frac{\partial \hat{p}}{\partial \theta} + \frac{1}{12} \frac{s}{\hat{h}}\right] d\theta \tag{A2.7}$$

where

$$\hat{ff} = \frac{1}{6\mu\omega r n L}\left[\frac{c}{L}\right]^2 ff$$

Further simplifications result by applying the divergence theorem :

$$\int \hat{h} \frac{\partial \hat{p}}{\partial \theta} d\theta = -\int \frac{\partial \hat{h}}{\partial \theta} \hat{p} \, d\theta + (\hat{p}\hat{h})|_{\theta_1}^{\theta_2} ,$$

the latter term being zero. Now from Section 3.1.3

$$\hat{h} = 1 - \hat{\epsilon}\cos(\phi - \theta) + \hat{u}_r \; ; \; \frac{\partial \hat{h}}{\partial \theta} = -\hat{\epsilon}\sin(\phi - \theta) + \hat{u}_r'$$

giving

$$\int \hat{h} \, \frac{\partial \hat{p}}{\partial \theta} \, d\hat{\theta} = \int \left[\hat{\epsilon}\sin(\phi - \theta) - \hat{u}_r'\right] \hat{p} \, d\hat{\theta}$$

$$= (\hat{\epsilon}_y \hat{f}_x - \hat{\epsilon}_x \hat{f}_y) - \int \hat{u}_r' \, \hat{p} \, d\hat{\theta}$$

Thus

$$\hat{ff}\, \underset{\sim}{k} = \frac{c}{r}\left[\frac{D}{L}\right]^2 \tfrac{1}{2}\left[\left[\frac{L}{D}\right]^2 \left[-\underset{\sim}{\hat{\epsilon}} \times \underset{\sim}{\hat{f}}\right] + \int_{\hat{\theta}} \left[\frac{1}{12}\frac{s}{\hat{h}} - \left[\frac{L}{D}\right]^2 \hat{u}_r' \hat{p}\right] d\hat{\theta}\, \underset{\sim}{k}\right] \qquad \text{(A2.8)}$$

where

$$\underset{\sim}{\hat{\epsilon}} = \left[\hat{\epsilon}_x \underset{\sim}{i} + \hat{\epsilon}_y \underset{\sim}{j}\right] \; ; \; \underset{\sim}{\hat{f}} = \left[\hat{f}_x \underset{\sim}{i} + \hat{f}_y \underset{\sim}{j}\right] \qquad \text{(Section 3.1.3)}$$

Local coordinates ξ can be introduced into the above integral as per Section 4.1.3.

Applying order of magnitude arguments to equation (A2.8), it can be seen that :

$$0(\hat{ff}) = \left[\frac{c}{r}\right] . \, 0(\hat{f},\hat{p}).$$

Shear tractions are consequently much smaller than external load and normal (pressure) tractions.

APPENDIX A3

VOLUME FLUX

Expressions for the various volume fluxes $\underset{\sim}{Q}$ can be determined by integrating velocity expression (2.2) through the fluid film :

$$\underset{\sim}{Q} = \int_{h_1}^{h_2} \underset{\sim}{v}\, dr = -\frac{(h_2 - h_1)^3}{12\mu} \underset{\sim}{\nabla} p + \frac{h_2 - h_1}{2}(\underset{\sim}{V}_1 + \underset{\sim}{V}_2)$$

Applying expressions from Section 2.1.2d gives :

$$\underset{\sim}{Q} = -\frac{h^3}{12\mu}\left[\frac{1}{r}\frac{\partial p}{\partial \theta}\underset{\sim}{e}_\theta + \frac{\partial p}{\partial z}\underset{\sim}{e}_z\right] + \frac{h}{2}(\omega rs)\,\underset{\sim}{e}_\theta \,.$$

Discretisation : Taking the expressions of Section 3.1.1 :

$$p \simeq \tilde{p}^e = g(z)N_i^e(\theta)\tilde{p}_i^e \;;\; g(z) = \left[1 - \left[\frac{2z}{L}\right]^2\right]$$

and substituting into the above form gives :

$$\underset{\sim}{Q} = -\frac{h^3}{12\mu}\left[\frac{g}{r}\frac{\partial N_i^e}{\partial \theta}\underset{\sim}{e}_\theta + \frac{\partial g}{\partial z}N_i^e\underset{\sim}{e}_z\right]\tilde{p}_i^e + \frac{h}{2}(\omega rs)\,\underset{\sim}{e}_\theta \,.$$

Non-dimensionalising according to Section 3.1.3 gives :

$$\hat{\underset{\sim}{Q}} = -3\hat{h}^3\left[\frac{L}{D}\right]\left[\left[\frac{L}{D}\right] g \frac{\partial \hat{p}}{\partial \theta}\underset{\sim}{e}_\theta - 2\left[\frac{2z}{L}\right]\hat{p}\,\underset{\sim}{e}_z\right] + \frac{\hat{h}s}{2}\underset{\sim}{e}_\theta$$

where $\hat{\underset{\sim}{Q}} = \frac{1}{\omega cr}\underset{\sim}{Q}$ or component-wise

$$\hat{Q}_\theta = \frac{Q_\theta}{\omega cr} = -3\hat{h}^3 \left[\frac{L}{D}\right]^2 g \frac{\partial \hat{p}}{\partial \theta} + \frac{\hat{h}s}{2}$$

$$\hat{Q}_z = \frac{Q_z}{\omega c r} = 6\hat{h}^3 \left[\frac{L}{D}\right]\left[\frac{2z}{L}\right] \hat{p}$$

where

$$\hat{\underset{\sim}{Q}} = \left[\hat{Q}_\theta \underset{\sim}{e}_\theta + \hat{Q}_z \underset{\sim}{e}_z\right].$$

APPENDIX A4

CONNECTING-ROD DYNAMICS

Development of connecting-rod kinematic and dynamic relationships is undertaken in this Appendix, emphasis being placed upon achieving structural, as well as dynamic equivalence. However, before proceeding some notation simplification is in order : in this Appendix

$$\omega = \omega_1;\ \phi = \omega_2 t$$

(a) **Kinematics**

Picking up the notation of Section 2.1.2, then with respect to the X-Y frame one can write :

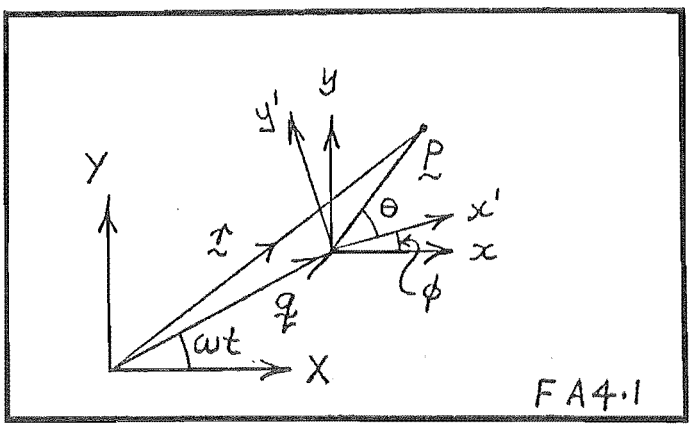

FA4·1

$$\underset{\sim}{r}(p,\theta) = \underset{\sim}{q} + \underset{\sim}{p} = R\left[e^{i\omega t} + \frac{p}{R}e^{i(\theta+\phi)}\right] \qquad (A4.1)$$

$$\dot{\underset{\sim}{r}}(p,\theta) = \omega Ri\left[e^{i\omega t} + \dot{\phi}\,\frac{p}{\omega R}e^{i(\theta+\phi)}\right] \qquad (A4.2)$$

$$\ddot{\underset{\sim}{r}}(p,\theta) = -\,\omega^2 R\left[e^{i\omega t} + (\dot{\phi}^2 - i\ddot{\phi})\,\frac{p}{\omega^2 R}e^{i(\theta+\phi)}\right] = (\ddot{r}_X,\ddot{r}_Y) \qquad (A4.3)$$

The acceleration at the big and small end is then, respectively :

$$\ddot{\underset{\sim}{r}}(0,0) = -\,\omega^2 R\, e^{i\omega t} = \ddot{\underset{\sim}{g}} \qquad (A4.4)$$

$$\ddot{\underset{\sim}{r}}(\ell,0) = -\,\omega^2 R\left[e^{i\omega t} + (\dot{\phi}^2 - i\ddot{\phi})\,\frac{\ell}{\omega^2 R}e^{i\phi}\right] \qquad (A4.5)$$

where ℓ is the rod length. Alternatively, in the x′-y′ frame the absolute acceleration is given by :

$$\ddot{r}'(p,\theta) = -\omega^2 R\left[e^{i(\omega t-\phi)} + (\dot{\phi}^2 - i\ddot{\phi})\frac{p}{\omega^2 R}e^{i\theta}\right]$$

giving big and little end accelerations :

$$\ddot{\underset{\sim}{r}}'(0,0) = -\omega^2 R\left[e^{i(\omega t-\phi)}\right] \qquad = \underset{\sim}{a}_b' \qquad \text{(A4.6)}$$

$$\ddot{\underset{\sim}{r}}'(\ell,0) = -\omega^2 R\left[e^{i(\omega t-\phi)} + (\dot{\phi}^2 - i\ddot{\phi})\frac{\ell}{\omega^2 R}\right] \qquad = \underset{\sim}{a}_\ell' \qquad \text{(A4.7)}$$

These expressions hold for any linkage undergoing circular translatory motion. For a connecting rod of length ℓ, the obliquity constraints

$$0 = r_Y = \dot{r}_Y = \ddot{r}_Y|_{(\ell,0)} \qquad \text{(A4.8)}$$

are introduced giving respectively the following ϕ constraints :

$$1 = -\frac{R}{\ell}\frac{\sin\omega t}{\sin\phi} \; ; \; \dot{\phi} = -\omega\frac{R}{\ell}\frac{\cos\omega t}{\cos\phi} \; ; \; \ddot{\phi} = \omega^2\frac{R}{\ell}\frac{\sin\omega t}{\cos\phi}\left[1 - \left[\frac{\dot{\phi}}{\omega}\right]^2\right] .$$

For a non-oblique rod, $\phi = \dot{\phi} = \ddot{\phi} = 0$.

(b) **Rod Dynamics**

Linear Momentum : Following Section 2.2.1 we have :

$$\int_V \rho \underset{\sim}{b} dV + \int_{S_\ell} (\underset{\sim}{t}_n)_\ell \, dS + \int_{S_b} (\underset{\sim}{t}_n)_b \, dS = 0 \qquad \text{(2.29)}$$

Now for a rigid body :

$$\int_V \rho \underset{\sim}{b} dV = - \int_V \rho \ddot{\underset{\sim}{r}}' dV = - m_g \underset{\sim}{a}_g'$$

where m_g is the total mass of the body, $\underset{\sim}{a}_g'$ the absolute acceleration of the centre of mass in reference frame x′-y′.

Conservation of linear momentum is then given by :

$$\underset{\sim}{t}_b' + \underset{\sim}{t}_\ell' - m_g \underset{\sim}{a}_g' = 0 \qquad \text{(A4.9)}$$

where $\underset{\sim}{t}_i' \equiv \int (\underset{\sim}{t}_n)_i \, dS$ (See F A4.2)

Angular Momentum :

Taking moments about point s, the expression of angular momentum becomes : (F A4.2)

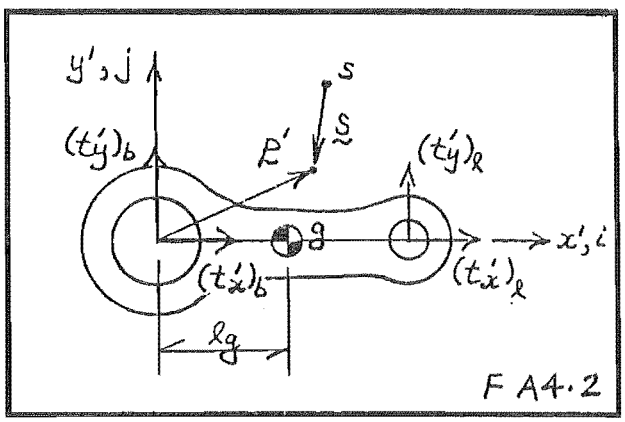

F A4·2

$$\int_V \underset{\sim}{s} \times \rho \underset{\sim}{b} dV + \int_{S_\ell} \underset{\sim}{s} \times (\underset{\sim}{t}_n)_\ell \, dS + \int_{S_b} \underset{\sim}{s} \times (\underset{\sim}{t}_n)_b \, dS = 0 \qquad \text{(A4.10)}$$

Writing $\underset{\sim}{r} = \underset{\sim}{q} + \underset{\sim}{p}$ and letting $\underset{\sim}{s} = \underset{\sim}{p}$, we obtain :

$$\underset{\sim}{s} \times \rho \underset{\sim}{b} = - \underset{\sim}{s} \times \rho \ddot{\underset{\sim}{r}} = - \left[\frac{d}{dt} (\underset{\sim}{s} \times \rho \dot{\underset{\sim}{p}}) + \underset{\sim}{s} \times \rho \ddot{\underset{\sim}{q}} \right]$$

but $$\dot{\underset{\sim}{p}} = \frac{d\underset{\sim}{p}'}{dt} + \dot{\underset{\sim}{\phi}} \times \underset{\sim}{p}' = \dot{\underset{\sim}{\phi}} \times \underset{\sim}{p}' \ , \text{ so}$$

$$\underset{\sim}{s} \times \rho \underset{\sim}{b} = -[\underset{\sim}{p}' \times \ddot{\underset{\sim}{\phi}} \times \rho \underset{\sim}{p}' + \underset{\sim}{p}' \times \rho \ddot{\underset{\sim}{q}}]$$

Now, for a rigid body :

$$\int \underset{\sim}{p}' \times \ddot{\underset{\sim}{\phi}} \times \rho \underset{\sim}{p}' dV = \ddot{\phi} \int \rho p^2 dV \quad \underset{\sim}{k} = I_b \ddot{\phi} \underset{\sim}{k}$$

$$\int \underset{\sim}{p}' \times \rho \ddot{\underset{\sim}{q}} dV = (m_g \ell_g \underset{\sim}{i}) \times \ddot{\underset{\sim}{q}}$$

where $I_b = I_g + m_g \ell_g^2$; I_b and I_g being respectively the mass moment of inertia about the big-end and centre of mass; ℓ_g the position of the centre of mass from the big-end. Conservation of angular momentum then becomes :

$$-\ddot{\phi}(I_g + m_g \ell_g^2)\underset{\sim}{k} - m_g \ell_g \underset{\sim}{i} \times \ddot{\underset{\sim}{q}} + \ell (t_y')_\ell \quad \underset{\sim}{k} = 0 \qquad \text{(A4.11)}$$

(c) **Piston Dynamics**

Linear Momentum : (F A4.3)

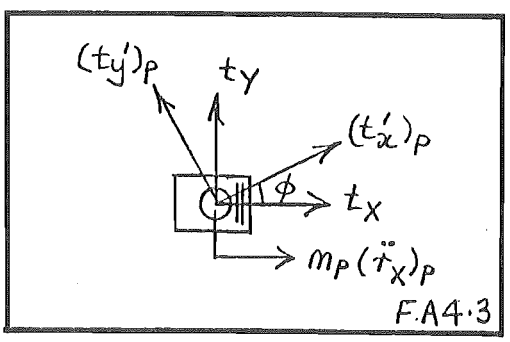

$$t_X = m_p(\ddot{r}_X)_p - pa \qquad \text{(A4.12)}$$

where m_p is the total piston mass,
pa the gas forces.

(d) **Rod-Piston Equilibrium** (F A4.2, A4.3)

$$\underset{\sim}{t}_\ell' + \underset{\sim}{t}_p' = 0 \quad \text{where} \quad \underset{\sim}{t}_p' = e^{-i\phi} \underset{\sim}{t}_X = \begin{bmatrix} \cos\phi & \sin\phi \\ -\sin\phi & \cos\phi \end{bmatrix} \begin{Bmatrix} t_X \\ t_Y \end{Bmatrix}$$

so

$$\underset{\sim}{t}_\ell' + e^{-i\phi} \underset{\sim}{t}_X = 0 \qquad \text{(A4.13)}$$

(e) System Solution

The above system of five equations (A4.9, .11, .13) in five unknowns ($\underset{\sim}{t}_b'$,$\underset{\sim}{t}_\ell'$,t_Y) is now fully determined. Taking A4.11, one obtains :

$$(t_y')_\ell = - m_\ell \omega^2 R\left[\sin(\omega t-\phi) - \frac{\ddot{\phi}\,\ell}{\omega^2 R}\left[\frac{I_g}{m_\ell \ell^2} + \frac{\ell_g}{\ell}\right]\right]$$

or rewriting in terms of A4.7 gives :

$$(t_y')_\ell = m_\ell (a_y')_\ell + m_* \ddot{\phi}\ell$$

where $$m_\ell = \frac{\ell_g}{\ell} m_g \;;\; m_b = \left[1 - \frac{\ell_g}{\ell}\right] m_g \;;\; m_* = \left[\frac{I_g - m_b \ell_g \ell}{\ell^2}\right]$$

$(t_y')_b$ can then be determined from A4.9 giving :

$$(t_y')_b = - m_b \omega^2 R\left[\sin(\omega t-\phi) + \frac{\ddot{\phi}\,\ell}{\omega^2 R}\left[\frac{I_g}{m_b \ell^2} - \frac{\ell_g}{\ell}\right]\right]$$

or, in terms of the big-end acceleration A4.6 :

$$(t_y')_b = m_b (a_y')_b - m_* \ddot{\phi}\ell$$

The x′ forces are next determined from A4.13 where :

$$t_Y = \frac{\sin\phi}{\cos\phi} t_X - \frac{1}{\cos\phi}(t_y')_\ell \quad \text{hence}$$

$$(t_x')_\ell = (t_y')_\ell \frac{\sin\phi}{\cos\phi} - t_X \frac{1}{\cos\phi}$$

$$= - m_\ell \omega^2 R\left[\cos(\omega t-\phi) + \frac{R}{\ell}\left[\frac{\cos\omega t}{\cos\phi}\right]^2 + \frac{\ddot{\phi}\,\ell}{\omega^2 R}\frac{\sin\phi}{\cos\phi}\left[1 - \frac{\ell_g}{\ell} - \frac{I_g}{m_\ell \ell^2}\right]\right]$$

$$+ (m_\ell + m_p)\omega^2 R\left[\frac{\cos\omega t}{\cos\phi} + \frac{R}{\ell}\left[\frac{\cos\omega t}{\cos\phi}\right]^2 + \frac{\ddot{\phi}\,\ell}{\omega^2 R}\frac{\sin\phi}{\cos\phi}\right] + \frac{pa}{\cos\phi} \quad .$$

Rewriting in terms of the small-end acceleration A4.7 :

$$(t_x')_\ell = m_\ell (a_x')_\ell + m_* \ddot{\phi}\ell \frac{\sin\phi}{\cos\phi} - \frac{1}{\cos\phi}[(m_\ell + m_p)(\ddot{r}_X)_p - pa] \quad .$$

The remaining big-end force is determined from A4.9 giving :

$$(t_x')_b = - m_b \omega^2 R\left[\cos(\omega t - \phi) + \frac{\ddot{\phi}\,\ell}{\omega^2 R}\left[\frac{I_g}{m_b \ell^2} - \frac{\ell_g}{\ell}\right]\right]$$

$$- (m_\ell + m_p)\omega^2 R\left[\frac{\cos\omega t}{\cos\phi} + \frac{R}{\ell}\left[\frac{\cos\omega t}{\cos\phi}\right]^2 + \frac{\ddot{\phi}\,\ell}{\omega^2 R}\frac{\sin\phi}{\cos\phi}\right] - \frac{pa}{\cos\phi} \quad .$$

Rewriting in terms of the big-end acceleration A4.6 :

$$(t_x')_b = m_b (a_x')_b - m_* \ddot{\phi}\ell \frac{\sin\phi}{\cos\phi} + \frac{1}{\cos\phi}\left[\left[m_\ell + m_p\right]\left[\ddot{r}_X\right]_p - pa\right] .$$

Summarising, the little-end forces are :

$$(t_x')_\ell = m_\ell(a_x')_\ell + \frac{\sin\phi}{\cos\phi}m_*\ddot{\phi}\ell - \frac{1}{\cos\phi}\left[\left[m_\ell + m_p\right]\left[\ddot{r}_X\right]_p - pa\right] \qquad (A4.14)$$

$$(t_y')_\ell = m_\ell(a_y')_\ell + m_*\ddot{\phi}\ell \qquad (A4.15)$$

whilst the big-end forces are given by :

$$(t_x')_b = m_b(a_x')_b - \frac{\sin\phi}{\cos\phi}m_*\ddot{\phi}\ell + \frac{1}{\cos\phi}\left[\left[m_\ell + m_p\right]\left[\ddot{r}_X\right]_p - pa\right] \qquad (A4.16)$$

$$(t_y')_b = m_b(a_y')_b - m_*\ddot{\phi}\ell \qquad (A4.17)$$

where

$$m_\ell = \frac{\ell_g}{\ell}m_g \; ; \; m_b = \left[1 - \frac{\ell_g}{\ell}\right]m_g \; ; \; m_* = \left[\frac{I_g - m_b\ell_g\ell}{\ell^2}\right] \; .$$

These expressions determine three appropriate mass lumpings for a dynamically equivalent connecting rod.

It will be observed that the linear accelerations $\underset{\sim}{a}'$, $\ddot{\phi}\ell$ and $(\ddot{r}_X)_p$ are all of similar magnitude, $0(\omega^2.R)$. The relative contributions to the big-end forces are therefore proportional to :

$$m_p,\ m_\ell,\ m_b,\ m_*$$

In practice, $m_\ell,\ m_b >> m_*$ allowing a two mass† lumping scheme to be used with little loss of accuracy.

---

† $m_b,\ (m_\ell + m_p)$

(f) Structural-Dynamic Consistency

Section 2.2.2 introduced body forces $\rho \underset{\sim}{b}^*$ in regions V* to achieve consistent structural loadings. Within frame x′ - y′ these are given by :

$$\underset{\sim}{b}^*(p,\theta) = \omega^2 R\left[e^{i(\omega t - \phi)} + \left[\dot{\phi}^2 - i\ddot{\phi}\right]\frac{p}{\omega^2 R}e^{i\theta}\right] . \qquad (A4.18)$$

However, to avoid further inconsistencies, the structural model to which these are applied must be of comparable geometry to that used in the dynamic model.

To this end, a structurally equivalent rod consisting of a ring of thickness t (with or without a neck) is firstly produced. (F A4.4 ii).

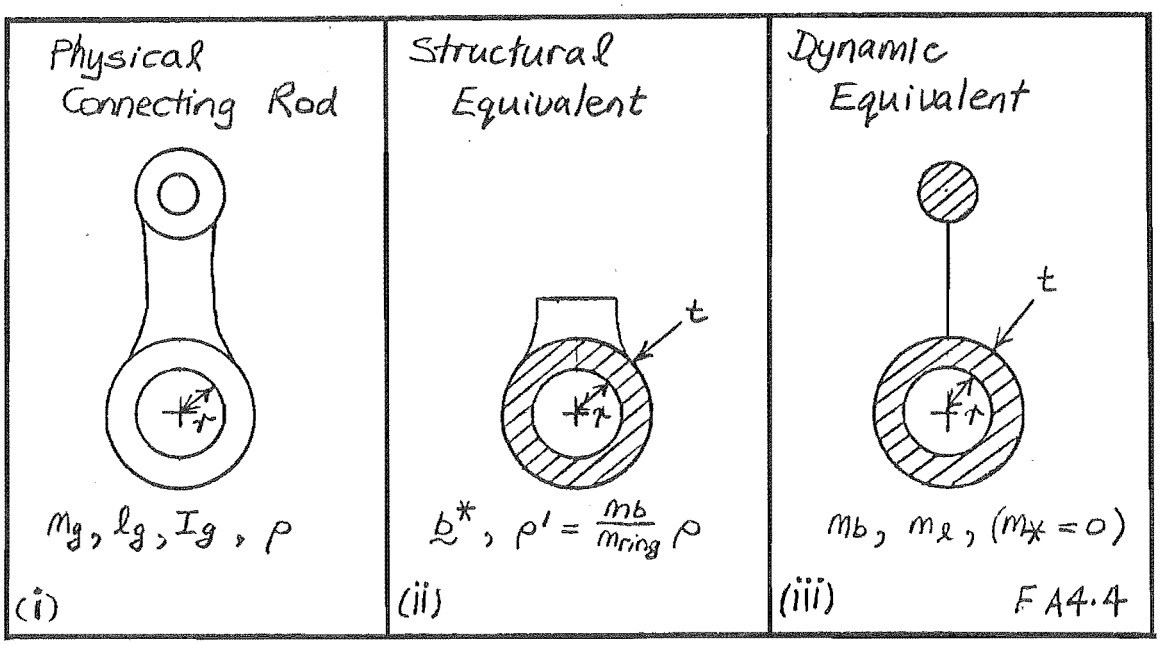

Thickness t is determined using equivalent cross-section second moments of area.

The dynamic equivalent is then constructed using a big-end ring of thickness t, density ρ' and small-end point mass m_ℓ (F A4.4 iii). Adjusted density ρ' is introduced to bring the ring mass in line with m_b, the dynamically

equivalent big-end mass :

$$\rho' = \frac{m_b}{m_{ring}} \cdot \rho$$

Such a construction has a small additional 'inertial mass' :

$$m_* = \frac{I_{ring}}{\ell^2} = \frac{m_b}{2}\left[\frac{(r + t)^2 - r^2}{\ell^2}\right] << m_b, m_\ell$$

This can be safely ignored along with the usual 'inertial mass' :

$$m_* = \left[\frac{I_g - m_b \ell_g \ell}{\ell^2}\right]$$

The application of $\underset{\sim}{b}^*$ to the structural model is then only on the ring (not the neck if one is present) using adjusted density ρ'. Structural and dynamic similarity are this way achieved.

(g) Non-Dimensional Load

To complete this Appendix, a non-dimensionalisation in keeping with the remainder of the work is presented :

Comparing forms (A4.9) and (2.30, .31, .32), it is apparent that $\underset{\sim}{f} = - \underset{\sim}{t}_b'$. Non-dimensionalising in accordance with (3.15,.16) we can write :

$$\hat{\underset{\sim}{f}} = \frac{m_t}{6} \frac{\omega R}{\mu n r L} \left[\frac{c}{L}\right]^2 \hat{\underset{\sim}{f}} \qquad \text{(A4.19)}$$

where m_t is the total rod/piston mass[†] and $\hat{\underset{\sim}{f}}$, dimensionless external load given by $-\underset{\sim}{t}_b/m_t\omega^2R$. Expanding :

$$\hat{f}_{x'} = \frac{m_b}{m_t}\cos(\omega t - \phi) + \frac{\sin\phi}{\cos\phi}\frac{m_*}{m_t}\frac{\ddot{\phi}\ell}{\omega^2 R} + \frac{1}{\cos\phi}\frac{pa}{m_t\omega^2 R}$$

$$+ \frac{1}{\cos\phi}\left[\frac{m_\ell + m_p}{m_t}\right]\left[\cos\omega t + \frac{\dot{\phi}^2\ell}{\omega^2 R}\cos\phi + \frac{\ddot{\phi}\ell}{\omega^2 R}\sin\phi\right]$$

$$\hat{f}_{y'} = \frac{m_b}{m_t}\sin(\omega t - \phi) + \frac{m_*}{m_t}\frac{\ddot{\phi}\ell}{\omega^2 R} \qquad \text{(A4.20)}$$

These are the forms used to generate the inertial and non-dimensional loads of Chapter Six and Seven.

[†] $m_t = (m_\ell + m_b + m_p)$

APPENDIX A5

CURVED BEAM CONSTANTS AND MATRICES

Constants c_i take on a variety of forms depending on the type of bending theory used :

c_i	Ref[62]	Thick Beam Theory	Thin Beam Theory	
			Extensional	Inextensional
c_1	-	$(1+iz)=\left[\frac{r_c}{r_o}\right]$	1	1
c_2	c_1	i	1	1
c_3	c_4	$\frac{1-iz(1-E/GK)}{1+iz(1+E/GK)}$	$\frac{1-z}{1+z}$	1
c_4	c_5	$\frac{2}{1+iz(1+E/GK)}$	$\frac{2}{1+z}$	1
c_5	c_6	$\frac{2i}{1+iz(1+E/GK)}$	$\frac{2}{1+z}$	1
c_6	c_7	$\frac{2i(1+iz)}{1+iz(1+E/GK)}$	$\frac{2}{1+z}$	1
				TA5

For rectangular sections :

$$z = \frac{I}{Ar_c^2} \; ; \; i = \frac{1}{z}\left[\frac{r_c}{r_e - r_i}\ell n\frac{r_e}{r_i} - 1\right] \quad .$$

See Timoshenko[95] for other sections (where m = iz).

Matrices X, Y and W of Section 3.2.1 are as follows :

$$X=\begin{bmatrix} 0 & -1 & 0 & 0 & -1 & 0 \\ -1 & 0 & 0 & c_3 & 0 & 1 \\ 0 & 0 & 0 & c_1c_4 & 0 & c_1 \\ -\sin\alpha & -\cos\alpha & -\alpha\sin\alpha & -\alpha\cos\alpha & -1 & 0 \\ -\cos\alpha & \sin\alpha & (c_3\sin\alpha-\alpha\cos\alpha) & (c_3\cos\alpha+\alpha\sin\alpha) & \alpha & 1 \\ 0 & 0 & c_1c_4\sin\alpha & c_1c_4\cos\alpha & c_1\alpha & c_1 \end{bmatrix}$$

$$Y=\begin{bmatrix} 0 & 0 & 0 & c_6 & 0 & 0 \\ 0 & 0 & c_6 & 0 & 0 & 0 \\ 0 & 0 & -c_5 & 0 & -c_2 & 0 \\ 0 & 0 & -c_6\sin\alpha & -c_6\cos\alpha & 0 & 0 \\ 0 & 0 & -c_6\cos\alpha & c_6\sin\alpha & 0 & 0 \\ 0 & 0 & c_5\cos\alpha & -c_5\sin\alpha & c_2 & 0 \end{bmatrix}$$

$$W=\begin{bmatrix} -\frac{\sin\alpha}{\alpha}-\frac{4\cos\alpha}{\alpha^2}-1+\frac{4}{\alpha^2} & -\frac{8}{\alpha^2}+\frac{4\sin\alpha}{\alpha}+\frac{8\cos\alpha}{\alpha^2} & (1-\frac{4}{\alpha^2})\cos\alpha-\frac{3\sin\alpha}{\alpha}+\frac{4}{\alpha^2} \\ -\frac{\cos\alpha}{\alpha}+\frac{4\sin\alpha}{\alpha^2}-\frac{3}{\alpha} & -\frac{8\sin\alpha}{\alpha^2}+\frac{4\cos\alpha}{\alpha}+\frac{4}{\alpha} & -(1-\frac{4}{\alpha^2})\sin\alpha-\frac{3\cos\alpha}{\alpha}-\frac{1}{\alpha} \\ (\frac{12}{\alpha^2}-1)\sin\alpha-\frac{6\cos\alpha}{\alpha}-\frac{6}{\alpha} & (4-\frac{24}{\alpha^2})\sin\alpha+\frac{16\cos\alpha}{\alpha}+\frac{8}{\alpha} & -(4-\frac{12}{\alpha^2})\sin\alpha-(\frac{10}{\alpha}-\alpha)\cos\alpha-\frac{2}{\alpha} \\ (\frac{12}{\alpha^2}-1)\cos\alpha+\frac{6\sin\alpha}{\alpha}-\frac{12}{\alpha^2}+1 & (4-\frac{24}{\alpha^2})\cos\alpha-\frac{16\sin\alpha}{\alpha}+\frac{24}{\alpha^2} & -(\alpha-\frac{10}{\alpha})\sin\alpha-(4-\frac{12}{\alpha^2})\cos\alpha-\frac{12}{\alpha^2} \\ -\frac{\alpha}{6} & -\frac{2\alpha}{3} & -\frac{\alpha}{6} \\ 0 & 0 & 0 \end{bmatrix}$$

where α is the included angle of the element.

APPENDIX A6

ELASTIC DISPLACEMENT TRIAL FUNCTIONS

A function ϕ, can be interpolated from four sets of nodal variables ϕ_i, $\frac{\partial \phi_i}{\partial u}$, $\frac{\partial \phi_i}{\partial v}$ through cubic Hermite functions N_i, M_i, P_i[69] :

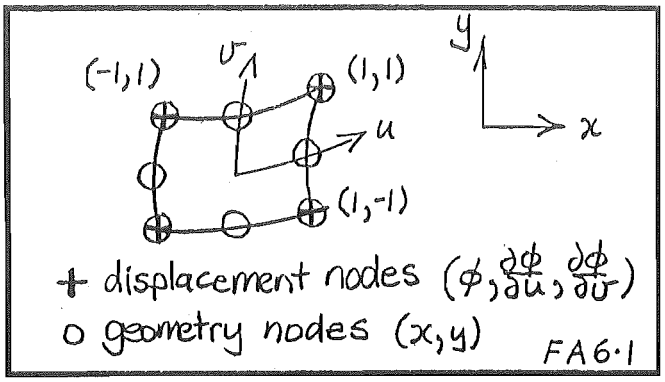

$$\phi = N_i(u,v)\phi_i + M_i(u,v)\frac{\partial \phi_i}{\partial u} + P_i(u,v)\frac{\partial \phi_i}{\partial v} \quad (i = 1,4)$$

where $$N_i = \frac{1}{8}(u_0 + 1)(v_0 + 1)(2 + u_0 + v_0 - u^2 - v^2)$$

$$M_i = \frac{1}{8}u_i(u_0 + 1)^2 (u_0 - 1)(v_0 + 1)$$

$$P_i = \frac{1}{8}v_i(u_0 + 1)(v_0 + 1)^2(v_0 - 1)$$

$$u_0 = u_i.u \; ; \; v_0 = v_i.v \quad .$$

This representation uses nodal derivatives set in the local coordinates u,v. More convenient global derivatives are obtained through a Jacobian representation of the chain-rule :

$$\begin{Bmatrix} \frac{\partial \phi}{\partial u} \\ \frac{\partial \phi}{\partial v} \end{Bmatrix}_i = [J]_i \begin{Bmatrix} \frac{\partial \phi}{\partial x} \\ \frac{\partial \phi}{\partial y} \end{Bmatrix}_i \; ; \; [J]_i = \begin{bmatrix} \frac{\partial x}{\partial u} & \frac{\partial y}{\partial u} \\ \frac{\partial x}{\partial v} & \frac{\partial y}{\partial v} \end{bmatrix}_i$$

giving $$\phi = \hat{N}_i \phi_i + \hat{M}_i \left[\frac{\partial \phi}{\partial x}\right]_i + \hat{P}_i \left[\frac{\partial \phi}{\partial y}\right]_i$$

where $$\hat{N}_i = N_i \; ; \; \hat{M}_i = M_i \left[\frac{\partial x}{\partial u}\right]_i + P_i \left[\frac{\partial x}{\partial v}\right]_i \; ; \; \hat{P}_i = M_i \left[\frac{\partial y}{\partial u}\right]_i + P_i \left[\frac{\partial y}{\partial v}\right]_i \; .$$

Jacobian [J] is determined from an 8-nodal quadratic geometry representation[69]:

$$x = Q_j x_j \; ; \; y = Q_j y_j \qquad (j = 1,8)$$

where $Q_j = \frac{1}{4}(1 + u_0)(1 + v_0)(u_0 + v_0 - 1)$ at corners.

$\frac{1}{2}(1 - u^2)(1 + v_0)$ at mid-sides, $u_j = 0$.

$\frac{1}{2}(1 + u_0)(1 - v^2)$ at mid-sides, $v_j = 0$.

Elastic displacement fields u_x and u_y are determined analogously :

$$\begin{Bmatrix} u_x \\ u_y \end{Bmatrix} = \begin{bmatrix} \hat{N} & O & \hat{M} & O & \hat{P} & O \\ O & \hat{N} & O & \hat{M} & O & \hat{P} \end{bmatrix}_i \qquad \begin{Bmatrix} u_x \\ u_y \\ \frac{\partial u_x}{\partial x} \\ \frac{\partial u_y}{\partial x} \\ \frac{\partial u_x}{\partial y} \\ \frac{\partial u_y}{\partial y} \end{Bmatrix}_i$$

If instead, nodal cylindrical polar coordinates are preferred, then [J] is evaluated with respect to cylindrical nodal coordinates and rotations performed on the pairs

(u_x,u_y), $\left[\frac{\partial u_x}{\partial x}, \frac{\partial u_y}{\partial x}\right]$, $\left[\frac{\partial u_x}{\partial y}, \frac{\partial u_y}{\partial y}\right]$. The nodal variables then become[60] :

$$\left\{u_r,u_\theta, \frac{\partial u_r}{\partial r}, \frac{\partial u_\theta}{\partial r}, \frac{1}{r}\left[\frac{\partial u_r}{\partial \theta} - u_\theta\right], \frac{1}{r}\left[\frac{\partial u_\theta}{\partial \theta} + u_r\right]\right\}_i$$

APPENDIX A7

RUSTON HORNSBY : 200, 400, 700 rpm RESULTS

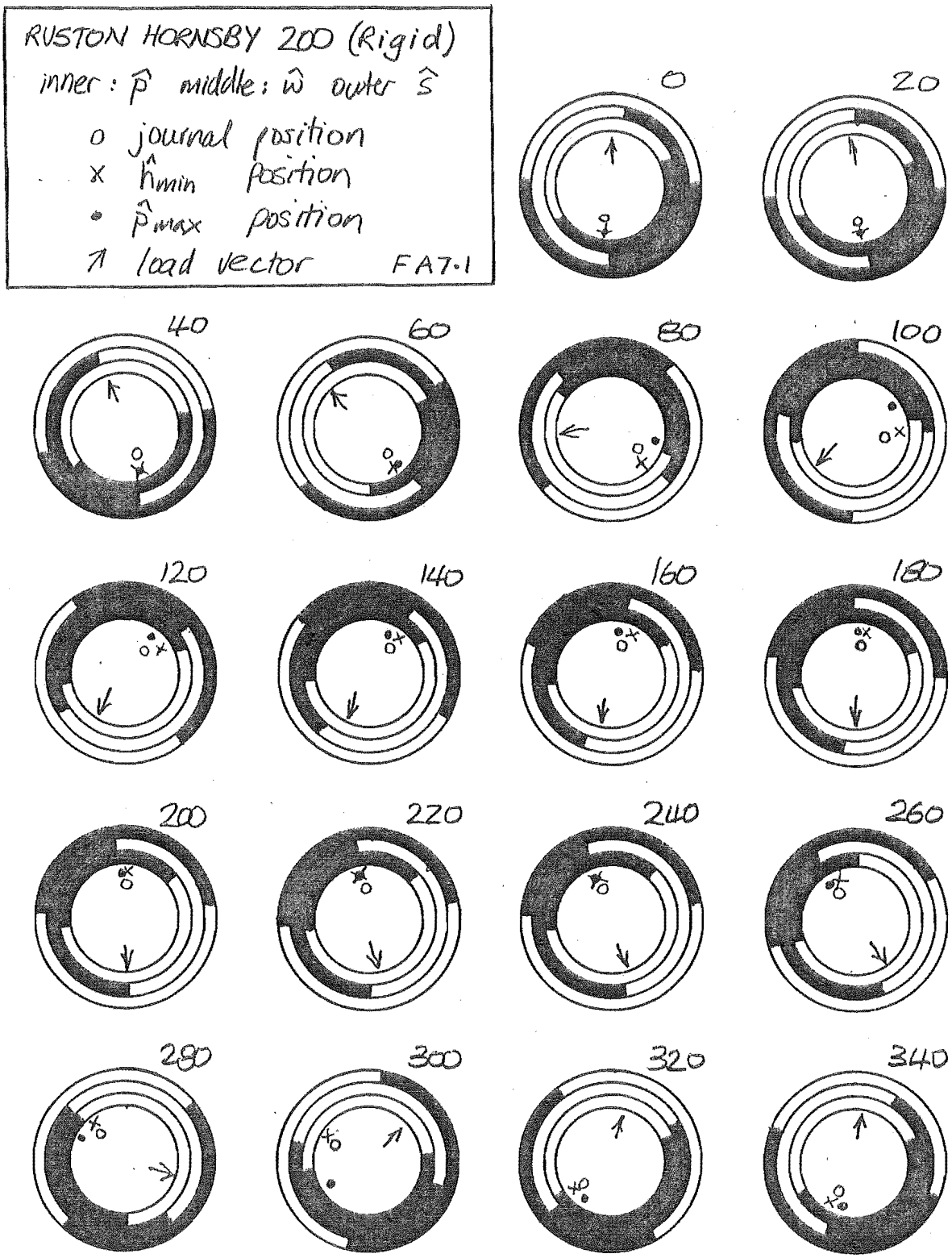

RUSTON HORNSBY 200 (Ring)
inner: $\hat{p}$ middle: $\hat{w}$ outer: $\hat{s}$

- o journal position
- x $\hat{h}_{min}$ position
- · $\hat{p}_{max}$ position
- ↗ load vector

FA7.2

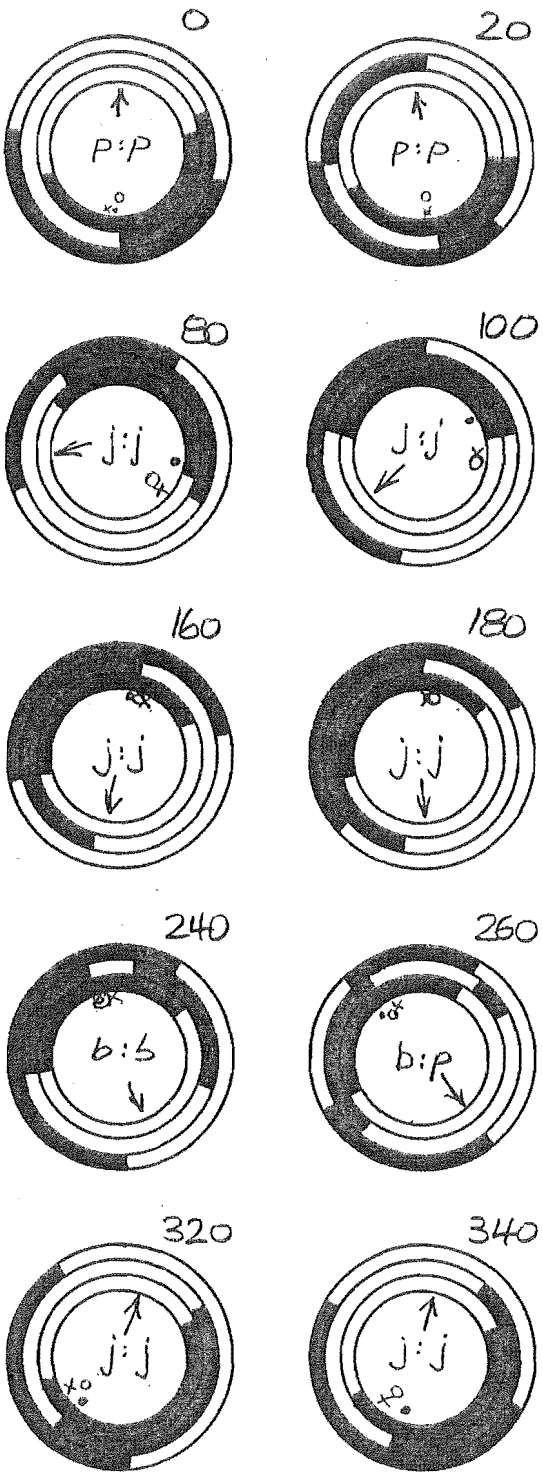

RUSTON HORNSBY 200 (Ring)
Elastic Distorsion
inner: total middle: $\hat{p}$ outer: $\hat{5}$
o journal position
• $\hat{p}_{max}$ position
↗ body-force
FA7.3

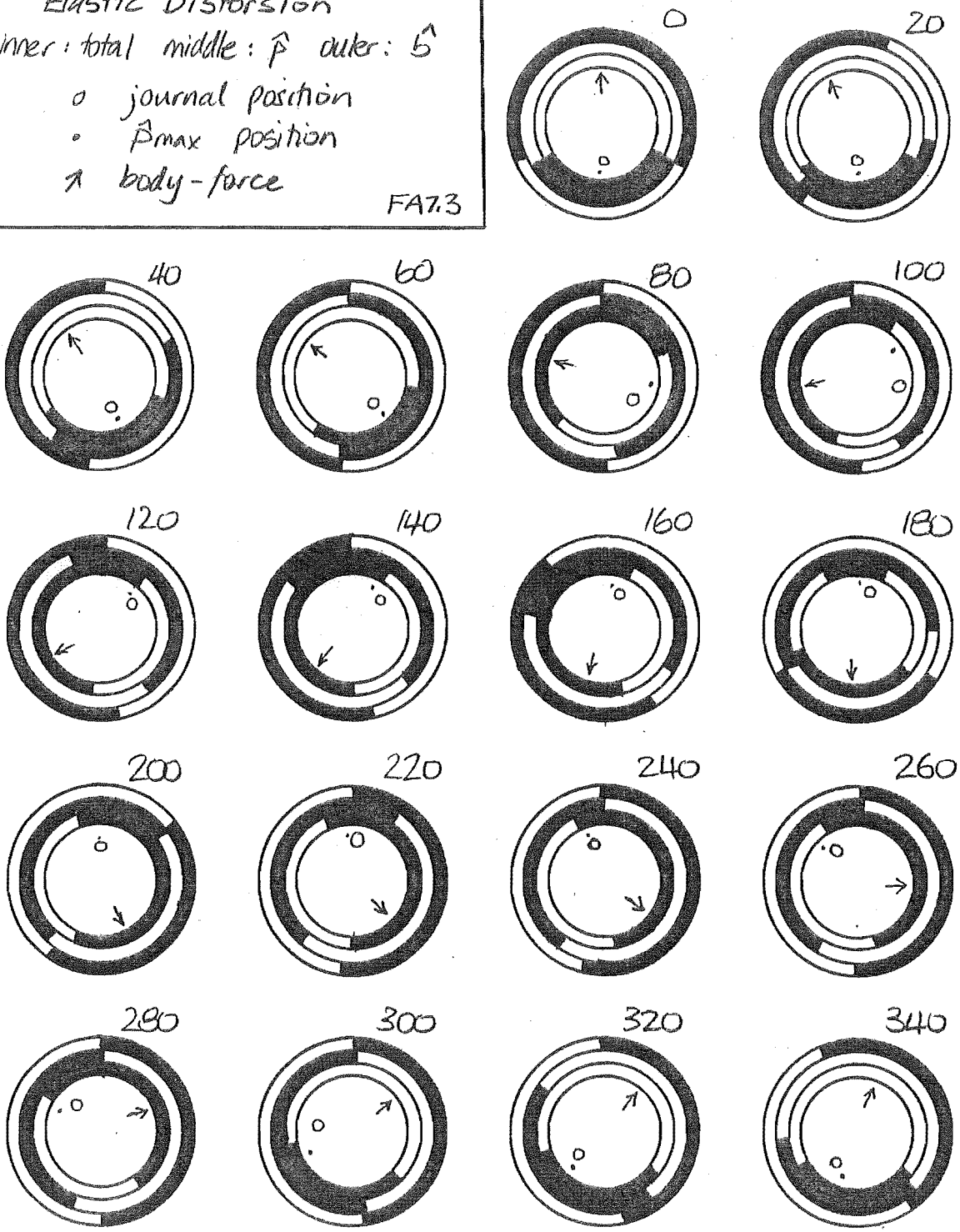

RUSTON HORNSBY 400 (Rigid)
inner: $\hat{p}$ middle: $\hat{w}$ outer: $\hat{s}$

o journal position
X $\hat{h}_{min}$ position
• $\hat{p}_{max}$ position
↗ load vector FA7.4

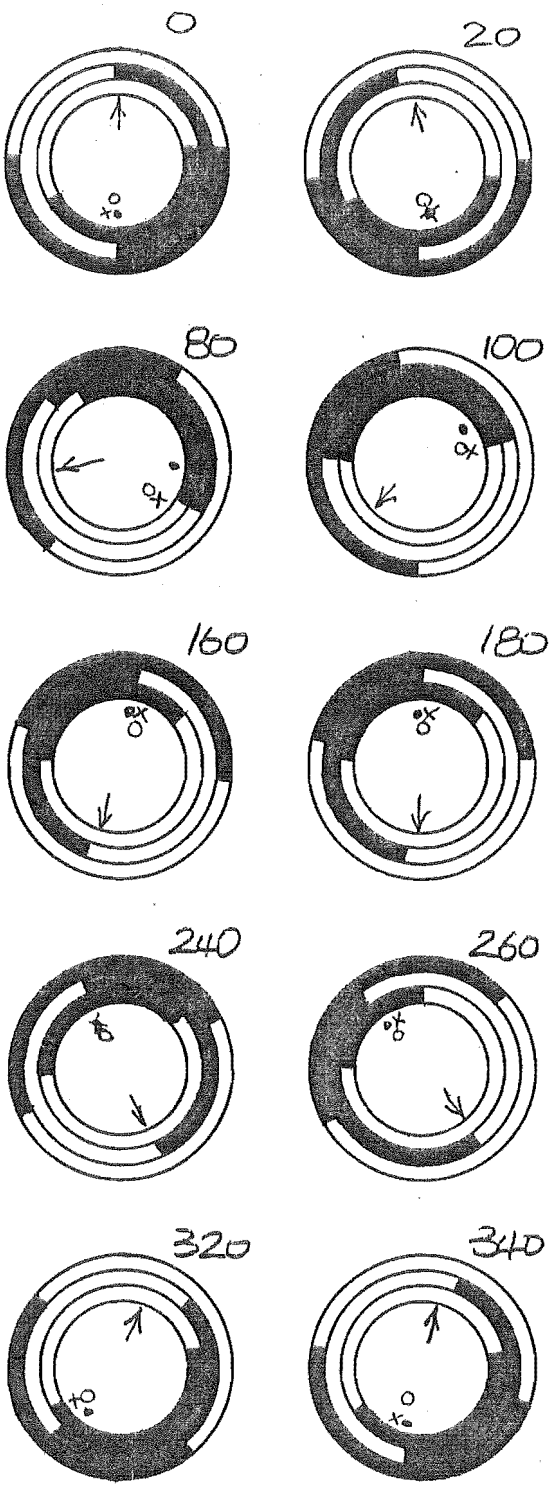

RUSTON HORNSBY 400 (Ring)
inner: $\hat{p}$ middle: $\hat{w}$ outer: $\hat{s}$

- o journal position
- x $\hat{h}_{min}$ position
- • $\hat{p}_{max}$ position
- ↗ load vector

F A7.5

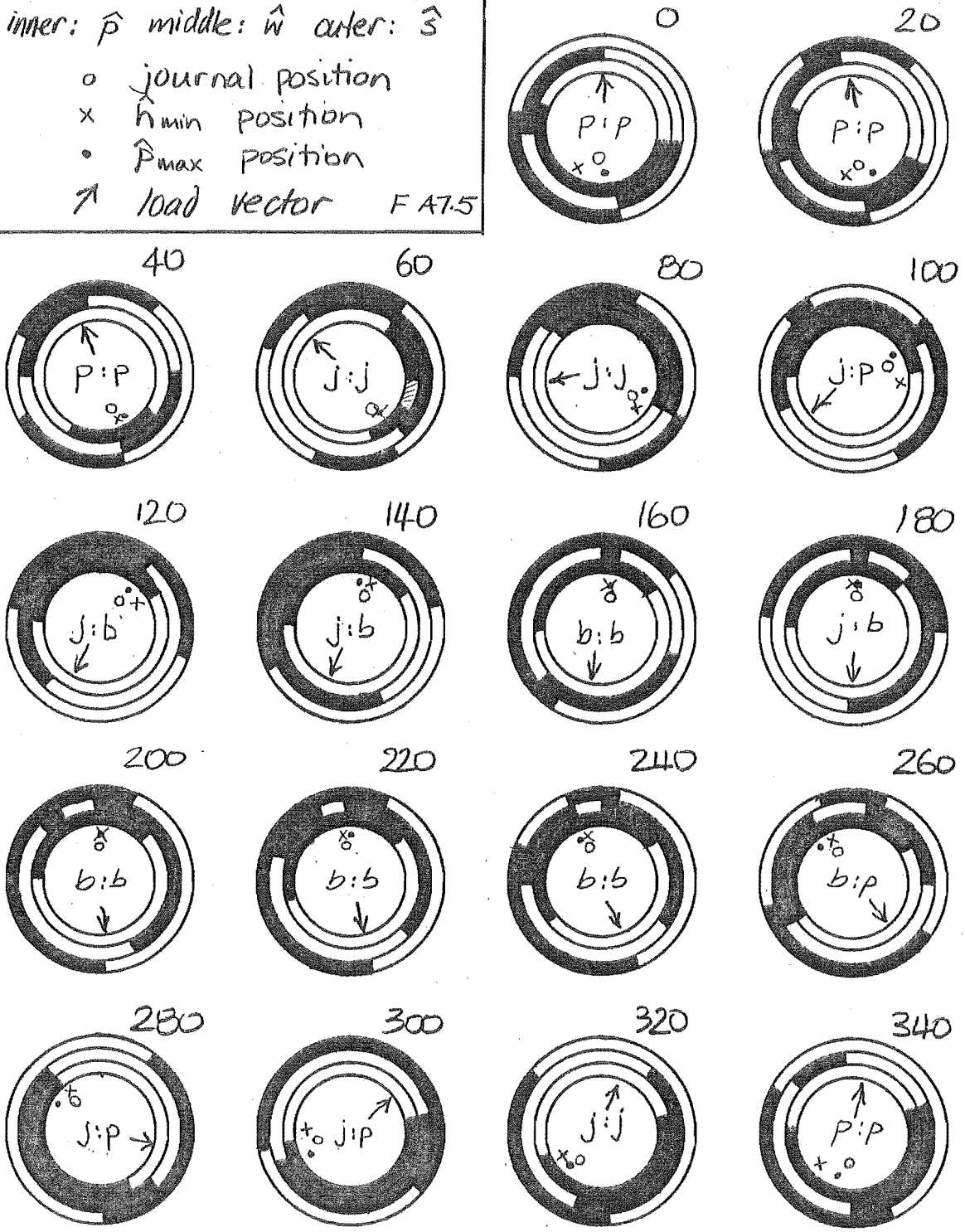

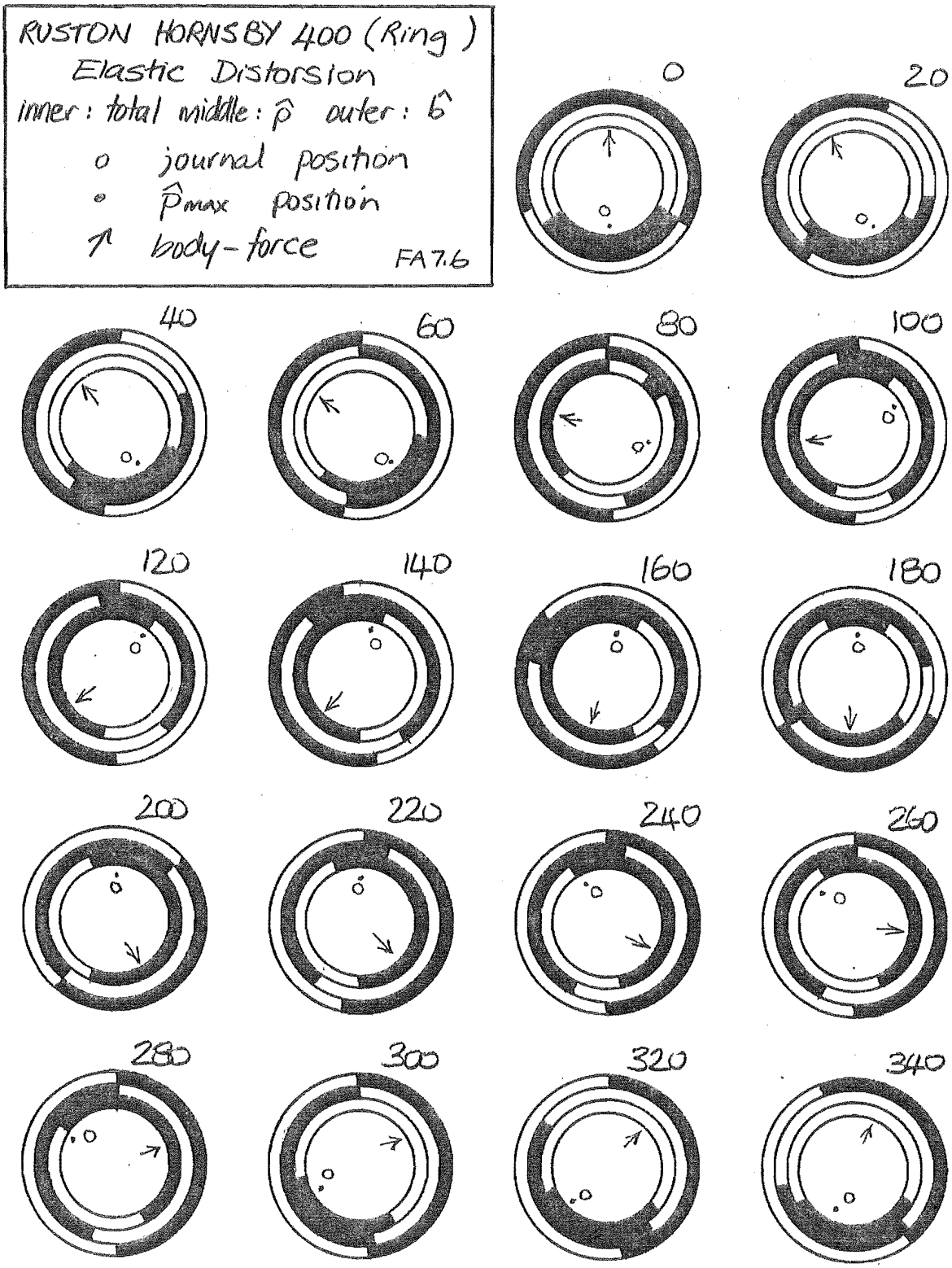
RUSTON HORNSBY 400 (Ring)
Elastic Distorsion
inner: total middle: $\hat{p}$ outer: $\hat{\sigma}$
o journal position
• $\hat{p}_{max}$ position
↑ body-force
FA7.6
0
20
40
60
80
100
120
140
160
180
200
220
240
260
280
300
320
340

KUSTON HORNSBY 700 (Rigid)

inner: $\hat{p}$ middle: $\hat{w}$ outer: $\hat{s}$

o journal position

× $\hat{h}_{min}$ position

• $\hat{P}_{max}$ position

↗ load vector FA7.7

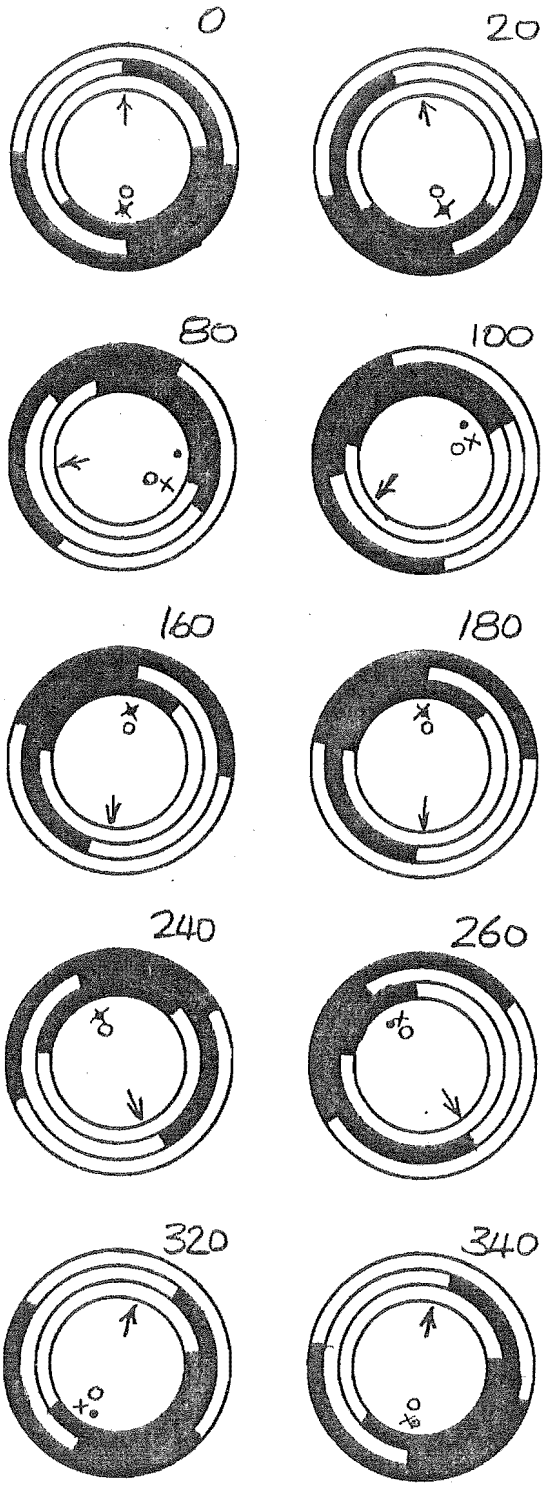

RUSTON HORNSBY 700 (Ring)

inner: $\hat{p}$ middle: $\hat{w}$ outer: $\hat{s}$

o journal position

× $\hat{h}_{min}$ position

• $\hat{P}_{max}$ position

↑ load vector F.A7.8

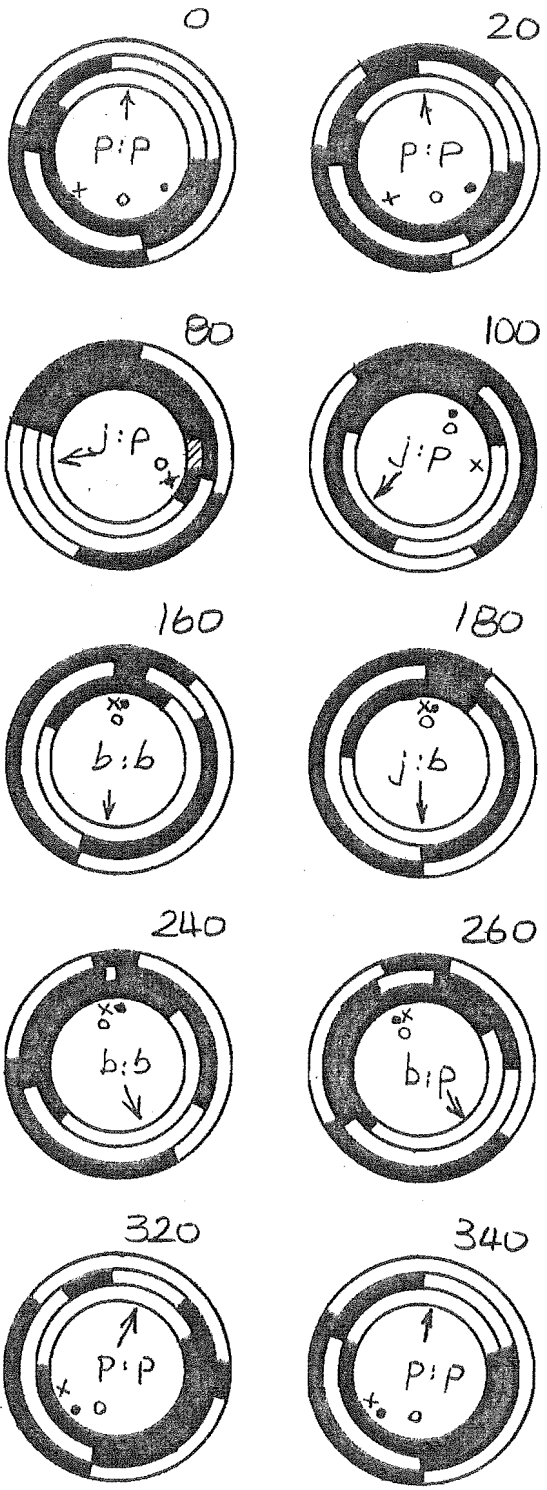

RUSTON HORNSBY 700 (Ring)
Elastic Distorsion
inner: total middle: $\hat{p}$ outer: $\hat{b}$

o journal position
• $\hat{p}_{max}$ position
↗ body-force F A7.9

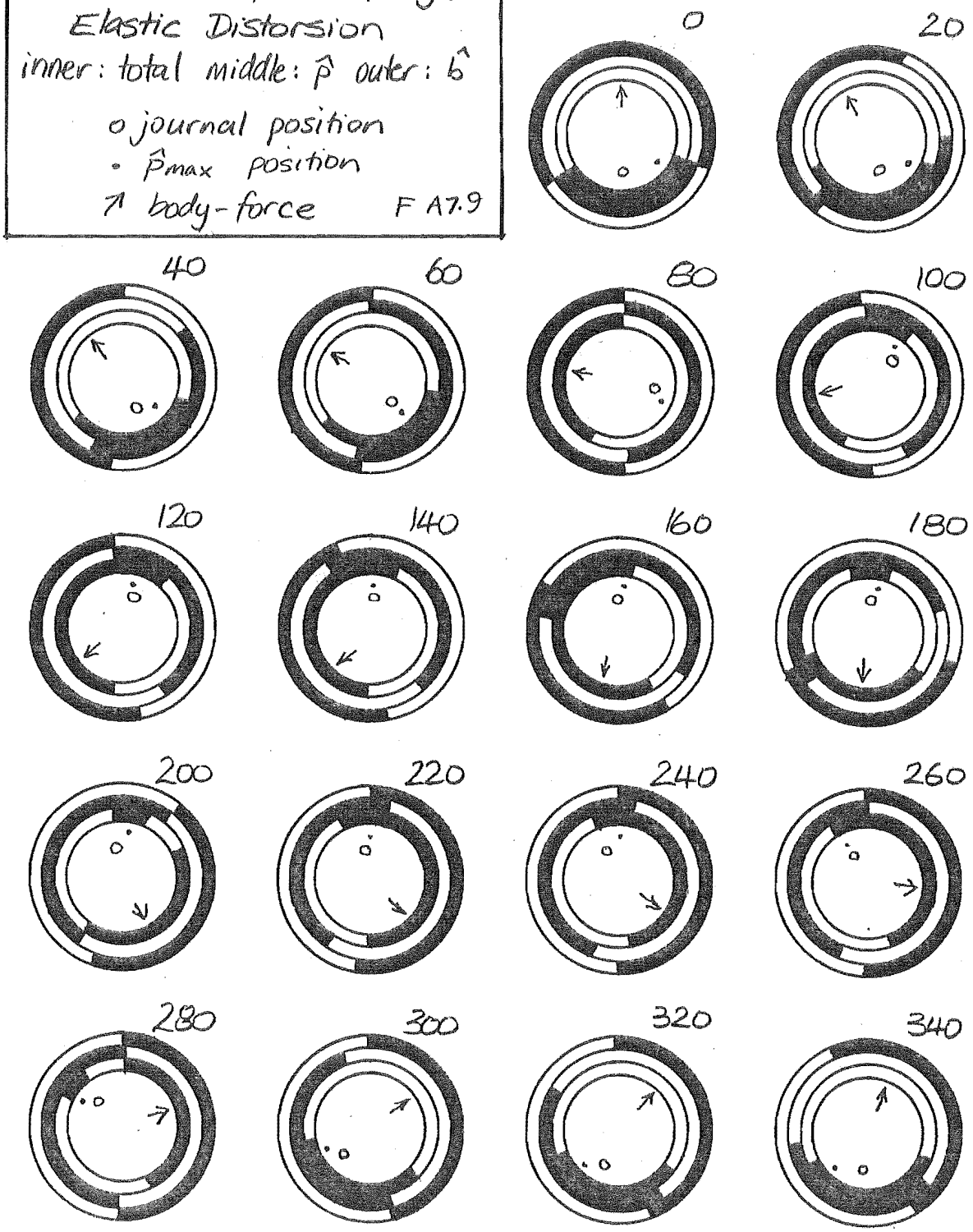

APPENDIX A8

BEARING PARAMETERS

(a) Ruston and Hornsby Bearing[6]

c = 0.00325" = 0.08255 mm

r = 4" = 0.1016 m

L = 2.25" = 0.05715 m

W = 5.2" = 0.1321 m

m_b = 120 lbf = 54.43 kg

m_t = 361 lbf = 163.74 kg

ω = 62.84 rad/sec (600 rpm)

$\mu = 2.17 \times 10^{-6}$ lbfs/in^2 = 0.01496 Ns/m^2

$E = 30 \times 10^6$ lbf/in^2 = 2.07×10^{11} N/m^2

t = 2" = 0.0508 m

ℓ = 30.8" = 0.7823 m

R = 7.25" = 0.1842 m

n = 2

L/D = 0.28125 $\quad$ R/ℓ = 0.2354 $\quad$ $\frac{r + t/2}{R} = 0.6897$

t/r = 0.5 $\quad$ $\frac{m_b}{m_t} = 0.3324$

$$\Lambda = \frac{24(.01496)(62.84)}{2.07 \times 10^{11}}(.28125)^2\left[\frac{4}{.00325}\right]^3 \cdot \frac{2(2.25)}{5.2} \cdot 96\,(1.25)^3$$

$= 2.61$

$$F = \frac{163.74}{6}\,\frac{(62.84)(.1842)}{(0.01496)2(0.05715)(.1016)}\left[\frac{.00325}{2.25}\right]^2$$

$= 3.79$

$$\Xi = \frac{m_b}{m_t} \cdot \Lambda F/2\pi = 0.5237$$

$\Delta = (2.61)(3.79) = 9.89$

(b) **Fantino's Bearing**[24]

The basic geometric parameters of Fantino's bearing are :

$L = 0.0228$ m — $m_p = 0.853$ kg

$R = 0.040$ m — $m_\ell = 0.316$ kg

$r = 0.027$ m — $m_b = 0.631$ kg

$c = 2\text{x}10^{-5}$ m — $m_t = 1.800$ kg

$\omega = 5500$ rpm $= 576$ rad/sec

$\mu = 0.0055$ Ns/m^2 — $\ell = 0.16$ m

$E = 2\text{x}10^{11}$ N/m^2 — $n = 1$

$\rho = 7860$ kg/m^3 — $W = 0.0228$ m

Standard Case : 5500 rpm

$t = 0.0135$ m — $t/r = 0.5$ — $R/\ell = 0.25$

$r = 0.027$ m — $L/D = 0.4222$ — $\frac{m_b}{m_t} = 0.351$

$$\Lambda = \frac{24(0.0055)(576)}{2\text{x}10^{11}}(0.4222)^2\left[\frac{0.027}{2\text{x}10^{-5}}\right]^3 12\left[\frac{1.25}{0.5}\right]^3$$

$$= 31.26$$

$$F = \frac{1.8}{6}\frac{(576)(0.040)}{(0.0055)(0.0228)(0.027)}\left[\frac{2\text{x}10^{-5}}{0.0228}\right]^2$$

$$= 1.57$$

$$\Xi = \frac{m_b}{m_t}\Lambda F/2\pi = 2.74$$

$$\Delta = \Lambda F = 49.08$$

For formulars based on density we note that :

$$m_{ring} = 4\pi(7860)(0.027)^3\frac{0.0228}{0.054}(0.5)(1.25) = 0.513 \text{ kg}$$

thus

$$\rho' = \frac{m_b}{m_{ring}}\rho = 1.23\rho = 9668 \text{ kg/m}^3$$

Effect of Reducing Journal Radius :

Taking the standard case and reducing journal radius 11% :

r = 0.024 m t/r = 0.5625 L/D = 0.4750

t = 0.0135 m

$$\Lambda = \frac{24(0.0055)(576)}{2x10^{11}}(0.4750)^2\left[\frac{0.024}{2x10^{-5}}\right]^3 12\left[\frac{1.28125}{0.5625}\right]^3$$

$$= 21.0$$

An estimate of total mass is obtained as follows :

$$m_b = 4\pi(9668)(0.024)^3\frac{0.0228}{0.048}(0.5625)(1.28125) = 0.575 \text{ kg}$$

$$m_t = m_b + m_\ell + m_p \simeq \frac{3}{2}m_b + m_p = 1.72 \text{ kg}$$

Hence our mass related numbers are :

$$F = \frac{1.72}{6}\frac{(576)(0.040)}{(0.0055)(0.0228)(0.024)}\left[\frac{2x10^{-5}}{0.0228}\right]^2$$

$$= 1.69$$

$$\Xi = \frac{0.575}{1.72}(1.69)(21.0)/2\pi = 1.89$$

$$\Delta = 35.49$$

Effect of Increasing the Radius of Gyration (k) :

Take the standard case and increase k (t) by 22% *without* increasing the rod mass, then :

t = 0.0165 m t/r = 0.6111

r = 0.027 m m_t = 0.631 kg

$$\Lambda = \frac{24(0.0055)(576)}{2x10^{11}}(0.4222)^2\left[\frac{0.027}{2x10^{-5}}\right] 12\left[\frac{1.3055}{0.6111}\right]^3$$

$$= 19.50$$

$$F = 1.57$$

$$\Xi = (0.351)(19.5)(1.57)/2\pi = 1.71$$

$$\Delta = 30.6$$

Reduce Radius and Increase Gyration :

Combining the above two effects we obtain :

r = 0.024 m t/r = 0.6875

t = 0.0165 m L/D = 0.4750

Notice that r + t is the same as the standard case; the standard rod is bored out to a smaller internal radius. This gives :

$$\Lambda = \frac{24(0.0055)(576)}{2x10^{11}}(0.4750)^2 \left[\frac{0.024}{2x10^{-5}}\right]^3 12\left[\frac{1.34375}{0.6875}\right]^3$$

$= 13.28$

F = 1.69 (mass unaltered by gyration increase)

$\Xi = 1.194$

$\Delta = 22.44$